Chapter 7

Reaction Path Modelling of Geological CO_2 Sequestration

In this chapter we will see how to predict the course of chemical reactions occurring during the geological disposal of CO_2, building on the thermodynamic and kinetic grounds that were reviewed in previous chapters.

It must be underscored that many early investigations on geological CO_2 storage took into account only trapping of gaseous or supercritical CO_2 as a separated "immiscible" phase under a low-permeability cap rock and CO_2 dissolution into the aqueous phase without considering the reactivity of the aquifer rock, although the latter effect can be very important, especially in the long term as shown below. However, recent studies devoted to geochemical modelling of CO_2 disposal in deep aquifers correctly took into account not only hydrodynamic and solubility trapping but also mineral trapping.

Let us return to suppose we want to know what happens if we inject CO_2 into a deep aquifer. Prior to CO_2 injection, it is reasonable to hypothesize that the aqueous solution stored in the deep aquifer is in (or close to) chemical equilibrium with a certain number of minerals, either the primary rock-forming minerals or, more likely, the authigenic solid phases produced through alteration of the primary minerals at *P–T–X* conditions different from those at which they formed. Although it makes a lot of difference to refer to the primary minerals rather than to the secondary minerals, here we do not want to reconstruct the evolution of the aquifer rock. Therefore, we simply hypothesize that we know somehow that the deep aqueous solution is in equilibrium with some specified minerals.

7.1. The reconstruction of the initial (before CO_2 injection) aqueous solution: speciation-saturation calculations

It was shown (e.g., Michard et al., 1981; Chiodini et al., 1991) that the chemical composition of an aqueous solution can be computed, by means of suitable speciation-saturation calculations, if we specify the temperature, the pressure, a certain number of minerals with which the aqueous solution is assumed to be in equilibrium (one for each compatible chemical component, e.g. Na^+, K^+, Ca^{2+}, Mg^{2+}, Al^{3+}, SiO_2), f_{CO_2}, which fixes HCO_3^- activity, and the total concentration of each mobile component (e.g., Cl^-). If multivalent elements, such as Fe, Mn and S, are also present in the considered system, further complications arise. A general, complete account on this subject is given by Van Zeggeren and Storey (1970) and Smith and Missen (1982). But let us proceed step by step.

7.1.1. The aqueous solution/calcite example

One of the simplest examples, which is treated in many textbooks, is that of computing the composition of the aqueous solution in equilibrium with calcite at given conditions, e.g. temperature = 25°C, pressure = 1 bar and $P_{CO_2} = 10^{-3.5}$ bar (average atmospheric value). In this case we have to take into account the thermodynamic constants of the dissociation reactions of apparent carbonic acid, bicarbonate ion and water (6-186, 6-187 and 6-188, respectively), i.e.:

$$K_{H_2CO_3^*} = \frac{a_{HCO_3^-} \cdot a_{H^+}}{a_{H_2CO_3^*}} = 10^{-6.35}, \tag{7-1}$$

$$K_{HCO_3^-} = \frac{a_{CO_3^{2-}} \cdot a_{H^+}}{a_{HCO_3^-}} = 10^{-10.33}, \tag{7-2}$$

$$K_{H_2O} = \frac{a_{OH^-} \cdot a_{H^+}}{a_{H_2O}} = 10^{-14.00}, \tag{7-3}$$

respectively, the thermodynamic constant of the dissolution reaction of gaseous CO_2 (6-200):

$$K_{CO_{2(g)}} = \frac{a_{H_2CO_3^*}}{f_{CO_2} \cdot a_{H_2O}} = 10^{-1.47}, \tag{7-4}$$

the solubility product of calcite, which is conveniently expressed as follows, referring to the sum of reaction (6-189) and the reverse of reaction (6-187):

$$K_{calcite} = \frac{K_{sp}}{K_{HCO_3^-}} = \frac{a_{HCO_3^-} a_{Ca^{2+}}}{a_{H^+} \cdot a_{calcite}} = 10^{+1.85}, \tag{7-5}$$

and the electroneutrality condition

$$2 \cdot m_{Ca^{2+}} + m_{H^+} = m_{HCO_3^-} + 2 \cdot m_{CO_3^{2-}} + m_{OH^-}. \tag{7-6}$$

Note that we have implicitly made some simplifications, in that we have neglected the formation of complex species, such as $CaHCO_3^+$ and $CaCO_3°$. If we want to keep calculations to a simple level, further simplifications are needed, namely $a_{H_2O} = 1$, $a_{calcite} = 1$, $f_{CO_2} = P_{CO_2}$ and $a_i = m_i$ (i.e. $\gamma_i = 1$) for all solutes. Through suitable substitutions, the

following equation is obtained:

$$\frac{2\cdot 10^{+1.85}\cdot a_{H^+}^2}{10^{-6.35}\cdot 10^{-1.47}\cdot 10^{-3.5}} + a_{H^+} - \frac{10^{-6.35}\cdot 10^{-1.47}\cdot 10^{-3.5}}{a_{H^+}} - \frac{2\cdot 10^{-10.33}\cdot 10^{-6.35}\cdot 10^{-1.47}\cdot 10^{-3.5}}{a_{H^+}^2} - \frac{10^{-14.00}}{a_{H^+}} = 0. \tag{7-7}$$

This is a fourth-order polynomial equation with respect to a_{H^+} and its solution without the aid of a computer is a formidable task. By using an electronic spreadsheet we can vary a_{H^+} until the left-hand side of equation (7-7) changes sign and tends to 0. In this way a pH of 8.26 is obtained. Based on this pH value, the concentrations of other solutes are then easily computed by means of equations (7-1) to (7-5).

Alternatively, we can assume that $m_{Ca^{2+}} \gg m_{H^+}$ and $m_{HCO_3^-} \gg 2\cdot m_{CO_3^{2-}} + m_{OH^-}$, conditions that have to be verified afterwards. Under these assumptions, equation (7-7) simplifies to

$$\frac{2\cdot 10^{+1.85}\cdot a_{H^+}^2}{10^{-6.35}\cdot 10^{-1.47}\cdot 10^{-3.5}} - \frac{10^{-6.35}\cdot 10^{-1.47}\cdot 10^{-3.5}}{a_{H^+}} = 0. \tag{7-8}$$

Equation (7-8) can be easily solved obtaining again pH = 8.26, the same pH value we have found by solving equation (7-7).

Although this coincidence is encouraging, we cannot think to export this approach to more complex problems. In addition, some of the assumptions introduced above may fail: for instance, at high temperature and high ionic strength $\gamma_i \neq 1$ and $a_{H_2O} \neq 1$; at high pressure $f_{CO_2} \neq P_{CO_2}$; if the considered mineral is not a pure phase its activity is different from unity.

The use of a speciation-saturation code, such as EQ3NR (Wolery, 1992) is mandatory if we want sound results, even in the simple aqueous solution/calcite example. The input file given in Table 7.1 can be used to compute the concentrations and activities of all solute species in an aqueous solution in equilibrium with calcite at temperature = 25°C, pressure = 1 bar and $f_{CO_2} = 10^{-3.5}$ bar. Without entering too much into the details of this code, we are basically saying that: (i) the activity of Ca^{2+} ion is fixed by equilibrium with calcite, (ii) the activity of HCO_3^- ion is governed by equilibrium with a hypothetical, infinite gas reservoir that fixes the f_{CO_2} of the considered system at $10^{-3.5}$ bar and (iii) pH is initially set at 8.26 ($\log a_{H^+} = -8.26$), but the code has to recalculate it by using the electroneutrality conditions. These are exactly the same conditions used above to compute the approximated pH value, which is now inserted as an input value in EQ3NR (note that it is not necessary to compute an approximated pH value to run this code; EQ3NR is able to run with any pH values or almost so). Note also that, although this exercise has no redox aspect, we set the log oxygen fugacity to −0.678 (the atmospheric value) to avoid possible computational problems.

TABLE 7.1

EQ3NR input file to compute the speciation of the aqueous solution in equilibrium with calcite at 25°C, 1 bar under a f_{CO_2} of $10^{-3.5}$ bar (required input formats are not fully respected).

```
Water in equilibrium with calcite at 25°C and atmospheric P_CO2
Use SUP database

endit.
      tempc = 2.50000E+01
        rho = 1.00000E+00    tdspkg = 0.00000E+00    tdspl = 0.00000E+00
        fep = −0.678         uredox =
      tolbt = 0.00000E+00    toldl = 0.00000E+00     tolsat = 0.00000E+00
     itermx= 0
*           1       2       3       4       5       6       7       8       9      10
  iopt1–10 = 0       0       0       0       0       0       0       0       0       0
  iopg1–10 = 0       0       0       0       0       0       0       0       0       0
  iopr1–10 = 0       0       0       1       0       0       0      −1       0       0
 iopr11–20 = 0       0       0       0       0       0       0       0       0       0
  iodb1–10 = 0       0       0       0       0       0       0       0       0       0
      uebal =  H+
     nxmod =   0
data file master species = H+
    switch with species =
    jflag = 16    csp =−8.26
data file master species = Ca++
    switch with species =
    jflag = 19    csp = 0.
mineral = Calcite
data file master species = HCO3-
    switch with species =
    jflag = 21    csp = −3.5000
 mineral = CO2(g)
endit.
```

The most important parts of the EQ3NR output file are summarized in Table 7.2, which indicates that the pH sought is 8.2748, which is only 0.01 pH units higher than the approximated value computed by means of equations (7-7) and (7-8). In spite of this small difference in pH, Table 7.2 shows that (i) activity coefficients computed by EQ3NR using the extended (B-dot) Debye–Hückel equation (see Chapter 4) deviate somewhat from the value of 1, which was assumed above; these deviations are greater for the divalent ions (e.g., $\gamma_{Ca^{2+}} = 0.8445$ and $\gamma_{CO_3^{2-}} = 0.8451$) than for the monovalent ions (e.g., $\gamma_{HCO_3^-} = 0.9587$ and $\gamma_{H^+} = 0.9598$); (ii) the aqueous complexes $CaCO_3^\circ$ and $CaHCO_3^+$ have concentrations of the same order of magnitude of CO_3^{2-} ion and, therefore, cannot be neglected.

7.1.2. The aqueous solution/multimineral paragenesis general case

A more general case is that of an aqueous solution assumed to be in equilibrium with a paragenesis comprising several solid phases. Again, in this case, the only way to

TABLE 7.2

Part of the EQ3NR output file showing the speciation of the aqueous solution saturated with calcite at 25°C, 1 bar under a f_{CO_2} of $10^{-3.5}$ bar

Species	Molality	Log molality	Log gamma	Log activity
HCO_3^-	9.5399E–04	−3.0205	−0.0183	−3.0388
Ca^{++}	4.8536E–04	−3.3139	−0.0734	−3.3874
O_2(aq)	2.6518E–04	−3.5765	0.0002	−3.5763
CO_2(aq)	1.0739E–05	−4.9691	0.0002	−4.9689
CO_3^{--}	9.5589E–06	−5.0196	−0.0731	−5.0927
$CaCO_3$(aq)	7.0307E–06	−5.1530	0.0000	−5.1530
$CaHCO_3^+$	4.3597E–06	−5.3605	−0.0189	−5.3794
OH^-	1.9873E–06	−5.7017	−0.0185	−5.7203
H^+	5.5335E–09	−8.2570	−0.0178	−8.2748

compute the speciation/saturation state of the aqueous solution is by running a suitable computer code, such as EQ3NR.

If the problem has a redox aspect, we have to assume redox equilibrium, at least if we are using version 7 of the software package EQ3/6, despite most natural systems are far from this ideal condition (e.g., Lindberg and Runnells, 1984), and we have to specify the redox potential of the system, in terms of f_{O_2}, or Eh, or pe, or through a suitable f_{O_2}-controlling reaction.

Let us assume that we want to compute the speciation/saturation state of the aqueous solution in equilibrium with analcime, calcite, kaolinite, daphnite, clinochlore, chalcedony and magnetite at 60°C, 1 bar under a f_{CO_2}, of 10^{-1} bar. Note that this paragenesis include a zeolite, analcime and some phyllosilicates, namely kaolinite, daphnite and clinochlore. The latter two minerals belong to the chlorite group and are assumed to have 14 Å basal spacing. These solid phases are typical of systems of relatively low temperature, as indicated by the relationship between hydrothermal alteration minerals and temperature in active geothermal systems and in hydrothermal ore deposits, representing their fossil analogues (e.g., Henley and Ellis, 1983).

In setting up the EQ3 input file (see Table 7.3), we state that Na^+ activity is fixed by analcime, Ca^{2+} activity by calcite, aqueous SiO_2 activity by chalcedony, Al^{3+} activity by kaolinite, Mg^{2+} activity by clinochlore [$Mg_5Al_2Si_3O_{10}(OH)_8$] and Fe^{2+} activity by daphnite [$Fe_5Al_2Si_3O_{10}(OH)_8$]. Since also magnetite [$FeO \cdot Fe_2O_3$] is part of our mineral paragenesis, the f_{O_2} of the system is uniquely fixed by daphnite–magnetite coexistence, under the redox equilibrium hypothesis. Note that the role of the daphnite–magnetite pair is explicitly declared in the input file (Table 7.3) by writing that daphnite controls Fe^{2+} activity and that magnetite constrains $O_{2(g)}$ activity (incidentally, we have also to set the switch iopt1 to −3, to follow EQ3 instructions).

Similar to the aqueous solution/calcite example: (i) the activity of HCO_3^-, ion is fixed setting f_{CO_2}, although a value of 10^{-1} bar is chosen in this case, and (ii) pH is initially set at 7.00, but the code is instructed to recompute it based on the electroneutrality conditions. In addition, total chloride concentration is assumed to be 0.03 mol kg^{-1}.

TABLE 7.3

EQ3NR input file to compute the speciation/saturation state of the aqueous solution in equilibrium with analcime, calcite, kaolinite, daphnite, clinochlore, chalcedony and magnetite at 60°C, 1 bar under a f_{CO_2} of 10^{-1} bar (required input formats are not fully respected).

```
. . . omissis
endit.
      tempc=  60.0000E+00
        rho=  1.00000E+00        tdspkg=  0.00000E+00        tdspl=  0.00000E+00
        fep=  0.00000E+00        uredox=
      tolbt=  0.00000E+00          toldl=  0.00000E+00        tolsat=  0.00000E+00
     itermx=  0
*                    1       2       3       4       5       6       7       8       9      10
   iopt1-10=        -3       0       0       0       0       0       0       0       0       0
   iopg1-10=         0       0       0       0       0       0       0       0       0       0
   iopr1-10=         0       0       0       0       0       0       0       0       0       0
  iopr11-20=         0       0       0       0       0       0       0       0       0       0
   iodb1-10=         0       0       0       0       0       0       0       0       0       0
       uebal= H+
      nxmod=  0
data file master species= Na+
     switch with species=
     jflag= 19    csp=    0.
  mineral= Analcime
data file master species= Al+++
     switch with species=
     jflag= 19    csp=    0.
  mineral= Kaolinite
data file master species= Cl-
     switch with species=
     jflag=0      csp=    3.00000E-02
data file master species= SiO2(aq)
     switch with species=
     jflag= 19    csp=    0.
  mineral= Chalcedony
data file master species= H+
     switch with species=
     jflag= 16    csp=    -7.0000
data file master species= Fe++
     switch with species=
     jflag= 19    csp=    0.
  mineral= Daphnite-14A
data file master species= O2(g)
     switch with species=
     jflag= 19    csp=    0.
  mineral= Magnetite
data file master species= Ca++
     switch with species=
     jflag= 19    csp=    0.
  mineral= Calcite
```

TABLE 7.3 (*Continued*)

```
data file master species= Mg++
    switch with species=
    jflag= 19    csp=   0.
 mineral= Clinochlore-14A
data file master species= HCO3-
    switch with species=
    jflag= 21    csp= -1.0000
      gas= CO2(g)
endit.
```

Results of the EQ3 run are listed in Table 7.4. The computed equilibrium pH is 7.68. At this pH value, $Al(OH)_4^-$, HCO_3^- and undissociated $SiO_{2(aq)}$ are by far the prevailing species of dissolved Al, carbonate and silica. Again, the $MeCO_3^\circ$ and $MeHCO_3^+$ complex species cannot be neglected, not only for Ca (as in the previous aqueous solution/calcite example), but also for divalent Fe and Mg. In contrast, the free ions Cl^-, Na^+ and K^+ are by far the prevailing dissolved species of these chemical components.

The code also indicates that the aqueous solution is saturated (i.e. $-0.3 < \log[Q/K] < +0.3$, but these limits can be reset by the user) with respect to several minerals, comprising aragonite, Mg- and Na-beidellite, böhmite, α-cristobalite, 7 Å-cronstedtite, diaspore, huntite, paragonite, quartz, 14 Å-ripidolite, siderite and trydimite. The solid phases with which the aqueous solution is oversaturated and undersaturated are also listed.

Finally, the $\log f_{O_2}$, resulted to be -61. Probably the $\log\left(f_{H_2}/f_{H_2O}\right)$ ratio, which is equal to -5.02 in this example, would be a better choice to describe redox conditions, for the reasons given by Giggenbach (1987).

If we also want to include S species into the geochemical model, we may add either pyrite [FeS_2] or anhydrite [$CaSO_4$] or both minerals to the input file. If we choose the pyrite constraint, total S concentration results to be 0.013 mmol kg^{-1} and the aqueous solution turns out to be strongly undersaturated with anhydrite. At equilibrium with anhydrite, total S concentration is 480 mmol kg^{-1} and the aqueous solution is strongly oversaturated with pyrite. At saturation with both pyrite and anhydrite, total S concentration results to be 472 mmol kg^{-1}. In all three cases, however, the $\log f_{O_2}$ of the system is constrained by daphnite–magnetite coexistence at -61. Looking at the thermodynamic constant of the $HS^- - SO_4^{2-}$ equilibrium reaction, written in logarithmic form:

$$\log K_{HS^-/SO_4^{2-}} = \log a_{SO_4^-} - \log a_{HS^-} - \mathrm{pH} - 2 \cdot \log f_{O_2}, \tag{7-9}$$

it is evident that pH differences are expected between the pyrite case and the anhydrite case. Indeed, the computed pH is 7.68 in the pyrite case and 6.85 in the anhydrite case (and 6.85 again in the pyrite plus anhydrite case).

TABLE 7.4

Part of the EQ3NR output file showing the speciation of the aqueous solution in equilibrium with analcime, calcite, kaolinite, daphnite, clinochlore, chalcedony and magnetite at 60°C, 1 bar under a f_{CO_2} of 10^{-1} bar

. . . omissis

	pH	Eh	pe
modified NBS pH scale	7.6822	−0.2918	−4.4142E+00

. . . omissis

—- Major Aqueous Species Contributing to Mass Balances —-

Aqueous species accounting for 99% or more of Al^{+++}

Species	Factor	Molality	Per Cent
$Al(OH)_4^-$	1.00	2.3351E–07	97.40
$NaAl(OH)_4(aq)$	1.00	3.5248E–09	1.47
$Al(OH)_3(aq)$	1.00	2.6892E–09	1.12
Total		2.3973E–07	100.00

Aqueous species accounting for 99% or more of Ca^{++}

Species	Factor	Molality	Per Cent
Ca^{++}	1.00	2.7410E–05	62.86
$CaHCO_3^+$	1.00	8.5013E–06	19.50
$CaCO_3(aq)$	1.00	7.6103E–06	17.45
Total		4.3605E–05	99.81

Aqueous species accounting for 99% or more of Cl^-

Species	Factor	Molality	Per Cent
Cl^-	1.00	2.9671E–02	98.90
NaCl(aq)	1.00	3.2737E–04	1.09
Total		3.0000E–02	100.00

Aqueous species accounting for 99% or more of Fe^{++}

Species	Factor	Molality	Per Cent
$FeHCO_3^+$	1.00	3.0519E–06	79.01
$FeCO_3(aq)$	1.00	5.3516E–07	13.86
Fe^{++}	1.00	2.7052E–07	7.00
Total		3.8625E–06	99.87

TABLE 7.4 (*Continued*)

Aqueous species accounting for 99% or more of HCO_3^-

Species	Factor	Molality	Per Cent
HCO_3^-	1.00	5.3742E–02	92.76
$NaHCO_3$(aq)	1.00	2.1026E–03	3.63
CO_2(aq)	1.00	1.6092E–03	2.78
Total		5.7936E–02	99.17

Aqueous species accounting for 99% or more of Mg^{++}

Species	Factor	Molality	Per Cent
Mg^{++}	1.00	1.0965E–04	68.44
$MgHCO_3^+$	1.00	3.8034E–05	23.74
$MgCO_3$(aq)	1.00	1.1295E–05	7.05
Total		1.6022E–04	99.22

Aqueous species accounting for 99% or more of Na^+

Species	Factor	Molality	Per Cent
Na^+	1.00	8.3906E–02	97.14
$NaHCO_3$(aq)	1.00	2.1026E–03	2.43
Total		8.6379E–02	99.57

Aqueous species accounting for 99% or more of SiO_2(aq)

Species	Factor	Molality	Per Cent
SiO_2(aq)	1.00	5.8790E–04	95.45
NaH_3SiO_4(aq)	1.00	1.5906E–05	2.58
$H_3SiO_4^-$	1.00	1.2131E–05	1.97
Total		6.1593E–04	100.00

. . . omissis

Mineral	Log *Q*/*K*	Aff, kcal	State
Albite	0.381	0.581	ssatd
Albite high	−0.735	−1.120	
Albite low	0.381	0.581	ssatd
Amesite–14A	−2.342	−3.570	
Analcime	0.000	0.000	satd
Analcime–dehy	−5.602	−8.541	
Andalusite	−4.423	−6.742	
Anthophyllite	−5.945	−9.063	
Antigorite	6.368	9.708	ssatd
Aragonite	−0.143	−0.218	satd
Artinite	−4.258	−6.492	

TABLE 7.4 (*Continued*)

Mineral	Log *Q/K*	Aff, kcal	State
Beidellite–Ca	−0.408	−0.621	
Beidellite–H	−1.308	−1.993	
Beidellite–Mg	−0.208	−0.317	satd
Beidellite–Na	−0.162	−0.247	satd
Boehmite	−0.315	−0.480	satd
Brucite	−3.237	−4.934	
Graphite	−1.862	−2.839	
Calcite	0.000	0.000	satd
Chalcedony	0.000	0.000	satd
Chamosite–7A	−2.207	−3.364	
Chrysotile	−0.367	−0.559	
Clinochlore–14A	0.000	0.000	satd
Clinochlore–7A	−3.133	−4.776	
Clinoptilolite–Ca	−1.610	−2.455	
Clinoptilolite–Na	1.534	2.338	ssatd
Clinoptilolite–hy–Ca	−1.782	−2.717	
Clinoptilolite–hy–Na	1.545	2.355	ssatd
Coesite	−0.488	−0.744	
Corundum	−3.208	−4.891	
Cristobalite(alpha)	−0.239	−0.364	satd
Cristobalite(beta)	−0.604	−0.921	
Cronstedtite–7A	−0.062	−0.095	satd
Daphnite–14A	0.000	0.000	satd
Daphnite–7A	−3.107	−4.737	
Dawsonite	−0.366	−0.557	
Diaspore	0.036	0.056	satd
Diopside	−3.398	−5.180	
Dolomite	1.981	3.019	ssatd
Dolomite–dis	0.662	1.009	ssatd
Dolomite–ord	1.981	3.020	ssatd
Enstatite	−1.931	−2.944	
Epidote	−5.113	−7.794	
Epidote-ord	−5.115	−7.797	
Fayalite	−2.702	−4.119	
$Fe(OH)_2$	−3.777	−5.758	
$Fe(OH)_3$	−5.075	−7.736	
FeO	−3.200	−4.878	
Ferrosilite	−1.155	−1.761	
Forsterite	−5.181	−7.898	
Gaylussite	−5.918	−9.022	
Gibbsite	−0.711	−1.084	
Goethite	−0.370	−0.563	
Greenalite	−0.810	−1.235	
Halite	−4.452	−6.786	
Hedenbergite	−4.854	−7.400	
Haematite	0.380	0.579	ssatd
Hercynite	−3.760	−5.731	
Huntite	0.269	0.411	satd
Hydromagnesite	−6.282	−9.577	
Ice	−0.287	−0.437	satd

TABLE 7.4 (*Continued*)

Mineral	Log *Q/K*	Aff, kcal	State
Jadeite	−1.493	−2.276	
Kaolinite	0.000	0.000	satd
Kyanite	−4.232	−6.451	
Lansfordite	−2.868	−4.372	
Laumontite	−2.181	−3.325	
Lawsonite	−3.304	−5.037	
Magnesite	0.541	0.824	ssatd
Magnetite	0.000	0.000	satd
Mesolite	1.666	2.540	ssatd
Minnesotaite	0.489	0.745	ssatd
Monohydrocalcite	−0.977	−1.489	
Montmor–Ca	0.728	1.110	ssatd
Montmor–Mg	0.986	1.503	ssatd
Montmor–Na	1.033	1.575	ssatd
Mordenite	−0.865	−1.318	
Na_2CO_3	−6.512	−9.927	
Nahcolite	−2.745	−4.185	
Natrolite	−1.264	−1.927	
Nepheline	−2.821	−4.300	
Nesquehonite	−2.843	−4.335	
Nontronite–Ca	2.242	3.418	ssatd
Nontronite–H	1.343	2.048	ssatd
Nontronite–Mg	2.442	3.722	ssatd
Nontronite–Na	2.488	3.792	ssatd
Okenite	−6.026	−9.187	
Paragonite	0.064	0.097	satd
Pirssonite	−6.073	−9.259	
Prehnite	−5.542	−8.449	
Pseudowollastonite	−5.302	−8.083	
Pyrophyllite	−0.828	−1.262	
Quartz	0.243	0.370	satd
Ripidolite–14A	0.261	0.397	satd
Ripidolite–7A	−2.864	−4.366	
Saponite–Ca	2.462	3.753	ssatd
Saponite–H	1.562	2.381	ssatd
Saponite–Mg	2.657	4.051	ssatd
Saponite–Na	2.707	4.127	ssatd
Scolecite	−0.856	−1.305	
Sepiolite	−2.437	−3.715	
SiO_2(am)	−0.824	−1.256	
Siderite	0.158	0.241	satd
Sillimanite	−4.727	−7.206	
Talc	2.059	3.140	ssatd
Thermonatrite	−6.532	−9.958	
Tremolite	−3.088	−4.707	
Tridymite	0.087	0.132	satd
Wairakite	−5.593	−8.526	
Wollastonite	−5.118	−7.802	
Wustite	−3.578	−5.455	

TABLE 7.4 (*Continued*)

. . . omissis

Gas	Fugacity	Log fugacity
$CH_4(g)$	1.0406E–06	−5.9827
CO(g)	4.4081E–11	−10.3558
$CO_2(g)$	1.0000E–01	−1.0000
$H_2(g)$	1.5491E–06	−5.8099
$H_2O(g)$	1.6325E–01	−0.7872
$O_2(g)$	1.0378E–61	−60.9839

7.2. Reaction path modelling

7.2.1. Fundamental relationships

As discussed above, prior to CO_2 injection into the deep aquifer, it is reasonable to hypothesize that the deep aqueous solution is in chemical equilibrium with a certain number of minerals. Upon CO_2 injection, this equilibrium is altered to an extent which depends on the imposed f_{CO_2} (possible temperature changes caused by isenthalpic CO_2 compression below the Joule-Thompson inversion curve – see Section 3.9 – are neglected in this discussion). As a consequence of this induced disequilibrium, the CO_2-containing aqueous solution will start to react with the primary minerals of the hosting rock. If the hosting rock is made up of silicates, they will be dissolved and carbonates, silicates, and/or silica minerals will the produced.

Compositional changes during these processes do not depend on the initial and final states only, that is the system can follow different paths in its evolution. In multi-phase systems, different chemical reactions can take place simultaneously and the global chemical evolution can be rather complex. The evolution of the system, possibly towards the final state of chemical equilibrium, is conveniently described by means of a variable named "reaction progress" or "extent of reaction", which is usually indicated by the letter ξ and is expressed in moles (Prigogine, 1955; Denbigh, 1971; Helgeson, 1979 and references therein). If only one reaction takes place in the system under consideration, the relationship between reaction progress, change in the number of moles of a generic species i (e.g., solutes, primary phases destroyed and secondary phases produced), dn_i and stoichiometric coefficients, v_i (adimensional), is

$$dn_i = v_i d\xi \tag{7-10}$$

which gives, through integration

$$n_i = n_i^\circ + v_i \Delta\xi. \tag{7-11}$$

The derivative of equation (7-10) with respect to time is (see equation 6-2):

$$\frac{dn_i}{dt} = v_i \cdot \frac{d\xi}{dt} \tag{7-12}$$

Since the ratio $d\xi/dt$ represents the rate of the reaction, R (mol s^{-1}), equation (7-12) can be rewritten as follows:

$$\frac{dn_i}{dt} = v_i \cdot R, \tag{7-13}$$

which gives the following equation, through integration:

$$n_i = n_i^\circ + v_i R \Delta t, \tag{7-14}$$

under the hypothesis of constant R. If the considered reaction is the dissolution of a mineral phase, the rate of the reaction, R (mol s^{-1}), is related to the dissolution rate, r (mol m^{-2} s^{-1}), and to the reaction surface, A_s (m^2), by the simple relationship:

$$R = r A_s. \tag{7-15}$$

Equation (7-14) can be rewritten as

$$n_i = n_i^\circ + v_i r A_s \Delta t, \tag{7-16}$$

Equations (7-11) and (7-16) are very similar. The former describes the increase in the number of moles of component i, with respect to the initial state, based on the reaction progress, whereas the latter makes reference to the time scale. In the second case, it is necessary to define both the rate of dissolution of the solid phase and its reaction surface, as indicated by equation (7-16).

Equations (7-11) and (7-16) are the pivotal relations for reaction path modelling, a technique which has received considerable attention in geochemistry. The thermodynamic relationships describing the irreversible water–rock mass transfers were established by Helgeson (1968). PATHI, the first software code for reaction path modelling, was developed by Helgeson and coworkers, who presented several applications in excellent scientific papers (e.g., Helgeson et al., 1969, 1970). Among the other codes developed afterwards, the EQ3/6 Software Package (Wolery, 1979, 1992; Wolery and Daveler, 1992) is one of the most known and used.

7.2.2. An example of reaction path modelling: the dissolution of albite in pure water

As an example, let us take into account the reaction path in a system made up of pure high-albite [$NaAlSi_3O_8$] reacting with pure water. This is similar to the K-feldspar example

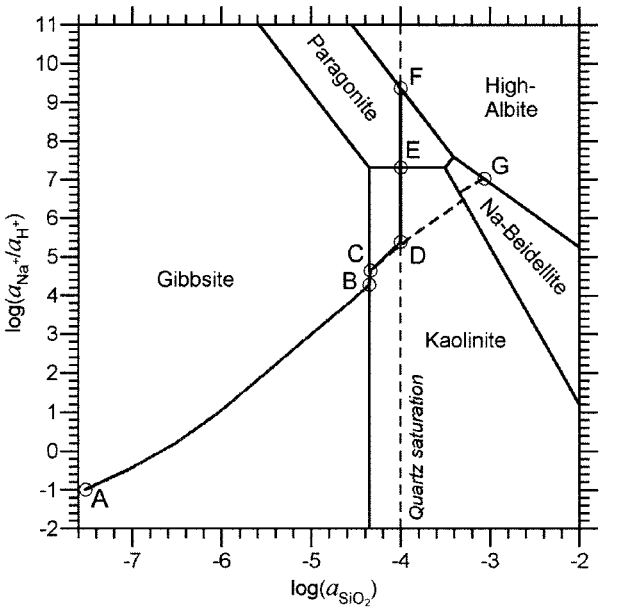

Figure 7.1. Activity plot for the system Na_2O–Al_2O_3–SiO_2–H_2O, showing two possible reaction paths for high-albite dissolution in pure water, at 25°C, 1 bar, one allowing quartz precipitation (solid grey line), the other preventing it (dashed grey line). Both reaction paths were simulated by means of EQ6.

proposed by Helgeson (1979) in one of his ground-breaking scientific papers. Initially albite and water are in disequilibrium. The activity plot for the system Na_2O–Al_2O_3–SiO_2–H_2O (Fig. 7.1) shows that the stability fields of kaolinite [$Al_2Si_2O_5(OH)_4$], Na-beidellite [$Na_{0.33}Al_{2.33}Si_{3.67}O_{10}(OH)_2$] and paragonite [$NaAl_3Si_3O_{10}(OH)_2$] are interposed between those of albite and gibbsite [$Al(OH)_3$].

The model assumes that albite dissolves congruently in pure water, at least in the initial stages, whereas albite dissolution becomes incongruent afterwards, upon attainment of saturation with respect to secondary solid phases. Speciation computations for the initial aqueous solution, containing Na, Al and Si in proportions 1:1:3 (i.e. those of albite), and in low concentrations, show that the dominant species in these initial conditions are Na^+, $Al(OH)_4^-$, $Al(OH)_3^\circ$ and $H_4SiO_4^\circ$. However, as dissolution of albite proceeds, the concentrations of other product species (e.g., $H_3SiO_4^-$, $NaH_3SiO_4^\circ$, $NaOH^\circ$, $NaAl(OH)_4^\circ$) increase too and have to be taken into account in calculations.

The ratios between the aqueous species produced by albite dissolution remain constant until the solution attains saturation with respect to solid product phases, that will precipitate during the process. This is the basic feature of the reaction path modelling. In order to recognize if the aqueous solution attains saturation with respect to a mineral phase, the solubility products of all the relevant minerals of the considered system have to be compared with the corresponding ion activity products after each increment of the reaction progress variable.

In the considered example, gibbsite is the first mineral with which the aqueous solution attains saturation, at point A of Fig. 7.1. The equilibrium between gibbsite and the aqueous solution is described by the following reaction:

$$Al(OH)_{3(s)} = Al^{3+} + 3OH^- \tag{7-18}$$

and the corresponding solubility product is

$$K_{gibbsite} = a_{Al^{3+}} \cdot a^3_{OH^-}. \tag{7-19}$$

During progressive albite dissolution, gibbsite continues to precipitate and the composition of the aqueous solution evolves along the path A–B in Fig. 7.1. During this process the concentration of dissolved silica (and Na^+) continues to increase until attainment, at point B, of saturation with respect to kaolinite, which becomes stable and precipitates. Coexistence of gibbsite and kaolinite buffers the activity of aqueous silica, as expressed by the reaction

$$2Al(OH)_{3(s)} + 2SiO_{2(aq)} \rightarrow Al_2Si_2O_5(OH)_{4(s)} + H_2O. \tag{7-20}$$

Therefore, further albite dissolution does not cause any increment in the concentration of dissolved silica, since this is consumed to convert the gibbsite, precipitated previously, in kaolinite. The Na^+ concentration continues to grow and the net result is path B–C in Fig. 7.1. At point C all the gibbsite has been consumed and the concentration of dissolved silica returns to increase with that of Na^+ following the path C–D along which kaolinite precipitates. At point D, quartz saturation is attained and this mineral starts to precipitate. Further albite dissolution moves the composition of the solution along the path D–E, along which the aqueous silica concentration is buffered by quartz saturation.

At point E the solution attains saturation with paragonite, which begins to precipitate. At point E, the aqueous solution is in equilibrium with quartz, paragonite and kaolinite. Since a maximum of four phases can coexist in a four components system (as stated above, our components are Na_2O, Al_2O_3, SiO_2, H_2O) under fixed T, P conditions (25°C, 1 bar in our case), the system has attained an invariant point. The composition of the solution cannot leave point E unless one of the three solids quartz, paragonite and kaolinite is dropped from the system. It must be underscored that albite does not have to be considered in the computation of the phases in equilibrium, since equilibrium between albite and the aqueous solution has not been attained yet and albite acts as supplier of solutes only. Therefore, the composition of the aqueous solution will remain at point E during further albite dissolution, while kaolinite reacts with the aqueous solution to form paragonite according to the reaction

$$1.5Al_2Si_2O_5(OH)_{4(s)} + Na^+ \rightarrow NaAl_3Si_3O_{10}(OH)_2 + 7.5H_2O + H^+. \tag{7-21}$$

Note that, again, minerals' coexistence buffers a parameter of the aqueous solution, this time the ratio between the activities of Na^+ and H^+.

When kaolinite has been totally consumed, further albite dissolution moves the composition of the solution along the path E–F, along which, again, the concentration of aqueous silica is fixed by quartz saturation. Finally, at point F, albite becomes stable, i.e. the condition of stable equilibrium between albite, paragonite, quartz and the aqueous solution is attained.

Note that, if quartz precipitation were prevented (for instance by kinetic constraints), the composition of the solution would evolve along path D–G. In this case, the condition of metastable equilibrium between albite, Na-beidellite and the aqueous solution would be attained.

The two reaction paths presented above and plotted in Fig. 7.1 simulate what happens if a limited amount of albite is dissolved in the aqueous solution and a constraint is then applied to prevent further dissolution and to allow attainment of equilibrium among all the chemical components. A second dissolution step is then allowed, followed by an equilibration step, and so on. After each step the system reaches a condition of metastable equilibrium for a very small progress of the irreversible reaction. The overall result is a series of metastable equilibrium states extending from the initial state of disequilibrium to the final state of stable equilibrium (point F) or metastable equilibrium (point G). The intermediate states are often named states of partial equilibrium, since the components in the aqueous solution are in mutual equilibrium but in disequilibrium with respect to albite.

7.2.3. The dissolution of albite in pure water: the numeric model

Referring to the albite example, albite dissolution accompanied by gibbsite precipitation is described by means of the following reaction, which includes the main aqueous species of interest:

$$\begin{aligned} \nu_{\mathrm{Alb}}\ \mathrm{NaAlSi_3O_{8(s)}} + \nu_{\mathrm{H_2O}}\ \mathrm{H_2O} \rightarrow\ & \nu_{\mathrm{Gibb}}\ \mathrm{Al(OH)_{3(s)}} + \nu_{\mathrm{Na^+}}\ \mathrm{Na^+} + \nu_{\mathrm{Al^{3+}}}\ \mathrm{Al^{3+}} \\ & + \nu_{\mathrm{Al(OH)_3^o}}\ \mathrm{Al(OH)_3^o} + \nu_{\mathrm{Al(OH)_4^-}}\ \mathrm{Al(OH)_4^-} + \nu_{\mathrm{H_4SiO_4^o}}\ \mathrm{H_4SiO_4^o} \\ & + \nu_{\mathrm{H_3SiO_4^-}}\ \mathrm{H_3SiO_4^-} + \nu_{\mathrm{H^+}}\ \mathrm{H^+} + \nu_{\mathrm{OH^-}}\ \mathrm{OH^-} \end{aligned} \tag{7-22}$$

Actually Al^{3+} ion is not a major dissolved species in the considered example but is retained as it is customarily used to describe the dissolution/precipitation of Al-bearing solid phases and the association/dissociation of aqueous Al-species.

Let us assume that the system contains 1,000 g of H_2O and that the reaction coefficient of albite, ν_{Alb}, is equal to 1. As already seen above, each ν_i represents the change in the number of moles of each species for an increment $d\xi$ of the reaction progress, as expressed by equation (7-10). Reactants have negative ν_i values, whereas the ν_i values of products are positive. In reaction (7-22) we could have erroneously considered as reactants some species that are actually products or vice versa. This is not important since the true situation comes out from computations. Apart from the ν_{Alb}, the other 10 ν_i are unknowns and depend on ξ. To compute these 10 unknowns a system of 10 equations is needed. Let

us start to write the thermodynamic equilibrium constant for the five independent reactions between the species involved in reaction (7-22):

$$a_{OH^-} \cdot a_{H^+} = K_W \tag{7-23}$$

$$a_{Al^{3+}} \cdot a_{OH^-}^3 = K_{sp,gibbsite} \tag{7-24}$$

$$\frac{a_{Al^{3+}} \cdot a_{OH^-}^4}{a_{Al(OH)_4^-}} = K_{Al(OH)_4^-} \tag{7-25}$$

$$\frac{a_{Al^{3+}} \cdot a_{OH^-}^3}{a_{Al(OH)_3^0}} = K_{Al(OH)_3^0} \tag{7-26}$$

$$\frac{a_{H^+} \cdot a_{H_3SiO_4^-}}{a_{H_4SiO_4}} = K_{H_4SiO_4}. \tag{7-27}$$

Now we have to take the derivative of each equation with respect to ξ and rearrange the results. Let us do this exercise for equation (7-23). The derivative of this relation with respect to ξ is

$$a_{OH^-} \cdot \frac{da_{H^+}}{d\xi} + a_{H^+} \cdot \frac{da_{OH^-}}{d\xi} = 0. \tag{7-28}$$

Based on equation (7-23), we can substitute K_W/a_{H^+} for a_{OH^-} and K_W/a_{OH^-} for a_{H^+}, obtaining

$$\frac{K_W}{a_{H^+}} \cdot \frac{da_{H^+}}{d\xi} + \frac{K_W}{a_{OH^-}} \cdot \frac{da_{OH^-}}{d\xi} = 0, \tag{7-29}$$

which can be simplified as follows:

$$\frac{1}{a_{H^+}} \cdot \frac{da_{H^+}}{d\xi} + \frac{1}{a_{OH^-}} \cdot \frac{da_{OH^-}}{d\xi} = 0. \tag{7-30}$$

Considering that $m_i = a_i/\gamma_i$, equation (7-10) can be rewritten in the following form:

$$v_i = \frac{dm_i}{d\xi} = \frac{1}{\gamma_i} \cdot \frac{da_i}{d\xi}. \tag{7-31}$$

Based on this result and through suitable substitution in equation (7-30), we get

$$\frac{v_{H^+} \cdot \gamma_{H^+}}{a_{H^+}} + \frac{v_{OH^-} \cdot \gamma_{OH^-}}{a_{OH^-}} = 0 \tag{7-32}$$

or

$$\frac{v_{H^+}}{m_{H^+}} + \frac{v_{OH^-}}{m_{OH^-}} = 0 \tag{7-33}$$

Following the same line of reasoning adopted for equation (7-23), similar relationships are obtained from the expressions of the other four thermodynamic equilibrium constants, equations (7-24) to (7-27):

$$\frac{v_{Al^{3+}}}{m_{Al^{3+}}} + \frac{3 \cdot v_{OH^-}}{m_{OH^-}} = 0 \tag{7-34}$$

$$\frac{v_{Al^{3+}}}{m_{Al^{3+}}} + \frac{4 \cdot v_{OH^-}}{m_{OH^-}} - \frac{v_{Al(OH)_4^-}}{m_{Al(OH)_4^-}} = 0 \tag{7-35}$$

$$\frac{v_{Al^{3+}}}{m_{Al^{3+}}} + \frac{3 \cdot v_{OH^-}}{m_{OH^-}} - \frac{v_{Al(OH)_3^o}}{m_{Al(OH)_3^o}} = 0 \tag{7-36}$$

$$\frac{v_{H^+}}{m_{H^+}} + \frac{v_{H_3SiO_4^-}}{m_{H_3SiO_4^-}} - \frac{v_{H_4SiO_4}}{m_{H_4SiO_4}} = 0. \tag{7-37}$$

The other five needed equations are simple mass balances describing the mass exchanges of the five elements involved in reaction (7-22), with respect to albite, under closed system conditions:

Na: $v_{Na^+} = -v_{Alb}$ (7-38)

Al: $v_{Al^{3+}} + v_{Al(OH)_3^o} + v_{Al(OH)_4^-} = -v_{Alb}$ (7-39)

Si: $v_{H_4SiO_4} + v_{H_3SiO_4^-} = -3 \cdot v_{Alb}$ (7-40)

O: $3 \cdot v_{Al(OH)_3^o} + 4 \cdot v_{Al(OH)_4^-} + 4 \cdot v_{H_4SiO_4} + 4 \cdot v_{H_3SiO_4^-} + v_{H_2O} + v_{OH^-} = -8 \cdot v_{Alb}$ (7-41)

H: $3 \cdot v_{Al(OH)_3^o} + 4 \cdot v_{Al(OH)_4^-} + 4 \cdot v_{H_4SiO_4} + 3 \cdot v_{H_3SiO_4^-} + 2 \cdot v_{H_2O} + v_{H^+} + v_{OH^-} = 0.$ (7-42)

Equations (7-33) to (7-42) make up the system of 10 equations which allows one to compute the 10 unknown v_i. The system is conveniently solved through matrix-algebra methods. The reaction progress calculations are initiated by assigning extremely small initial concentrations to the 10 aqueous species involved in reaction (7-22). The system is then solved for the 10 stoichiometric coefficients v_i. These coefficients are used to compute the new concentrations of all the species after a small reaction step $\Delta\xi$, through equation (7-11). It must be underscored that n_i in equation (7-11) stands for both the molality of aqueous species and the moles of solid phases precipitated from 1 kg of water. For each increment in the reaction progress variable, the speciation of the aqueous solution is computed to evaluate if the aqueous solution has attained saturation with respect to a new solid phase. When a new solid phase is precipitated, the system of equations is suitably modified to incorporate the new products and/or reactants. Since stoichiometric reaction coefficients change along the reaction path, small increments of ξ, e.g. 10^{-8} mol, have to be used. The best results are obtained modifying equation (7-11), that is including the first derivative of the stoichiometric coefficients with respect to the reaction progress variable:

$$\Delta m_i = v_i \cdot \Delta\xi + \frac{dv_i}{d\xi} \cdot \left(\frac{\Delta\xi}{2!}\right)^2 . \tag{7-43}$$

This is simply a truncated Taylor's series in m_i. Equations describing the first derivative of the stoichiometric coefficients with respect to the reaction progress variable, $dv_i/d\xi$, are given by Helgeson (1979). These relationships are inserted in the system of equations and at each step of $\Delta\xi$ the system is solved for v_i and $dv_i/d\xi$. As already said, the reaction progress computation proceeds iteratively, using the concentrations m_i of each step to calculate the new reaction coefficients v_i. These, in turn, are used to compute the new concentrations, i.e. the m_i values pertinent to the subsequent step, and so on. The results obtained through reaction path modelling include the concentrations of all the aqueous species and the number of moles of all the minerals either produced or consumed, for each step of advancement of the reaction progress variable.

The EQ6 input file for albite dissolution is reported in Table 7.5. Results are summarized in Fig. 7.2. Letters A to F in Fig. 7.2 correspond to those in Fig. 7.1. It is clear that both the concentrations of aqueous species and the moles of product minerals vary of several orders of magnitude during the reaction path. The condition of final equilibrium is attained when the total Gibbs free energy of the system $G = \Sigma\mu_i n_i$ reaches the minimum value. The test concerning this condition is carried out at each step of ξ and, in the albite example, the minimization of G is achieved for $\xi = 0.01323$ mol.

7.2.4. The dissolution of albite in pure water: simulations in time frame

We have already underscored above the importance of equations (7-11) and (7-16) and their similarity. Equation (7-11) was used to simulate the dissolution of albite through a merely stoichiometric approach (i.e. in reaction progress frame) in the previous section.

TABLE 7.5

EQ6 input file for modeling the dissolution of albite in pure water at 25°C, 1 bar in stoichiometric mode (reaction progress frame). Quartz is allowed to form (required input formats are not fully respected).

```
USE the database SUP
The option switch IOPT1 is set to 0 to direct the code to compute the simulation in a reaction progress frame.
The option switch IOPT4 is set to 0 to ignore solid solutions.
The print option switch IOPR8 is set to 1 to direct the code to print a table of equilibrium gas fugacities at each
print point.
endit.
    nmodl1= 1                    nmodl2= 0
    tempc0= 2.50000E+01           jtemp= 0
       tk1= 0.00000E+00             tk2= 0.00000E+00          tk3= 0.00000E+00
    zistrt= 0.00000E+00          zimax= 1.00000E+00
    tstrt= 0.00000E+00          timemx= 0.00000E+00
           kstpmx=300            cplim= 0.00000E+00
    dzprnt= 0.00000E+00          dzprlg= 0.00000E+00        ksppmx=100
    dzplot= 0.10000E+00          dzpllg= 0.00000E+00        ksplmx= 10000
      ifile= 60
*          1     2     3     4     5     6     7     8     9    10
 iopt1-10 = 0     2     0     0     0     0     0     0     0     0
iopt11-20 = 0     0     0     0     0     0     0     0     0     0
 iopr1-10 = 0     0     0     1     1     0    -1     1     0     0
iopr11-20 = 0     0     0     0     0     0     0     0     0     0
 iodb1-10 = 0     0     0     0     0     0     0     0     0     0
iodb11-20 = 0     0     0     0     0     0     0     0     0     0
     nxopt= 1
    option= all
    nxopex= 6
 exception = Gibbsite
 exception = Kaolinite
 exception = Quartz
 exception = Paragonite
 exception = Albite high
 exception = Beidellite-Na
      nffg= 0
      nrct= 1
*-------------------------------------------------------------------------------
   reactant= Albite high
     jcode= 0                    jreac = 0
      morr= 1.00000E+01          modr = 0.00000E+00
       nsk= 0                      sk = 0.00000E+00          fk= 0.00000E+00
       nrk= 1                    nrpk = 0
       rk1= 1.00000E+00           rk2 = 0.00000E+00          rk3= 0.00000E+00
*-------------------------------------------------------------------------------
    dlzidp= 0.00000E+00
     tolbt= 0.00000E+00          toldl= 0.00000E+00          tolx= 0.00000E+00
    tolsat= 0.00000E+00          tolsst= 0.00000E+00
   screw1= 0.00000E+00          screw2= 0.00000E+00        screw3= 0.00000E+00
   screw4= 0.00000E+00          screw5= 0.00000E+00        screw6= 0.00000E+00
    zklogu= 0.000               zklogl = 0.000              zkfac = 0.000
   dlzmx1= 0.00000E+00          dlzmx2= 0.00000E+00        nordlm = 0
```

TABLE 7.5 (*Continued*)

itermx= 0		ntrymx= 0	
npslmx= 0		nsslmx= 0	ioscan= 0
*			
* pickup file written by EQ3NR, version 7.2b (R139)			
* supported by EQLIB, version 7.2b (R168)			
Pure water			
endit.			
tempci = 2.50000E+01			
nxmod = 0			
iopg1 = 0		iopg2 = 0	iopg3 = 0
iopg4 = 0		iopg5 = 0	iopg6 = 0
iopg7 = 0		iopg8 = 0	iopg9 = 0
iopg10 = 0			
kct = 5		ksq = 6	kmt = 6
kxt = 6		kdim = 6	kprs = 0
O	5.550896571687376E+01		
Al	9.999999999999892E–21		
H	1.110168703247900E+02		
Na	1.000000000000000E–20		
Si	9.999999999999974E–21		
Electr	–2.442121511592103E–23		
H_2O	H_2O	1.744358983526984E+00	
Al^{+++}	Al^{+++}	–2.522092083305848E+01	
H^+	H^+	–6.997388938332554E+00	
Na^+	Na^+	–2.000000000692422E+01	
SiO_2(aq)	SiO_2(aq)	–2.000048167543259E+01	
O_2(g)	O_2(g)	–6.780000000000000E–01	

The same process can be transposed in a time frame by using equation (7-16), which indicates that the rate of dissolution of albite, the rate of precipitation of solid product phases and the reaction surfaces of all minerals, reactant and products, have to be specified to accomplish this task.

The characterization of reaction surface areas of mineral phases is probably the highest difficulty of reaction path modelling, as recognized by many authors in water–rock interaction studies (e.g., Lichtner, 1996, 1998). In particular, the surface of contact between minerals and percolating meteoric waters in soils and rocks may deviate from the surface area under controlled mineral dissolution/precipitation experiments conducted in the laboratory. According to Appelo and Postma (1996), the estimation of mineral surface areas in field situation has hardly passed the stage of educated guessing at present. Marini et al. (2000) have modelled the chemistry of Bisagno Valley (Genoa, Italy) groundwaters, focussing on the main dissolved constituents, using an inverse approach, i.e. introducing the experimental kinetic rate constants of dissolving and precipitating mineral phases and solving for their surface areas. It turns out that computed surface areas of solid phases change substantially during progressive water–rock interaction and differ by several orders of magnitude from those obtained on the basis of modal mineralogy, grainsize and intergranular

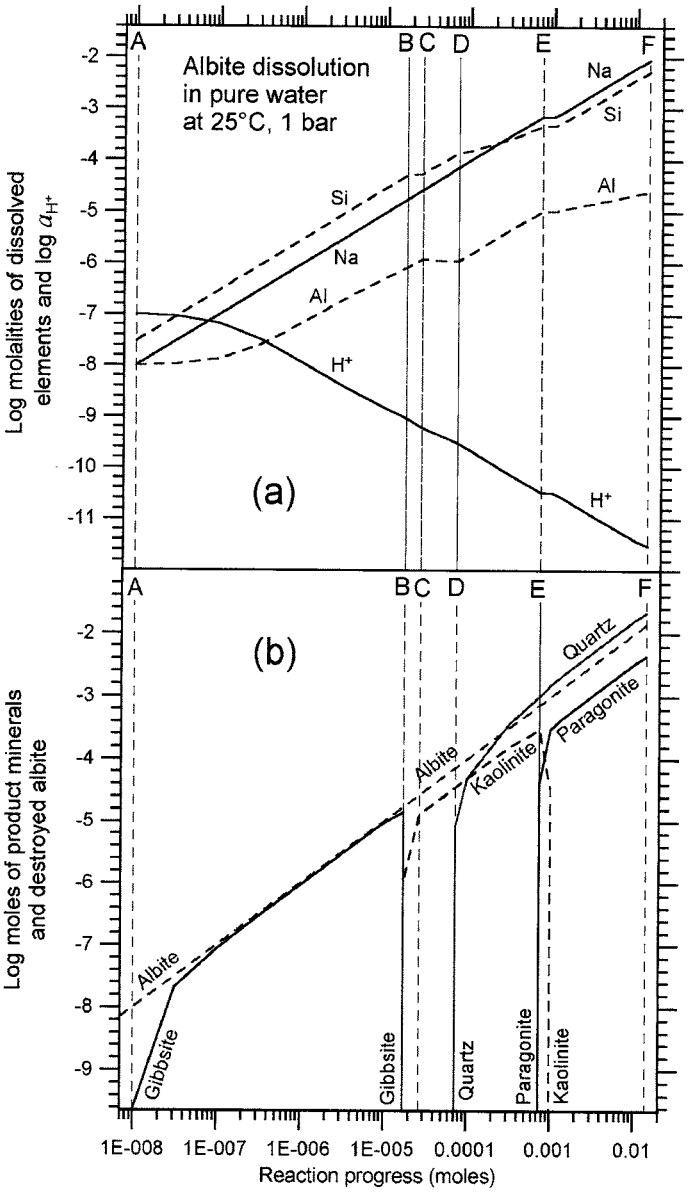

Figure 7.2. (a) Log-molalities of dissolved elements and log-activity of H^+ ion and (b) log-moles of secondary phases and of destroyed albite, as a function of the reaction progress variable, during the progressive dissolution of albite in pure water at 25°C, 1 bar, simulated by means of EQ6. Quartz is allowed to precipitate in the simulation. Letters A to F correspond to those in Figure 7.1.

porosity. Thus, even the relative surface areas do not appear to correlate with the modal abundance of minerals in the rocks.

In spite of these difficulties, it is instructive to simulate albite dissolution in kinetic mode, activating quartz precipitation. To keep these runs to a simple level, only the rate of dissolution of albite and its initial reaction surface area are specified in the EQ6 input files of Table 7.6, whereas product minerals are assumed to attain instantaneous equilibrium. This choice is dictated by the difficulty in defining the surface area for solid phases which are initially absent in the system.

In the first input file (see Table 7.6A), the dissolution of albite is described by means of a TST-based rate law, comprising the proton-, water- and hydroxyl-promoted mechanisms, whose rate constants and reaction orders are derived from Table 6.1. Note that the reaction orders in Table 6.1, +0.457 for the acid mechanism, 0.000 for the neutral mechanism and −0.572 for the basic mechanism, are all referred to proton activity, whereas in the EQ6 input file (Table 7.6) the reaction orders have to be referred to H^+, H_2O and OH^- activities, respectively, and consequently they become +0.457, +1.000 and +0.572. In addition, the rate constant for the basic mechanism given in Table 6.1 is multiplied times $K_W^{-0.572}$, to refer it to OH^- activity rather than to H^+ activity.

In the second input file (see Table 7.6B), the dissolution of albite is described by means of the rate law proposed by Oelkers et al. (1994), see equation (6-113). The purpose of this run is to show that this kind of rate laws can also be taken into account by the EQ6 code. Since equation (6-113) holds at pH 9 and 150°C, albite dissolution is simulated in a 1*N* solution of Na–HCO_3–CO_3 whose initial speciation, as computed by EQ3NR, is reported below.

Species	Molality	Log molality	Log gamma	Log activity
Na^+	9.9941E–01	−0.0003	−0.2462	−0.2464
HCO_3^-	5.9758E–01	−0.2236	−0.2313	−0.4549
CO_3^{--}	1.9873E–01	−0.7017	−0.9534	−1.6552
OH^-	4.3691E–03	−2.3596	−0.2840	−2.6436
CO_2(aq)	1.4647E–03	−2.8343	0.1157	−2.7185
NaOH(aq)	5.8880E–04	−3.2300	0.0000	−3.2300
O_2(aq)	1.4821E–04	−3.8291	0.1157	−3.7134
H^+	1.3149E–09	−8.8811	−0.1189	−9.0000

Carbonate equilibria and pH constrain CO_2 fugacity at $10^{-0.6728}$. This f_{CO_2} value is imposed on the system during the subsequent EQ6 simulation of albite dissolution, to maintain the pH constant at the desired value of 9.

As shown in Table 7.6B, the dissolution rate of albite is also described in this second case by means of a TST-based rate law, but contrary to the previous case, it includes one mechanism only, involving the activities of hydrogen ion and aluminium ion with exponents 1 and −1/3, respectively, as dictated by equation (6-113). The rate constant, expressed in mol cm^{-2} s^{-1}, is inserted in the input file as rk0.

TABLE 7.6A

EQ6 input file for modeling the dissolution of albite in pure water at 25°C, 1 bar in kinetic mode (time frame). Quartz is allowed to form (required input formats are not fully respected).

```
USE the database COM
The option switch IOPT1 is set to 1 to direct the code to compute the simulation in a TIME frame.
The option switch IOPT4 is set to 0 to ignore solid solutions.
The print option switch IOPR8 is set to 1 to direct the code to print a table of equilibrium gas fugacities at each
print point.
endit.
  nmodl1=1                    nmodl2=0
  tempc0=2.50000E+01          jtemp=0
      tk1=0.00000E+00           tk2=0.00000E+00          tk3=0.00000E+00
   zistrt=0.00000E+00         zimax=1.00000E-08
    tstrt=0.00000E+00         timemx=0.00000E+00
  kstpmx=300                  cplim=0.00000E+00
   dzprnt=0.00000E+00         dzprlg=0.00000E+00        ksppmx=100
   dzplot=0.10000E+00         dzpllg=0.00000E+00        ksplmx=10000
    ifile = 60
*          1     2     3     4     5     6     7     8     9     10
 iopt1-10=1     2     0     0     0     0     0     0     0     0
iopt11-20=0     0     0     0     0     0     0     0     0     0
 iopr1-10=0     0     0     1     1     0    -1     1     0     0
iopr11-20=0     0     0     0     0     0     0     0     0     0
 iodb1-10=0     0     0     0     0     0     0     0     0     0
iodb11-20=0     0     0     0     0     0     0     0     0     0
    nxopt=1
   option=all
  nxopex=6
exception=Gibbsite
exception=Kaolinite
exception=Quartz
exception=Paragonite
exception=Albite high
exception=Beidellite-Na
     nffg=0
     nrct=1
*-------------------------------------------------------------------------------
  reactant=Albite high
    jcode=0                   jreac=0
     morr=1.00000E+00         modr=0.00000E+00
      nsk=1                     sk=1000.00E+00          fk=0.00000E+00
      nrk=2                   nrpk=-1
    imech=3
      rk0=1.34900E-14          trk0=25.0000E+00         iact=0
     eact=0.00000E+00          hact=0.00000E+00
    ndact=1                  csigma=1.00000E+00
     udac=H+                   cdac=0.45700E+00
```

TABLE 7.6A (*Continued*)

```
      rk0=9.12010E-17          trk0=25.0000E+00          iact=0
     eact=0.00000E+00          hact=0.00000E+00
    ndact=1                   csigma=1.00000E+00
     udac=H2O                   cdac=1.00000E+00
      rk0=1.06660E-13          trk0=25.0000E+00          iact=0
     eact= 0.00000E+00         hact=0.00000E+00
    ndact=1                   csigma=1.00000E+00
     udac=OH-                   cdac=0.57200E+00
*---------------------------------------------------------------------------
   dlzidp=0.00000E+00
    tolbt=0.00000E+00          toldl=0.00000E+00          tolx=0.00000E+00
   tolsat=0.00000E+00          tolsst=0.00000E+00
  screw1=0.00000E+00          screw2=0.00000E+00         screw3=0.00000E+00
  screw4=0.00000E+00          screw5=0.00000E+00         screw6=0.00000E+00
   zklogu=0.000                zklogl=0.000               zkfac=0.000
  dlzmx1=0.00000E+00          dlzmx2=0.00000E+00         nordlm=0
   itermx=0                   ntrymx=0
   npslmx=0                   nsslmx=0                   ioscan=0
*---------------------------------------------------------------------------
* pickup file written by EQ3NR, version 7.2b (R139)
* supported by EQLIB, version 7.2b (R168)
Pure water
endit.
   tempci=2.50000E+01
   nxmod=0
    iopg1=0                   iopg2=0                   iopg3=0
    iopg4=0                   iopg5=0                   iopg6=0
    iopg7=0                   iopg8=0                   iopg9=0
   iopg10=0
      kct=5                     ksq=6                     kmt=6
      kxt=6                    kdim=6                    kprs=0
O       5.550896571687376E+01
Al      9.999999999999892E-21
H       1.110168703247900E+02
Na      1.000000000000000E-20
Si      9.999999999999974E-21
electr -2.442121511592103E-23
H2O     H2O                      1.744358983526984E+00
Al+++   Al+++                   -2.522092083305848E+01
H+      H+                      -6.997388938332554E+00
Na+     Na+                     -2.000000000692422E+01
SiO2(aq) SiO2(aq)               -2.000048167543259E+01
O2(g)   O2(g)                   -6.780000000000000E-01
```

TABLE 7.6B

EQ6 input file for modeling the dissolution of albite in a 1 N solution of Na-HCO_3–CO_3 (pH 9) at 150°C, 4.76 bar in kinetic mode (time frame). Quartz is allowed to form (required input formats are not fully respected).

```
USE the database COM
The option switch IOPT1 is set to 1 to direct the code to compute the simulation in a TIME frame.
The option switch IOPT4 is set to 0 to ignore solid solutions.
The print option switch IOPR8 is set to 1 to direct the code to print a table of equilibrium gas fugacities at each
print point.
endit.
   nmodl1= 1                    nmodl2= 0
   tempc0= 150.000E+00           jtemp= 0
      tk1= 0.00000E+00             tk2= 0.00000E+00        tk3= 0.00000E+00
   zistrt= 0.00000E+00           zimax= 2.30400E-03
    tstrt= 0.00000E+00          timemx= 0.00000E+00
   kstpmx= 300                   cplim= 0.00000E+00
   dzprnt= 1.00000E-04          dzprlg= 0.00000E+00    ksppmx= 100
   dzplot= 0.10000E+00          dzpllg= 0.00000E+00    ksplmx= 10000
     ifile= 60
*          1     2     3     4     5     6     7     8     9    10
 iopt1-10= 1     2     0     0     0     0     0     0     0     0
iopt11-20= 0     0     0     0     0     0     0     0     0     0
 iopr1-10= 0     0     0     1     1     0    -1     1     0     0
iopr11-20= 0     0     0     0     0     0     0     0     0     0
 iodb1-10= 0     0     0     0     0     0     0     0     0     0
iodb11-20= 0     0     0     0     0     0     0     0     0     0
    nxopt= 1
   option= all
   nxopex= 6
exception= Gibbsite
exception= Kaolinite
exception= Quartz
exception= Paragonite
exception= Albite high
exception= Beidellite-Na
     nffg= 1
  species= CO2(g)
   moffg= 1.00000E+00          xlkffg= -0.67280E+00
     nrct= 1
*-------------------------------------------------------------------------------
 reactant= Albite high
    jcode= 0                    jreac= 0
     morr= 1.00000E+00          modr= 0.00000E+00
      nsk= 1                      sk= 1000.0E+00        fk= 0.00000E+00
      nrk= 2                    nrpk= -1
    imech= 1
      rk0= 2.90000E-12           trk0= 150.000E+00     iact= 0
```

TABLE 7.6B (*Continued*)

```
      eact= 0.00000E+00      hact= 0.00000E+00
     ndact= 2                csigma= 1.00000E+00
      udac= H+               cdac= 1.00000E+00
      udac= Al+++            cdac= -0.33333E+00
*-----------------------------------------------------------------------
    dlzidp= 0.00000E+00
     tolbt= 0.00000E+00      toldl= 0.00000E+00     tolx= 0.00000E+00
     tolsat= 0.00000E+00     tolsst= 0.00000E+00
    screw1= 0.00000E+00      screw2= 0.00000E+00    screw3= 0.00000E+00
    screw4= 0.00000E+00      screw5= 0.00000E+00    screw6= 0.00000E+00
     zklogu= 0.000           zklogl= 0.000          zkfac= 0.000
    dlzmx1= 0.00000E+00      dlzmx2= 0.00000E+00    nordlm= 0
     itermx= 0               ntrymx= 0
    npslmx= 0                nsslmx= 0              ioscan= 0
*-----------------------------------------------------------------------
* pickup file written by EQ3NR, version 7.2b (R139)
* supported by EQLIB, version 7.2b (R168)
Soluzione a pH 9, 150ØC
endit.
    tempci= 1.50000E+02
    nxmod= 0
     iopg1= 0               iopg2= 0               iopg3= 0
     iopg4= 0               iopg5= 0               iopg6= 0
     iopg7= 0               iopg8= 0               iopg9= 0
    iopg10= 0
       kct= 6                 ksq= 7                 kmt= 7
       kxt= 7                kdim= 7                kprs= 0
  O        5.790555475213318E+01
  Al       1.000000140335818E-20
  H        1.116194099975864E+02
  C        7.977766682638062E-01
  Na       1.000000000012290E+00
  Si       1.000000019167043E-20
  electr   1.690239705560677E-08
  H2O      H2O                    1.744358983526984E+00
  Al+++    Al+++                 -4.121808857987895E+01
  H+       H+                    -8.881099514946308E+00
  HCO3-    HCO3-                 -2.236025491244946E-01
  Na+      Na+                   -2.557881778253819E-04
  SiO2(aq) SiO2(aq)              -2.116808380506397E+01
  O2(g)    O2(g)                 -6.780000000000000E-01
```

Some interesting results are summarized below:

ξ	Time days	pH	m_{Al}	m_C	m_{Na}	m_{SiO_2}	$a_{Al^{3+}}$	Affinity kcal×mol^{-1}	Rate mol×cm^{-2}×s^{-1}
0.00E+00	0.00E+00	9	*1.00E-20*	0.798	1.000	*1.00E-20*	*6.05E-42*	*−135.5676*	*4.94E-07*
1.00E-09	2.34E-11	9	1.00E-09	0.798	1.000	3.00E-09	6.05E-31	−47.6005	1.06E-10
3.16E-09	2.71E-07	9	3.16E-09	0.798	1.000	9.49E-09	1.91E-30	−43.7280	7.25E-11
1.00E-08	1.62E-06	9	1.00E-08	0.798	1.000	3.00E-08	6.05E-30	−39.8554	4.94E-11
3.16E-08	8.02E-06	9	3.16E-08	0.798	1.000	9.49E-08	1.91E-29	−35.9829	3.36E-11
1.00E-07	3.77E-05	9	1.00E-07	0.798	1.000	3.00E-07	6.05E-29	−32.1104	2.29E-11
3.16E-07	1.76E-04	9	3.16E-07	0.798	1.000	9.49E-07	1.91E-28	−28.2378	1.56E-11
1.00E-06	8.16E-04	9	1.00E-06	0.798	1.000	3.00E-06	6.05E-28	−24.3653	1.06E-11
3.16E-06	3.79E-03	9	3.16E-06	0.798	1.000	9.49E-06	1.91E-27	−20.4928	7.25E-12
1.00E-05	1.76E-02	9	1.00E-05	0.798	1.000	3.00E-05	6.05E-27	−16.6202	4.94E-12
3.16E-05	8.16E-02	8.9999	3.16E-05	0.798	1.000	9.49E-05	1.91E-26	−12.7475	3.36E-12
1.00E-04	3.79E-01	8.9999	1.00E-04	0.798	1.000	3.00E-04	6.05E-26	−8.8745	2.29E-12
3.16E-04	1.76E+00	8.9997	3.16E-04	0.797	1.000	9.49E-04	1.91E-25	−5.0006	1.56E-12
1.00E-03	8.80E+00	8.9992	1.00E-03	0.796	1.001	3.00E-03	6.10E-25	−1.1236	7.84E-13
1.10E-03	1.05E+01	8.9992	1.10E-03	0.796	1.001	3.31E-03	6.73E-25	−0.7916	6.28E-13
2.30E-03	1.34E+02	8.9990	6.89E-04	0.795	1.002	5.30E-03	4.21E-25	−0.0002	2.90E-16

The total molalities of Na and dissolved carbonates and pH remain nearly constant throughout the simulation, whereas the total molalities of dissolved Al and SiO_2 experience remarkable increases from "virtually zero" in the beginning to the final concentrations of 0.689 and 5.30 mmol kg^{-1}, respectively. This increment in total Al is accompanied by an increase in the activity of Al ion (of course the initial value of 6.05×10^{-42} is meaningless). Also the thermodynamic affinity changes substantially during the simulation attaining the equilibrium value ("virtually zero") in the last step, after 134 days.

Interestingly, the rate of albite dissolution experiences a substantial decrease (again, the initial value has no meaning) and this change is dictated by the increase in Al ion activity, apart from the decrease in rate for $A > -2$ kcal mol^{-1}. These findings are in marked contrast with the constant rate that would be predicted, at constant pH, by a TST-based rate law, comprising the proton-, water- and hydroxyl-promoted mechanisms, apart from the decrease in rate for $A > -2$ kcal mol^{-1}. These considerations underscore the importance of the approach by Oelkers, Schott and coworkers for a correct evaluation of the dissolution rate of silicate minerals. Unfortunately, this approach cannot be used extensively due to the present lack of experimental data.

The albite surface area specified in the EQ6 input files of Table 7.6, $A_{s,tot}$ = sk = 1,000, represents the area (in cm^2) in contact with (i.e. exposed to) 1,000 g of water. To understand the physical meaning of this parameter, let us consider an hypothetical system made up of N_s minerals spheres, all of the same radius r_s, and 1,000 g of water occupying the pore spaces (porosity is assumed to be 0.3), although natural systems can be different from this simple geometric analogue. The total volume of the mineral spheres, $V_{tot,s}$, can be computed based on the definition of porosity, η:

$$\eta = \frac{V_W}{V_W + V_{tot,s}}, \tag{7-44}$$

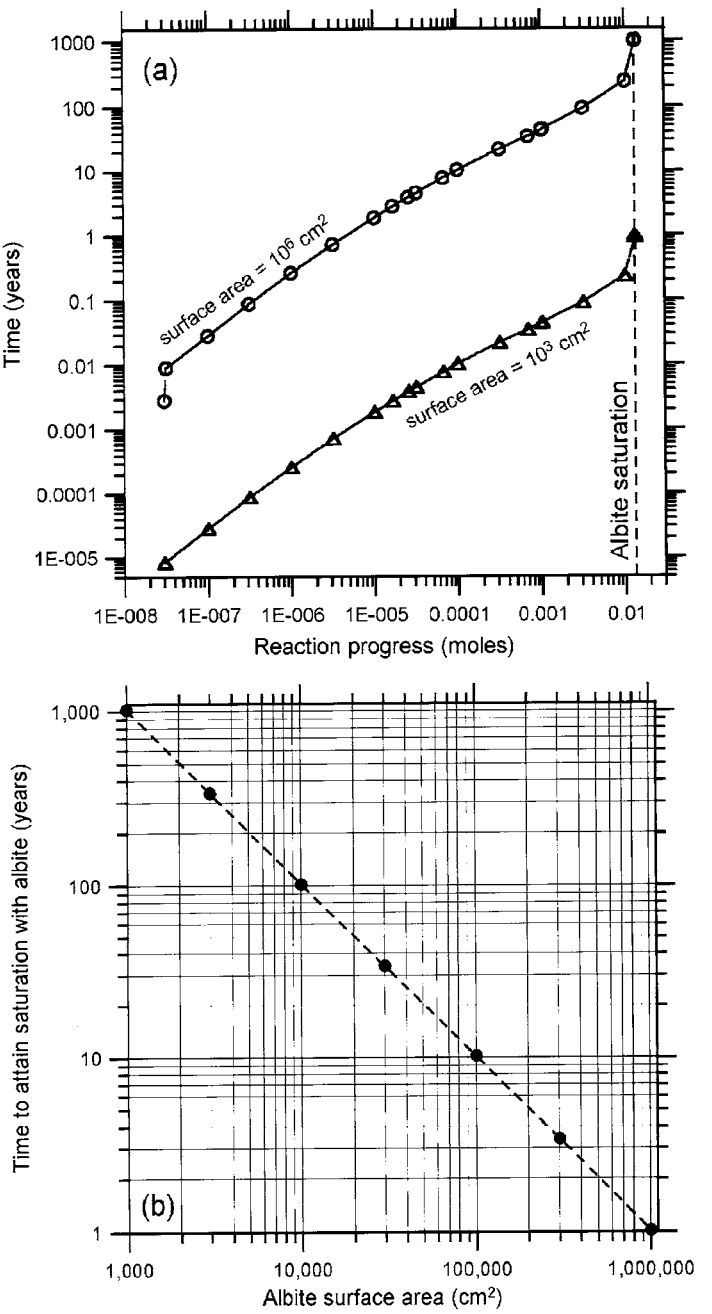

Figure 7.3. Progressive dissolution of albite in pure water at 25°C, 1 bar, simulated by means of EQ6. (a) Relations between time and reaction progress for two different values of the albite surface area and (b) Inverse correlation between the time needed to attain saturation with albite and the albite surface area.

where V_W identifies the pore volume occupied by water. For a selected radius r_s, the volume of a single mineral sphere V_s is calculated by means of equation (6-93), and the number of minerals spheres is $N_s = V_{tot,s}/V_s$. The surface of a single mineral sphere, A_s, is obtained by using equation (6-92) and the total surface area is $A_{s,tot} = A_s N_s$. These simple calculations indicate that the lowest value of the total surface area, 851 cm^2, is obtained for $N_s = 1$ (N_s cannot be less then 1!) and $r_s = 8.23$ cm. Both $A_{s,tot}$ and N_s increase as r_s decreases; for instance, a total surface area of 5,000 cm^2 pertains to a system comprising 203 spheres whose radius is 1.4 cm; $A_{s,tot}$ becomes 50,000 cm^2 for a system made up of 203,004 spheres whose r_s is 0.14 cm and attains 1,000,000 cm^2, for a system comprising 1.62×10^9 spheres whose radius is 0.007 cm.

During the EQ6 simulation, the surface area of albite can be kept constant or automatically changed by the code in proportion to its remaining mass. In the considered example, the difference between these two approaches is negligible, owing to the comparatively high mass of albite present in the system with respect to dissolved mass of albite.

In different EQ6 runs, the surface area of albite was varied from a minimum of 1,000 cm^2 up to a maximum of 1,000,000 cm^2, by changing accordingly the input file of Table 7.6a. It is important to underscore that these differences in the albite surface area do not change the results of the simulation (which are depicted in Fig. 7.2), apart from time. The reason for this is that the number of moles of any species, i.e. solutes, primary phases destroyed and secondary phases produced during the progressive dissolution of albite in pure water at 25°C, 1 bar are uniquely described by the reaction progress variable, as indicated by equation (7-11).

The relations between time and ξ are shown in Fig. 7.3a for the minimum and maximum values of the albite surface area introduced in the simulation. At the extreme right of this plot, a dashed-vertical line marks albite saturation, which is uniquely defined by $\xi = 0.01323$ mol. The different times needed to attain this condition for different values of the albite surface area are plotted in Fig. 7.3b as a function of the albite surface area itself. As expected, this plot confirms that there is a simple inverse linear relation between the logarithms of these two variables, namely, $\log time_{sat}$ (years) $= -1.00 \times \log A_{s,albite}$ (cm^2) + 6.00. Therefore, uncertainties in the surface area of reacting minerals brings about corresponding uncertainties in the timing of the dissolution/precipitation process.

7.3. Reaction path modelling of geological CO_2 sequestration in ultramafic rocks

As discussed by Lackner et al. (1995, 1997), ultramafic rocks have the highest potential of CO_2 sequestration through mineral fixation, owing to their high concentrations of MgO and CaO. Ultramafic rocks are chiefly made up of four minerals, i.e. olivine, orthopyroxene, clinopyroxene and hornblende, accompanied by small amounts of biotite, garnet and spinel (Le Maitre, 2002). Ultramafic rocks are customarily divided in three broad groups, namely peridotites, pyroxenites and hornblendites, whose names evidently indicate the prevailing mineral. Peridotites contain more than 40% by volume of olivine and, based on the relative amounts of olivine (ol), orthopyroxene (opx) and clinopyroxene (cpx), they are further subdivided in dunite (ol > 90%), harzburgite (ol < 90%,

cpx < 10%), wehrlite (ol < 90%, opx < 10%) and lherzolite (ol < 90%, cpx > 10%, opx > 10 %) (Le Maitre, 2002). Pyroxenites are further subdivided in clinopyroxenite, websterite, orthopyroxenite, olivine-clinopyroxenite, olivine-websterite and olivine-orthopyroxenite (see Le Maitre, 2002).

A dunite contains 49.5 wt% MgO and 0.3 wt% CaO only, a harzburgite is constituted by 45.4 wt% MgO and 0.7 wt% CaO, whereas a lherzolite is made up of 28.1 wt% MgO and 7.3 wt% CaO on average (Lackner et al., 1995). Ultramafic rocks are often affected by serpentinization and the resulting rocks, serpentinites, typically contain 40 wt% MgO and CaO close to 0 (Lackner et al., 1995).

Simple stoichiometric calculations shows that the amounts of ultramafic rocks required to bind chemically 1 kg of CO_2 through reaction with CaO and MgO are 1.8 kg of dunite, 2.0 kg of harzburgite, 2.7 kg of lherzolite and 2.3 kg of sepentinite (Lackner et al., 1995). Hence dunite has the highest potential of CO_2 sequestration among the ultramafic rocks.

Ultramafic rocks typically occur as components of ophiolite complexes, which are interpreted as slices of ancient oceanic crust and upper mantle which were tectonically uplifted and incorporated into the continental crust. Steinmann (1905) was probably the first one who recognized that ophiolites are igneous rocks emplaced on the ocean floor, an interpretation which was enriched by several details in subsequent years. Ultramafic rocks are relatively common at the earth surface and the total amount of MgO stored by these rocks far exceeds the worldwide coal reserves which are currently estimated to be ~10^{16} kg (Lackner et al., 1995, 1997).

7.3.1. Previous works

Xu et al. (2000, 2004) simulated the geological sequestration of CO_2 into different aquifers, including a dunite, by means of TOUGHREACT (Xu and Preuss, 1998). This code can be used to model reactive transport in a non-isothermal multi-phase system. In simple words, reaction path modelling is coupled with solute-transport modelling to simulate the reactive processes occurring into an aquifer. In TOUGHREACT the reaction and transport equations are solved separately. Consequently, TOUGHREACT can be used for reaction path modelling (or batch geochemical modelling to use the words of Xu and coworkers). Adopting this modelling feature, as Xu et al. (2000, 2004) did, TOUGHREACT is equivalent to EQ3/6.

The dunite case is of interest for the present discussion and is briefly presented here. Xu and coworkers considered an initial porosity of 5% for the dunite rock, which was assumed to be made up of forsterite (85.5% by volume) and fayalite (9.5%). Dissolution rates at 25°C were taken equal to 10^{-13} mol m^{-2} s^{-1} for forsterite and fayalite and precipitation rates at 25°C were fixed at 10^{-12} mol m^{-2} s^{-1} for all secondary non-carbonate minerals and 0.6×10^{-8} mole m^{-2} s^{-1} for magnesite and siderite. Apparent activation energy was considered to be 41.87 kJ mol^{-1} for magnesite and siderite and 62.76 kJ mol^{-1} for all other solid phases. Initial surface areas (in m^2 dm^{-3}) were fixed at 8.55 m^2 dm^{-3} for forsterite and 0.95 m^2 dm^{-3} for fayalite, which means to assume a total surface area of 10 m^2 dm^{-3} and to distribute it in proportion to the volume percentages of the two primary

phases. Note that this total surface area value corresponds to a surface area of 2×10^6 cm^2 exposed to 1,000 g of water, owing to the relatively low porosity of the dunite rock.

In a background run, a dilute aqueous solution (with initial pH of 7 and initial Eh of −100 mV) was equilibrated with forsterite and fayalite at a temperature of 80°C. The aqueous solution thus attained stable pH and Eh values of 10.7 and −520 mV, respectively, through generation of H_2, owing to the strongly reducing conditions present in the system, and precipitation of magnetite, chrysotile and even elemental Fe. The production of these minerals would decrease porosity to 0.5% in 15,000 years.

In a distinct simulation, a CO_2 pressure of 260 bar was imposed and temperature was maintained at 80°C. This causes a remarkable decrease in pH down to 4.8 and an Eh increase up to 100 mV. Of course, under these more oxidising conditions (with respect to the background run), both H_2 generation and separation of metallic Fe do not occur anymore. The continuous supply of CO_2 to the system activates the dissolution of forsterite and fayalite and, consequently, the precipitation of magnesite and siderite and, to a lesser extent, of talc and amorphous silica as well. After ~1,000 years, ~100 kg of CO_2 are sequestered into 1 m^3 of the considered system (corresponding to approximately 2000 g kg^{-1} water) but these processes cause a decrease in porosity to 0.6%. Therefore, it seems likely that both rock alteration and geological CO_2 sequestration end owing to this reduction in porosity.

It must be underscored the prevailing reaction in the model of Xu and coworkers:

$$0.8\,Mg_2SiO_4 + CO_2 + 0.2\,H_2O \rightarrow MgCO_3 + 0.2\,Mg_3Si_4O_{10}(OH)_2 \qquad (7\text{-}45)$$

is characterized by a reaction volume for solids (*see* Section 5.5), ΔV_r of 20.2 cm^3. In contrast, if the dominant reaction would involve (i) a serpentine mineral instead of forsterite and (ii) chalcedony instead of talc, things might be different. This means to take into account, instead of reaction (7-45), the following reaction:

$$0.33\,Mg_3Si_2O_5(OH)_4 + CO_2 \rightarrow MgCO_3 + 0.67\,SiO_2 + 0.67\,H_2O, \qquad (7\text{-}46)$$

whose ΔV_r would be 7.0 cm^3 only or 11.2 cm^3, if amorphous silica were precipitated instead of chalcedony. Note that both reactions (7-45) and (7-46) involve 1 mol of CO_2 to obtain comparable results (*see* Section 5.5). Therefore, porosity being equal, a rock including a serpentine mineral as primary phase is probably able to sequester more CO_2 than a rock made up of forsteritic olivine.

Based on this expectation, the geological CO_2 sequestration in serpentinitic rocks was investigated by Cipolli et al. (2004), who modelled the irreversible mass exchanges taking place during high-pressure CO_2 injection into a deep aquifer hosted in these kind of rocks by means of the software package EQ3/6 version 7.2b.

Previous researches by Bruni et al. (2002) and Marini and Ottonello (2002) were devoted to understand the origin of the waters circulating in deep aquifers hosted in ultramafic rocks variably affected by serpentinization, which are representative of the initial (prior to CO_2 injection) aqueous solution. These waters have high pH, typically in the 11.3–11.9 range at the surface outlet, and unusual chemistry, with Ca^{2+} and OH^- as

prevailing cation and anion, respectively. Other characteristics of these waters are: negative Eh (typically −460 to −520 mV), low Mg^{2+} concentrations (as low as 0.001 mg kg^{-1}), low total dissolved carbonate (generally between 0.5 and 17 mg kg^{-1} as HCO_3^-) and, consequently, very low P_{CO_2} values, from 10^{-8} to 10^{-11} bar (as already recalled in Section 5.1.4.1). Besides, Ca-OH waters are close to saturation with respect to calcite and brucite, undersaturated with forsterite and enstatite, and strongly oversaturated with respect to antigorite, chrysotile, talc and tremolite.

To understand the origin of Ca-OH waters, the dissolution of a local serpentinite was simulated by means of the EQ3/6 software package by Bruni et al. (2002) and Marini and Ottonello (2002). In this way, it was shown that Ca-OH compositions are produced through prolonged water–rock interaction in a system closed to CO_2, under strongly reducing conditions, in agreement with previous findings by Pfeifer (1977). This chemical evolution is due to C depletion in a system closed with respect to C sources. This C depletion was attributed to calcite precipitation by Bruni et al. (2002), although the possible reduction of carbonate-C to organic-C and ultimately to CH_4 might also be important. Further research is needed on this subject.

Since serpentinites are almost monomineralic rocks, stoichiometric serpentine [$Mg_3Si_2O_5(OH)_4$] was considered to be the only solid phase under dissolution by Cipolli et al. (2004). Simulation was carried out in kinetic mode, assuming constant values for both the dissolution rate of serpentine and its reactive surface area exposed to 1,000 g of water. The latter was set at 4,100 cm^2 based on geochemical evidence. Note that this value is approximately 500 times lower than that considered by Xu and coworkers in their dunite example.

7.3.2. Reaction path modelling of the geological CO_2 sequestration in a serpentinitic rock

7.3.2.1. Setting up the water–rock interaction model

Here, the geochemical model by Cipolli et al. (2004) will be extended to include other two chemical components, Al and Fe. Although serpentinites are almost monomineralic rocks, they main contain significant amounts of Fe oxides (7.9 ± 1.4 wt% as Fe_2O_3, based on the data summarized by Bruni et al., 2002) and Al_2O_3 (2.1 ± 1.0 wt%), which follow SiO_2 (40.6 ± 1.1 wt%), MgO (35.4 ± 1.4 wt%) and H_2O (12.4 ± 1.6 wt%), in order of decreasing importance. Assuming that Fe and Al are chiefly present as magnetite and kaolinite, respectively, simple mass balances shows that the molar amounts of serpentine, magnetite and kaolinite for a typical serpentinitic rock (Table 7.7) are 0.9116, 0.0282 and 0.0602, respectively. The corresponding volume fractions are 0.9317, 0.0118 and 0.0565, respectively. Accepting that the total surface area in contact with 1,000 g of water is 4,100 cm^2, as hypothesized by Cipolli et al. (2004), the initial surface areas of serpentine, magnetite and kaolinite are 3,820, 48.51 and 231.5 cm^2, respectively. Assuming that initial porosity is 0.3, geometric calculations (*see* Section 7.2.4) indicate that the initial amounts of serpentine, magnetite and kaolinite in the considered system are 20.04, 0.62 and 1.32 mol, respectively.

TABLE 7.7

Whole-rock chemical analysis of a typical serpentinitic rock from Monte Roccaprebalza (Dinelli et al., 1997) and its computed mineralogic composition

Oxide	Wt%	Element	Mol%
SiO_2	40.14	Si	10.29
TiO_2	0.08	Ti	0.02
Al_2O_3	2.20	Al	0.66
$Fe_2O_{3,tot}$	5.88	Fe	1.13
MnO	0.12	Mn	0.03
MgO	37.31	Mg	14.25
CaO	0.18	Ca	0.05
Na_2O	0.03	Na	0.01
K_2O	0.05	K	0.02
H_2O	14.00	O	49.61
		H	23.93

Minerals	Mol %	Vol %	Initial moles	Initial surfaces
Serpentine	91.16	93.17	20.04	3,820.10
Magnetite	2.82	1.18	0.62	48.51
Kaolinite	6.02	5.65	1.32	231.54

Again, following Cipolli et al. (2004), aquifer temperature was assumed to be 60°C and the aqueous solution hosted in the serpentinitic aquifer was hypothesized to be represented by the local Ca-OH spring water BR2. Heating of this aqueous solution from the emergence temperature, 20.3°C, to the aquifer temperature, 60°C ,was simulated by means of EQ6. This process does not cause any change in the total concentrations of solute species, whereas pH decreases from the outlet value, 11.73, to 10.6 and the logarithm of f_{O_2} increases from −73.6 to −67.9. Results of the heating simulation were used to prepare the EQ3NR input file of Table 7.8. Note that (i) the redox potential is assumed to be fixed by the SO_4^{2-}/HS^- redox couple and (ii) negligible molal concentrations, 10^{-20}, are hypothesized for dissolved Al and Fe, whose analytical concentrations are both below detection limits, to activate these two chemical components.

Injection of pure CO_2 at 100 bar pressure was hypothesized. To this purpose, a constant f_{CO_2} of 67.9 bar was set in EQ6 input file (*see* Table 7.9). This f_{CO_2} value is obtained considering that Γ_{CO_2} is equal to 0.679 at 60°C and 100 bar total pressure (*see* Section 3.4). The dissolution of the serpentinitic rock upon continuous CO_2 injection was simulated in kinetic mode, specifying both the dissolution rates at 60°C and the initial surface areas (see above) of the three solid reactants in the EQ6 input file.

The dissolution kinetics of reactant minerals was described by means of the TST rate law, involving the proton- and water-promoted mechanisms, whereas the hydroxyl-promoted dissolution mechanism was neglected, owing to the low pH values attained by the aqueous solution upon CO_2 injection (see below). Owing to the lack of dissolution rate parameters for the proton-promoted mechanism of chrysotile, those of lizardite were assumed to be representative of chrysotile. Dissolution rates at 60°C were computed by

TABLE 7.8

EQ3NR input file to compute the speciation/saturation state of the aqueous solution assumed to be hosted in the serpentinitic reservoir prior to CO_2 injection. This water composition was obtained through heating of spring water BR2 at 60°C (see Cipolli et al., 2004). (Required input formats are not fully respected.)

```
. . . omissis
endit.
    tempc= 60.0000E+00
      rho= 1.00000E+00          tdspkg= 0.00000E+00      tdspl= 0.00000E+00
      fep= 0.00000E+00          uredox= HS-
    tolbt= 0.00000E+00            toldl= 0.00000E+00     tolsat= 0.00000E+00
   itermx= 0
*              1    2    3    4    5    6    7    8    9   10
 iopt1-10=     1    0    0    0    0    0    0    0    0    0
 iopg1-10=     0    0    0    0    0    0    0    0    0    0
 iopr1-10=     0    0    0    1    0    0    1   -1    0    0
iopr11-20=     0    0    0    0    0    0    0    0    0    0
 iodb1-10=     0    0    0    0    0    0    0    0    0    0
     uebal=
    nxmod= 18
    uxmod= S2O3--
           0                    -1
    uxmod= HSO3-
           0                    -1
    uxmod= SO2(aq)
           0                    -1
    uxmod= SO3--
           0                    -1
    uxmod= S4O6--
           0                    -1
    uxmod= S5--
           0                    -1
    uxmod= S4--
           0                    -1
    uxmod= HSO5-
           0                    -1
    uxmod= S2--
           0                    -1
    uxmod= CO(aq)
           0                    -1
    uxmod= Formaldehyde(aq)
           0                    -1
    uxmod= Methanol(aq)
           0                    -1
    uxmod= Acetic acid(aq)
           0                    -1
    uxmod= Acetate
           0                    -1
    uxmod= Formic acid(aq)
           0                    -1
```

TABLE 7.8 (*Continued*)

```
    uxmod= Formate
           0                                    -1
    uxmod= Ethane(aq)
           0                                    -1
    uxmod= Methane(aq)
           0                                    -1
data file master species=H+
     switch with species=
     jflag=16     csp=-10.6081
data file master species=Ca++
     switch with species=
     jflag= 3     csp= 61.8
data file master species= Mg++
     switch with species=
     jflag= 3     csp= 0.001
data file master species= Na+
     switch with species=
     jflag= 3     csp= 41.1
data file master species= K+
     switch with species=
     jflag= 3     csp= 5.51
data file master species= HCO3-
     switch with species=
     jflag= 3     csp= 0.55
data file master species= SO4--
     switch with species=
     jflag= 3     csp= 0.3
data file master species= Cl-
     switch with species=
     jflag= 3     csp= 30.47
data file master species= SiO2(aq)
     switch with species=
     jflag= 3     csp= 3.1
data file master species= HS-
     switch with species=
     jflag= 3     csp= 0.22
data file master species= B(OH)3(aq)
     switch with species=
     jflag= 3     csp= 0.57
data file master species= Fe++
     switch with species=
     jflag= 0     csp= 1.00E-20
data file master species= Al+++
     switch with species=
     jflag= 0     csp= 1.00E-20
endit.
```

TABLE 7.9

EQ6 input file for modeling high-pressure ($P_{tot} = P_{CO2} = 100$ bar) CO_2 injection in a deep aquifer hosted in serpentinitic rocks at 60°C in kinetic mode (time frame). (Required input formats are not fully respected.)

```
The option switch IOPT1 is set to 1 to direct the code to compute the simulation in time frame
The print option switch IOPR8 is set to 1 to direct the code to print a table of equilibrium gas fugacities at each
print point.
endit.
   nmodl1= 1                    nmodl2= 0
   tempc0= 60.0000E+00           jtemp= 0
       tk1= 0.00000E+00            tk2= 0.00000E+00        tk3= 0.00000E+00
    zistrt= 0.00000E+00          zimax= 1.00000E-06
     tstrt= 0.00000E+00         timemx= 0.00000E+00
   kstpmx= 500                   cplim= 0.00000E+00
    dzprnt= 1.00000E+00          dzprlg= 0.00000E+00     ksppmx= 100
    dzplot= 0.10000E+00          dzpllg= 0.00000E+00     ksplmx= 10000
      ifile= 60
*              1    2    3    4    5    6    7    8    9   10
 iopt1-10=     1    0    0    0    0    0    0    0    0    0
iopt11-20=     0    0    0    0    0    0    0    0    0    0
 iopr1-10=     0    0    0    0    1    0    0    1    0    0
iopr11-20=     0    0    0    0    0    0    0    0    0    0
 iodb1-10=     0    0    0    0    0    0    0    0    0    0
iodb11-20=     0    0    0    0    0    0    0    0    0    0
*-------------------------------------------------------------------------------
    nxopt= 1
   option= all
   nxopex= 15
exception= Gibbsite
exception= Kaolinite
exception= Chrysotile
exception= Sepiolite
exception= Hydromagnesite
exception= Nesquehonite
exception= Magnesite
exception= Calcite
exception= Dolomite
exception= Chalcedony
exception= Magnetite
exception= Siderite
exception= Pyrite
exception= Goethite
exception= Dawsonite
*-------------------------------------------------------------------------------
     nffg= 1
  species= CO2(g)
    moffg= 1.00000E+01          xlkffg= +1.83187E+00
*-------------------------------------------------------------------------------
     nrct= 3
*-------------------------------------------------------------------------------
 reactant= Chrysotile
    jcode= 0                    jreac= 0
```

TABLE 7.9 (*Continued*)

```
      morr= 20.0400E+00          modr= 0.00000E+00
       nsk= 1                      sk= 3,820.000E+00      fk= 0.00000E+00
       nrk= 2                    nrpk= 0
     imech= 2
       rk0= 4.89000E-09          trk0= 6.00000E+01      iact= 0
      eact= 0.00000E+00          hact= 0.00000E+00
     ndact= 1                  csigma= 1.00000E+00
      udac= H+                   cdac= 0.80000E+00
       rk0= 2.25000E-15          trk0= 6.00000E+01      iact= 0
      eact= 0.00000E+00          hact= 0.00000E+00
     ndact= 1                  csigma= 1.00000E+00
      udac= H2O                  cdac= 1.00000E+00
*-------------------------------------------------------------------------------
  reactant= Magnetite
    jcode= 0                    jreac= 0
     morr= 0.62000E+00          modr= 0.00000E+00
      nsk= 1                      sk= 48.5000E+00      fk= 0.00000E+00
      nrk= 2                    nrpk= 0
    imech= 2
      rk0= 5.65000E-13          trk0= 5.00000E+01      iact= 0
     eact= 0.00000E+00          hact= 0.00000E+00
    ndact= 1                  csigma= 1.00000E+00
     udac= H+                   cdac= 0.27900E+00
      rk0= 3.65000E-15          trk0= 5.00000E+01      iact= 0
     eact= 0.00000E+00          hact= 0.00000E+00
    ndact= 1                  csigma= 1.00000E+00
     udac= H2O                  cdac= 1.00000E+00
*-------------------------------------------------------------------------------
  reactant= Kaolinite
    jcode= 0                    jreac= 0
     morr= 1.32000E+00          modr= 0.00000E+00
      nsk= 1                      sk= 231.500E+00      fk= 0.00000E+00
      nrk= 2                    nrpk= 0
    imech= 2
      rk0= 8.00000E-15          trk0= 6.00000E+01      iact= 0
     eact= 0.00000E+00          hact= 0.00000E+00
    ndact= 1                  csigma= 1.00000E+00
     udac= H+                   cdac= 0.77700E+00
      rk0= 1.69000E-17          trk0= 6.00000E+01      iact= 0
     eact= 0.00000E+00          hact= 0.00000E+00
    ndact= 1                  csigma= 1.00000E+00
     udac= H2O                  cdac= 1.00000E+00
*-------------------------------------------------------------------------------
   dlzidp= 0.00000E+00
    tolbt= 0.00000E+00          toldl= 0.00000E+00      tolx= 0.00000E+00
   tolsat= 0.00000E+00         tolsst= 0.00000E+00
  screw1= 0.00000E+00         screw2= 0.00000E+00     screw3= 0.00000E+00
  screw4= 0.00000E+00         screw5= 0.00000E+00     screw6= 0.00000E+00
   zklogu= 0.000               zklogl= 0.000           zkfac= 0.000
  dlzmx1= 0.00000E+00         dlzmx2= 0.00000E+00     nordlm= 0
```

TABLE 7.9 (*Continued*)

```
   itermx= 0                    ntrymx= 0
  npslmx= 0                     nsslmx= 0                    ioscan= 0
*---------------------------------------------------------------------------
* pickup file written by EQ3NR, version 7.2b (R139 )
* supported by EQLIB, version 7.2b (R168 )
Spring water BR2 heated at 60°C
endit.
   tempci= 6.00000E+01
   nxmod= 18
   species= S2O3--
      type= 0                   option= -1                xlkmod= 0.00000E+00
   species= HSO3-
      type= 0                   option= -1                xlkmod= 0.00000E+00
species= SO2(aq)
      type= 0                   option= -1                xlkmod= 0.00000E+00
   species= SO3--
      type= 0                   option= -1                xlkmod= 0.00000E+00
   species= S4O6--
      type= 0                   option= -1                xlkmod= 0.00000E+00
   species= S5--
      type= 0                   option= -1                xlkmod= 0.00000E+00
   species= S4--
      type= 0                   option= -1                xlkmod= 0.00000E+00
   species= HSO5-
      type= 0                   option= -1                xlkmod= 0.00000E+00
   species= S2--
      type= 0                   option= -1                xlkmod= 0.00000E+00
   species= CO(aq)
      type= 0                   option= -1                xlkmod= 0.00000E+00
   species= Formaldehyde(aq)
      type= 0                   option= -1                xlkmod= 0.00000E+00
   species= Methanol(aq)
      type= 0                   option= -1                xlkmod= 0.00000E+00
   species= Acetic acid(aq)
      type= 0                   option= -1                xlkmod= 0.00000E+00
species=Acetate
      type= 0                   option= -1                xlkmod= 0.00000E+00
   species= Formic acid(aq)
      type= 0                   option= -1                xlkmod= 0.00000E+00
   species= Formate
      type= 0                   option= -1                xlkmod= 0.00000E+00
species=Ethane(aq)
      type= 0                   option= -1                xlkmod= 0.00000E+00
species=Methane(aq)
      type= 0                   option= -1                xlkmod= 0.00000E+00
     iopg1= 0                    iopg2= 0                  iopg3= 0
     iopg4= 0                    iopg5= 0                  iopg6= 0
     iopg7= 0                    iopg8= 0                  iopg9= 0
    iopg10= 0
       kct= 13                     ksq= 14                   kmt= 14
       kxt= 14                    kdim= 14                  kprs= 0
```

TABLE 7.9 (*Continued*)

O	5.551282557733262E+01	
Al	1.000000000335209E–20	
B	9.218375990262418E–06	
Ca	1.541993186674240E–03	
Cl	8.594550329665458E–04	
Fe	1.000000000144592E–20	
H	1.110211073777142E+02	
C	9.013861125756066E–06	
K	1.409268500602602E–04	
Mg	4.114379952680602E–08	
Na	1.787751767510004E–03	
S	9.774694209498928E–06	
Si	5.159417928970046E–05	
electr	−1.150065192877400E–04	
H_2O	H_2O	1.744358983526984E+00
Al^{+++}	Al^{+++}	−4.257641064725003E+01
$B(OH)_3(aq)$	$B(OH)_3(aq)$	−6.725193420264618E+00
Ca^{++}	Ca^{++}	−2.815981346143646E+00
Cl^-	Cl^-	−3.066044127812017E+00
Fe^{++}	Fe^{++}	−2.130818472540851E+01
H^+	H^+	−1.057158162952603E+01
HCO_3^-	HCO_3^-	−6.323495220189614E+00
K^+	K^+	−3.851088497828405E+00
Mg^{++}	Mg^{++}	−7.387095228892170E+00
Na^+	Na^+	−2.748464060961117E+00
SO_4^{--}	SO_4^{--}	−5.564691145737220E+00
$SiO_2(aq)$	$SiO_2(aq)$	−5.509600627218712E+00
$O_2(g)$	$O_2(g)$	−6.354977441383422E+01

means of equation (6-26), based on the pre-exponential factors, A_i, and apparent activation energies, E_i, given in Table 6.1. Again, note that the reaction order of the water-promoted mechanism was set to +1.000 in the EQ6 input file (Table 7.9). The EQ6 code was instructed to change the surface areas of primary minerals during the simulation in proportion to their remaining masses.

Instantaneous partial equilibrium was assumed for precipitating, secondary solid phases. Again, this choice is due to the difficulty in defining the surface area for minerals which are initially absent in the considered system. The hypothesis of instantaneous equilibrium for secondary minerals means to assume that the dissolution of reactants is the rate limiting step of the overall process. Results are presented against both the reaction progress variable, ξ, and time in the plots of Figs. 7.4 to 7.7.

7.3.2.2. Solid reactants

The amounts of reactant minerals destroyed during continuous CO_2 injection are shown as a function of time and reaction progress in Fig. 7.4. The solid phase contributing most chemical components to the considered system through its destruction is chrysotile. This reflects not only its high abundance and surface area (see Table 7.7) but

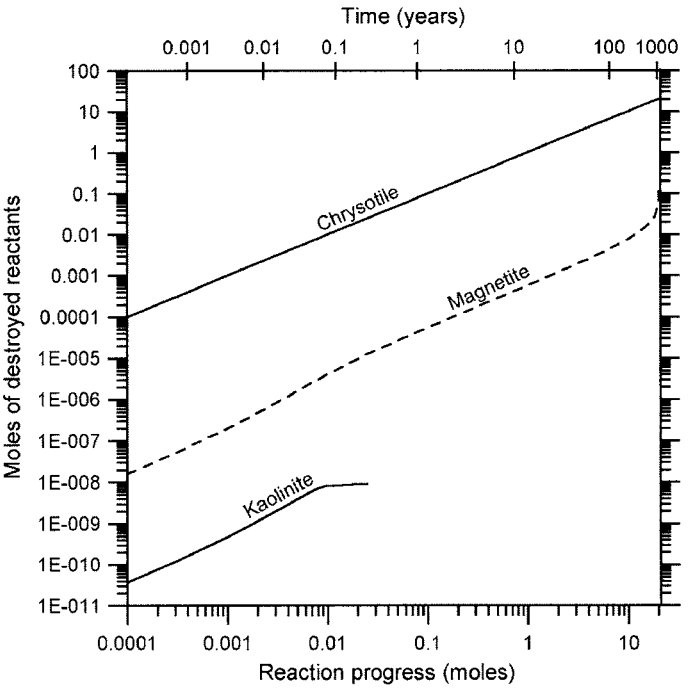

Figure 7.4. Moles of reactant minerals destroyed during high-pressure (P_{tot} = P_{CO_2} = 100 bar) CO_2 injection in a deep aquifer (T = 60°C) hosted in serpentinitic rocks as a function of time and the reaction progress variable.

also the comparatively high dissolution rate (in mol cm^{-2} s^{-1}) of serpentine minerals in acidic solutions (e.g., lizardite in Table 6.1, since the dissolution rate of chrysotile in acidic solutions was never investigated, as already recalled).

Although kaolinite is much more abundant than magnetite (see Table 7.7), the moles of magnetite destroyed are over two orders of magnitude higher than those of kaolinite, owing to the higher dissolution rate (in mol cm^{-2} s^{-1}) of magnetite with respect to kaolinite (see Table 6.1).

The aqueous solution remains strongly undersaturated with respect to chrysotile ($A<-16$ kcal mol^{-1}) and magnetite ($A<-3.4$ kcal mol^{-1}) throughout the process. For these low values of A, the dissolution rate is virtually independent of thermodynamic affinity (see Section 6.4.2) and is a function of pH only.

In contrast, the aqueous solution saturates with kaolinite for ξ of 0.025 mol. Before attainment of this condition the thermodynamic affinity with respect to kaolinite increases significantly, determining a substantial decrease in the dissolution rate. For instance, the dissolution rate of kaolinite is 1.90×10^{-17} mol cm^{-2} s^{-1} at ξ of 3.16 mmol, where A is -3.59 kcal mol^{-1} and pH is 4.49, but it reduces to 3.00×10^{-18} mol cm^{-2} s^{-1} at ξ of 10 mmol, where A is -0.12 kcal mol^{-1} and pH is 4.85. Upon attainment of equilibrium with kaolinite, this phase was dropped from the considered primary paragenesis.

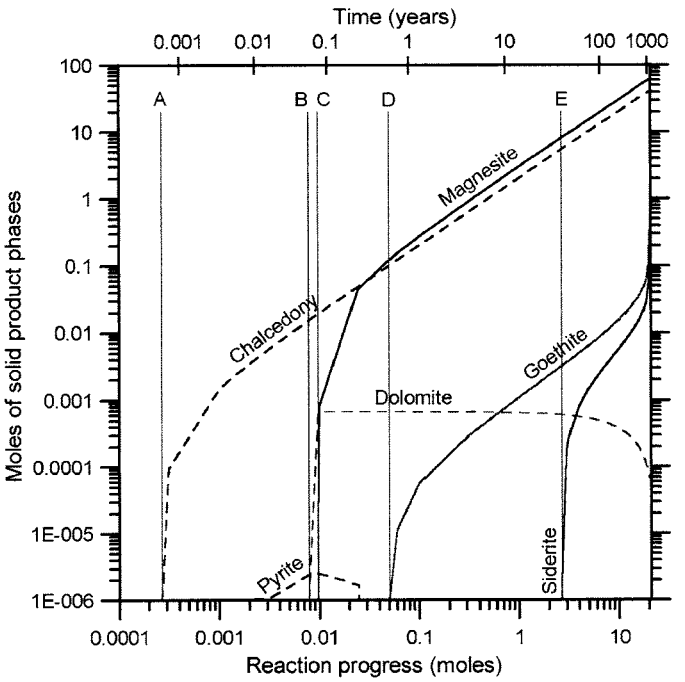

Figure 7.5. Moles of product minerals formed during high-pressure (P_{tot} = P_{CO_2} = 100 bar) CO_2 injection in a deep aquifer (T = 60°C) hosted in serpentinitic rocks as a function of time and the reaction progress variable. Note that letters A to E mark the onset of the precipitation of different secondary minerals.

Chrysotile is exhausted after 4,300 years, for ξ of 20.04 mol, which corresponds to the initial amount of this mineral in the considered serpentinitic rock. The simulation ends for ξ of 20.66 mol, upon exhaustion of magnetite.

7.3.2.3. Solid product phases

The solid phases which are considered to be produced through high-pressure (P_{tot} = P_{CO_2} = 100 bar) CO_2 injection in a deep aquifer hosted in serpentinitic rocks are, in order of appearance, chalcedony, pyrite, dolomite, magnesite, goethite and siderite (Fig. 7.5). However, pyrite is produced in very small amounts (< 3 μmol) and has ephemeral existence; dolomite never exceeds 0.001 mol; goethite and siderite are always ≤ 0.1 mol. As already recognized by Cipolli et al. (2004), only chalcedony and magnesite are produced in significant quantities and for ξ > 0.05 mol the stoichiometry of the process is adequately described by reaction (7-46). In other words, 3 mol of magnesite and 2 mol of chalcedony are produced for each mole of serpentine dissolved. The masses of magnesite and chalcedony increase almost linearly with time (not shown) and the magnesite mass is 2.32 mol kg^{-1} water (196 g) after 10 years and 10.4 mol kg^{-1} water (874 g) after 50 years, and so on, indicating the high CO_2 sequestration capacity of this process. A time of tens of years is apparently large, but it is actually small if compared with the residence times of high-pH Ca-OH waters in deep aquifers, which is estimated to be in the order of 100 to 10,000 years (Cipolli et al., 2004).

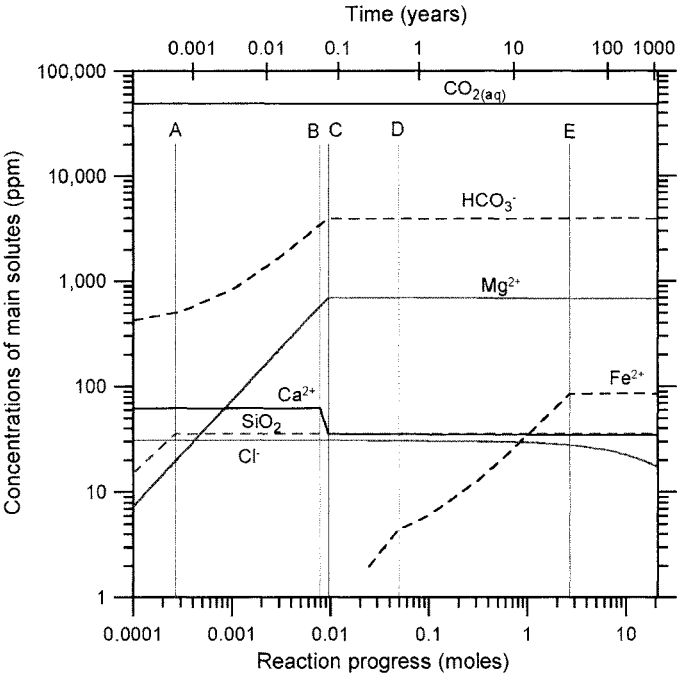

Figure 7.6. Concentrations of solutes during high-pressure (P_{tot} = P_{CO_2} = 100 bar) CO_2 injection in a deep aquifer (T = 60°C) hosted in serpentinitic rocks as a function of time and the reaction progress variable. Note that letters A to E marks the onset of the precipitation of different secondary minerals as shown in Figure 7.5.

7.3.2.4. The aqueous solution

Throughout continuous CO_2 injection, the main solute is aqueous CO_2, whose concentration is fixed at 1.1 mol kg^{-1} (48,400 ppm) by constant f_{CO_2}, under specified temperature–pressure conditions (Fig. 7.6). Aqueous CO_2 is followed by HCO_3^- and Mg^{2+}, whose concentrations, after an initial increase (for $\xi < 0.01$), stabilize at 0.062 and 0.028 mol kg^{-1}, respectively, when magnesite begins to form at point C. Note that at this point also Ca^{2+}concentration is fixed by saturation with dolomite which is attained at point B.

Also plotted in Fig. 7.6 is chloride, the most typical mobile solute, whose concentration experiences a significant decrease for high values of ξ. This effect is caused by a substantial increase in the mass of water, which is provided to the considered system by the dissolution of chrysotile, a H_2O-containing mineral. This effect is exactly the opposite of dry-up, a phenomenon due to incorporation of water in hydrous minerals (see Reed, 1997).

During the considered process, the pH of the aqueous solution changes from 3.83 to 4.85 (Fig. 7.7a). Most of this pH increase occurs between the onset of chalcedony precipitation (point A) and the beginning of magnesite precipitation (point C), after which pH is buffered by carbonate equilibria, similar to what was discussed for the aqueous solution/calcite example in Section 7.1.1.

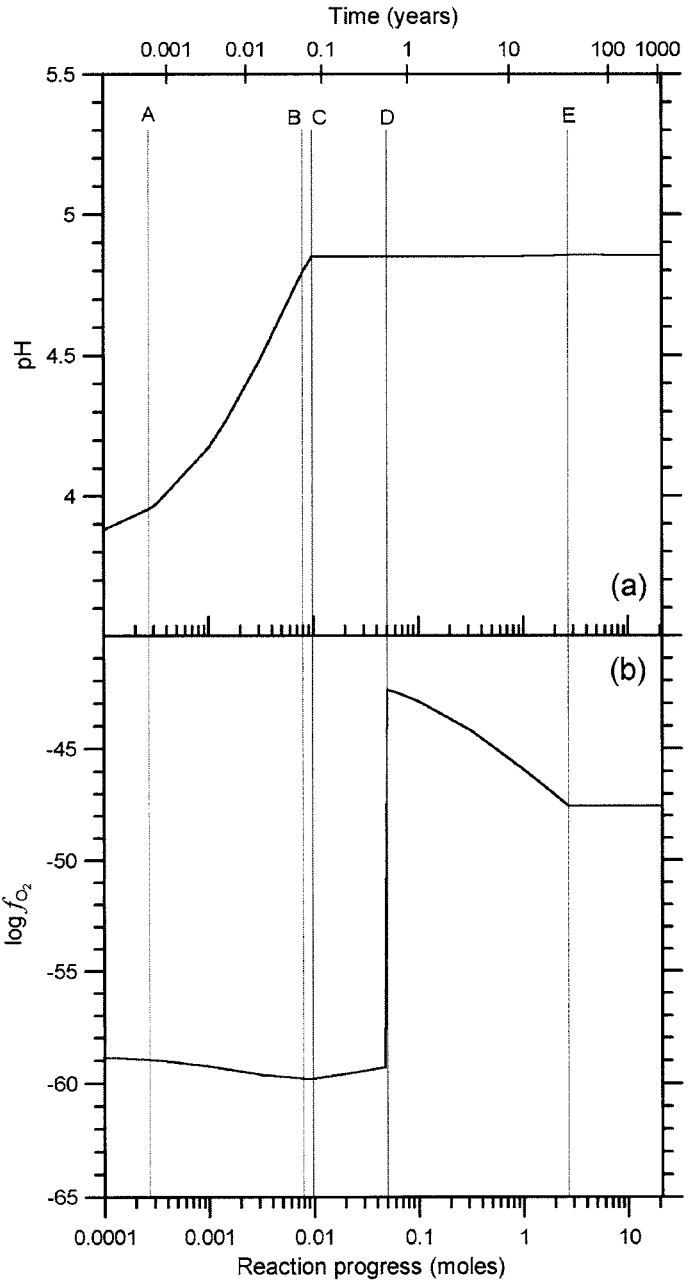

Figure 7.7. Evolution of (a) pH and (b) f_{O_2} during high-pressure ($P_{tot} = P_{CO_2} = 100$ bar) CO_2 injection in a deep aquifer ($T = 60°C$) hosted in serpentinitic rocks as a function of time and the reaction progress variable. Note that letters A to E mark the onset of the precipitation of different secondary minerals as shown in Figure 7.5.

In spite of its relatively low concentration in the aqueous phase and the small amounts of Fe-bearing secondary minerals produced during continuous CO_2 injection, equilibria between Fe product minerals and the aqueous solution govern the f_{O_2} of the system, at least after the onset of goethite precipitation (Fig. 7.7b, point D). This event brings about a sharp, remarkable increase in the logarithm of oxygen fugacity from −59.3 to −42.4. The log f_{O_2} is finally fixed at −47.53, for $\xi > 2.7$ (to the right of point E), by coexistence of goethite and siderite at constant f_{CO_2}, temperature and pressure, as expressed by the reaction:

$$FeOOH_{(s)} + CO_{2(g)} = FeCO_{3(s)} + \frac{1}{4}O_{2(g)} + \frac{1}{2}H_2O. \quad (7\text{-}47)$$

7.3.2.5. The CO_2 sequestration

The masses of CO_2 sequestered during the considered process through dissolution (and speciation) in the aqueous solution (solubility trapping) and through incorporation in solid carbonates, mainly magnesite and subordinately siderite and dolomite (mineral fixation) are plotted against both the reaction progress and time in Fig. 7.8. The total mass of sequestered CO_2, corresponding to the sum of these two terms, is also shown.

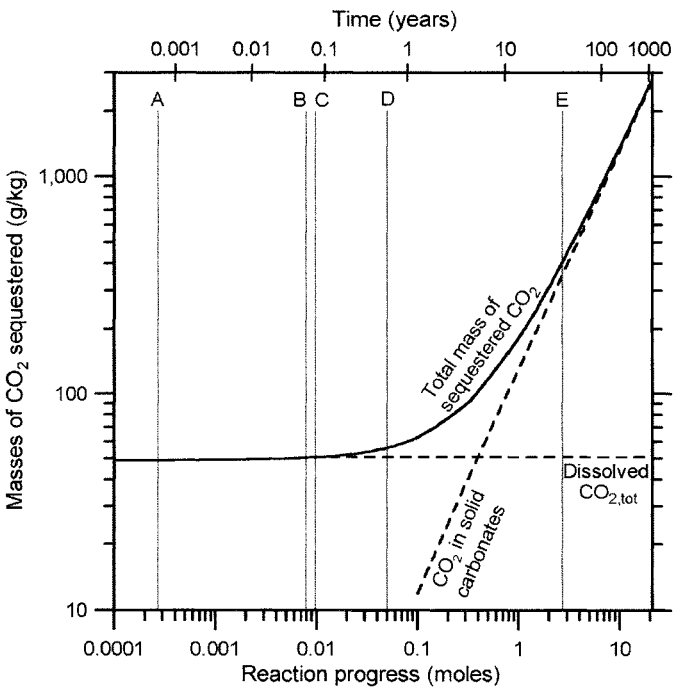

Figure 7.8. High-pressure ($P_{tot} = P_{CO_2}$ = 100 bar) CO_2 injection in a deep aquifer (T = 60°C) hosted in serpentinitic rocks: masses of CO_2 sequestered through dissolution in the aqueous solution (solubility trapping) and incorporation in solid carbonates (mineral fixation), and total mass of sequestered CO_2 as a function of time and the reaction progress variable. Note that letters A to E mark the onset of the precipitation of different secondary minerals as shown in Figure 7.5.

Inspection of Fig. 7.8 shows that CO_2 sequestration through dissolution in the aqueous solution is instantaneous, but relatively limited, as the maximum amount of CO_2 which can be dissolved in 1 kg of water is ~50 g, at the specified conditions of 100 bar $P_{tot} = P_{CO_2}$ and 60° C. Carbon dioxide incorporation in secondary solid carbonates begins later on, namely at points B (dolomite), C (magnesite) and E (siderite). The log-mass of CO_2 incorporated in precipitating solid carbonates increases linearly with log ξ, attaining values much greater than the mass of CO_2 dissolved in the aqueous solution, but this process requires comparatively long time intervals. For instance, the contribution of mineral fixation attains the same level of solubility trapping after 5 years. However, mineral carbonation becomes more and more important afterwards, whereas solubility trapping does not change with time. Again, the sequestration capacity of the process is large and time is less than the residence times of high-pH waters in deep aquifers. In particular the value of 2,000 g kg^{-1} water is attained in 350 years. The same sequestration capacity is attained in 1,000 years in the dunite model by Xu and coworkers, who used somewhat different figures for several parameters (*see* Section 7.3.1).

7.3.2.6. Changes in the porosity of aquifer rocks

To evaluate the changes in the porosity of aquifer rocks in response to high-pressure ($P_{tot} = P_{CO2} = 100$ bar) CO_2 injection we continue to make reference to 1 kg of water. In this way, the model is kept completely independent of the effective porosity of the aquifer. For our purpose, it is useful to take into account the percentual change in the volume of solid phases, $\Delta V/V$. This parameter was already defined in equation (5-125). Here it is re-defined, more correctly, as follows:

$$\Delta V/V = \frac{\sum_P n_P \cdot v_P^o - \sum_R n_R \cdot v_R^o}{\sum_R n_R \cdot v_R^o} \cdot 100 \qquad (7\text{-}48)$$

where v_i^o and n_i represent the molar volume and the moles of the ith solid phase, respectively, and subscripts P and R indicate products and reactants, respectively. Indeed equation (7-48) is similar to the simplified relation (5-125), in which the stoichiometric coefficients of solid phases were used instead of their moles.

The variation of the $\Delta V/V$ parameter as a function of both reaction progress and time is shown in Fig. 7.9. During the first stages of the process (for $\xi < 0.0003$ moles) the $\Delta V/V$ is -100% as rock-forming minerals dissolve congruently, i.e. without precipitation of secondary solid phases. Formation of chalcedony (point A) brings about an initially sharp increase in $\Delta V/V$ and its subsequent stabilization close to -60%. Upon the onset of carbonate minerals precipitation, dolomite at point B and magnesite at point C, the $\Delta V/V$ parameter experiences a new initially sharp increase and gradually approaches $+19.3\%$, which is the limiting value constrained by dissolution of chrysotile accompanied by stoichiometric precipitation of magnesite and quartz (or chalcedony; note that the molar volumes of chalcedony and quartz are virtually equal; see Table 5.11). A value of $\Delta V/V$ close to 17% is attained in ~4 years (Fig. 7.9).

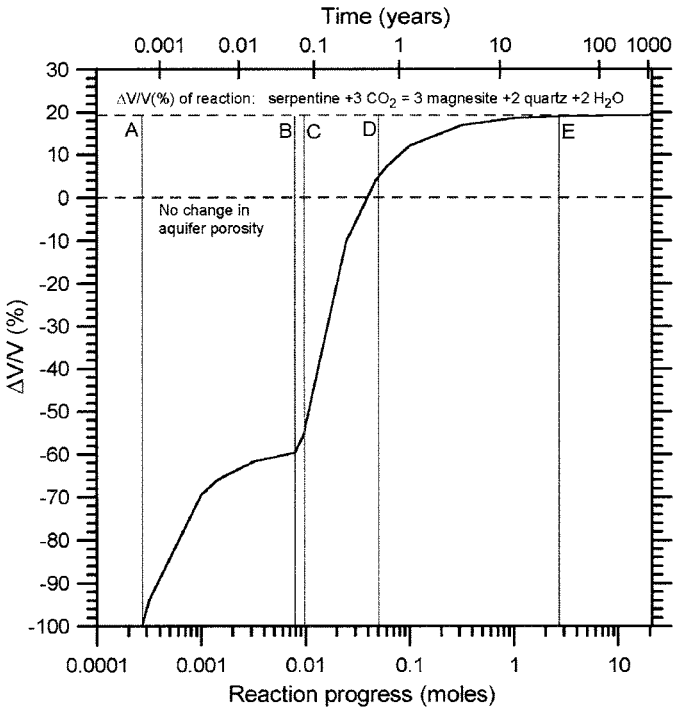

Figure 7.9. Variation of the $\Delta V/V$ parameter as a function of both reaction progress and time during high-pressure ($P_{tot} = P_{CO_2} = 100$ bar) CO_2 injection in a deep aquifer ($T = 60°C$) hosted in serpentinitic rocks. Note that letters A to E mark the onset of the precipitation of different secondary minerals as shown in Figure 7.5.

Obviously, for $\Delta V/V = 0$, the rock-forming minerals dissolved (mainly serpentine) are substituted by an equal volume of secondary solid phases and the porosity of the system does not change. Unfortunately, in the case under consideration, the $\Delta V/V$ is positive and significantly different from zero. Consequently, the occurring reactions, mainly serpentine dissolution accompanied by precipitation of magnesite and chalcedony causes a progressive reduction in the effective porosity of the aquifer. This would drop to zero if its initial value were 19%, whereas effective porosities >0 are only possible for initial values $>19\%$. If precipitation of amorphous silica takes place instead of chalcedony, the reduction in porosity could be even larger, with a maximum $\Delta V/V$ of 30.9%.

Although an initial porosity of 19% seems to be too high a value for serpentinites, it must be emphasized that (1) the natural system might behave as an open, flow-through system (rather than as a closed system), in which case secondary solid phases might deposit outside the reference volume affected by serpentine dissolution; (2) fracturing induced by injection of pressurized CO_2 might occur, with consequent increases in the effective porosity and permeability. As a matter of fact, magnesite veins with nodules of opal are common in the serpentinitic rocks of Southern Tuscany (Arisi Rota et al., 1971), a region characterized by high thermal fluxes (>100 mW m^{-2}, Baldi et al., 1994) and high

CO_2 fluxes (Marini and Chiodini, 1994), indicating that reaction (7-46) occurred naturally in these environments.

In contrast, as the magnesite and silica precipitate in the serpentinitic aquifer, these minerals will likely armor the remaining reactants, thereby further decreasing effective surface area in addition to decreasing porosity. These effects could represent serious obstacles for the implementation of this methodology of CO_2 sequestration and their importance must be evaluated by means of laboratory experiments first and field tests afterwards.

7.3.3. Reaction path modelling of the geological CO_2 sequestration in a serpentinitic aquifer: salinity effects

7.3.3.1. Setting up a water–rock interaction model involving a brine

To investigate the influence of salinity on the geological sequestration of CO_2, it would be desirable to carry out the same simulation of Section 7.3.2, but involving a brine instead of a dilute aqueous solution. As discussed in Sections 4.4 and 4.5, the best way to take into account the interactions among solutes in very concentrated electrolytes is by use of the Pitzer's equations. This capability is available in the software package EQ3/6 and we took advantage of it to carry out some calculations in Section 4.5. Unfortunately, the Pitzer's interaction parameters are not available for fundamental chemical components such as $SiO_{2(aq)}$ and Al^{3+} and are also restricted at relatively low temperatures, sometimes at 25°C only. This is the case, for instance, of the model by Harvie, Møller and Weare (1984) and the corresponding HMW database of EQ3/6, which is based on the system $Na–K–Mg–Ca–H–Cl–SO_4–OH–HCO_3–CO_3–CO_2–H_2O$ and works at 25°C only, as already recalled in Section 4.4.2.

If we want to perform the simulation of Section 7.3.2 but taking into account a brine, we have to accept some limitations and introduce some assumptions. One possibility, that is further detailed below, is to carry out a simplified simulation at the temperature of 25°C, considering only chrysotile as reactant. Accepting to work at 25°C, the HMW database can be used, but $SiO_{2(aq)}$ has to be introduced into it. Strictly speaking, this requires the time-consuming search and processing of the experimental data (admitting that they do exist !) which are needed to derive the Pitzer's interaction parameters between $SiO_{2(aq)}$ and other chemical species, an exercise that goes well beyond the purpose of this book. This serious obstacle can be overcome through a sort of crafty trick, that is hypothesizing that the interaction parameters of $SiO_{2(aq)}$ are equal to those of dissolved CO_2, since both species are neutral. The HMW database was therefore changed accordingly. Of course, this is a very rough choice, but still it is better than nothing.

Again, we assume to inject pure CO_2 at a fugacity of 67.9 bar. Note that since at the considered temperature of 25°C, the fugacity coefficients of CO_2 are smaller than at 60°C (*see* Figure 3.5b), a total pressure ($=P_{CO_2}$) of 263 bar (where Γ_{CO_2} is 0.258) is needed to attain this f_{CO_2} value.

Two simulations were carried out, one involving a brine, initially at saturation with halite, the other with pure water. The results of the pure-water run represent the term of comparison to evaluate salinity effects. Indeed, the simulation of Section 7.3.2 cannot be used for reference due to differences not only in salinity but also in temperature, pressure,

primary phases and secondary minerals (these are really too many differences). The EQ3 input file for the brine was prepared setting a pH of 7, imposing halite saturation to constrain the concentration of Na^+, and assuming $m_{Na^+,tot} = m_{Cl^-,tot}$. Negligible total concentrations (10^{-20} mol kg^{-1}) were assigned to Mg^{2+}, HCO_3^- and $SiO_{2(aq)}$ to activate these chemical components. Pure water was assumed to have initial pH 7 and initial negligible concentrations (10^{-20} mol kg^{-1}) of Mg^{2+}, HCO_3^- and $SiO_{2(aq)}$.

As anticipated, chrysotile was considered to be the only primary solid phase. Values of 4,100 cm^2 and 20.04 mol were assigned to its initial surface area exposed to 1,000 g of water and to its initial amount (see Section 7.3.2.1). Dissolution rate constants were set at 2.00×10^{-10} and 1.00×10^{-16} mol cm^{-2} s^{-1} for the proton- and water-promoted mechanisms, respectively. These are the values for lizardite and chrysotile, respectively, listed in Table 6.1. The reaction orders with respect to H^+ and H_2O are 0.8 and 1.0, respectively, as reported in Table 7.9. Chalcedony, magnesite and halite (in the brine run) were considered to be the only precipitating solid-product phases and instantaneous partial equilibrium was assumed for all secondary minerals.

7.3.3.2. Solid-product phases

The amounts of secondary solid phases produced through high-pressure ($P_{tot} = P_{CO_2} = 263$ bar) CO_2 injection in a system comprising chrysotile and an aqueous solution are displayed in Figure 7.10 for the two runs, involving either a brine, initially saturated with halite, or pure water. In this way the two sets of results can be compared and possible salinity effects can be evaluated. In the pure water run, the onset of chalcedony and magnesite precipitation is somewhat delayed with respect to the brine run, as indicated by the spacings between points A and A′ and between points B and B′. However, the amounts of chalcedony and magnesite produced are equal for $\xi > 0.003$ and $\xi > 0.1$ mol, respectively. The most striking difference between the two simulations, however, is the appearance, in the brine run, of halite whose precipitation occurs immediately upon CO_2 injection. Since the brine was initially saturated with halite under a negligible f_{CO_2}, close to 10^{-20} bar, the increase in f_{CO_2} makes the brine to become oversaturated with halite and a significant amount of this mineral, 0.24 moles, is immediately precipitated. Upon progressive chrysotile dissolution (for $\xi < 0.1$ mol approximately), no further precipitation of halite occurs and this mineral simply remains in the system. However, the dissolution of chrysotile also causes an increase in the mass of water (as already recalled in Section 7.3.2.4, see Figure 7.11a), which becomes significant for $\xi > 0.1$ mol approximately. This increase in water brings about re-dissolution of halite, which disappears from the system at $\xi = 1$ mol (point C). For higher values of the reaction progress, the two runs provide the same results in terms of precipitating solid phases.

7.3.3.3. The aqueous solution

The concentrations of relevant solutes and pH during progressive chrysotile dissolution triggered by high-pressure ($P_{tot} = P_{CO_2} = 263$ bar) CO_2 injection are shown in Figure 7.11 for both the brine run and the pure-water run, to facilitate the comparison of the two series of results and to infer salinity effects.

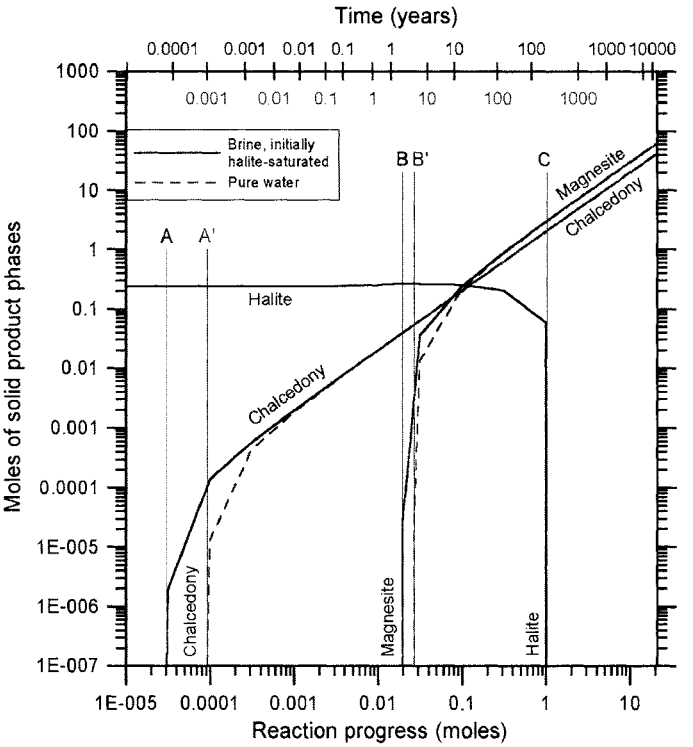

Figure 7.10. Moles of product minerals formed during high-pressure ($P_{tot} = P_{CO_2} = 263$ bar) CO_2 injection in a system ($T = 25°C$) comprising chrysotile and an aqueous solution, either a brine, initially halite-saturated (solid black lines and black time scale) or pure water (dashed grey lines and grey time scale), as a function of time and the reaction progress variable.

First, it must be underscored that after halite re-dissolution (point C), the addition of water to the system through chrysotile dissolution continues and brings about a significant decrease in the concentrations of Na^+ and Cl^-, which behave as mobile components in the final part of the brine simulation.

The main differences between the two simulations, especially before halite re-dissolution, are in pH and in the concentrations of $CO_{2(aq)}$ and $SiO_{2(aq)}$ (although the latter ones can be biased by the assumption on the interaction parameters between $SiO_{2(aq)}$ and the other dissolved species), whereas the differences in the concentrations of Mg^{2+} and HCO_3^- are comparatively small.

Dissolved CO_2 concentration in the halite-saturated brine is 32.3 g kg^{-1}, approximately 1/3 of that in pure water, 101 g kg^{-1}. The $CO_{2(aq)}$ concentration increases somewhat upon halite re-dissolution and brine dilution, i.e. after point C, and attain the maximum value of 48.8 g kg^{-1}, about ½ of the pure water value, at the end of the simulation.

The pH of the halite-saturated brine increases from the initial value of 2.27 to 4.48 at point C but remains 0.7 to 0.5 pH-units lower than the pure-water pH. The maximum

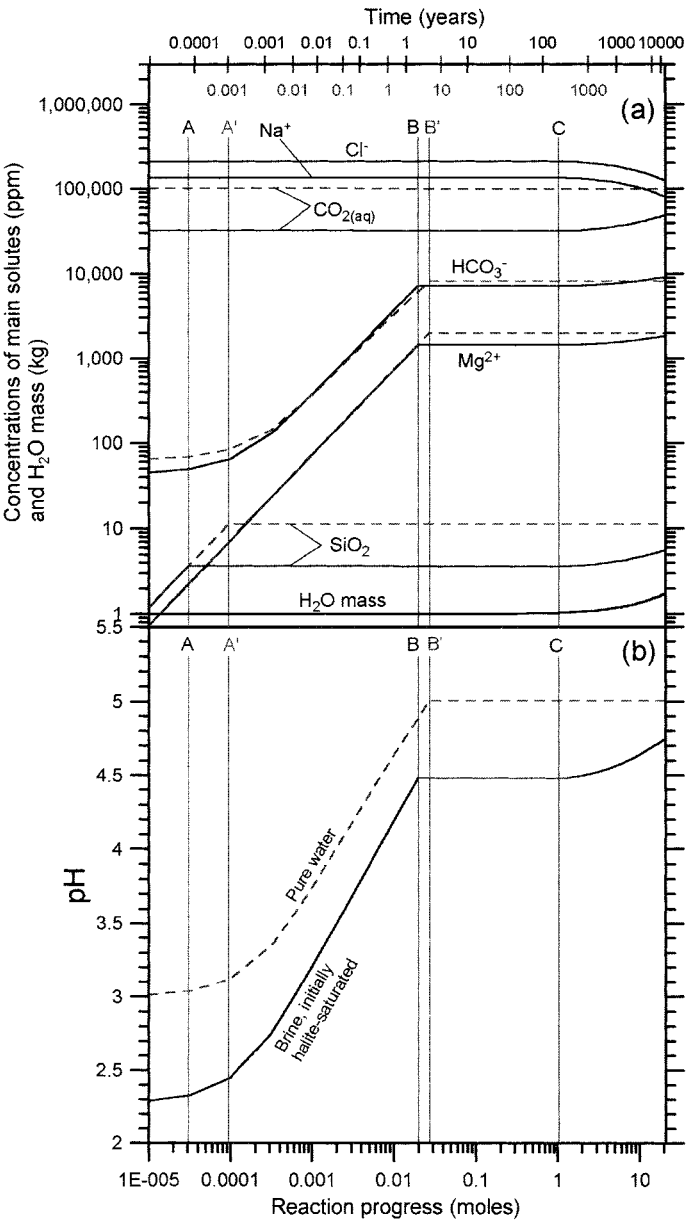

Figure 7.11. (a) concentrations of relevant solutes, mass of water, and (b) pH during high-pressure (P_{tot} = P_{CO_2} = 263 bar) CO_2 injection in a system (T = 25°C) comprising chrysotile and an aqueous solution, either a brine, initially halite-saturated (solid black lines and black time scale) or pure water (dashed grey lines and grey time scale), as a function of time and the reaction progress variable. Letters A, A', B, B' and C correspond to those in Figure 7.10.

increase in pH takes place between the beginning of chalcedony precipitation (point A, pH = 2.33) and the onset of magnesite precipitation (point B, pH = 4.48), after which pH is fixed by carbonate equilibria, as already noticed in Sections 7.1.1 and 7.3.2.4. The difference in pH between the brine and pure water reduces after point C due to dilution of the brine.

7.3.3.4. The CO_2 sequestration

The total mass of CO_2 sequestered through high-pressure ($P_{tot} = P_{CO_2} = 263$ bar) CO_2 injection in a system made up of chrysotile and a brine, initially saturated with halite is compared with that sequestered in a reference system constituted by chrysotile and pure water in Figure 7.12. Also shown are the separated contributions of CO_2 dissolution (and speciation) in the aqueous solution (solubility trapping) and incorporation in precipitating magnesite (mineral fixation).

The plot shows that solubility trapping is strongly dependent on the salinity of the aqueous solution. Nevertheless, the spacing between the two lines outlining solubility trapping, for the brine and pure water, decreases with increasing reaction progress owing

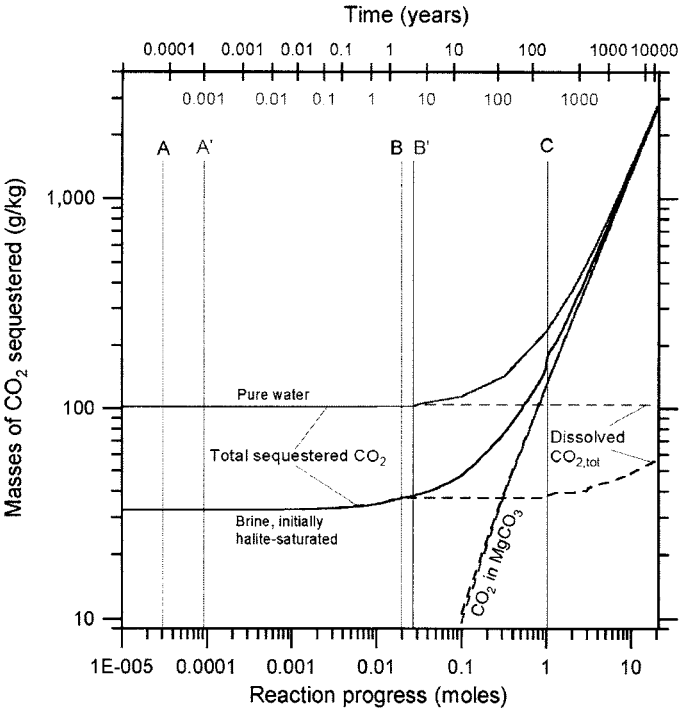

Figure 7.12. High-pressure ($P_{tot} = P_{CO_2} = 263$ bar) CO_2 injection in a system ($T = 25$°C) comprising chrysotile and an aqueous solution, either a brine, initially halite-saturated (solid black lines and black time scale) or pure water (dashed grey lines and grey time scale). The masses of CO_2 sequestered through both dissolution in the aqueous solution (solubility trapping) and incorporation in precipitating magnesite (mineral fixation) as well as the total mass of sequestered CO_2 are shown as a function of time and the reaction progress variable. Letters A, A', B, B' and C correspond to those in Figure 7.10.

to progressive dilution of the brine, as discussed in the previous section. In contrast, mineral fixation is similar for the chrysotile–brine and the chrysotile–pure water systems. Consequently, the difference between the total masses of CO_2 undergoing geological sequestration in these two distinct systems decreases with increasing reaction progress owing to the decreasing contribution of solubility trapping and the increasing contribution of mineral fixation.

Finally, it must be underscored that the time scales are different for the two considered systems. The time needed to exhaust 95% of chrysotile is 12,650 years for the chrysotile–brine system, whereas it amounts to 23,080 years for the chrysotile–pure water system. These values are much higher than the corresponding 758 years of the simulation presented in Section 7.3.2, owing to the different temperatures, 60°C in Section 7.3.2 against 25°C in this section.

7.4. Reaction path modelling of geological CO_2 sequestration in continental tholeiitic flood basalts

Continental tholeiitic flood basalts represent another type of rocks with a relatively high potential of CO_2 sequestration, owing to relatively high contents of MgO and CaO, namely 6.2 and 9.4 wt% on average, respectively (Lackner et al., 1995, 1997). The CO_2 sequestration potential is enhanced further by the significant Na_2O and FeO contents, 2.7 and 9.2 wt% on average, respectively, based on the data reported by Wilson (1989).

A typical example of this kind of rocks is represented by the Columbia River tholeiitic flood basalts in northwestern USA, which extend over an area of ~200,000 km^2 with an average thickness of ~1 km and a maximum thickness> 1.5 km (Wilson, 1989). This volume of rocks would be enough to fix over twice the amount of CO_2 produced through combustion of the global coal reserves, which are estimated to be in the order of 10^{16} kg (Lackner et al., 1995), as already recalled above.

Among the other major continental flood-basalt provinces, we may quote the Siberian Platform, with an extension > 1,500,000 km^2 and a maximum thickness of 3.5 km and the Paranà (Brazil)-Etendeka (Namibia) province, covering a total area of 1,200,000 km^2 with a maximum thickness of 1.8 km (Wilson, 1989).

Therefore it is instructive to model the sequestration of CO_2 through reaction with this type of rock.

7.4.1. Setting up the water–rock interaction model

Starting from the whole-rock chemical analysis of a continental tholeiitic flood basalt from the Columbia River Province (Table 7.10) and assuming that its main constituting mineral phases are a labradoritic plagioclase ($X_{Anorthite}$ = 0.55, X_{Albite} = 0.45), clinopyroxene ($X_{Diopside}$ = 0.75, $X_{Hedenbergite}$ = 0.25), orthopyroxene ($X_{Enstatite}$ = 0.60, $X_{Ferrosilite}$ = 0.40), magnetite, apatite and ilmenite (as suggested by available petrographic data, see Wilson, 1989), simple mass balance calculations show that the molar fractions of these phases are 0.5454, 0.1968, 0.1464, 0.0253, 0.0047 and 0.0210, respectively. Apatite and ilmenite were

neglected from subsequent data elaboration owing to the low content and relatively high chemical durability, respectively; rock composition was then recomputed imposing that the sum of the molar fractions of the other minerals is equal to 1. In this way, the mineralogic composition reported in Table 7.10 was obtained.

The total surface area in contact with 1,000 g of water was set again at 4,100 cm^2, as in the serpentinite case (Sections 7.3.2 and 7.3.3), for comparative purposes. It was distributed in proportion to the volume percentages of the main rock-forming minerals obtaining the initial surface areas reported in Table 7.10. Their initial amounts in the considered system (which are also given in Table 7.10) were then computed through simple geometric computations (*see* Section 7.2.4), assuming an initial porosity of 0.3.

Again, for comparative purposes, aquifer temperature was kept at 60°C and injection of pure CO_2 at a constant pressure of 100 bar (f_{CO_2} of 67.9 bar) was imposed. The initial aqueous solution was assumed to be in equilibrium with analcime, calcite, kaolinite, daphnite, clinochlore, chalcedony and magnetite at 60°C, 1 bar under a f_{CO_2} of 10^{-1} bar (*see* Section 7.1.2).

The computer simulation was performed in kinetic mode, specifying the initial surface areas of primary minerals (which are then changed by the code in proportion to their remaining masses) and describing their dissolution kinetics by means of the TST-based rate law (see Table 7.11). Again, the proton- and water-promoted mechanisms were considered but the hydroxyl-promoted dissolution mechanism was neglected, owing to the

TABLE 7.10

Whole-rock chemical analysis of a typical continental tholeiitic flood basalt from the Columbia River Province (Wilson, 1989) and its computed mineralogic composition

Oxide	Wt%	Element	Mol%
SiO_2	48.35	Si	17.19
TiO_2	1.57	Ti	0.42
Al_2O_3	15.49	Al	6.49
Fe_2O_3	3.26	Fe	3.27
FeO	8.05		
MnO	0.17	Mn	0.05
MgO	7.03	Mg	3.72
CaO	9.92	Ca	3.78
Na_2O	2.76	Na	1.90
K_2O	0.51	K	0.23
P_2O_5	0.24	P	0.07
CO_2	0.05	C	0.02
H_2O	1.52	O	59.29
		H	3.55

Minerals	Mol %	Vol %	Initial moles	Initial surfaces
Plagioclase	59.68	73.86	17.14	3,028.3
Clinopyroxene	21.54	18.32	6.19	751.3
Orthopyroxene	16.02	6.30	4.60	258.2
Magnetite	2.77	1.52	0.80	62.2

TABLE 7.11

EQ6 input file for modeling high-pressure ($P_{tot} = P_{CO2} = 100$ bar) CO_2 injection in a deep aquifer hosted in continental tholeiitic flood basalts at 60°C in kinetic mode (time frame). (Required input formats are not fully respected.)

```
The option switch IOPT1 is set to 1 to direct the code to compute the simulation in time frame.
The option switch IOPT4 is set to 1 to activate solid solutions.
The print option switch IOPR8 is set to 1 to direct the code to print a table of equilibrium gas fugacities at each
print point.
endit.
   nmodl1= 1                        nmodl2= 0
   tempc0= 60.0000E+00               jtemp= 0
      tk1= 0.00000E+00                 tk2= 0.00000E+00        tk3= 0.00000E+00
    zistrt= 0.00000E+00              zimax= 1.00000E-06
    tstrt= 0.00000E+00              timemx= 0.00000E+00
   kstpmx= 500                       cplim= 0.00000E+00
    dzprnt= 1.00000E+00             dzprlg= 0.00000E+00     ksppmx= 100
    dzplot= 0.10000E+00             dzpllg= 0.00000E+00     ksplmx= 10000
      ifile= 60
*              1     2     3     4     5     6     7     8     9     10
 iopt1-10=     1     0     0     1     0     0     0     0     0     0
iopt11-20=     0     0     0     0     0     0     0     0     0     0
 iopr1-10=     0     0     0     0     1     0     0     1     0     0
iopr11-20=     0     0     0     0     0     0     0     0     0     0
 iodb1-10=     0     0     0     0     0     0     0     0     0     0
iodb11-20=     0     0     0     0     0     0     0     0     0     0
*-------------------------------------------------------------------------
    nxopt= 1
   option= all
   nxopex= 10
 exception= Gibbsite
 exception= Kaolinite
 exception= Chalcedony
 exception= Magnetite
 exception= Goethite
 exception= Dawsonite
 exception= Calcite
 exception= Magnesite
 exception= Siderite
 exception= Dolomite
*-------------------------------------------------------------------------
     nffg= 1
  species= CO2(g)
    moffg= 1.00000E+01              xlkffg= +1.83187E+00
*-------------------------------------------------------------------------
     nrct= 4
*-------------------------------------------------------------------------
  reactant= Plagioclase
    jcode= 1                         jreac= 0
     morr= 17.1407E+00               modr= 0.00000E+00
     Albite high     4.53500E-01
     Anorthite       5.46500E-01
endit.
```

TABLE 7.11 (*Continued*)

```
      nsk= 1                    sk= 3028.29E+00          fk= 0.00000E+00
      nrk= 2                  nrpk= -1
    imech= 2
      rk0= 8.03000E-12         trk0= 6.00000E+01        iact= 0
     eact= 0.00000E+00         hact= 0.00000E+00
    ndact= 1                 csigma= 1.00000E+00
     udac= H+                  cdac= 0.62600E+00
      rk0= 8.35000E-15         trk0= 6.00000E+01        iact= 0
     eact= 0.00000E+00         hact= 0.00000E+00
    ndact= 1                 csigma= 1.00000E+00
     udac= H2O                 cdac= 1.00000E+00
*-------------------------------------------------------------------------------
  reactant= Clinopyroxene
    jcode= 1                   jreac= 0
     morr= 6.1863E+00          modr= 0.00000E+00
    Diopside        7.50000E-01
    Hedenbergite    2.50000E-01
endit.
      nsk= 1                    sk= 751.265E+00          fk= 0.00000E+00
      nrk= 2                  nrpk= -1
    imech= 2
      rk0= 4.13000E-10         trk0= 6.00000E+01        iact= 0
     eact= 0.00000E+00         hact= 0.00000E+00
    ndact= 1                 csigma= 1.00000E+00
     udac= H+                  cdac= 0.70000E+00
      rk0= 2.92000E-15         trk0= 6.00000E+01        iact= 0
     eact= 0.00000E+00         hact= 0.00000E+00
    ndact= 1                 csigma= 1.00000E+00
     udac= H2O                 cdac= 1.00000E+00
*-------------------------------------------------------------------------------
  reactant= Orthopyroxene
    jcode= 1                   jreac= 0
     morr= 4.60010E+00         modr= 0.00000E+00
    Enstatite       6.00000E-01
    Ferrosilite     4.00000E-01
endit.
      nsk= 1                    sk= 258.226E+00          fk= 0.00000E+00
      nrk= 2                  nrpk= -1
    imech= 2
      rk0= 4.57000E-12         trk0= 6.00000E+01        iact= 0
     eact= 0.00000E+00         hact= 0.00000E+00
    ndact= 1                 csigma= 1.00000E+00
     udac= H+                  cdac= 0.65000E+00
      rk0= 6.02000E-15         trk0= 6.00000E+01        iact= 0
     eact= 0.00000E+00         hact= 0.00000E+00
    ndact= 1                 csigma= 1.00000E+00
     udac= H2O                 cdac= 1.00000E+00
*-------------------------------------------------------------------------------
```

TABLE 7.11 (*Continued*)

```
  reactant= Magnetite
    jcode= 0                    jreac= 0
     morr= 0.79530E+00          modr= 0.00000E+00
      nsk= 1                      sk= 62.2180E+00        fk= 0.00000E+00
      nrk= 2                    nrpk= -1
    imech= 2
      rk0= 5.65000E-13           trk0= 6.00000E+01      iact= 0
     eact= 0.00000E+00           hact= 0.00000E+00
    ndact= 1                   csigma= 1.00000E+00
     udac= H+                    cdac= 0.27900E+00
      rk0= 3.65000E-15           trk0= 5.00000E+01      iact= 0
     eact= 0.00000E+00           hact= 0.00000E+00
    ndact= 1                   csigma= 1.00000E+00
     udac= H2O                   cdac= 1.00000E+00
*---------------------------------------------------------------------------
   dlzidp= 0.00000E+00
    tolbt= 0.00000E+00          toldl= 0.00000E+00      tolx= 0.00000E+00
   tolsat= 0.00000E+00          tolsst= 0.00000E+00
  screw1= 0.00000E+00          screw2= 0.00000E+00     screw3= 0.00000E+00
  screw4= 0.00000E+00          screw5= 0.00000E+00     screw6= 0.00000E+00
   zklogu= 0.000                zklogl= 0.000           zkfac= 0.000
  dlzmx1= 0.00000E+00          dlzmx2= 0.00000E+00     nordlm= 0
   itermx= 0                   ntrymx= 0
  npslmx= 0                    nsslmx= 0               ioscan= 0
*---------------------------------------------------------------------------
* pickup file written by EQ3NR, version 7.2b (R139 )
* supported by EQLIB, version 7.2b (R168 )
Water in equilibrium with analcime, calcite, kaolinite,
chalcedony, daphnite, clinochlore, magnetite
at 60øC, 0.1 bar PCO2
endit.
   tempci= 6.00000E+01
   nxmod= 0
    iopg1= 0                   iopg2= 0                iopg3= 0
    iopg4= 0                   iopg5= 0                iopg6= 0
    iopg7= 0                   iopg8= 0                iopg9= 0
  iopg10= 0
     kct= 10                     ksq= 11                 kmt= 11
     kxt= 11                    kdim= 11                kprs= 0
O        5.568190070346440E+01
Al       2.397285511182285E-07
Ca       4.360523578853289E-05
Cl       3.000000000355616E-02
Fe       3.862527706607725E-06
H        1.110727982477859E+02
C        5.793621436309842E-02
Mg       1.602243822990042E-04
Na       8.637858497535496E-02
Si       6.159324420874708E-04
electr   1.323234709603221E-11
```

TABLE 7.11 (*Continued*)

H_2O	H_2O	1.744358983526984E+00
Al^{+++}	Al^{+++}	− 1.710395611381481E+01
Ca^{++}	Ca^{++}	− 4.562090256614116E+00
Cl^-	Cl^-	− 1.527663478385729E+00
Fe^{++}	Fe^{++}	− 6.567807046642986E+00
H^+	H^+	− 7.592429061239226E+00
HCO_3^-	HCO_3^-	− 1.269686271112627E+00
Mg^{++}	Mg^{++}	− 3.959985610775256E+00
Na^+	Na^+	− 1.076209250999970E+00
$SiO_2(aq)$	$SiO_2(aq)$	− 3.230700000000000E+00
$O_2(g)$	$O_2(g)$	− 6.098389925982678E+01

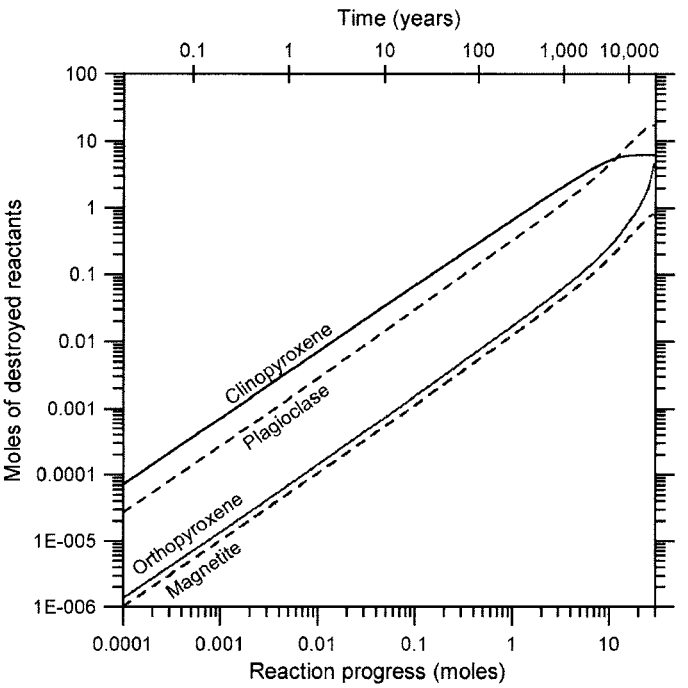

Figure 7.13. Moles of reactant minerals destroyed during high-pressure ($P_{tot} = P_{CO_2} = 100$ bar) CO_2 injection in a deep aquifer ($T = 60°C$) hosted in continental tholeiitic flood basalts as a function of time and the reaction progress variable.

low pH values constrained by CO_2 injection (see below). As in previous cases, selected secondary minerals were assumed to attain instantaneous partial equilibrium, owing to the difficulty in determining the surface area for solid phases which are not present in the considered system at the beginning of the simulation.

The diagrams of Figures 7.13 to 7.18 depict the main results of this reaction path modelling exercise against both the reaction progress variable, ξ, and time.

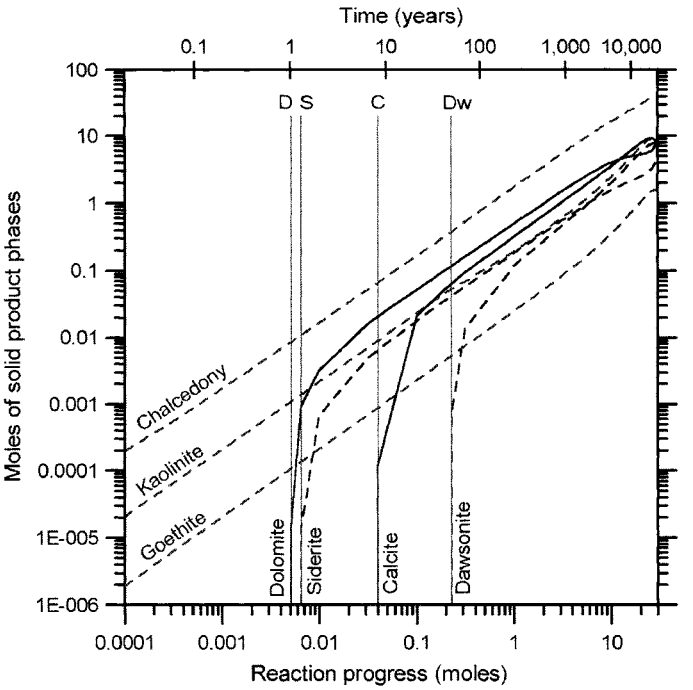

Figure 7.14. Amounts of product minerals formed during high-pressure ($P_{tot} = P_{CO_2} = 100$ bar) CO_2 injection in a deep aquifer ($T = 60°C$) hosted in continental tholeiitic flood basalts as a function of time and the reaction progress variable. Letters D, S, C and Dw mark the onset of the precipitation of secondary dolomite, siderite, calcite and dawsonite, respectively.

7.4.2. Solid reactants

Throughout CO_2 injection coupled with basalt dissolution, the aqueous solution remains strongly undersaturated with respect to plagioclase ($A \leq -9.6$ kcal mol^{-1}), clinopyroxene ($A \leq -16.3$ kcal mol^{-1}), orthopyroxene ($A \leq -8.3$ kcal mol^{-1}) and magnetite ($A \leq -3.4$ kcal mol^{-1}). Owing to these relatively low values of A, the dissolution rates of primary phases are always independent of thermodynamic affinity (*see* Section 6.4.2) and depend on pH only.

The moles of primary minerals consumed during continuous CO_2 injection and basalt dissolution are presented in Figure 7.13. The two most abundant solid phases, plagioclase and clinopyroxene, contribute most chemical components to the considered system, but their contributions are generally reversed with respect to their surface areas, owing to the overwhelming weight of the dissolution rate (in mol cm^{-2} s^{-1}), which is much higher for clinopyroxene than for the labradoritic plagioclase, in acidic solutions (see Tables 6.1 and 7.11). Only in the final part of the simulation, namely upon exhaustion of clinopyroxene, plagioclase becomes the top provider of chemical components.

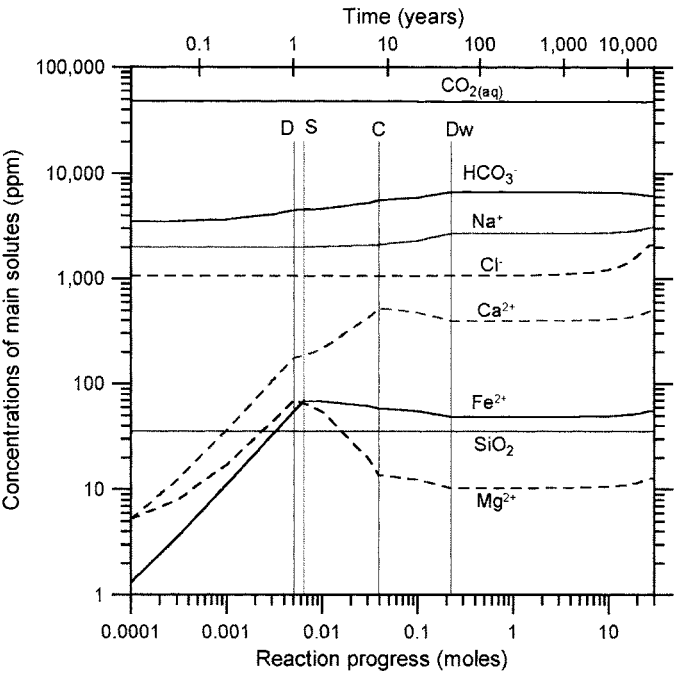

Figure 7.15. Concentrations of solutes during high-pressure (P_{tot} = P_{CO_2} = 100 bar) CO_2 injection in a deep aquifer (T = 60°C) hosted in continental tholeiitic flood basalts as a function of time and the reaction progress variable. Letters D, S, C and Dw mark the onset of the precipitation of secondary dolomite, siderite, calcite and dawsonite, respectively, as shown in Figure 7.14.

The contributions of orthopyroxene and magnetite are generally subordinate owing to their comparatively low dissolution rates (in mol cm^{-2} s^{-1}) and amounts; however, orthopyroxene becomes an important supplier of chemical components in the final part of the simulation, upon exhaustion of other solid reactants.

Clinopyroxene is totally consumed after 26,100 years, for ξ of 22.9 mol, plagioclase is exhausted after 191,300 years, for ξ of 28.4 mol, and magnetite is completely consumed after 280,600 years, for ξ of 28.6 mol. The simulation ends for ξ of 28.7 mol, upon exhaustion of orthopyroxene.

7.4.3. Solid product phases

The solid phases which are precipitated during continuous CO_2 injection in a deep aquifer hosted in tholeiitic continental flood basalts are, in order of appearance, chalcedony, kaolinite, goethite, dolomite, siderite, calcite and dawsonite [$NaAlCO_3(OH)_2$] (Figure 7.14). Both chalcedony and kaolinite form immediately upon CO_2 injection, goethite production begins after 9 h and 10 min (ξ = 5.76 μmol), whereas the precipitation of carbonate minerals starts much later: that of dolomite after 1 year (ξ = 5.12 mmol),

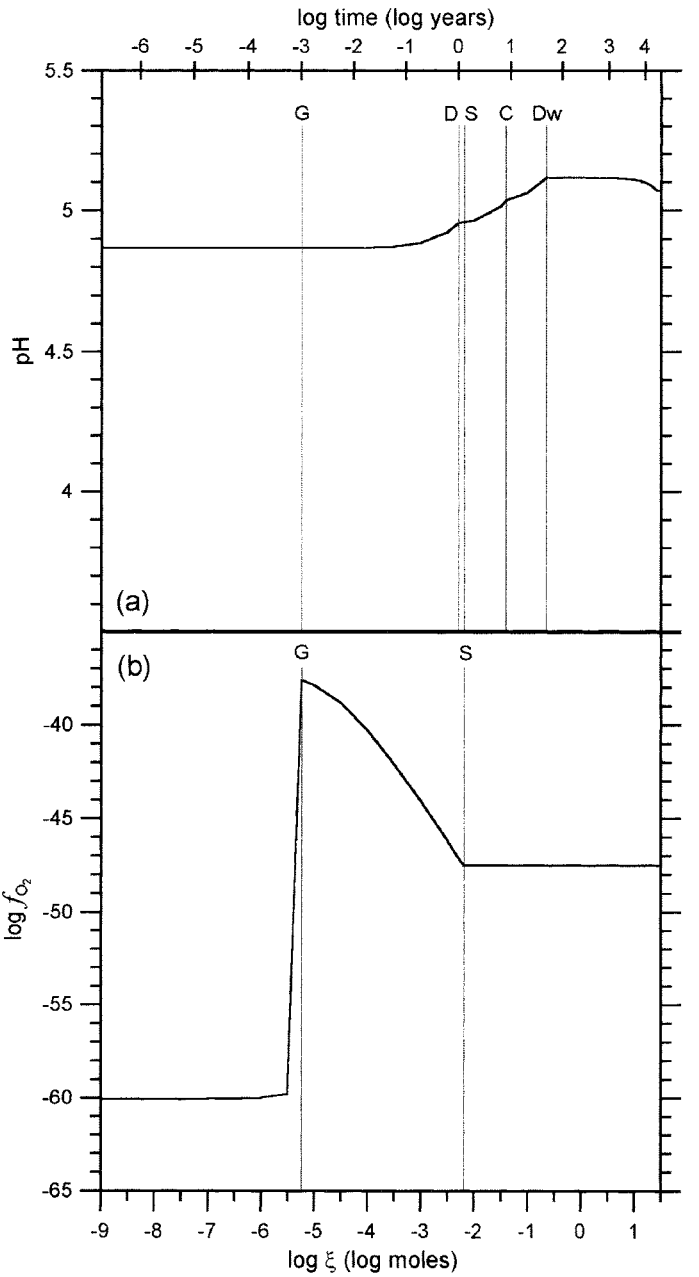

Figure 7.16. Changes in (a) pH and (b) f_{O_2} during high-pressure (P_{tot} = P_{CO_2} = 100 bar) CO_2 injection in a deep aquifer (T = 60°C) hosted in continental tholeiitic flood basalts as a function of time and the reaction progress variable. Letters G, D, S, C and Dw mark the onset of the precipitation of secondary goethite, dolomite, siderite, calcite and dawsonite, respectively.

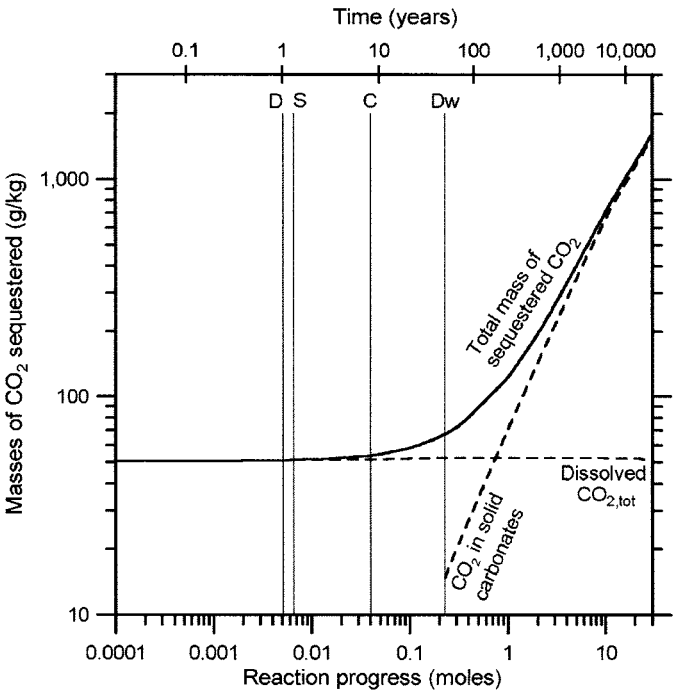

Figure 7.17. High-pressure (P_{tot} = P_{CO_2} = 100 bar) CO_2 injection in a deep aquifer (T = 60°C) hosted in continental tholeiitic flood basalts: masses of CO_2 sequestered through dissolution in the aqueous solution (solubility trapping) and incorporation in solid carbonates (mineral fixation), and total mass of sequestered CO_2 as a function of time and the reaction progress variable. Letters D, S, C and Dw mark the onset of the precipitation of secondary dolomite, siderite, calcite and dawsonite, respectively, as shown in Figure 7.14.

that of siderite after 1 year and 3 months (ξ = 5.12 mmol), that of calcite after 8 years and 5 months (ξ = 39.8 mmol) and that of dawsonite after 53 years and 5 months (ξ = 227 mmol).

The log-moles of each solid phase increase close to linearly with log ξ after an initial non-linear trend, which is evident for carbonate minerals only in Figure 7.14. Chalcedony is by far the most important solid product phase throughout the process, carbonate minerals and kaolinite are produced in similar amounts (after an initial settling-down period), whereas goethite is the least important secondary phase.

The masses of produced carbonate minerals amount to: (i) 91.7 g of dolomite, 31.9 g of calcite, 20.9 g of siderite and 16.6 g of dawsonite, for a total of 161.1 g, after 255 years (ξ = 1 mol); (ii) 736 g of dolomite, 355 g of calcite, 180 g of siderite and 288 g of dawsonite, for a total of 1,559 g, after 4,080 years (ξ = 10 mol); (iii) 1,015 g of dolomite, 871 g of calcite, 319 g of siderite and 960 g of dawsonite, for a total of 3,165 g, after 26,100 years (ξ = 22.9 mol), upon exhaustion of clinopyroxene. These figures confirm the high potential of CO_2 sequestration of these basaltic rocks, including the important role of dawsonite, in spite of the long time required for mineral fixation.

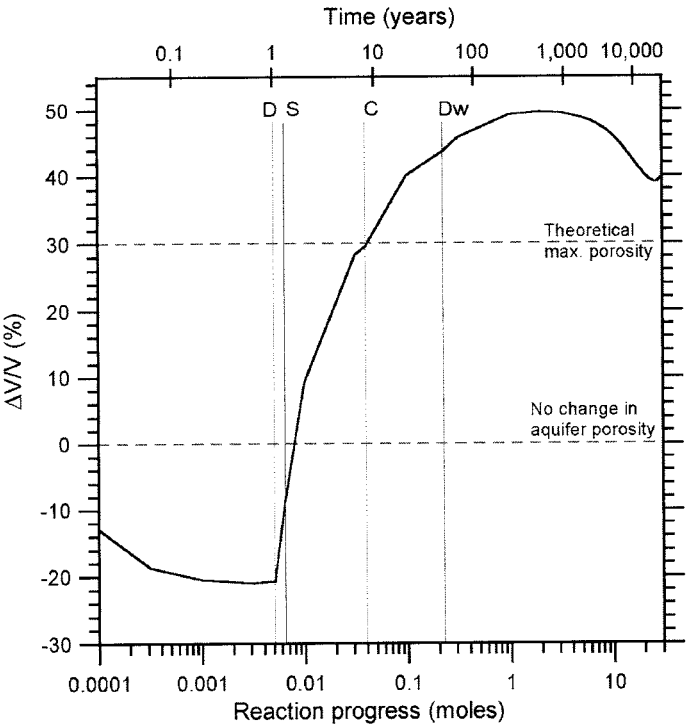

Figure 7.18. Variation of the $\Delta V/V$ parameter as a function of both reaction progress and time during high-pressure ($P_{tot} = P_{CO_2} = 100$ bar) CO_2 injection in a deep aquifer ($T = 60°C$) hosted in continental tholeiitic flood basalts. Letters D, S, C and Dw mark the onset of the precipitation of secondary dolomite, siderite, calcite and dawsonite, respectively, as shown in Figure 7.14.

7.4.4. The aqueous solution

Also throughout this computer experiment, the main solute is aqueous CO_2, with a concentration varying between 48,100 and 47,200 ppm (Figure 7.15). In other words, CO_2 concentration remains practically constant at 1.1 mol kg^{-1}, the same figure of the serpentinite experiment (*see* Section 7.3.2.4.), owing to the constancy in f_{CO_2}, at fixed temperature and pressure.

Aqueous CO_2 is followed in order of decreasing importance (at least for $\xi > 0.01$ mol) by HCO_3^-, Na^+, Cl^-, Ca^{2+}, Fe^{2+}, SiO_2 and Mg^{2+}. Dissolved SiO_2 is kept constant throughout the simulation by saturation with chalcedony, a condition which is attained immediately upon CO_2 injection. Chloride concentration remains constant at the initial value, 1,060 mg kg^{-1}, for over 22 years and then it increases. Such an increase is initially weak but becomes more and more important with time, especially after 4,000 years ($\xi > 10$ mol). This effect is caused by the progressive incorporation of water in precipitating hydrous minerals (kaolinite, dawsonite and goethite), a phenomenon known as dry-up (Reed, 1997), as already recalled above.

The concentrations of all the other solutes, i.e. HCO_3^-, Na^+, Ca^{2+}, Fe^{2+} and Mg^{2+} experience an initial increase (very pronounced for Ca^{2+}, Fe^{2+} and Mg^{2+} and rather weak for HCO_3^- and Na^+), before the attainment of saturation with respect to carbonate minerals. This is followed by a general stabilization after the onset of dawsonite precipitation (i.e. after 53 years and 5 months, for ξ of 227 mmol, point Dw in Fig. 7.15), with more or less important changes in the intermediate period. It must be underscored that for $\xi > 227$ mmol, calcite, dolomite, siderite and dawsonite are in equilibrium with the aqueous solution, a condition which fixes the activities of free Ca^{2+}, Mg^{2+}, Fe^{2+} and Na^+, respectively. Only limited changes in the total concentrations of these solutes are possible, owing to variations in salinity and consequent changes in the concentrations of complex species.

The simulation predicts that upon CO_2 injection, the pH of the aqueous solution attains immediately the value of 4.87 (Fig. 7.16a), which is higher by one unit than the initial pH value of the serpentinite case, 3.83, and comparable with its final pH value, 4.85 (*see* Section 7.3.2.4). This relatively high initial pH value of the basalt case is consistent with the high concentrations of Na^+ and HCO_3^- in the aqueous solution, which are the two prevailing solutes (see above). During progressive CO_2 injection and basalt dissolution, the pH of the aqueous solution increases up to the maximum value of 5.12 at point Dw and remains stable afterwards, since it is buffered by coexistence of carbonate minerals, apart from a minor decrease to 5.07 in the final part of the simulation.

Changes in $\log f_{O_2}$ are similar to those of the serpentinite case, with a sharp increase from -59.8 to -37.6 concurrent with the attainment of goethite saturation (Fig. 7.16b, point G), which is followed by a gradual decrease until the aqueous solution saturates with siderite (point S). From this point, coexistence of goethite and siderite at constant f_{CO_2}, temperature and pressure (reaction 7-47) fixes the $\log f_{O_2}$ at -47.53, as already mentioned in Section 7.3.2.4.

7.4.5. The CO_2 sequestration

The masses of CO_2 sequestered through both solubility trapping (i.e. as dissolved CO_2 and related carbonate aqueous species) and mineral fixation (i.e. the CO_2 stored in secondary carbonate minerals, namely dolomite, siderite, calcite and dawsonite in the considered case), as well as their sum are shown in Figure 7.17 as a function of the reaction progress and time.

As already discussed above, CO_2 sequestration through solubility trapping is instantaneous, but quite small, as it amounts to ~50 g in 1 kg of water at the specified conditions of 60°C and $P_{tot} = P_{CO_2} = 100$ bar. Incorporation of CO_2 in product carbonates begins at the onset of dolomite precipitation (point D) and continues with the contributions of siderite from point S, calcite from point C and dawsonite from point Dw. Although mineral fixation is a late process, it becomes more and more important with time and the overall sequestration potential of the process is considerable, with 1,580 g kg^{-1} of water upon exhaustion of primary minerals. However, the contribution of mineral fixation equals that of solubility trapping only after 175 years, against the 5 years of the serpentinite case (*see* Section 7.3.2.5).

7.4.6. Changes in the porosity of aquifer rocks

Also for the tholeiitic basalt case, the $\Delta V/V$ parameter was computed and plotted as a function of both the reaction progress and time (Fig. 7.18) to estimate the variations in the porosity of aquifer rocks consequent to high-pressure CO_2 injection (*see* equation (7-48) and Section 7.3.2.6). The $\Delta V/V$ parameter exhibits a sharp increase when carbonate minerals begin to precipitate, achieves the 30% value soon after point C, where the aqueous solution saturates with calcite after 8 years and 5 months (ξ = 39.8 mmol), and attains the maximum value close to 50% after 250−1,500 years. Considering that the 30% value represents a sort of upper threshold even for high-porosity rocks, continuous CO_2 injection in a deep aquifer hosted in tholeiitic continental flood basalts is expected to reduce dramatically its porosity. The long-term sustainability of this process is therefore dubious.

These volume changes are not surprising, since the considered primary phases (plagioclase, clinopyroxene, orthopyroxene and magnetite) have very low molar volumes, a situation quite similar to the dunite example of Xu et al. (2000, 2004).

All in all, the basalt example provide contrasting results, as the positive findings concerning the potential of CO_2 sequestration of Na-bearing minerals and rocks, in the form of secondary dawsonite, are in striking contrast with the negative findings regarding the huge reduction in the effective porosity of the aquifer.

7.5. Reaction path modelling of geological CO_2 sequestration in basaltic glass

In Section 7.4, the continental tholeiitic flood basalt involved in CO_2 sequestration was considered holocrystalline, that is composed entirely of crystals. This is a limiting, somewhat unlikely case for volcanic rocks, which are usually composed by varying amounts of glass, mostly depending on their cooling history and age. Glasses are typically formed by quenching of silicate melts that prevents the organization of the random liquid structure into ordered crystalline structures. Glasses are metastable and are doomed to crystallize, soon or later. They are often believed to be more reactive than their crystalline counterparts, but this is not always the case, as discussed in Section 6.6.6.

The dissolution kinetics of silicate glasses has received considerable attention (*see* Sections 6.3.2 and 6.6.6) and, in particular, that of a basaltic glass from Stapafell mountain in southwestern Iceland was investigated experimentally and described in the framework of the multi-oxide dissolution model by Oelkers, Gislason and coworkers (Section 6.6.6.2). As already recalled, the chemical composition normalized to 1 Si atom of this basaltic glass is $Si\ Ti_{0.02}\ Al_{0.36}\ Fe(III)_{0.02}\ Fe(II)_{0.17}\ Mg_{0.28}\ Ca_{0.26}Na_{0.08}\ K_{0.008}\ O_{3.38}$. As underscored by Oelkers and Gislason (2001), the basaltic glass from Stapafell is similar in chemical composition to both the average oceanic crust [$Si\ Ti_{0.02}\ Al_{0.37}\ Fe(III)_{0.04}\ Fe(II)_{0.13}\ Mg_{0.23}\ Ca_{0.27}\ Na_{0.10}\ K_{0.008}\ O_{3.35}$] and the average mid ocean ridge basalt [$Si\ Ti_{0.02}\ Al_{0.36}\ Fe(III)_{0.04}\ Fe(II)_{0.13}\ Mg_{0.24}\ Ca_{0.25}Na_{0.10}\ K_{0.003}\ O_{3.33}$], which is usually indicated by the acronym MORB. Note that since the separate contents of Fe(III) and Fe(II) are not reported for the average MORB, its Fe(III)/Fe(II) ratio was assumed to be equal to that of

average oceanic crust to distribute total Fe between the ferric and ferrous reservoirs. The basaltic glass from Stapafell mountain is also quite similar to the continental tholeiitic flood basalt considered in Section 7.4, whose chemical composition normalized to 1 Si atom is Si $Ti_{0.02}$ $Al_{0.38}$ $Fe(III)_{0.05}$ $Fe(II)_{0.14}$ $Mg_{0.22}Ca_{0.22}$ $Na_{0.11}$ $K_{0.01}$ $O_{3.34}$.

In spite of the compositional similarity, the basaltic glass from Stapafell mountain is obviously different from the holocrystalline continental tholeiitic flood basalt considered in previous section from the mineralogical point of view and, consequently, a different reaction path is expected upon interaction with water and CO_2. To evaluate these differences, in this section we simulate the geological storage of CO_2 in a hypothetical aquifer hosted in the basaltic glass from Stapafell mountain.

7.5.1. Setting up the water–rock interaction model

7.5.1.1. The need for two solid reactants

As anticipated in Section 6.6.6.2, Gislason and Oelkers (2003) considered the hydrolysis reaction (6-142) for the hydrated basaltic glass of composition $SiAl_{0.36}O_2(OH)_{1.08}$, which presumably forms a thin layer at the surface of the basaltic glass during its dissolution. Incidentally, note that the chemical formula of hydrated basaltic glass can also be expressed as $SiO_2 \cdot 0.18Al_2O_3 \cdot 0.54\ H_2O$, in terms of the component oxides, or $SiO_2 \cdot 0.36Al(OH)_3$, in terms of the hypothetical component minerals. The equilibrium constants of the hydrolysis reaction of hydrated basaltic glass (reaction 6-142) was evaluated by Gislason and Oelkers (2003) based on the latter chemical formula. First, they assumed that amorphous silica and gibbsite are the two hypothetical component minerals of hydrated basaltic glass, in a molar ratio 1:0.36. Then, they computed the equilibrium constants of the hydrolysis reaction of hydrated basaltic glass by summing $\log K_{sp,\ amorphous\ silica}$ plus 0.36 $\log K_{sp,\ gibbsite}$. The obtained $\log K_{sp}$ values of hydrated basaltic glass at varying temperatures are reported in Section 6.6.6.2.

Before running EQ6, the $\log K_{sp}$ of hydrated basaltic glass were re-computed at the temperature, pressure grid required by EQ3/6, through simple interpolation, and inserted in the thermodynamic database of EQ3/6. After this necessary preparatory step, the saturation state of any aqueous solution with respect to this hydrated basaltic glass can be computed by means of EQ3/6. Moreover, this hydrated basaltic glass can be treated as a pure mineral reactant and its dissolution can be properly simulated by running EQ6 (Table 7.12).

To this purpose, the dissolution rate law proposed by Gislason and Oelkers (2003), equation (6-143), is inserted in the EQ6 input file as a TST rate law involving the activities of both H^+ and Al^{3+} ions, as we have already seen in the albite example (*see* Section 7.2.4). It must be recalled that Gislason and Oelkers (2003) report the dissolution rate of the basaltic glass normalized to its geometric surface area, $r_{+,GEOM}$. However, they also underscore that these $r_{+,GEOM}$ are 92 times larger than the dissolution rates normalized to the BET surface area, $r_{+,BET}$. Both values were inserted in two separated EQ6 input files, to evaluate the effects of these limiting dissolution rates on the EQ6 simulation.

Only Al and Si are released to the aqueous solution through dissolution of the hydrated basaltic glass involved so far in the model. In contrast, we know that dissolution

TABLE 7.12

EQ6 input file for modeling high-pressure ($P_{tot} = P_{CO_2} = 100$ bar) CO_2 injection in a hypothetical deep aquifer hosted in basaltic glass at 60°C in kinetic mode (time frame). The rk0 value of 2.52370×10^{-10} mol cm^{-2} s^{-1} is the dissolution rate constant normalized to the geometric surface of the basaltic glass at 60°C (from Oelkers and Gislason, 2003). (Required input formats are not fully respected.)

```
The option switch IOPT1 is set to 1 to direct the code to compute the simulation in time frame.
The option switch IOPT4 is set to 1 to activate solid solutions.
The print option switch IOPR8 is set to 1 to direct the code to print a table of equilibrium gas fugacities at each
print point.
endit.
   nmodl1= 1                        nmodl2= 0
   tempc0= 60.0000E+00               jtemp= 0
      tk1= 0.00000E+00                 tk2= 0.00000E+00        tk3= 0.00000E+00
    zistrt= 0.00000E+00              zimax= 1.00000E-01
    tstrt= 0.00000E+00             timemx= 0.00000E+00
   kstpmx= 500                       cplim= 0.00000E+00
    dzprnt= 1.00000E-02              dzprlg= 0.00000E+00    ksppmx= 100
    dzplot= 0.10000E+00              dzpllg= 0.00000E+00    ksplmx= 10000
      ifile= 60
*                1    2    3    4    5    6    7    8    9   10
 iopt1-10=       1    0    0    1    0    0    0    0    0    0
iopt11-20=       0    0    0    0    0    0    0    0    0    0
 iopr1-10=       0    0    0    0    1    0    0    1    0    0
iopr11-20=       0    0    0    0    0    0    0    0    0    0
 iodb1-10=       0    0    0    0    0    0    0    0    0    0
iodb11-20=       0    0    0    0    0    0    0    0    0    0
*-------------------------------------------------------------------------------
    nxopt= 1
   option= all
   nxopex= 10
 exception= Gibbsite
 exception= Kaolinite
 exception= Chalcedony
 exception= Magnetite
 exception= Goethite
 exception= Dawsonite
 exception= Calcite
 exception= Magnesite
 exception= Siderite
 exception= Dolomite
*-------------------------------------------------------------------------------
     nffg= 1
  species= CO2(g)
    moffg= 1.00000E+01              xlkffg= +1.83187E+00
*-------------------------------------------------------------------------------
     nrct= 2
*-------------------------------------------------------------------------------
  reactant= Hyd-basalt-glass
    jcode= 0                         jreac= 0
     morr= 56.09000E+00              modr= 0.00000E+00
      nsk= 1                           sk= 4100.00E+00        fk= 0.00000E+00
```

TABLE 7.12 (*Continued*)

```
      nrk= 2                    nrpk= -1
    imech= 1
      rk0= 2.52370E-10          trk0= 6.00000E+01        iact= 0
     eact= 0.00000E+00          hact= 0.00000E+00
    ndact= 2                   csigma= 1.00000E+00
     udac= H+                   cdac= 1.00000E+00
     udac= Al+++                cdac= -0.33333E+00
*---------------------------------------------------------------------
  reactant= rock
    jcode= 2                    jreac= 0
     morr= 56.09000E+00         modr= 0.00000E+00
    vreac= 0.00000E+00
     Fe      1.9000E-01
     Mg      2.8000E-01
     Ca      2.6000E-01
     Na      8.0000E-02
     O       7.8000E-01
endit.
      nsk= 0                     sk= 0.00000E+00          fk= 0.00000E+00
      nrk= 1                    nrpk= 0
      rk1= 1.00000E+00          rk2= 0.00000E+00          rk3= 0.00000E+00
*---------------------------------------------------------------------
   dlzidp= 0.00000E+00
    tolbt= 0.00000E+00          toldl= 0.00000E+00          tolx= 0.00000E+00
   tolsat= 0.00000E+00         tolsst= 0.00000E+00
   screw1= 0.00000E+00         screw2= 0.00000E+00         screw3= 0.00000E+00
   screw4= 0.00000E+00         screw5= 0.00000E+00         screw6= 0.00000E+00
    zklogu= 0.000               zklogl= 0.000               zkfac= 0.000
   dlzmx1= 0.00000E+00         dlzmx2= 0.00000E+00         nordlm= 0
    itermx= 0                  ntrymx= 0
   npslmx= 0                   nsslmx= 0                   ioscan= 0
*---------------------------------------------------------------------
* pickup file written by EQ3NR, version 7.2b (R139 )
* supported by EQLIB, version 7.2b (R168 )
Water in equilibrium with analcime, calcite, kaolinite,
chalcedony, daphnite, clinochlore, magnetite
at 60ØC, 0.1 bar PCO2
endit.
    tempci= 6.00000E+01
    nxmod= 0
     iopg1= 0                   iopg2= 0                 iopg3= 0
     iopg4= 0                   iopg5= 0                 iopg6= 0
     iopg7= 0                   iopg8= 0                 iopg9= 0
    iopg10= 0
       kct= 10                    ksq= 11                  kmt= 11
       kxt= 11                   kdim= 11                 kprs= 0
O         5.568190070346440E+01
Al        2.397285511182285E-07
Ca        4.360523578853289E-05
Cl        3.000000000355616E-02
Fe        3.862527706607725E-06
```

TABLE 7.12 (*Continued*)

H	1.110727982477859E+02	
C	5.793621436309842E–02	
Mg	1.602243822990042E–04	
Na	8.637858497535496E–02	
Si	6.159324420874708E–04	
electr	1.323234709603221E–11	
H_2O	H_2O	1.744358983526984E+00
Al^{+++}	Al^{+++}	– 1.710395611381481E+01
Ca^{++}	Ca^{++}	– 4.562090256614116E+00
Cl^-	Cl^-	– 1.527663478385729E+00
Fe^{++}	Fe^{++}	– 6.567807046642986E+00
H^+	H^+	– 7.592429061239226E+00
HCO_3^-	HCO_3^-	– 1.269686271112627E+00
Mg^{++}	Mg^{++}	– 3.959985610775256E+00
Na^+	Na^+	– 1.076209250999970E+00
SiO_2(aq)	SiO_2(aq)	– 3.230700000000000E+00
O_2(g)	O_2(g)	– 6.098389925982678E+01

of basaltic glass adds also several other metals to the aqueous phase. To take into account the fate of all these metals, it is necessary to involve a second reactant in the EQ6 simulation. This second reactant can be treated as a so-called *special reactant* (in EQ6 meaning), that is a substance whose chemical composition is known but whose thermodynamic properties are not. Obviously, substances of this kind (e.g., any rock) cannot be inserted in the thermodynamic database of EQ3/6.

In the basaltic glass case, the special reactant has composition $Ti_{0.02}$ $Fe(III)_{0.02}$ $Fe(II)_{0.17}$ $Mg_{0.28}$ $Ca_{0.26}$ $Na_{0.08}$ $K_{0.008}$ $O_{0.82}$, since it is the Si-free, Al-free portion of the whole basaltic glass. Titanium and K are not considered in the EQ6 simulation owing to the low solubility of Ti minerals and the low content of K, which was also neglected in the tholeiitic basalt case. The number of oxygen atoms have to be decreased, therefore, to 0.78 to balance the metal charges. Note that it is very important to maintain the chemical formula of special reactants stoichiometrically balanced by adjusting the number of oxygen atoms, otherwise incorrect f_{O_2} values are computed by EQ6. Besides, it is necessary to instruct EQ6 to dissolve this special reactant at the same rate of the hydrated basaltic glass. This is accomplished by setting the rsk1 flag to 1.

7.5.1.2. The molar volume of basaltic glass

Let us assume again that the considered system comprises 1,000 g of water and has an initial porosity of 0.3. Equation (7-44) dictates that initially basaltic glass occupies a volume of 2,333 cm^3. The molar volume of the basaltic glass is needed to compute both the moles of basaltic glass initially present in the system and the changes in the $\Delta V/V$ parameter during the simulation by using equation (7-48).

The molar volume of the basaltic glass can be calculated based on the partial molar volumes and the volumetric thermal expansion coefficients of the component oxides, whereas their compressibilities can be neglected at the relatively low pressures of interest.

These volumetric parameters of the component oxides of silicate melts and glasses have been the subject of several investigations (e.g., Bottinga et al., 1982; Lange and Carmichael, 1987, 1990; Knoche et al., 1995; Lange, 1997; Toplis and Richet, 2000). Inserting the partial molar volumes $\overline{V}_i$ ($cm^3\ mol^{-1}$) and the thermal expansions $d\overline{V}_i/dT$ ($cm^3\ mol^{-1}\ K^{-1}$) given by Lange and Carmichael (1987) into the simplified relation (T in K):

$$v_{liq} = \sum_i X_i \cdot \left[\overline{V}_{i,1673K} + \frac{d\overline{V}_i}{dT} \cdot (T - 1673) \right] \tag{7-49}$$

the molar volume of the basaltic glass of interest at 60°C, 1 bar results to be 21.05 $cm^3\ mol^{-1}$, corresponding to 41.60 $cm^3\ mol^{-1}$ for the chemical formula normalized to 1 Si atom. Therefore, the moles of basaltic glass initially contained in the considered system amount to 2,333 cm^3/41.60 $cm^3\ mol^{-1}$ = 56.09 mol. Some words of caution are needed on the possible contribution of water to the molar volume of the basaltic glass. Water was not considered in previous calculations since its content in the basaltic glass of Stapafell is not reported by Oelkers and Gislason (2001) and Gislason and Oelkers (2003). Owing to its low molecular weight (18.015 g mol^{-1}) compared to other component oxides of silicate melts and glasses, relatively small amounts by weight of water correspond to much higher amounts on a molar scale. Since the partial molar volume of water in silicate glasses is relatively low (Richet and Polian, 1998 estimated a value of 12 ± 0.5 $cm^3\ mol^{-1}$ for andesite glasses), the molar volume estimated for the anhydrous basaltic glass of Stapafell is doomed to decrease, albeit to an unknown extent, upon consideration of water.

7.5.1.3. Completion of the EQ6 input file

The preparation of the input file for the EQ6 simulation is completed by setting temperature at 60°C, f_{CO_2} at 67.9 bar (which means to assume injection of pure CO_2 at a constant pressure of 100 bar) and the surface area of hydrated basalt glass in contact with 1,000 g of water at the initial value of 4,100 cm^2 (which is automatically changed by EQ6 proportionally to its remaining mass). Note that the values of these variable are the same as in previous cases. As in the tholeiitic basalt run, the initial aqueous solution was assumed to be in equilibrium with analcime, calcite, kaolinite, daphnite, clinochlore, chalcedony and magnetite at 60°C, 1 bar under a f_{CO_2} of 10^{-1} bar (*see* Section 7.1.2).

Again, instantaneous precipitation was hypothesized for the secondary solid phases, as it is difficult to constrain the initial value of the surface area for minerals which are not present in the system at the beginning of the simulation.

7.5.2. The time scales

The main results of reaction path modelling are depicted against both the reaction progress variable, ξ, and time in the diagrams of Figures 7.19 to 7.23, in which two time scales are reported. They refer to the dissolution rate of the basaltic glass normalized to either the geometric surface area, $r_{+,GEOM}$, or the BET surface area, $r_{+,BET}$. As expected on

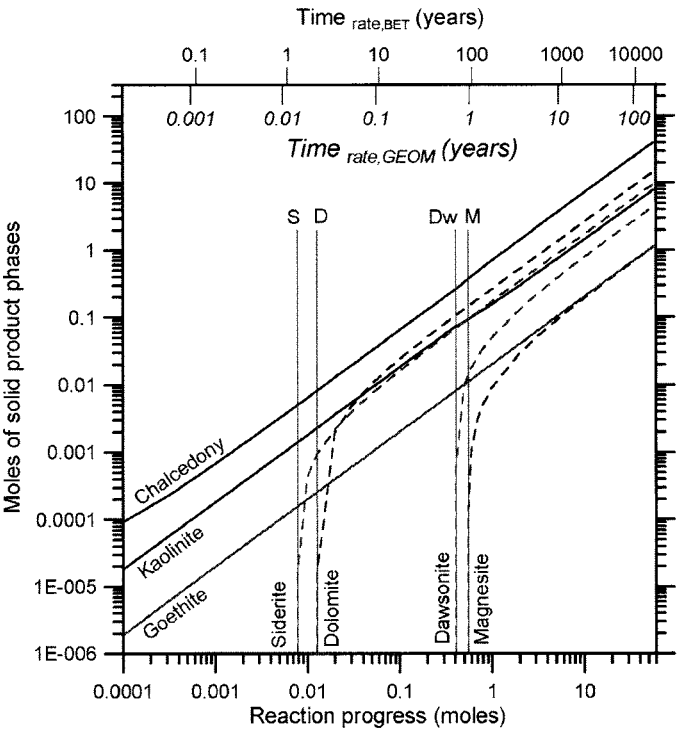

Figure 7.19. Amounts of secondary product phases generated during high-pressure (P_{tot} = P_{CO_2} = 100 bar) CO_2 injection in a hypothetical deep aquifer (T = 60°C) hosted in basaltic glass as a function of time and the reaction progress variable. Letters S, D, Dw and M mark the onset of the precipitation of secondary siderite, dolomite, dawsonite and magnesite, respectively.

the basis of equation (7-16), the $r_{+,GEOM}/r_{+,BET}$ ratio of 92 constrains the $time_{rate,GEOM}$/ $time_{rate,BET}$ ratio at 1/92 and brings about a corresponding shift in the two time scales.

The results of the two separate simulations (concentrations of solutes, pH of the aqueous phase, oxygen fugacity, moles of secondary solid phases, etc.) are exactly the same for any given value of the reaction progress variable, ξ. However, the same values of ξ are attained at different times in the two simulations.

This example demonstrates once more that it is advisable to consider ξ as the true master variable, owing to possible uncertainties in the time scale brought about by poor knowledge of the dissolution rates and/or reactive surface areas of solid phases.

7.5.3. Solid product phases

The secondary carbonate minerals generated during high-pressure CO_2 injection in a hypothetical deep aquifer hosted in basaltic glass are, in order of appearance, siderite, dolomite, dawsonite and magnesite (Fig. 7.19). The precipitation of these solid phases

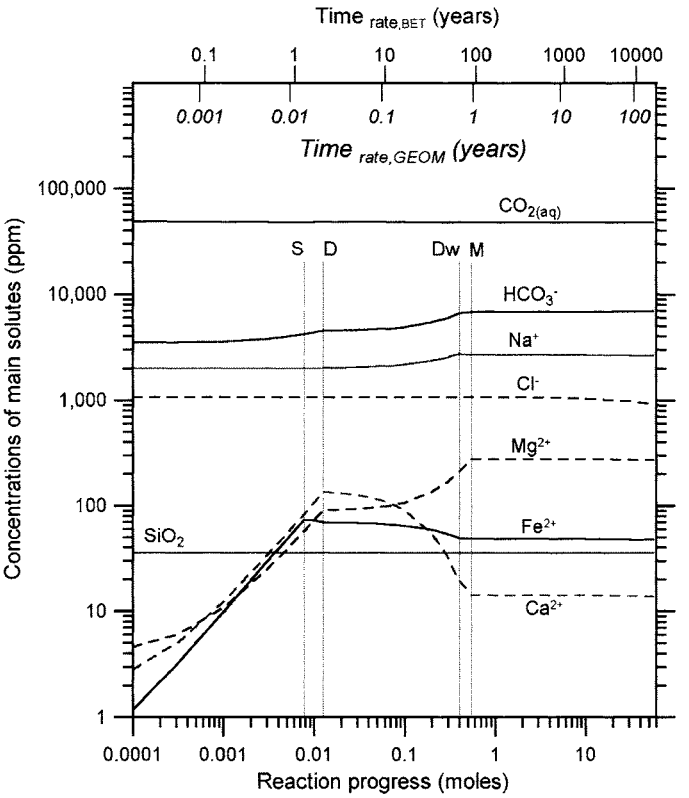

Figure 7.20. Concentrations of solutes during high-pressure ($P_{tot} = P_{CO_2} = 100$ bar) CO_2 injection in a hypothetical deep aquifer ($T = 60°C$) hosted in basaltic glass as a function of time and the reaction progress variable. Letters S, D, Dw and M mark the onset of the precipitation of secondary siderite, dolomite, dawsonite and magnesite, respectively, as shown in Figure 7.19.

begins at values of ξ indicated by the labels S, D, Dw and M, respectively. These labels are also reported in the following plots. The most important of these solid phases, in terms of mass, is dolomite followed by siderite, dawsonite and magnesite.

Comparison of Fig. 7.19 with Fig. 7.14 shows that magnesite precipitation occurs in the basaltic glass run instead of calcite production during the tholeiitic basalt example. At first sight, this difference might seem surprising, since the Ca/Mg molar ratio of the basaltic glass, 0.93, is similar to that of the tholeiitic basalt, 1.000. In order to explain this difference in secondary carbonate minerals let us consider the two dissolution processes in detail.

As discussed in Section 7.4.2, the dissolution of the holocrystalline tholeiitic basalt is dominated by destruction of clinopyroxene (10% of Ca and 7.5% of Mg on an elemental basis) and plagioclase (4.2% of Ca and no Mg), with a subordinate contribution of orthopyroxene (12% of Mg and no Ca), apart from the last steps of the simulation, upon exhaustion of clinopyroxene, when orthopyroxene dissolution becomes important. This

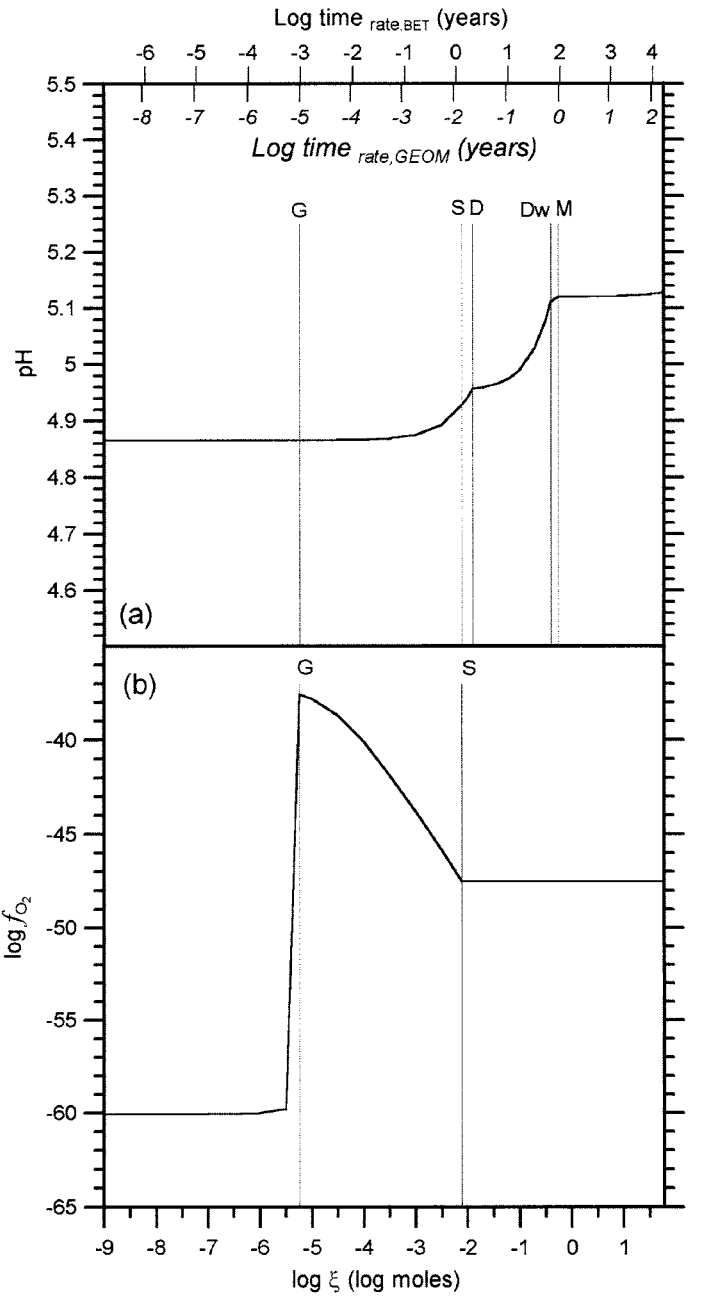

Figure 7.21. Changes in (a) pH and (b) f_{O_2} during high-pressure ($P_{tot} = P_{CO_2} = 100$ bar) CO_2 injection in a hypothetical deep aquifer ($T = 60°C$) hosted in basaltic glass as a function of time and the reaction progress variable. Letters G, S, D, Dw and M mark the onset of the precipitation of secondary goethite, siderite, dolomite, dawsonite and magnesite, respectively.

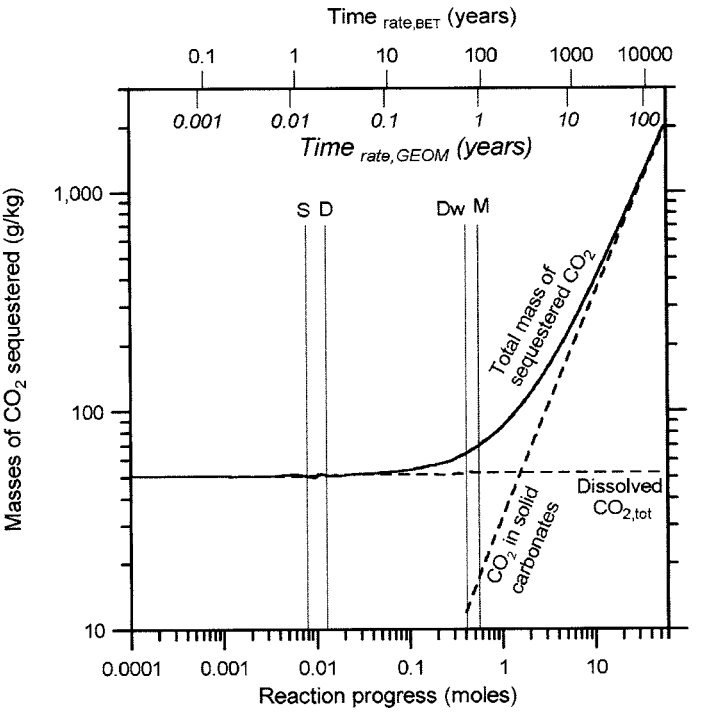

Figure 7.22. High-pressure (P_{tot} = P_{CO_2} = 100 bar) CO_2 injection in a hypothetical deep aquifer (T = 60°C) hosted in basaltic glass: masses of CO_2 sequestered through dissolution in the aqueous solution (solubility trapping) and incorporation in solid carbonates (mineral fixation), and total mass of sequestered CO_2 as a function of time and the reaction progress variable. Letters S, D, Dw and M mark the onset of the precipitation of secondary siderite, dolomite, dawsonite and magnesite, respectively, as shown in Figure 7.19.

larger availability of Ca with respect to Mg during the dissolution of tholeiitic basalt is in line with the production of calcite and dolomite in similar amounts.

In contrast, dissolution of basaltic glass contributes chemical constituents to the aqueous phase in the same stoichiometric proportions of the glass itself, i.e. with a Ca/Mg molar ratio of 0.93. This explains the overwhelming production of dolomite accompanied by subordinate magnesite.

Comparison of Fig. 7.19 with Fig. 7.14 also shows that during the dissolution of the basaltic glass, precipitating carbonate minerals are accompanied by secondary chalcedony, kaolinite and goethite in amounts comparable with those of the tholeiitic basalt case.

7.5.4. The aqueous solution

Inspection of Figs. 7.20 and 7.15 indicates that the concentrations of aqueous CO_2, HCO_3^-, Na^+, Cl^-, Fe^{2+} and SiO_2 during high-pressure CO_2 injection in a hypothetical deep aquifer hosted in basaltic glass are comparable with those of the tholeiitic basalt simulation. Also the concentration of dissolved Al^{3+} (not shown) is similar in the two runs. This

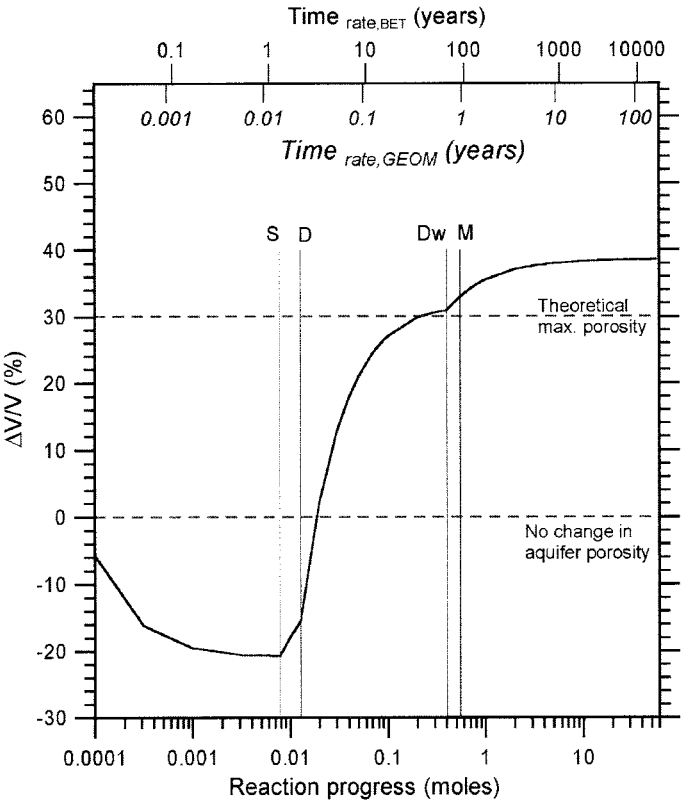

Figure 7.23. Variation of the $\Delta V/V$ parameter as a function of both reaction progress and time during high-pressure ($P_{tot} = P_{CO_2} = 100$ bar) CO_2 injection in a hypothetical deep aquifer ($T = 60°C$) hosted in basaltic glass. Letters S, D, Dw and M mark the onset of the precipitation of secondary siderite, dolomite, dawsonite and magnesite, respectively, as shown in Figure 7.19.

is due to the fact that imposed temperature and f_{CO_2} and the relevant product solid phases (chalcedony, kaolinite, siderite and dawsonite) are the same.

In contrast, the aqueous solution interacting with the basaltic glass is richer in dissolved Mg^{2+} and poorer in Ca^{2+} with respect to the aqueous phase circulating into the tholeiitic basalt. This difference in dissolved Mg^{2+} and Ca^{2+}concentrations reflects the different dissolution behaviour of the two basaltic rocks, as discussed in the previous section.

Not surprisingly, also the pH values during the basaltic glass simulation span a limited range, from 4.87 to 5.13, (Fig. 7.21a) which coincides with that of the tholeiitic basalt run, from 4.87 to 5.12 (Fig. 7.16a).

The f_{O_2} values predicted by the two simulations are also identical (see Figs. 7.21b and 7.16b), and are largely controlled by precipitation of goethite (after point G) and coexistence of goethite and siderite (after point S), as already noted above.

7.5.5. The CO_2 sequestration

Figure 7.22 depicts the amounts of CO_2 sequestered through both solubility trapping (i.e. as aqueous CO_2 and other dissolved carbonates) and mineral fixation (i.e. the CO_2 stored in dolomite, siderite, dawsonite and magnesite), as well as the total mass of sequestered CO_2 as a function of the reaction progress. The three CO_2–ξ curves are almost identical to those of the tholeiitic basalt case (Fig. 7.17) and the same considerations of Section 7.4.5 apply also to the basaltic glass example.

Considering the process with respect to time, it must be underscored that the time scale of basaltic glass carbonation, based on the results obtained for $r_{+,\mathrm{BET}}$, is comparable to that of the carbonation of holocrystalline tholeiitic basalt. In contrast, basaltic glass carbonation occurs two orders of magnitude faster than the carbonation of holocrystalline tholeiitic basalt if the results computed for $r_{+,\mathrm{GEOM}}$ are taken into account. This matter requires further investigation for its important practical implications, in that basaltic glass and other silicate glasses could be very interesting materials for the geological storage of CO_2 and mineral carbonation, if the $r_{+,\mathrm{GEOM}}$ values were representative of their dissolution rates.

7.5.6. Changes in the porosity of aquifer rocks

During high-pressure CO_2 injection in a hypothetical deep aquifer hosted in basaltic glass the $\Delta V/V$ parameter experiences a pronounced increase upon the onset of siderite and dolomite precipitation (points S and D, respectively) and a corresponding marked decrease in aquifer porosity is expected. Upon the onset of dawsonite precipitation (point Dw), the $\Delta V/V$ parameter exceeds 30%, which is a sort of upper threshold even for high-porosity rocks. Therefore, total clogging of pore spaces and voids is expected after point Dw.

Although the $\Delta V/V$ parameter remains below 40% throughout the simulation and it is somewhat lower than in the tholeiitic basalt case, the same negative consideration of Section 7.4.6 applies also in this case. To be quite explicit, the long-term sustainability of the process under consideration appears unlikely, owing to the dramatic reduction in the effective porosity of the aquifer. However, further investigations are warranted on the molar volume of silicate glasses and the role of water in these potentially interesting materials (*see* Section 7.5.1.2).

7.6. Reaction path modelling of geological CO_2 sequestration in sedimentary basins

As shown above, ultramafic and mafic rocks have very high CO_2 sequestration capacities. Nevertheless, they are not in general the best targets for geological CO_2 disposal, owing to an unfavourable geological–hydrogeological framework.

First, rock matrix has low porosity and permeability, which determine low availability of water. The permeability of lavas develops mainly along fractures, cooling joints and discontinuous scoriaceous layers. The permeability of ophiolitic complexes is largely due to fracturing induced by the tectonic events that have determined the uplift of these bodies towards the surface and their emplacement at relatively shallow levels.

Second, effective cap rocks are unlikely to be present at the top of tholeiitic basalt lava successions and ultramafic rocks variably affected by serpentinization, although relatively impervious layers may be locally present within these rock sequences. For instance, tuffs affected by argillic alteration may be associated with tholeiitic basalt lavas and clay-rich, deep-sea sediments usually occur together with ultramafic rocks in ophiolitic sequences. However, these impervious levels are randomly interposed into them, have limited lateral continuity and/or irregular shape due to the effects of tectonic events.

Favourable situations may be locally present, such as in southern Piedmont, Italy (Roberto Bencini, written communication). In this region, CO_2 injection could be performed in the conglomerate layers, chiefly made up of serpentinitic clasts, which occur at the top of the serpentinites of the Voltri Group. Clogging of pore spaces should not be a major problem in these conglomerates, due to their high porosity and permeability. Besides, the overlying sedimentary rocks of the Piedmont Tertiary Basin should act as an efficient cap rock, preventing the escape of gaseous CO_2 towards the surface. This fact must be absolutely avoided for obvious safety reasons! Further studies are needed to prove the feasibility of geological CO_2 disposal in this region.

In contrast to mafic and ultramafic rocks, sedimentary basins are very promising targets for geological CO_2 disposal. They have a favourable geological–hydrogeological framework, owing to the presence of both (i) high-porosity, high-permeability layers typically represented by sandstones and (ii) low-permeability layers of shales, potentially limiting the transfer of CO_2 towards the surface. Besides, sedimentary basins host huge amounts of waters. At sufficiently deep levels, these waters typically have high salinities and, therefore, they are of no interest as sources of drinking water. The long residence times of these waters in the deep aquifers of sedimentary basins is an other requirement for the occurrence of carbonation reactions (mineral trapping) that are very slow processes, as already discussed above.

Sedimentary basins were often drilled at depth for the exploitation of oil and natural gas. Upon completion of the extraction of these valuable resources and perhaps after a first phase in which high-pressure CO_2 is injected for enhanced oil recovery, abandoned wells can be used for geological CO_2 disposal, without the need for drilling any new borehole. This is a very attractive situation, from the economic point of view, and money often makes things move.

For instance, 1 million ton of waste CO_2 per year has been injected since September 1996 into the Utsira aquifer in the North Sea, to avoid a Norwegian tax of about 50 US$ per ton of CO_2 emitted offshore (Baklid et al., 1996; Torp and Gale, 2004). An other example is constituted by the Weyburn Oil Field in south central Saskatchewan, Canada which is currently the site of a large CO_2 injection project for enhanced oil recovery (Emberley et al., 2004, 2005). Although this is not a geological CO_2 sequestration project, approximately 30% of the injected CO_2 will be trapped in the reservoir at the end of project activities (Gunter et al., 2000). Besides, the geological CO_2 sequestration in sedimentary basins has been the subject of feasibility studies in The Netherlands (Lohuis, 1993) and in the Alberta Basin, Canada (Gunter et al., 1993; Bachu et al., 1994; Law and Bachu, 1996; Gunter et al., 1996, 1997, 2000).

Among the numerous modelling investigations on the geological CO_2 sequestration in sedimentary basins, some selected examples are discussed in the following sections. Related experimental and field studies are treated in Sections 7.7 and 7.8.

7.6.1. The glauconitic sandstone aquifer of the Alberta Sedimentary Basin

Reaction path modelling of geological CO_2 sequestration in a glauconitic sandstone aquifer of the Alberta Sedimentary Basin, Western Canada was studied by Gunter et al. (1997, 2000) by using the PATHARC.94 computer code (Perkins and Gunter, 1995).

This glauconitic sandstone aquifer has an average porosity of 12% and its average mineral composition comprises 87% quartz, 2% K-feldspar, 1% plagioclase (which was taken into account in the geochemical simulation introducing the two endmember components albite and anorthite), 5% glauconite (which was hypothesized to be represented by annite in reaction path modelling), 2% kaolinite, 1% calcite, 1% dolomite and 1% siderite. The reactive surface area was assumed to be equal to the geometrical surface area and individual mineral grains were considered constant-volume sphere with an average radius of 0.05 mm. The average temperature of the aquifer is 54°C. The average chemical composition of formation water is (concentration in mg L^{-1}) Na 28,800, K 690, Ca 2,970, Mg 578, HCO_3 198, Cl 51,600 and SO_4 366, with a pH of 7.2.

Gunter et al. (1997) simulated the injection of CO_2 into the glauconitic sandstone aquifer at a constant P_{CO_2} of 260 bar. Substantial trapping of CO_2 through precipitation of siderite (and subordinate calcite) and solubility trapping was predicted to take place in a time considerably smaller than the residence time of water in the sedimentary basin aquifer. The main occurring reaction was considered to be

$$3\text{annite} + 11CO_2 \rightarrow \text{muscovite} + 9\text{siderite} + 6\text{quartz} + H_2O + 2K^+ + 2\,HCO_3^-. \qquad (7\text{-}50)$$

Gunter et al. (2000) chosen instead to dissolve a finite amount of CO_2, 1 mol, in 1,000 g of water at the beginning of the simulation. In this way, P_{CO_2} decreases with ξ, simulating the conditions prevailing upon termination of CO_2 injection. They found that equilibrium is expected to be attained in hundreds of years with a drop of P_{CO_2} from 87 to 0.02 bar and the generation of 1 mol of siderite, 0.05 mol of calcite and 0.02 mol of dolomite. These figures confirm the relatively high CO_2-trapping capacity of siliciclastic rocks containing Fe(II) minerals, such as annite.

However, these findings were questioned by Xu et al. (2000, 2004) who modelled the geological sequestration of CO_2 in the same glauconitic sandstone aquifer of the Alberta Sedimentary Basin by means of TOUGHREACT. They recognized that use of annite $[KFe(II)_3AlSi_3O_{10}(OH)_2]$ as a proxy for glauconite $[K_{0.75}Mg_{0.25}Fe(II)_{0.25}Fe(III)_{1.25}Al_{0.5}Si_{3.75}O_{10}(OH)_2]$ leads to overestimate the amount of precipitating siderite and, consequently, the CO_2-sequestration capacity. Therefore they considered glauconite in reaction path modelling instead of annite. They also introduced oligoclase instead of albite plus anorthite and illite instead of muscovite. Note that the latter choice determines a moderate increase in the CO_2-sequestration capacity, owing to the presence in illite of some Mg

$[K_{0.6}Mg_{0.25}Al_{1.8}(Al_{0.5}Si_{3.5}O_{10})(OH)_2]$ which is absent in muscovite. Besides, they assumed the presence of organic matter, namely type II kerogen.

To keep the description of precipitation kinetics to a simple level, backward rate constants were assumed to be one order of magnitude larger than forward (dissolution) rate constants. The total surface area was set at 10 m^2 dm^{-3} of medium, corresponding to a surface of 8.33×10^5 cm^2 in contact with 1,000 g of water based on the average porosity of 12%. The surface area of secondary minerals was set to 0.25 m^2 dm^{-3} throughout the simulation, apart from clay minerals, whose surface area was assumed to be one order of magnitude higher, for glauconite, and two orders of magnitude higher, for all the other clay minerals. Note that some of these phases are not initially present in the considered system, but they are considered to have an initial surface area different from zero. This arbitrary assumption (or an alternative one, e.g., instantaneous equilibrium as we assumed above) is needed to describe the precipitation of secondary minerals in a kinetic framework.

The initial aqueous solution was assumed to be a 1 M NaCl solution. The geological CO_2 sequestration was simulated by setting the CO_2 injection pressure at 260 bar and temperature at 54°C at all times. The main precipitating solid phases resulted to be illite, K-feldspar, siderite, and ankerite accompanied by minor amounts of dawsonite and dolomite. Carbon dioxide is mainly incorporated in ankerite and siderite. After ~15,000 years, the total CO_2 sequestration capacity (solubility trapping plus mineral trapping) increases close to linearly with time, attaining the value of 17 kg m^{-3} of medium in 100,000 years. This corresponds to approximately 140 g kg^{-1} water, a value which is attained much earlier in the cases of dunite, serpentinite, tholeiitic basalt and basaltic glass that were discussed above. This indicates that the sequestration capacity of glauconitic sandstones is much lower than those of previously considered lithotypes, in line with the smaller total contents of Mg-, Ca-, Fe(II)- and Na-bearing silicates. Porosity is expected to decrease very slightly with time from the initial value of 12% to 11.6% in 100,000 years.

A possible uncertainty relates to the exclusion of reduced sulphur species from geochemical modelling. Indeed, Xu and coworkers recognize that even low P_{H_2S} would determine the production of pyrite, which could fix a significant proportion of Fe^{2+}, thus decreasing the amount of precipitating siderite (and ankerite, but calcite and dolomite would form instead of it) and, consequently, the CO_2 sequestration capacity of the process.

7.6.2. The sediments of the Gulf Coast

After a preliminary study of Apps (1996), reaction path modelling of geological CO_2 sequestration in the Gulf Coast sediments was investigated by Xu et al. (2000, 2004), again by means of TOUGHREACT.

These sediments have been considered to have an average porosity of 10% and to be made up of 49.7% (by volume) quartz, 1.8% kaolinite, 1.7% calcite, 0.85% illite, 2.6% organic matter (type II kerogen), 17.8% oligoclase, 7.4% K-feldspar, 3.5% Na-smectite, 2.7% clinochlore-14Å, 1.4% daphnite-14Å, 0.44% haematite. The total surface area was assumed to be 10 m^2 dm^{-3} of medium, corresponding to a surface of 1×10^6 cm^2 in contact with 1,000 g of water.

Again, a 1 M NaCl solution was taken into account as initial aqueous solution. The geological CO_2 sequestration was simulated by setting the CO_2 injection pressure at 260 bar and temperature at 80°C. The most important product solid phases resulted to be illite, dawsonite and ankerite, whereas calcite and siderite initially precipitated and then re-dissolved. Carbon dioxide is mainly incorporated in dawsonite and ankerite. Precipitation of carbonate minerals determines an increase in the total CO_2 sequestration capacity up to a maximum of 90 kg m^{-3} of medium (900 g kg^{-1} water) after 100,000 years. Porosity decreases with time from the initial value of 10% to a value somewhat higher than 6% after 100,000 years. The sequestration capacity of these sediments is significantly higher than that of the glauconitic sandstones, mainly owing to the abundance of oligoclase and chlorite minerals.

The geochemical processes occurring in a sandstone–shale system representative of the Gulf Coast sediments upon injection of high-pressure CO_2 at depths of ~2 km were investigated further by Xu et al. (2005). They performed numerical simulations of reactive fluid flow and geochemical transport by fully exploiting the capabilities of the computer code TOUGHREACT. Although the theoretical treatment of this subject goes beyond the aims of this book (the interested reader is referred to Lichtner et al., 1997), it is very interesting to give a look at the results of this type of advanced geochemical–hydrogeological modelling.

Xu et al. (2005) adopted a simplified one-dimensional model made up of a 10-m-thick layer of shale overlying a layer of sandstone of the same thickness. The model grid (comprising all the blocks in this 1-D space) is finer in the shale near the sandstone/shale boundary, to appreciate the concentration gradients that are expected to develop in the shale, owing to its low permeability. In contrast, perfect mixing was assumed to occur in the sandstone layer, which was modelled by using a single block.

The same primary minerals listed above were considered to be present in the sandstone and in the shale layers, but in different amounts. Initial porosity was assumed to be 30% in the sandstone and 10% in the shale. Initial water chemistry was computed by reacting a 1 M NaCl solution with the primary minerals at 75°C under a P_{CO_2} of 0.01 bar. The obtained solution composition was taken as an initial condition in reactive transport modelling.

At the beginning of the reactive transport simulation, CO_2 was added to the sandstone block to achieve a gas phase saturation of 0.5 and a P_{CO_2} of 201 bar, whereas no CO_2 was added to the blocks of the shale layer, which were considered to be water saturated.

Changes with time in both water chemistry and the amounts of primary and secondary minerals along the sandstone–shale transect are computed by TOUGHREACT. For instance, the H^+ ion and aqueous CO_2 are found to diffuse from the sandstone to the shale, in line with the high P_{CO_2} imposed to the sandstone, which increases the H^+ activity of the aqueous phase. Initially carbonate mineral precipitation takes place chiefly in the sandstone, but afterwards it extends to the shale (though in lower amounts) owing to diffusive transport of CO_2 from the sandstone to the shale. Total dissolved Fe and Ca are expected to diffuse from the shale to the sandstone, since precipitation of siderite and ankerite causes a decrease in Fe^{2+} and Ca^{2+} concentrations in the sandstone. Precipitation of carbonate minerals (mainly dawsonite and ankerite) brings about a decrease in porosity from

30% to 24% after 100,000 years in the sandstone and rather complex changes in porosity in the shale.

The impacts of NO_x, SO_x and H_2S (which are typically present together with CO_2 in coal-fired waste streams) on the geological disposal of CO_2 in the sands of the Frio Formation was investigated by Knauss et al. (2005, see also Knauss et al., 2001). They carried out reactive transport modelling by using the reactive transport simulator CRUNCH and showed that the presence of H_2S should not interfere with CO_2 injection, whereas oxidation of small amounts of SO_2 could determine a significant decrease in pH and substantial differences in the process. This study has a very important applied component as the separation and compression of CO_2 is very expensive and represent the 75% of the total cost of the whole geological disposal process.

7.6.3. The White Rim Sandstone

This case history was investigated by White et al. (2005) along a cross section beneath the Hunter Power Plant in Central Utah, emitting yearly 15×10^6 tons of CO_2. The Permian White Rims Sandstone with a thickness of 61–244 m, high porosity and permeability and lying at over 1 km depth beneath the power plant was selected as the best potential reservoir. It is overlied by some potential seals, represented by shale and evaporite levels. In the investigated area, the sedimentary sequence is a sort of gently dipping cuesta, constituting the western flank of the San Rafael asymmetrical anticline. Owing to the regional dip, the White Rims Sandstone crops out at the surface some 40 km to the SE, posing a possible problem of lateral migration and approach to the surface of the CO_2-charged aqueous solution after prolonged CO_2 disposal.

Particular attention was devoted to the sealing properties of potential cap rocks, which were measured through mercury injection porosimetry by White et al. (2005). As an example, it was found that the second most effective cap rock (Mancos Shale) could withhold a CO_2 column of the order of 500–900 m in thickness.

Reactive transport modelling of CO_2 injection in the White Rims Sandstone was carried out by using the ChemTOUGH code (White, 1995), which is based on the porous media multiphase mass and energy flow code TOUGH2 (Preuss, 1991).

The reservoir rock was assumed to be made up of quartz (77% by volume), kaolinite (2.25%), Na-smectite (2.25%), calcite (1.8%), anorthite (0.66%), albite (0.60%), K-feldspar (0.60%). Note that the complement to 100% is represented by porosity, approximately 15%. Dolomite, siderite and dawsonite are not initially present in the reservoir rock but were considered as possibly precipitating solid phases. Aquifer temperature was fixed at 54°C. Initial water chemistry was computed by reacting a 3 M NaCl brine with the reservoir minerals for 1,000 years.

In the simulation, injection of CO_2 was terminated after 30 years. It was found that 1,000 years after the end of the injection period ~21% of the injected CO_2 was trapped in carbonate minerals (calcite and dawsonite), ~52% was present underground as a separate gas phase or dissolved in groundwaters and ~17% had leaked to the ground surface, a process that was still going on.

7.6.4. The shales of the North Sea

Gaus et al. (2005) carried out reaction path modelling (both in stoichiometric mode and in time frame) and reactive transport modelling to investigate the impact of high-pressure CO_2 injection on the porosity of the cap rock at the Sleipner site, Norwegian part of the North Sea, where CO_2 has been injected since 1996. The code PHREEQC v2.6 (Parkhurst and Appelo, 1996) was used to this purpose.

Carbon dioxide is currently injected in the sands of the Utsira Formation but it migrates upward, due to buoyancy effects, and accumulates below the overlying cap rock, represented by the shales of the 250-m-thick Nordland Group. Then CO_2 dissolves into the formation water of the cap rock and diffuse upward into it. At Sleipner, the migration of injected CO_2 is predicted and monitored by means of seismic surveys and reservoir modelling (Arts et al., 2004; Torp and Gale, 2004).

The mineral constituents of the cap rock considered in geochemical modelling are illite (24.7 wt.%), chalcedony (21.5%), kaolinite (18.0%), plagioclase (12.4%), a high-Fe–Mg smectite (8.8%), 14 Å-clinochlore (4.1%), pyrite (2.8%), K-feldspar (2.1%), siderite (1.6%) and calcite (1.0%). In three separate runs plagioclase was considered to be represented by either albite, or 50% albite plus 50% anorthite, or oligoclase (An_{20}).

Initial porosity was set to 5%. Initial chemistry of formation water was computed equilibrating an aqueous solution containing 0.479 M chloride with cap rock minerals at 37°C.

Isothermal, isobaric injection of CO_2 was assumed at P_{CO_2} of 101 bar (f_{CO_2}=52 bar) and temperature of 37°C. In addition to primary minerals, dawsonite, disordered-dolomite and magnesite were selected as possible secondary minerals, defining suitable rate constants and reactive surface areas different from zero (these are arbitrary but necessary assumptions, as already noted above).

Reaction path modelling in time frame shows that the main secondary carbonate mineral is calcite accompanied by a limited amount of dawsonite in all the three runs with different plagioclase composition. Small changes in porosity (<0.05 %) are calculated for the albite case, whereas a certain decrease in porosity (up to 2.8% in the first meter) is predicted for the albite plus anorthite case. This is attributed to the dissolution of anorthite and the subsequent precipitation of calcite and kaolinite by Gaus et al. (2005). It must be noted that the volume of the reaction:

$$CaAl_2Si_2O_{8(s)} + CO_{2(g)} + 2H_2O \rightarrow CaCO_{3(s)} + Al_2Si_2O_5(OH)_{4(s)}, \quad (7\text{-}51)$$

ΔV_r, is 35.7 cm^3 (per mole of anorthite, that is referring to the reaction as it is written) and the corresponding $\Delta V/V$ parameter is 35.4% (*see* equation (5-125)), if consideration is restricted to the solid phases only, as was done in the previous sections of this chapter and in Section 5.5. The ΔV_r reduces to −0.37 cm^3 and the $\Delta V/V$ parameter becomes −0.27% if water is also included in calculations as evidently assumed by Gaus et al. (2005). In my opinion, this assumption is reasonable as long as water is forced to remain in the considered system, which is rather unrealistic in natural systems. Therefore, porosity changes have to be taken with some caution. In spite of this divergent opinion, the study by

Gaus et al. (2005) is very important as it focuses the attention on the integrity of the cap rock, which is a very important issue for the safe geological disposal of CO_2.

The processes relevant for the geological sequestration of CO_2 at the Sleipner site were also investigated in a very interesting study by Johnson et al. (2001), who used an integrated toolbox comprising NUFT, a software package for the numerical simulation of multiphase/multicomponent flow and reactive transport (Nitao, 1998), GEMBOCHS, a thermodynamic/kinetic database and dedicated software library (Johnson and Lundeen, 1994a, b, 1995), and the graphic utility Xtool (Daveler, 1998). The Sleipner environment is represented by a spatial domain comprising an Utsira-like 200-m-thick saline aquifer confined by a 25-m-thick shale cap-rock, which in turn is overlain by a 25-m-thick aquifer. Three distinct aquifer scenarios were considered, differing for the absence or presence of intra-aquifer shales of different lateral continuity and permeability (the latter parameter was varied to simulate the absence or presence of microfractures). A 20-year-long time frame was adopted, comprising a prograde phase (in which the injection rate is kept constant at 10,000 ton CO_2/year), a transition phase (in which the injection rate is decreased to 0 in 3 months) and a retrograde phase (in which the injection rate is maintained at 0 for 9.75 years).

The study by Johnson et al. (2001) showed that the migration of immiscible CO_2 and the relative importance of solubility and mineral trapping processes are chiefly controlled by the distribution of intra-aquifer permeability, whereas the long-term storage security is mainly affected by cap-rock integrity. Intra-aquifer shales retard the vertical migration of the immiscible CO_2 plume and promote its lateral expansion (in agreement with the results of seismic surveys; Torp and Gale, 2004), thus increasing the spatial extent of plume–aquifer interaction and the efficacy of intraplume solubility and mineral trapping processes. The 25-m-thick shale cap-rock resulted to be an efficacious barrier prohibiting the vertical migration of the immiscible CO_2 plume (again, in agreement with seismic evidence; Torp and Gale, 2004). In the relatively short interval of time considered in the simulation, ~85% of the injected CO_2 constitutes an immiscible supercritical fluid phase, ~15% dissolves in the aqueous solution and $<1\%$ precipitates as carbonate minerals, in the form of dawsonite, magnesite/siderite and calcite. However, mineral trapping is enhanced during the retrograde phase and has very important consequences, in that it limits the lateral extent of plume migration and increases the cap-rock integrity, through carbonate sealing of microfracture porosity.

7.6.5. The carbonate rocks of the Alberta sedimentary basin

Similar to the glauconitic sandstone case (*see* Section 7.6.1), Gunter et al. (2000) modelled the effects of the dissolution of a finite amount of CO_2 (1 mol in 1,000 g of water) also on the Nisku carbonate aquifer of the Alberta Sedimentary Basin. These carbonate rocks consist of prevailing dolomite and/or calcite (both containing traces of Fe), possibly accompanied by small amounts ($<1\%$ in general) of anhydrite, illite, pyrite and quartz. Silicate and sulphide minerals were excluded from the simulation, which was carried out for a system comprising 14,000 g of dolomite, 1,100 g of calcite, 262 g of siderite and 1,000 g of water.

Equilibrium is predicted to be achieved in less than 1 day in the carbonate aquifer, owing to the occurrence of fast reactions, with a small reduction in P_{CO2} from 87 to 86 bar, the dissolution of small amounts of calcite (0.06 mol) and siderite (10^{-5} mol) and the precipitation of 0.02 mol of dolomite.

7.7. Water–rock reactions during geological CO_2 sequestration: the experimental evidence

7.7.1. Laboratory experiments on rocks from sedimentary basins

Precipitation of clay minerals and carbonate minerals as a consequence of dissolution of primary silicates and Al-silicates was generally not observed in laboratory experiments aimed at evaluating the interactions between CO_2, formation water and rocks from sedimentary basins. This is due to the slow kinetics of these processes. Exceptions are represented by the recent experimental works by Kaszuba et al. (2003, 2005).

Pearce et al. (1996) and Rochelle et al. (1996) injected supercritical CO_2, at pressures of 90 and 200 bar, into a sandstone at temperatures of 105° and 80°C, for periods of 1 and 8 months. Significant alteration of pre-existing calcite and dolomite was observed, as well as dissolution of anhydrite accompanied by precipitation of calcite and possible corrosion of detrital feldspars with precipitation of Na-smectite, although the evidence supporting this last process was not conclusive.

Gunter et al. (1997) performed 1-month-long experimental tests at 105°C and 90 bar of P_{CO_2} on glauconitic sandstones from the Alberta sedimentary basin. Under these conditions, only a small amount of CO_2 was trapped through reactions with Al-silicate minerals, whereas dissolution of mineral carbonates took place.

Sass et al. (2001) reacted anorthite and glauconite with CO_2 and a Na–Ca–Cl synthetic brine (containing other major components and several traces) at 50°C, 41 bar P_{CO_2} and 150°C, 138 bar P_{CO_2}, under a total pressure of 138 bar. The water–rock–gas interaction experiments were carried out in vessels placed on a shaker table or rocker for a duration of approximately 1 month. Anorthite incorporated some Na in the lattice and released a corresponding amount of Ca to the aqueous solution but precipitation of carbonate minerals did not occurred. In the experimental runs with glauconite, the Na content of the solid phase increased, K, Fe and Si decreased, whereas Al, Mg and Ca did not change. Also in this case, no carbonate mineral formed as a reaction product.

Kaszuba et al. (2003, 2005) simulated a brine–aquifer–aquitard system in a flexible cell hydrothermal reactor. A synthetic arkose, assumed to represent the aquifer, was prepared by mixing equal amounts of quartz, oligoclase (An_{17-21}) and microcline (Or_{91-97}) showing perthitic lamellae (Or_{3-9}) and adding some biotite. An argillaceous shale, made up of clay minerals (65%, by volume) quartz (27%), feldspar (5%), chlorite (2%, possibly including some kaolinite) and trace amounts of framboidal pyrite, was used for the aquitard. Kaszuba et al. (2003) used a synthetic brine containing Na^+, Mg^{2+}, K^+ and Cl^- as prevailing constituents whereas a pure Na–Cl brine was employed by Kaszuba et al. (2005), both with ionic strength of 5.5 mol kg^{-1}. In a first step, the system was maintained

at 200°C, 200 bar for several days (59 in the 2003 run, 32 in the 2005 run) to attain steady state. Then CO_2 was added to the reactor. In a second step, the system was kept again at 200°C, 200 bar, for 80 days in the 2003 run and 77 days in the 2005 run. Kaszuba et al. (2005) performed also a reference experiment on the same system, at the same P, T conditions and for the same time, without CO_2 injection.

Kaszuba et al. (2003) documented (i) etching of potassic lamellae in perthitic microcline with respect to sodic lamellae; (ii) growth of clay minerals on oligoclase; (iii) coatings of magnesite associated with clay minerals on biotite grains; (iv) growth of analcime with skeletal habit.

Kaszuba et al. (2005) observed the (i) presence of corroded magnesite and euhedral siderite, suggesting the early occurrence of magnesite precipitation followed by magnesite dissolution and siderite precipitation; (ii) growth of clay minerals and analcime. Analcime was found to be more abundant in the CO_2-free experiment where it shows an euhedral texture. In contrast, analcime crystals with skeletal texture grew in the CO_2–brine–rock experiment, as also found by Kaszuba et al. (2003).

Significant variations were also detected in brine chemistry. In particular, the significant increase in the concentrations of several components, initially absent in the Na–Cl brine used by Kaszuba et al. (2005), undoubtedly indicate the occurrence of rock dissolution through reaction with CO_2 and brine. All in all, these observations are consistent with the occurrence of dissolution of primary silicate minerals and precipitation of both carbonates and silicates.

Kaszuba et al. (2005) underscored that "precipitation of the mixed hydroxyl carbonate mineral dawsonite ($NaAlCO_3(OH)_2$), predicted as a stable carbonate phase in reactive transport models of carbon sequestration (Johnson et al., 2002; Knauss et al., 2002) was not observed in this study." They estimated that the aqueous solution was probably undersaturated with dawsonite, although the thermodynamic affinity with respect to this mineral and other Al-bearing solid phases could not be computed because the Al concentration in the brine was below detection limit throughout the CO_2–brine–rock experiment. To try to elucidate this matter, it is worth taking into account the equilibrium reaction between dawsonite and analcime, an ubiquitous phase in the experiments of Kaszuba and coworkers:

$$Na_{0.96}Al_{0.96}Si_{2.04}O_6 \cdot H_2O + 0.96\,CO_{2(g)} \Leftrightarrow 0.96\,NaAlCO_3(OH)_2 + 2.04\,SiO_2 + 0.04\,H_2O. \quad (7\text{-}52)$$

Assuming that the activity of aqueous SiO_2 is fixed by equilibrium with chalcedony and the activity of water and solid phases are equal to 1, it results $\log f_{CO_2} = -\log K_{7\text{-}52} / -0.96$. Using the thermodynamic equilibrium constants of EQ3/6, it turns out that at 200°C, dawsonite is stable for $f_{CO_2} > 7.8$ kbar and analcime is stable below this f_{CO_2} value. Since CO_2 fugacities were much lower than 7.8 kbar in the experiments of Kaszuba and coworkers, the absence of dawsonite as a solid product phase is not surprising. We may also note that the f_{CO_2} of analcime–dawsonite–chalcedony equilibrium coexistence is 0.23 bar at 60°C, 7.2 bar at 100°C and 296 bar at 150°C. In spite of possible uncertainties on the thermodynamic

data of dawsonite, these figures confirm that dawsonite likes cool environments, in line with what was inferred in Section 5.1.6 on the albite–dawsonite–quartz coexistence. Therefore, high temperature (200°C) has certainly enhanced the kinetics of dissolution/precipitation reactions, but has also stabilized analcime at the expense of dawsonite, in the experiments by Kaszuba and coworkers.

7.7.2. Laboratory experiments on forsterite and serpentine

The carbonation reactions of forsterite and serpentine have been the subject of several studies, after Lackner et al. (1995, 1997) underscored that these Mg silicates obtained from ultramafic rocks are abundant and thermodynamically convenient primary minerals for mineral carbonation.

McKelvy et al. (2001) showed that dehydroxylated samples of serpentine (meta-serpentine), obtained through heat treatment, undergo carbonation more readily than untreated samples. The optimum temperature of heat treatment was found to be 600–650°C by O'Connor et al. (2001), with little increase in reactivity upon heat treatment at higher temperatures. O'Connor et al. (2001) investigated also the mineral carbonation of olivine and meta-serpentine in aqueous slurries and found optimum results at 155°C under a P_{CO_2} of 185 bar for a 0.64 M $NaHCO_3$ and 1.0 M NaCl aqueous solution containing 15% of solids. Under these conditions a 78% conversion of the Mg-silicates to carbonate was attained in 30 min.

Guthrie et al. (2001) carried out experiments of serpentine, meta-serpentine and olivine carbonation in a stirred reaction vessel typically containing ~0.8 L of water plus solids and ~1 L of supercritical CO_2 at temperatures up to 185°C and pressures up to ~160 bar. They proposed a geochemical model assuming (i) occurrence of dissolution and precipitation processes in the aqueous phase and not in the supercritical CO_2 phase and (ii) occurrence of carbonation via dissolution–precipitation and not through direct carbonation of the Mg-silicate. The geochemical model comprises four steps: (i) dissolution of CO_2 into the aqueous phase and of H_2O into the CO_2-rich phase; (ii) release of Mg^{2+} ion to the aqueous phase, which is considered to be the rate limiting step; (iii) speciation reactions in the aqueous phase; (iv) precipitation of magnesium carbonate. Magnesite resulted to be the most typical product, but hydromagnesite was observed in several runs upon either alteration of fluid chemistry or CO_2 venting before quenching of the reaction vessel.

Based on the findings of O'Connor et al. (2001), Wolf et al. (2004) performed the carbonation of meta-serpentine in a solution 0.64 M $NaHCO_3$ and 1.0 M NaCl under a P_{CO_2} of 150 bar, by using a suitably implemented externally-controlled microreaction system. This allows *in situ* monitoring of the reaction process by synchrotron X-ray diffraction and Raman spectroscopy. By progressively heating the system, they were able to detect the first X-ray reflections of magnesite at 150°C, which is the temperature at which carbonation reaction begins. Further carbonation of meta-serpentine to magnesite occurred upon continuous heating to 180°C. However, no reflection caused by Si-bearing minerals was detected, indicating that SiO_2-like products are highly disordered.

Further studies of this type were carried out by McKelvy et al. (2004), who used *in situ* synchrotron X-ray diffraction to investigate the reactivity of meta-serpentine (obtained

through heat activation of lizardite at different temperatures) under the optimal conditions of carbonation established by O'Connor et al. (2001). Trace carbonation was observed at 120°C for the meta-serpentine obtained at 580°C, but further heating did not cause any further carbonation, indicating that the meta-serpentine was only partially activated. Substantial carbonation was found at 125°C for the 610°C meta-serpentine. The best results were obtained for the 650 and 720°C meta-serpentine in terms of progress and onset temperature of the carbonation reaction, which resulted to be 100 and 105°C, respectively. Besides, McKelvy et al. (2004) investigated the structure and composition of meta-serpentine by using TGA/DTA, XRD and FTIR analyses. Longer-range ordering, possibly due to doubling of the basal spacing from the characteristic value of 7.3 Å (*see* Section 5.3.2.1) to 14.7 Å, was observed in the material treated at 580°C, whereas the crystalline features disappear at 650°C indicating formation of amorphous meta-serpentine.

Schulze et al. (2004) used XPS and TEM to investigate the surface of ground lizardite, untreated, heat-treated at 630°C in a CO_2 flux for 3 h and heat-treated and reacted with a Na–Cl–HCO_3 solution and CO_2 at 155°C for 2 h, thus achieving a 22% conversion to carbonate. The latter treatment determined the formation of a 40–100 nm surface layer constituted by amorphous silica containing Mg. According to Schulze et al. (2004), the rate-limiting step of lizardite carbonation is the diffusion of Mg^{2+} ion from the amorphous phase.

Since heat treatment is a rather expensive operation, a different approach based on the physical activation of serpentine at low temperature coupled with a pH swing process was investigated by Park and Fan (2004). Fluidation of a serpentine slurry with 2 mm glass beads resulted to be the most effective method for removing the silica-rich surface layer and promoting further serpentine dissolution.

Giammar et al. (2005) investigated forsterite dissolution and magnesite precipitation through a series of batch experiments. Forsterite dissolution tests were carried out in dilute solutions (I 0.003 to 0.018 mol kg^{-1}) at 30 and 95°C under initial P_{CO_2} of 1 or 100 bar, whereas magnesite precipitation experiments were run in $MgCl_2$–$NaHCO_3$ solutions (I 0.07 to 1.25 mol kg^{-1}) under initial P_{CO_2} of 100 bar. Several analytical methods (elemental analysis of the aqueous solution, SEM, FTIR and XRD for the solids) and geochemical modelling were used to elucidate reaction products and progress.

The extent of forsterite dissolution was found to increase with increasing P_{CO_2} and temperature. The release of Mg and Si during forsterite dissolution was stoichiometric, but the concentration of dissolved Si was limited by saturation with respect to amorphous silica. Even though the aqueous phase attained conditions of oversaturation with respect to magnesite (saturation index up to 0.25) during forsterite dissolution experiments, $MgCO_3$ did not precipitated.

Magnesite precipitation occurred in ad hoc experiments designed to estimate the influence of suspended solid particles (of either forsterite or magnesite), time and saturation index with respect to magnesite. The composition of the aqueous solution, $MgCl_2$–$NaHCO_3$, was selected to simulate extensive forsterite dissolution. Magnesite precipitation was found to be controlled by nucleation, which requires a critical saturation index between 0.25 and 1.14 at 95°C and P_{CO_2} of 100 bar. Magnesite seeds accelerate magnesite precipitation, whereas forsterite particles do not, although magnesite forms on their surfaces.

7.8. Water–rock reactions during geological CO_2 sequestration: the field evidence

Emberley et al. (2004, 2005) evaluated the gas–water–rock interactions that occurred upon miscible CO_2 injection into the oil reservoir of Weyburn, Saskatchewan (Canada) for enhanced oil recovery (EOR). Oil is hosted into the carbonate rocks known as Midale beds, which are sealed by an anhydrite cap. The reservoir has an average temperature of 60°C and initial pressure was 146 bar on average. The CO_2 is generated by the Great Plains Synfuel coal gasification plant in Beulah, North Dakota (USA) and is transported at Weyburn by a 320-km-long pipeline. Note that CO_2 is injected together with water to retard CO_2 mobility. Since CO_2 is more soluble in oil than in water, it is released from water to oil. Owing to absorption of CO_2, oil experiences a decrease in viscosity and an increase in mobility. Besides, the low pH of the CO_2-rich aqueous solution can cause dissolution of carbonate minerals and increase in reservoir permeability. Although the aim of the miscibile CO_2 injection project is EOR, there are also important environmental aspects since up to 30% of the injected CO_2 is expected to be trapped in the reservoir.

To evaluate gas–water–rock interactions, a baseline fluid sampling was carried out before the onset of the CO_2 injection project and a second sampling survey (known as Monitoring-1) was performed 7 months after this date, when a total of approximately 150.6×10^6 standard m^3 of CO_2 (corresponding to ~3×10^5 tons) were disposed in the oil reservoir. Data on water and gas chemistry and isotope compositions were obtained in both surveys.

The samples collected during Monitoring-1 differ from the baseline data for lower pH values with differences of 0.5–0.6 pH units, higher alkalinity which has doubled compared to the baseline values (although a significant fraction of titration alkalinity is due to dissolved sulphide), higher Ca concentrations and higher $\delta^{13}C$ values of dissolved CO_2 by one to some ‰ units. All these differences were attributed to: (i) dissolution of the injected CO_2 in the aqueous phase as both carbonic acid and bicarbonate ion and (ii) concurrent dissolution of carbonate minerals, chiefly calcite and dolomite.

Nevertheless other chemical changes (e.g., in chloride and sulphate concentrations) also took place, indicating possible flushing of waters from other geological formations to the Midale beds and entrance in the monitored wells. Therefore, the overall picture is probably somewhat more complicated than that of simple CO_2 absorption in the aqueous phase and consequent dissolution of carbonate minerals. Data obtained during subsequent monitoring phases add further complexities to the overall picture rather than clarifying it.

7.9. The need for a synergistic approach

Based on what was discussed in previous sections, it is quite evident that the reactions of dissolution of primary silicates and precipitation of secondary minerals, including carbonates, proceed to relatively limited extents in some laboratory experiments and field tests and do not occur at all in others. Geochemical modelling generally predicts that comparatively long lapses of time, in the order of hundreds, thousands, or even tens of thousands years, are needed for the significant progress of carbonation reactions. Therefore,

there is no contrast between the results of geochemical modelling and those of laboratory experiments and field tests. Experiments and tests are entirely compatible with the computer simulation of geochemical processes and, in our opinion, a synergistic use of the two approaches is recommendable, as already done in some high-quality studies (e.g., Gunter et al., 1997 and Giammar et al., 2005 among the others).

Geochemical models are very attractive as it takes a comparatively short lapse of time to obtain results that would be achieved after much longer intervals of time, sometimes not accessible to humans, by means of real experiments either in the laboratory or in the field. However, users of geochemical models must be aware of possible dangers.

One of these is to rely too much on computer experiments or to expect too much from them. This was clearly discussed by Giggenbach (1984), by means of the following words.

> *As the reality of these models increases there is a danger, however, that their complexity and intractability will soon rival those of the natural systems studied. The emerging gap between human and machine understanding of these systems is illustrated by a remark by Reed (1982) in which he stresses the utility of the computer approach "when one considers how difficult it would be to apply intuitive reasoning and partial calculations to determine the course of a water–rock reaction. The large number of unknowns and the non-linearity of the equations make it difficult to understand the complexly intertwined processes." Taking into account the fact that intuitive thinking, a prerogative of human mind, is the basis of all scientific progress, relegating the process of understanding our environment to machines may eventually stifle rather than further scientific development.*

Besides, it must be noticed that the validity of the results of computer experiments depends chiefly on how we have set up the model at the beginning of the simulation. No good answer can be expected from an ill-posed question whereas a good answer can be obtained if we succeed to formulate a correct question. Again, *setting-up a valid model requires an at least general, but conceptually accurate understanding of the processes active*, as underscored by Giggenbach (1984).

The outputs of computer experiments are also influenced by the quality of the thermodynamic and kinetic data, the validity of the used algorithms and many other "details". For instance, the application of geochemical models at high pressures and salinities is not straightforward, as discussed by Allen et al. (2005). See also Section 7.3.3 for the salinity effects.

Last but not least, presently available models are far from perfect as already discussed above and summarized in the next section.

7.9.1. Current limitations and future developments of reaction path modelling

The chemical reactions between minerals, the aqueous solution and CO_2 occurring upon high-pressure CO_2 injection are very complex and the theoretical framework needed

for their description is not fully incorporated in existing computer codes. Some of these deficiencies are summarized below.

(1) Available codes incorporate at best the extended (B-dot) Debye–Hückel equation to compute *individual ion activity coefficients*, γ_i, although its application to brines is not advisable. Ideally, one should use the Pitzer's approach to compute the γ_i of solute species, but needed parameters are generally not available at high temperature and are also lacking at all temperatures for pivotal aqueous species such as dissolved SiO_2, Al^{3+} and related complex species.

(2) The *thermodynamic properties of some mineral phases* of interest are unknown or poorly known. This is especially true for clay minerals, which are usually described in terms of idealized, limiting compositions.

(3) The *kinetic database* is even less complete than the thermodynamic database and it is difficult to fill this gap as *no general laws of overall reaction kinetics exist in parallel with the general laws of thermodynamics, and no necessary genetic relationship with which to connect kinetic species to thermodynamic species is known* (Sposito, 1994).

(4) In particular, the *influence of CO_2* on the dissolution rate has been investigated for a limited number of mineral phases up to 1 bar P_{CO2} and only for labradorite, calcite, dolomite and magnesite up to 50–68 bar P_{CO2}. Although available data indicate that the effect of CO_2 is that of controlling the pH of the aqueous solution rather than participating directly to the dissolution mechanism of solid phases, this matter deserves further consideration.

(5) The processes occurring during the *precipitation of solid phases* (e.g., nucleation and crystal growth) are not described adequately. The backward (precipitation) rate laws incorporated in available codes require the knowledge of the initial surface area, but this is zero for a phase that is not present in the system at the beginning of the simulation. Adoption of a value different from zero or assumption of instantaneous precipitation are two possible choices for circumventing this difficulty but this way to proceed is far from satisfactory.

(6) Possible variations of the *reactive surface areas* with reaction progress, due to armouring of mineral phases by other phases and/or other reasons, cannot be described.

(7) In natural systems, the formation of a secondary phase rather than another often depends on their different kinetics of growth, which lead to *different reaction paths*. This kind of problem cannot be tackled by means of available codes.

For all these deficiencies, the geochemical evolution of the systems of interest upon high-pressure CO_2 injection cannot be predicted with sufficient accuracy by means of computer experiments at present. However, geochemical modelling is the only available tool for the evaluation of long-term geochemical processes, including those of interest for geological CO_2 sequestration. In spite of possible improvements in the experimental approach, there is little hope to extend their duration to multiples of the life time of humans even from a very optimistic point of view. In contrast, computer experiments can be improved in future to understand the long-term evolution of the systems of interest.

7.10. A final note

I tried to be consistent throughout this book in the use of symbols and unit of measurements, and, even more important, in the adoption of chemical species. For what concerns the symbols, I am aware that I was not able to fulfil my initial purposes and, more important, the expectations of possible readers.

For what concerns the units, I preferred to use the bar and sometimes the atmosphere (1 atm = 1.01325 bar) instead of the recommended unit, i.e. the Pascal (1 MPa = 1×10^6 Pa = 10 bar), as I think that bar and atm are more immediate and related to the real world than Pa. I expressed the thermodynamic affinity A in J mol^{-1} (or kJ mol^{-1}) in Chapter 6 but I used cal mol^{-1} (or kcal mol^{-1}) in Chapter 7, as this is the unit adopted by EQ3/6. After all, one has to be able to do conversions. This is especially important for energies, as they are also involved in dietetic suggestions. Energy conversions are done by multiplying the A value expressed in cal mol^{-1} (or kcal mol^{-1}) times 4.184 to obtain the corresponding value in J mol^{-1} (or kJ mol^{-1}).

Unfortunately, the adoption of chemical species is not always the same in the geochemical literature and, in particular, there is some confusion on the species adopted to describe neutral dissolved CO_2 species. As already recalled (see Chapter 2), both true dissolved molecular carbon dioxide, $CO_2°$, and true carbonic acid, $H_2CO_3°$, coexist in the aqueous solution and, at equilibrium, the $m_{H_2CO_3°}/m_{CO_2°}$ ratio is 0.0026 at 25°C, 1 bar (Sposito, 1994). However, in the geochemical literature the equilibrium between $CO_2°$ and $H_2CO_3°$ is usually neglected and these two species are considered together in a lumped parameter. This is called apparent carbonic acid, H_2CO_3*, by some authors and aqueous carbon dioxide, $CO_{2(aq)}$, by others.

In this book, I have decided to follow the approach of each author, although this brings about some inconsistencies, of which the careful reader has already been aware at this point.

References

Aagaard, P. and Helgeson, H.C. (1982) Thermodynamic and kinetic constraints on reaction rates among minerals and aqueous solutions. I. Theoretical considerations. *Am. J. Sci.*, **282**, 237–285.

Aagaard, P. and Helgeson, H.C. (1983) Activity/composition relations among silicates and aqueous solutions. II. Chemical and thermodynamic consequences of ideal mixing of atoms on homological sistes in montmorillonites, illites, and mixed-layer clays. *Clays Clay Miner.*, **31**, 207–217.

Acker, J.G. and Bricker, O.P. (1992) The influence of pH on biotite dissolution and alteration kinetics at low temperature. *Geochim. Cosmochim. Acta*, **56**, 3073–3092.

Agricola, G. (1556) *De Re Metallica.* Hieronimo Frobenio et Nicolao Episcopio, Basel.

Alekseyev, V.A., Medvedeva, L.S., Prisyagina, N.I., Meshalkin, S.S. and Balabin, A.I. (1997) Change in the dissolution rates of alkali feldspars as a result of secondary mineral precipitation and approach to equilibrium. *Geochim. Cosmochim. Acta*, **61**, 1125–1142.

Alkattan, M., Oelkers, E.H., Dandurand, J.-L. and Schott, J. (1998) An experimental study of calcite and limestone dissolution rates as a function of pH from −1 to 3 and temperature from 25 to 80°C. *Chem. Geol.*, **151**, 199–214.

Alkattan, M., Oelkers, E.H., Dandurand, J.-L. and Schott J. (2002) An experimental study of calcite dissolution rates at acidic conditions and 25°C in the presence of $NaPO_3$ and $MgCl_2$. *Chem. Geol.*, **190**, 291–302.

Allen, D.E., Strazisar, B.R., Soong, Y. and Hedges, S.W. (2005) Modeling carbon dioxide sequestration in saline aquifers: Significance of elevated pressures and salinities. *Fuel Process. Technol.*, **86**, 1569–1580.

Allison, J.D., Brown, D.S. and Novo-Gradac, K.J. (1991) MINTEQA2/PRODEFA2, A Geochemical Assessment Model for Environmental Systems: Version 3.0 User's Manual, Report EPA/600/3-91/021, U. S. Environmental Protection Agency, Office of Research and Development, Environmental Research Laboratory, Athens, GA, 106pp.

Amrhein, C. and Suarez, D.L. (1992) Some factors affecting the dissolution kinetics of anorthite at 25°C. *Geochim. Cosmochim. Acta*, **56**, 1815–1826.

Anbeek, C. (1992) Surface roughness of minerals and implications for dissolution studies. *Geochim. Cosmochim. Acta*, **56**, 1461–1469.

Anderson, G.K. (2002) Solubility of carbon dioxide in water under incipient clathrate formation condition. *J. Chem. Eng. Data*, **47**, 219–222.

Anderson, G.M. and Crerar, D.A. (1993) *Thermodynamics in Geochemistry. The Equilibrium Model.* New York: Oxford University Press, 588pp.

Anderson, M.S. (1991) Reactivity of San Andreas dolomite, *SPE 20115, 1990 SPE Permian Basin Oil and Gas Recovery Conference*, March 8–9, Midland, TX.

Angell, C.A. (1983) Supercooled water. *Annu. Rev. Phys. Chem.*, **34**, 593–630.

Angus, S., Armstrong, B. and de Reuck, K.M. (1976) *International Thermodynamic Tables of the Fluid State – 3 Carbon Dioxide.* New York: Pergamon.

Appelo, C.A.J. and Postma, D. (1996) *Geochemistry, Groundwaters and Pollution.* Rotterdam: A.A. Balkema, 536pp.

Apps, J.A. (1996) An approach to modeling of the chemistry of waste fluid disposal in deep saline aquifers. In: Apps J.A. and Tsang C.F. (eds.), *Deep Injection Disposal of Hazardous and Industrial Waste: Scientific and Engineering Aspects.* San Diego, CA: Academic Press, pp. 465–488.

Arakaki, T. and Mucci, A. (1995) A continuous and mechanistic representation of calcite reaction-controlled kinetics in dilute solutions at 25°C and 1 atm total pressure. *Aquat. Geochem.*, **1**, 105–130.

Arakaki, T. and Mucci, A. (1999) Errata. A continuous and mechanistic representation of calcite reaction-controlled kinetics in dilute solutions at 25°C and 1 atm total pressure. *Aquat. Geochem.*, **5**, 225.

Arisi Rota, F., Brondi, A., Dessau, G., Branzini, M., Stea, B. and Vighi, L. (1971) I giacimenti minerari. In: "*La Toscana Meridionale. Fondamenti geologico-minerari per una prospettiva di valorizzazione delle risorse naturali*". *Rendiconti S.I.M.P.*, **27**, 357–544.

Arrhenius, S. (1889) Ober die reacktionsgeschwindigkeit bei der inversion von rohrzucker durch sauren. *Z. Physik. Chem.*, **4**, 226–248.

Arrhenius, S. (1896) On the influence of carbonic acid in the air upon the temperature of the ground. *Philos. Mag., Ser.* **5**, 237–275.

Arts, R., Eiken, O., Chadwick, A., Zweigel, P., van der Meer, L. and Zinszner, B. (2004) Monitoring of CO_2 injected at Sleipner using time-lapse seismic data. *Energy*, **29**, 1383–1392.

Arvidson, R.S., Ertan, I.E., Amonette, J.E. and Luttge, A. (2003) Variation in calcite dissolution rates: A fundamental problem? *Geochim. Cosmochim. Acta*, **67**, 1623–1634.

Arvidson, R.S. and Mackenzie, F.T. (2000) Temperature dependence of mineral precipitation rates along the $CaCO_3$–$MgCO_3$ join. *Aquat. Geochem.*, **6**, 249–256.

Awad, A., Koster van Groos, A. F. and Guggenheim, S. (2000) Forsteritic olivine: Effect of crystallographic direction on dissolution kinetics. *Geochim. Cosmochim. Acta*, **64**, 1765–1772.

Bacastow, R.B. (1976) Modulation of atmospheric carbon dioxide by the southern oscillation. *Nature*, **261**, 116–118.

Bachu, S., Gunter, W.D. and Perkins, E.H. (1994) Aquifer disposal of CO_2: Hydrodynamic and mineral trapping. *Energy Convers. Manage.*, **35**, 269–279.

Bailey, A. (1974) Effects of temperature on the reaction of silicates with aqueous solutions in the low temperature range. *First International Symposium on Water–Rock Interaction*. 1976, Praha, pp. 375–380.

Bailey, S.W. (ed.) (1988) *Hydrous Phyllosilicates (exclusive of micas). Reviews in Mineralogy*. Washington, DC: Mineralogical Society of America, **19**, 725pp.

Baker, J.C., Bai, G.P., Hamilton, P.J., Golding, S.D. and Keene, J.B. (1995) Continental-scale magmatic carbon dioxide seepage recorded by dawsonite in the Bowen–Gunnedah–Sydney basin system, Eastern Australia. *J. Sedimentary Res.*, **A65**, 522–530.

Baklid, A., Korbøl, R. and Owren, G. (1996) Sleipner vest CO_2 disposal. CO_2 injection into a shallow underground aquifer. SPE paper no. 36600.

Baldi, P., Bellini, S., Ceccarelli, A., Fiordalisi, A., Squarci, P. and Taffi, L. (1994) Correlazioni fra le anomalie termiche ed altri elementi geofisici e strutturali della Toscana Meridionale. *Studi Geol. Camerti*, **1**, 139–149.

Bales, R.C. and Morgan, J.J. (1985) Dissolution kinetics of chrysotile at pH 7 to 10. *Geochim. Cosmochim. Acta*, **49**, 2281–2288.

Bamberger, A., Sieder, G. and Maurer, G. (2000) High-pressure (vapor + liquid) equilibrium in binary mixtures of (carbon dioxide + water or acetic acid) at temperatures from 313 to 353 K. *J. Supercrit. Fluids*, **17**, 97–100.

Banwart, S., Davies, S. and Stumm, W. (1989) The role of oxalate in accelerating the reductive dissolution of hematite (α-Fe_2O_3) by ascorbate. *Colloid Surf.*, **39**, 303–309.

Barnola, J.-M., Anklin, M., Porcheron, J., Raynaud, D., Schwander, J. and Stauffer, B. (1995) CO_2 evolution during the last millenium as recorded by Antarctic and Greenland ice. *Tellus Ser. B-Chem. Phys. Meteorol.*, **47**, 264–272.

Barnola, J.M., Raynaud, D., Lorius, C. and Barkov, N.I. (2003) Historical CO_2 record from the Vostok ice core. In *Trends: A Compendium of Data on Global Change. Carbon Dioxide Information Analysis Center.* Oak Ridge, Tenn., USA: Oak Ridge National Laboratory, U.S. Department of Energy.

Barta, L. and Bradley, D.J. (1985) Extension of the specific interaction model to include gas solubilities in high temperature brines. *Geochim. Cosmochim. Acta*, **49**, 195–203.

Bartholomé, E. and Friz, H. (1956) *Chem. Ing. Technol.*, **28**, 706–708 (cited in Diamond and Akinfiev, 2003).

Battle, M., Bender, M., Tans, P.P., White, J.W.C., Ellis, J.T., Conway, T. and Francey, R.J. (2000) Global carbon sinks and their variability, inferred from atmospheric O_2 and $\delta^{13}C$. *Science*, **287**, 2467–2470.

Bauer, A. and Berger, G. (1998) Kaolinite and smectite dissolution rate in high molar KOH solutions at 35° and 80°C. *Appl. Geochem.*, **13**, 905–916.

Bayer, G. (1971) Thermal expansion anisotropy of dolomite-type borates $Me^{2+}Me^{4+}B_2O_6$. *Zeit. Kristallogr.*, **133**, 85–90.

Bender, M., Ellis, T., Tans, P., Francey, R. and Lowe, D. (1996) Variability in the O_2/N_2 ratio of southern hemisphere air, 1991–1994 – Implications for the carbon cycle. *Global Biogeochem. Cycles*, **10**, 9–21.

Bender, M., Sowers, T. and Labeyrie, L. (1994) The Dole effect and its variations during the last 130,000 years as measured in the VOSTOK ice core. *Global Biogeochem. Cycles*, **8**, 363–376.

Bennett, P.C. (1991) Quartz dissolution in organic-rich aqueous systems. *Geochim. Cosmochim. Acta*, **55**, 1781–1797.

Benson, S.W. (1968) *Thermochemical Kinetics*. New York: Wiley, 223pp.

Berg, A. and Banwart, S.A. (2000) Carbon dioxide mediated dissolution of Ca-feldspar: Implications for silicate weathering. *Chem. Geol.*, **163**, 25–42.

Berger, G., Cadore, E., Schott, J. and Dove, P.M. (1994a) Dissolution rate of quartz in lead and sodium electrolyte solutions between 25 and 300°C: Effect of the nature of surface complexes and reaction affinity. *Geochim. Cosmochim. Acta*, **58**, 541–551.

Berger, G., Claparols, C., Guy, C. and Daux, V. (1994b) Dissolution rate of a basalt glass in silica-rich solutions: Implications for long-term alteration. *Geochim. Cosmochim. Acta*, **58**, 4875–4886.

Berman, R.G. (1988) Internally-consistent thermodynamic data for minerals in the system Na_2O–K_2O–CaO–MgO–FeO–Fe_2O_3–Al_2O_3–SiO_2–TiO_2–H_2O–CO_2. *J. Petrol.*, **29**, 445–522.

Berner, R.A. (1978) Rate control of mineral dissolution under earth surface conditions. *Am. J. Sci.*, **278**, 1235–1252.

Berner, R.A. (1983) Kinetics of weathering and diagenesis. In: Lasaga, A.C. and Kirkpatrick, R.J. (eds.), *Kinetics of Geochemical Processes*: *Reviews in Mineralogy*, Mineralogical Society of America, 2nd printing, **8**, 111–134.

Berner, R.A. (1997) The rise of plants and their effect on weathering and atmospheric CO_2. *Science*, **276**, 544–546.

Berner, R.A. and Holdren, G.R., Jr. (1977) Mechanism of feldspar weathering: Some observational evidence. *Geology*, **5**, 369–372.

Berner, R.A. and Holdren, G.R., Jr. (1979) Mechanism of feldspar weathering – II. Observations of feldspars from soils. *Geochim. Cosmochim. Acta*, **43**, 1173–1186.

Berner, R.A., Sjöberg, E.L., Velbel, M.A. and Krom, M.D. (1980) Dissolution of pyroxenes and amphiboles during weathering. *Science*, **207**, 1205–1206.

Bevan, J. and Savage, D. (1989) The effect of organic acids on the dissolution of K-feldspar under conditions relevant to burial diagenesis. *Mineral. Mag.*, **53**, 415–425.

Beyer, A. (1871) Über die Zersetzung des Feldspathes unter dem Einfluss von Salzlösungen und einigen anderen Agentien. *Landwirtschaftliche Versuchs-Sta.*, **14**, 314–322.

Biber, M.V., Dos Santos Afonso, M. and Stumm, W. (1994) The coordination chemistry of weathering: IV. Inhibition of the dissolution of oxide minerals. *Geochim. Cosmochim. Acta*, **58**, 1999–2010.

Binning, G., Quate, C.F. and Gerber, Ch. (1986) Atomic force microscopy. *Phys. Rev. Lett.*, **56**, 930–933.

Bjerrum, N. (1929) Neuere auschauungen über elektrolyte. *Deutsche Chem. Gesell Ber.*, **62**, 1091–1103.

Blake, R.E. and Walter, L.M. (1999) Kinetics of feldspar and quartz dissolution at 70–80°C and near-neutral pH: Effect of organic acids and NaCl. *Geochim. Cosmochim. Acta*, **63**, 2043–2059.

Blanchard, I. G. (1994) *Epidote dissolution kinetics: An experimental study at 250°C and 500 bars between pH 3.4 and pH 12*. M. Sc. Thesis, University of Leeds, UK.

Blatt, H., Middleton, G. and Murray, R. (1980) *Origin of Sedimentary Rocks*, 2nd ed. NJ: Prentice-Hall, 782pp.

Bloom (1983) The kinetics of gibbsite dissolution in nitric acid. *Soil Sci. Soc. Am. J.*, **47**, 164–168.

Bloom, P.R. and Erich, M.C. (1987) Effect of solution composition on the rate and mechanism of gibbsite dissolution in acid solutions. *Soil Sci. Soc. Am. J.*, **51**, 1131–1136.

Blum, A.E. and Lasaga, A.C. (1986) Forsterite dissolution kinetics. *EOS*, **67**, 1278–1279.

Blum, A.E. and Lasaga, A.C. (1988) Role of surface speciation in the low-temperature dissolution of minerals. *Nature*, **331**, 431–433.

Blum, A.E. and Lasaga, A.C. (1991) The role of surface speciation in the dissolution of albite. *Geochim. Cosmochim. Acta*, **55**, 2193–2201.

Blum, A.E. and Stillings, L.L. (1995) Feldspar dissolution kinetics. In: White, A.F. and Brantley, S.L. (eds.), *Chemical Weathering Rates of Silicate Minerals*, *Reviews in Mineralogy*, Mineralogical Society of America, **31**, 291–351.

Blum, A.E., Yund, R.A. and Lasaga, A.C. (1990) The effect of dislocation density on the dissolution rate of quartz. *Geochim. Cosmochim. Acta*, **54**, 283–297.

Blum, E.H. and Luus, R. (1964) Thermodynamic consistency of reaction rate expressions. *Chem. Eng. Sci.*, **19**, 322–323.

Boettcher, A.L. and Wyllie, P.J. (1968) The calcite–aragonite transition measured in the system CaO–CO_2–H_2O. *J. Geol.*, **76**, 314–330.

Bolin, B., Sukumar, R., Ciais, P., Cramer, W., Jarvis, P., Kheshgi, H., Nobre, C., Semenov, S. and Steffen, W. (2000) Global perspective. In: Watson, R.T., Noble, I.R., Bolin, B., Ravindranath, N.H., Verardo, D.J. and Dokken, D.J. (eds.), *IPCC, Land Use, Land-Use Change, and Forestry. A Special Report of the IPCC*. Cambridge, UK: Cambridge University Press, pp. 23–51.

Bondam, J. (1967) Structural changes in adularia in hydrolytic environments. *Medd. Dansk Geol. For.*, **17**, 357–370.

Bondietti, G., Sinniger, J. and Stumm, W. (1993) The reactivity of Fe(III) (hydr)oxides: Effects of ligands in inhibiting the dissolution. *Colloids Surf. A*, **79**, 157–167.

Born, M. (1920) Volumen und hydratationswärme der ionen. *Zeitschr. Phys.*, **21**, 45–48.

Borodin, V.L., Lyntin, V.I., Ilyukhin, V.V. and Belov, N.V. (1979) Isomorphous calcite–otavite series. *Soviet Phys. Dokl.*, **24**, 226–227.

Bottinga, Y., Weill, D. and Richet, P. (1982) Density calculations for silicate liquids. I. Revised method for aluminosilicate compositions. *Geochim. Cosmochim. Acta*, **46**, 909–919.

Bowers, T.S., Jackson, K.J. and Helgeson, H.C. (1984). *Equilibrium Activity Diagrams for Coexisting Minerals and Aqueous Solutions at Pressures and Temperatures to 5 kb and 600°C*. New York: Springer, 397pp.

Boyd, F.R. and England, J.L. (1960) The quartz-coesite transition. *J. Geophys. Res.*, **65**, 749–756.

Brady, P.V. (1992) Silica surface chemistry at elevated temperatures. *Geochim. Cosmochim. Acta*, **56**, 2941–2946.

Brady, P.V. and Carrol, S.A. (1994) Direct effect of CO_2 and temperature on silicate weathering: Possible implications for climate control. *Geochim. Cosmochim. Acta*, **58**, 1853–1856.

Brady, P.V. and Gislason, S.R. (1997) Seafloor weathering controls on atmospheric CO_2 and global climate. *Geochim. Cosmochim. Acta*, **61**, 965–973.

Brady, P.V. and Walther, J.V. (1989) Controls on silicate dissolution rates in neutral and basic pH solutions at 25°C. *Geochim. Cosmochim. Acta*, **53**, 2823–2830.

Brady, P.V. and Walther, J.V. (1990) Kinetics of quartz dissolution at low temperatures. *Chem. Geol.*, **82**, 253–264.

Bragg, W.L. (1914) The analysis of crystals by the x-ray spectrometer. *Proc. R. Soc. London*, **A89**, 468–489.

Brandon, A.D., Creaser, R.A. and Chacko, T. (1996) Constraints on rates of granitic magma transport from epidote dissolution kinetics. *Science*, **271**, 1845–1848.

Brandt, F., Bosbach, D., Krawczyk-Bärsch, E., Arnold, T. and Bernhard, G. (2003) Chlorite dissolution in the acid pH-range: A combined microscopic and macroscopic approach. *Geochim. Cosmochim. Acta*, **67**, 1451–1461.

Brantley, S.L. and Chen, Y. (1995) Chemical weathering rates of pyroxenes and amphiboles. In: White, A. F. and Brantley, S.L. (eds.), *Chemical Weathering Rates of Silicate Minerals*, *Reviews in Mineralogy*, Mineralogical Society of America, **31**, 119–172.

Brantley, S.L. and Mellott, N.P. (1999) Surface area and porosity of primary silicate minerals. *Am. Mineral.*, **85**, 1767–1783.

Brantley, S.L. and Stillings, L.L. (1996) Feldspar dissolution at 25°C and low pH. *Am. J. Sci.*, **296**, 101–127.

Brindley, G.W. and Brown, G. (eds.) (1980) *Crystal Structures of Clay Minerals and their X-ray Identification*. London: Mineralogical Society Monograph No. **5**, Mineralogical Society, 495pp.

Briones, J.A., Mullins, J.C. and Thies, M.C. (1987) Ternary phase equilibria for acetic acid-water mixtures with supercritical carbon dioxide. *Fluid Phase Equilib.*, **36**, 235–246.

Broecker, W.S. and Peng, T.H. (1982) *Tracers in the Sea*. Palisades: Eldigio, 691pp.

Brönsted, J.N. (1928) Acid and basic catalysis. *Chem. Rev.*, **5**, 231–338.

Brown, C.A., Compton, R.G. and Narramore, C.A. (1993) The kinetics of calcite dissolution/precipitation. *J. Colloid Interface Sci.*, **160**, 372–379.

Brown, I.D. and Shannon, R.D. (1973) Empirical bond length–bond strength curves for oxides. *Acta Crystallogr.*, **A29**, 266–282.

Brunauer, S., Emmett, P. H. and Teller, E. (1938) Adsorption of gases in multimolecular layers. *J. Am. Chem. Soc.*, **60**, 309–319.

Bruni, J., Canepa, M., Cipolli, F., Marini, L., Ottonello, G., Vetuschi Zuccolini, M., Chiodini, G., Cioni, R. and Longinelli, A. (2001) Reactions governing the chemistry of waters interacting with serpentinites. In: Cidu, R. (ed.), *Water-Rock Interaction 2001*. Lisse: Balkema, pp. 145–148.

Bruni, J., Canepa, M., Cipolli, F., Marini, L., Ottonello, G., Vetuschi Zuccolini, M., Chiodini, G., Cioni, R. and Longinelli, A. (2002) Irreversible water–rock mass transfer accompanying the generation of the neutral, Mg-HCO_3 and high-pH, Ca-OH spring waters of the Genova province, Italy. *Appl. Geochem.*, **17**, 455–474.

Bruno, J., Stumm, W., Wersin, P. and Brandberg, F. (1992) On the influence of carbonate in mineral dissolution: I. The thermodynamics and kinetics of hematite dissolution in bicarbonate solutions at T = 25°C. *Geochim. Cosmochim. Acta*, **56**, 1139–1147.

Budyko, M.I. and Ronov, A.B. (1979) Chemical evolution of the atmosphere in the Phanerozoic. *Geochem. Int.*, **16**, 1–9.

Burton, W.K., Cabrera, N. and Frank, F.C. (1951) The growth of crystals and the equilibrium structure of their surfaces. *Philos. Trans. R. Soc. London,* **A243**, 299–358.

Busenberg, E. and Clemency, C.V. (1976) The dissolution kinetics of feldspars at 25°C and 1 atm CO_2 partial pressure. *Geochim. Cosmochim. Acta*, **40**, 41–49.

Busenberg, E. and Plummer, L.N. (1982) The kinetics of dissolution of dolomite in CO_2–H_2O systems at 1.5 to 65°C and 0 to 1 atm pCO_2. *Am J. Sci.*, **282**, 45–78.

Busenberg, E. and Plummer, L.N. (1986) A comparative study of the dissolution and crystal growth kinetics of calcite and aragonite. In: Mumpton, F.A. (ed.) *Studies in Diagenesis*. U.S.G.S. Bull., **1578**, 139–168.

Callendar, G.S. (1938) The artificial production of carbon dioxide and its influence on temperature. *R. Meteorol. Soc. Quart. J.*, **64**, 224–237.

Cama, J., Ganor, J., Ayora, C. and Lasaga, A.C. (2000) Smectite dissolution kinetics at 80°C and pH 8.8. *Geochim. Cosmochim. Acta*, **64**, 2701–2717.

Cama, J., Metz, V. and Ganor, J. (2002) The effect of pH and temperature on kaolinite dissolution rate under acidic conditions. *Geochim. Cosmochim. Acta*, **66**, 3913–3926.

Carlson, W.D. (1990) The polymorphs of $CaCO_3$ and the aragonite-calcite transformation. In: Reeder, R.J. (ed.), *Carbonates: Mineralogy and Chemistry, Reviews in Mineralogy*, Mineralogical Society of America, 2nd printing, **11**, 191–225.

Carpenter, M.A., Salje, E.K.H., Graeme-Barber, A., Wruck, B., Dove, M.T. and Knight, K.S. (1998) Calibration of excess thermodynamic properties and elastic constant variations associated with the $\alpha \leftrightarrow \beta$ phase transition in quartz. *Am. Mineral.*, **83**, 2–22.

Carroll, J.J. and Mather, A.E. (1992) The system carbon dioxide-water and the Krichevsky-Kasarnovsky equation. *J. Solut. Chem.*, **21**, 607–621.

Carroll, S.A. and Knauss, K.G. (2001) Experimental determination of Ca-silicate dissolution rates: A source of calcium for geologic CO_2 sequestration. *First National Conference on Carbon Sequestration*, National Energy Technology Laboratory, Washington DC, http://www.netl.doe.gov.

Carroll, S.A. and Knauss, K.G. (2005) Dependence of labradorite dissolution kinetics on $CO_{2(aq)}$, $Al_{(aq)}$, and temperature. *Chem. Geol.*, **217**, 213–225.

Carroll, S.A. and Walther, J.V. (1990) Kaolinite dissolution at 25°, 60°, and 80°C. *Am. J. Sci.*, **290**, 797–810.

Carroll-Webb, S.A. and Walther, J.V. (1988) A surface complex reaction model for the pH-dependence of corundum and kaolinite dissolution rates. *Geochim. Cosmochim. Acta*, **52**, 2609–2623.

Casey, W. H. (1991) On the relative dissolution rates of some oxide and orthosilicate minerals. *J. Colloid Interface Sci.*, **146**, 586–589.

Casey, W. H. and Bunker, B. (1990) Leaching of mineral and glass surfaces during dissolution. In: Hochella, M.F., Jr and White, A.F. (eds.), *Mineral–Water Interface Geochemistry, Reviews in Mineralogy*, Mineralogical Society of America, **23**, 397–424.

Casey, W.H. and Ludwig, C. (1995) Silicate mineral dissolution as a ligand-exchange reaction. In: White, A.F. and Brantley, S.L. (eds.), *Chemical Weathering Rates of Silicate Minerals, Reviews in Mineralogy*, Mineralogical Society of America, **31**, 87–117.

Casey, W.H. and Ludwig, C. (1996) The mechanism of dissolution of oxide minerals. *Nature*, **381**, 506–509.

Casey, W.H. and Westrich, H.R., (1992) Control of dissolution rates of orthosilicate minerals by divalent metal–oxygen bonds. *Nature*, **355**, 157–159.

Casey, W.H., Carr, M.J. and Graham, R.A. (1988) Crystal defects and the dissolution kinetics of rutile. *Geochim. Cosmochim. Acta*, **52**, 1545–1556.

Casey, W.H., Westrich, H.R., Arnold, G.W. and Banfield, J.F. (1989) The surface chemistry of dissolving labradorite feldspar. *Geochim. Cosmochim. Acta*, **53**, 821–832.

Casey, W.H., Westrich, H.R., Banfield, J.F., Ferruzzi, G. and Arnold, G.W. (1993) Leaching and reconstruction at the surface of dissolving chain-silicate minerals. *Nature*, **366**, 253–256.

Casey, W.H., Westrich, H.R. and Holdren, G.R. (1991) Dissolution rates of plagioclase at pH = 2 and 3. *Am. Mineral.*, **76**, 211–217.

Casey, W.H., Ludwig, C. and Holmén, B. (1998) Toward understanding the rates of reactions at mineral surfaces. In: Marini, L. and Ottonello, G. (eds.), *Proceedings of the Rome Seminar of Environmental Geochemistry*, Pacini, Pisa, 197pp.

Castellan, G.W. (1971) *Physical Chemistry*, 2nd ed.. Reading, MA: Addison-Wesley, 866pp.

Cellai, D. Carpenter, M.A., Wruck, B. and Salje, E.K.H. (1994) Characterization of high-temperature phase transitions in single crystals of Steinbach tridymite. *Am. Mineral.*, **79**, 606–614.

Chamberlin, T.C. (1898) The influence of great epochs of limestone formation upon the constitution of the atmosphere. *J. Geol.*, **6**, 609–621.

Chang, B.-T., Pak, L.-H. and Li, Y.-S. (1979) Solubilities and rates of dissolution of diaspore in NaOH aqueous solutions. *Bull. Chem. Soc. Japan*, **52**, 1321–1326.

Chang, L.L.Y. (1965) Subsolidus phase relations in the systems $BaCO_3$–$SrCO_3$, $SrCO_3$–$CaCO_3$, and $BaCO_3$–$CaCO_3$. *J. Geol.*, **73**, 346–368.

Chen, Y. and Brantley, S. L. (1997) Temperature- and pH-dependence of albite dissolution rate at acid pH. *Chem. Geol.*, **135**, 275–290.

Chen, Y. and Brantley, S. L. (1998) Diopside and anthophyllite dissolution at 25°C and 90°C and acid pH. *Chem. Geol.*, **147**, 233–248.

Chen, Y. and Brantley, S. L. (2000) Dissolution of forsteritic olivine at 65°C and $2 < pH < 5$. *Chem. Geol.*, **165**, 267–281.

Chessin, N., Hamilton, W.C. and Post, B. (1965) Position and thermal parameters of oxygen atoms in calcite. *Acta Crystallogr.*, **18**, 689–693.

Chiodini, G., Cioni, R., Guidi, M. and Marini, L. (1991) Chemical geothermometry and geobarometry in hydrothermal aqueous solutions: A theoretical investigation based on a mineral–solution equilibrium model. *Geochim. Cosmochim. Acta*, **55**, 2709–2727.

Chou, L. and Wollast, R. (1984) Study of the weathering of albite at room temperature and pressure with a fluidized bed reactor. *Geochim. Cosmochim. Acta*, **48**, 2205–2217.

Chou, L. and Wollast, R. (1985) Steady-state kinetics and dissolution mechanisms of albite. *Am. J. Sci.*, **285**, 963–993.

Chou, L., Garrels, R.M. and Wollast, R. (1989) Comparative study of the kinetics and mechanisms of dissolution of carbonate minerals. *Chem. Geol.*, **78**, 269–282.

Ciais, P., Denning, A.S., Tans, P.P., Berry, J.A., Randall, D.A., Collatz, G.J., Sellers, P.J., White, J.W.C., Trolier, M., Meijer, H.A.J., Francey, R.J., Monfray, P. and Heimann, M. (1997) A three-dimensional synthesis study of $\delta^{18}O$ in atmospheric CO_2. 1. Surface fluxes. *J. Geophys. Res.–Atmos.*, **102**, 5857–5872.

Cipolli, F., Gambardella, B., Marini, L., Ottonello, G. and Vetuschi Zuccolini, M. (2004) Geochemistry of high-pH waters from serpentinites of the Gruppo di Voltri (Genova, Italy) and reaction path modeling of CO_2 sequestration in serpentinite aquifers. *Appl. Geochem.*, **19**, 787–802.

Clay, J.P. and Thomas, A.W. (1938) The catalytic effect of anions upon the rate of dissolution of hydrous alumina by acids. *J. Am. Chem. Soc.*, **60**, 2384–2390.

Clegg, S.L. and Brimblecombe, P. (1990) Solubility of volatile electrolytes in multicomponent solutions with atmospheric applications. In: Melchior, D.C. and Bassett, R.L. (eds.), *Chemical Modeling of Aqueous Systems II*, American Chemical Society Symposium Series, **416**, 58–73.

Clemency, C.V. and Lin, F.-C. (1981) Dissolution kinetics of phlogopite. II. Open-system using an ion-exchange resin. *Clays Clay Miner.*, **29**, 107–112.

Coan, C.R. and King, A.D., Jr. (1971) Solubility of water in compressed carbon dioxide, nitrous oxide, and ethane. Evidence for hydration of carbon dioxide and nitrous oxide in the gas phase. *J. Am. Chem. Soc.*, **93**, 1857–1862.

Compton, R.G., Pritchard, K.L. and Unwin, P.R. (1989) The dissolution of calcite in acid waters: Mass transport versus surface control. *Freshwater Biol.*, **22**, 286–288.

Connaughton, L.M., Millero, F.J. and Pitzer, K.S. (1989) Volume changes for mixing the major sea salts: Equations valid to ionic strength 3.0 and temperature 95°C. *J. Solution Chem.*, **18**, 1007–1017.

Conway, T.J., Tans, P.P., Waterman, L.S., Thoning, K.W., Kitzis, D.R., Masarie, K.A. and Zhang, N. (1994) Evidence for interannual variability of the carbon cycle from the National Oceanic and Atmospheric Administration/Climate Monitoring and Diagnostics Laboratory global air sampling network. *J. Geophys. Res.*, **99**, 22831–22855.

Corazza, E., Sabelli, C. and Vannucci, S. (1977) Dawsonite: New mineralogical data and structure refinement. *Neues Jahrb. Mineral. Monatshefte*, **9**, 381–397.

Correns, C.W. (1940) Die Chemische Verwitterung der Silikate. *Naturw.*, **28**, 369–376.

Correns, C. W. and von Engelhardt W. (1938) Neue Untersuchungen über die Verwitterung des Kalifeldspates. *Chemie der Erde*, **12**, 1–22.

Corti, H.R., De Pablo, J.J. and Prausnitz, J.M. (1990) Phase equilibria for aqueous systems containing salts and carbon dioxide. Application of Pitzer's theory for electrolyte solutions. *J. Phys. Chem.*, **94**, 7876–7880.

Coveney, R.M. and Kelly, W.C. (1971) Dawsonite as a daughter mineral in hydrothermal fluid inclusions. *Contrib. Mineral. Petrol.*, **32**, 334–342.

Crovetto, R. (1991) Evaluation of solubility data for the system CO_2–H_2O from 273 K to the critical point of water. *J. Phys. Chem. Ref. Data*, **20**, 575–589.

Cygan, R.T., Casey, W.H., Roslough, M.B., Westrich, H.R., Carr, M.J. and Holdren, G.R. (1989) Dissolution kinetics of experimentally shocked silicate minerals. *Chem. Geol.*, **78**, 229–244.

D'Souza, R., Patrick, J.R. and Teja, A.S. (1988) High pressure phase equilibria in the carbon dioxide-*n*-hexadecane and carbon dioxide–water systems. *Can. J. Chem. Eng.*, **66**, 319–323.

Daubrée, A. (1867) Expériences sur les décompositions chimiques provoquées par les actions méchaniques dans divers minéraux tels que le feldspath. *Acad. Sci. Paris, Comptes Rendus*, **64**, 339–346.

Daux, V., Guy, C., Advocat, T., Crovisier, J.-L. and Stille P. (1997) Kinetic aspects of basaltic glass dissolution at 90°C: Role of aqueous silicon and aluminum. *Chem. Geol.*, **142**, 109–126.

Daveler, S.A. (1998) XTOOL 7.15 user's manual. Lawrence Livermore National Laboratory. Report UCRL-MA-130654, 32pp.

Debenedetti, P.G. and Stanley, H.E. (2003) Supercooled and glassy water. *Phys. Today*, **56**(6), 40–46.

Debye, P. and Hückel, E. (1923a) The theory of electrolytes. I. Lowering of freezing point and related phenomena. *Zeitschr. Physik*, **24**, 185–206.

Debye, P. and Hückel, E. (1923b) The theory of electrolytes. II. The limiting law of electrical conductivity. *Zeitschr. Physik*, **24**, 305–325.

Debye, P.J. (1954) *The Collected Papers of P.J. Debye*. New York: Wiley-Interscience, 700pp.

De Donder, T. (1920) *Leçons de Thermodynamique et de Chimie-Physique*. Paris: Gauthier-Villars.

Deer, W.A., Howie, R.A. and Zussman, J. (1992) *An Introduction to the Rock-forming Minerals*. London: Longman, 712pp.

Denbigh, K. (1971) *The Principles of Chemical Equilibrium*, 3rd ed. London: Cambridge University Press, 494pp.

Deng, Y. (1997) Effect of pH on the reductive dissolution rates of iron (III) hydroxide by ascorbate. *Langmuir*, **13**, 1835–1839.

Devidal, J.-L., Schott, J. and Dandurand, J.-L. (1997) An experimental study of kaolinite dissolution and precipitation kinetics as a function of chemical affinity and solution composition at 150°C, 40 bars, and pH 2, 6.8, and 7.8. *Geochim. Cosmochim. Acta*, **61**, 5165–5186.

Diamond, L.W. and Akinfiev, N.N. (2003) Solubility of CO_2 in water from −1.5 to 100°C and from 0.1 to 100 MPa: Evaluation of literature data and thermodynamic modelling. *Fluid Phase Equilib.*, **208**, 265–290.

Dibble, W.E., Jr. and Tiller, W.A. (1981) Non-equilibrium water/rock interactions – I. Model for interface-controlled reactions. *Geochim. Cosmochim. Acta*, **45**, 79–92.

Dietzel, M. and Böhme, G. (2005) The dissolution rates of gibbsite in the presence of chloride, nitrate, silica, sulfate, and citrate in open and closed systems at 20°C. *Geochim. Cosmochim. Acta*, **69**, 1199–1211.

Dinelli, E., Lombini, A., Simoni, A. and Ferrari, C. (1997) Heavy metals in serpentinite soils of selected outcrops of Piacenza and Parma provinces (Northern Apennines, Italy). *Miner. Petrogr. Acta*, **40**, 241–255.

Dohrn, R., Bünz, A.P., Devlieghere, F. and Thelen, D. (1993) Experimental measurements of phase equilibria for ternary and quaternary systems of glucose, water, CO_2 and ethanol with a novel apparatus. *Fluid Phase Equilib.*, **83**, 149–158.

Dollase, W.A. (1967) The crystal structure at 220 C of orthorhombic high tridymite from the Steinbach meteorite. *Acta Crystallogr.*, **23**, 617–623.

Dollase, W.A. and Baur, W.H. (1976) The superstructure of meteoritic low tridymite solved by computer simulation. *Am. Mineral.*, **61**, 971–978.

Dos Santos, M. and Stumm, W. (1992) Reductive dissolution of iron (III) (hydr)oxides by hydrogen sulfide. *Langmuir*, **8**, 1671–1675.

Dove, P.M. (1994) The dissolution kinetics of quartz in sodium chloride solutions at 25° to 300°C. *Am. J. Sci.*, **294**, 665–712.

Dove, P.M. (1995) Kinetic and thermodynamic controls on silica reactivity in weathering environments. In: White, A. F. and Brantley, S.L. (eds.), *Chemical Weathering Rates of Silicate Minerals*, *Reviews in Mineralogy*, Mineralogical Society of America, **31**, 235–290.

Dove, P.M. (1999) The dissolution kinetics of quartz in aqueous mixed cation solutions. *Geochim. Cosmochim. Acta*, **63**, 3715–3727.

Dove, P.M. and Crerar, D.A. (1990) Kinetics of quartz dissolution in electrolyte solutions using a hydrothermal mixed flow reactor. *Geochim. Cosmochim. Acta*, **54**, 955–969.

Dove, P.M. and Elston, S.F. (1992) Dissolution kinetics of quartz in sodium chloride solutions: Analysis of existing data and a rate model for 25°C. *Geochim. Cosmochim. Acta*, **56**, 4147–4156.

Dove, P.M. and Nix, C.J. (1997) The influence of the alkaline earth cations, magnesium, calcium, and barium on the dissolution kinetics of quartz. *Geochim. Cosmochim. Acta*, **61**, 3329–3340.

Drever, J.I. (1982) *The Geochemistry of Natural Waters*. NJ: Prentice-Hall, 437pp.

Duan, Z., Møller, N. and Weare, J.H. (1992) An equation of state for the CH_4–CO_2–H_2O system: II. Mixtures from 50 to 1000°C and 0 to 1000 bars. *Geochim. Cosmochim. Acta*, **56**, 2619–2631.

Duval, Y., Mielczarski, J.A., Pokrovsky, O.S., Mielczarski, E. and Ehrhardt, J.J. (2002) Evidence of the existence of three types of species at the quartz–aqueous solution interface at pH 0–10: XPS surface group quantification and surface complexation modeling. *J. Phys. Chem. B*, **106**, 2937–2945.

Dyne, J.R. (1996) *Sodium Carbonate Resources of the Green River Formation*, U.S. Geological Survey, Open-file report, pp. 96–729.

Effenberger, H., Mereiter, K. and Zemann, J. (1981) Crystal structure refinements of magnesite, calcite, rhodochrosite, siderite, smithsonite and dolomite, with discussion of some aspects of the stereochemistry of calcite-type carbonates. *Zeit. Kristallogr.*, **156**, 233–243.

Efremova, G.D. and Shvarts, A.V. (1972) Higher-order critical phenomena in ternary systems. The methanol–carbon dioxide–ethane system. *Russ. J. Phys. Chem.* (Engl. Transl.), **46**, 237–239.

Eggleston, C.M., Hochella, M.F., Jr. and Parks, G.A. (1989) Sample preparation and aging effects on the dissolution rate and surface composition of diopside. *Geochim. Cosmochim. Acta*, **53**, 797–804.

Ellis, A.J. and Golding, R.M. (1963) The solubility of carbon dioxide above 100°C in water and in sodium chloride solutions. *Am. J. Sci.* **261**, 47–60.

Elzinga, E.J., Reeder, R.J., Withers, S.H., Peale, R.E., Mason, R.A., Beck, K.M. and Hess, W.P. (2002) EXAFS study of rare-earth element coordination in calcite. *Geochim. Cosmochim. Acta*, **66**, 2875–2885.

Emberley, S., Hutcheon, I., Shevalier, M., Durocher, K., Gunter, W.D. and Perkins, E.H. (2004) Geochemical monitoring of fluid-rock interaction and CO_2 storage at the Weyburn CO_2-injection enhanced oil recovery site, Saskatchewan, Canada. *Energy*, **29**, 1393–1401.

Emberley, S., Hutcheon, I., Shevalier, M., Durocher, K., Mayer, B., Gunter, W.D. and Perkins, E.H. (2005) Monitoring of fluid–rock interaction and CO_2 storage through produced fluid sampling at the Weyburn CO_2-injection enhanced oil recovery site, Saskatchewan, Canada. *Appl. Geochem.*, **20**, 1131–1157.

Ernst, W.G. (1976) *Petrologic Phase Equilibria*. San Francisco: W.H. Freeman and Co., 333pp.

Etheridge, D.M., Steele, L.P., Langenfelds, R.L., Francey, R.J., Barnola, J.M. and Morgan, V.I. (1996) Natural and anthropogenic changes in atmospheric CO_2 over the last 1000 years from air in Antarctic ice and firn. *J. Geophys. Res.–Atmos.*, **101**, 4115–4128.

Etheridge, D.M., Steele, L.P., Langenfelds, R.L., Francey, R.J., Barnola, J.-M. and Morgan, V.I. (1998) Historical CO_2 records from the Law Dome DE08, DE08-2, and DSS ice cores. In *Trends: A Compendium of Data on Global Change*. Oak Ridge, TN, USA: Carbon Dioxide Information Analysis Center, Oak Ridge National Laboratory, U.S. Department of Energy.

Evans, B. (1965) Application of a reaction-rate method to the breakdown equilibria of muscovite and muscovite plus quartz. *Am. J. Sci.*, **263**, 647–667.

Eyring, H. (1935a) The activated complex in chemical reactions. *J. Chem. Phys.*, **3**, 107–115.

Eyring, H. (1935b) The activated complex and the absolute rate of chemical reactions. *Chem. Rev.*, **17**, 65–77.

Falkowski, P.G., Barber, R.T. and Smetacek, V. (1998) Biogeochemical controls and feedbacks on ocean primary production. *Science*, **281**, 200–206.

Fan, S.-S. and Guo, T.-M. (1999) Hydrate formation of CO_2-rich binary and quaternary gas mixtures in aqueous sodium chloride solutions. *J. Chem. Eng. Data*, **44**, 829–832.

Fei, Y. (1995) Thermal expansion. In: Ahrens, T.J. (ed.), *Mineral Physics and Crystallography: A Handbook of Physical Constants*, AGU Reference Shelf, **2**, 29–44.

Feigenbaum, S. and Shainberg, I. (1975) Dissolution of illite – A possible mechanism of potassium release. *Soil Sci. Soc. Am. Proc.*, **39**, 985–990.

Ferrante, M.J., Stuve, J.M. and Richardson, D.W. (1976) *Thermodynamic data for synthetic dawsonite*. 8129, Washington DC: U.S. Bureau of Mines Report Investigation, 13pp.

Ferruzzi, G.G. (1994) *The character and rates of dissolution of pyroxenes and pyroxenoids*. M. Sc. Thesis, University of California, Davis.

Finger, L.W. (1975) Least-squares refinement of the rigid-body motion parameters of CO_3 in calcite and magnesite and correlation with lattice vibrations. *Carnegie Inst. Washington, Year Book*, **74**, 572–575.

Fischer, A.G. (1983) The two Phanerozoic subcycles. In: Berggren, W. and Van Couvering, J. (eds.) *Catastrophies in Earth History; The New Uniformitarianism*. Princetown: Princetown University Press.

Fischer, H., Whalen, M., Smith, J., Mastroianni, D. and Deck, B. (1999) Ice core records of atmospheric CO_2 around the last three glacial terminations. *Science*, **283**, 1712–1714.

Fisher, D. (ed.) (1991) *Rules of Thumb for Engineers and Scientists*. Houston: Gulf Publishing Co., 242pp.

Flörke, O.W., Jones, J.B. and Schmincke, H.U. (1976) A new microcrystalline silica from Gran Canaria. *Zeit. Kristallogr.*, **143**, 156–165.

Fournier, R.O. (1973) Silica in thermal waters: Laboratory and field investigations. *Proceedings of the International Symposium on Hydrogeochemistry and Biogeochemistry, Tokyo*, pp. 122–139.

Fournier, R.O. (1991) Water geothermometers applied to geothermal energy. In: D'Amore, F. (co-ordinator), *Application of Geochemistry in Geothermal Reservoir Development*. Roma, Italy: UNITAR, pp. 37–69.

Francey, R.J., Tans, P.P. and Allison, C.E. (1995) Changes in oceanic and terrestrial carbon uptake since 1982. *Nature*, **373**, 326–330.

Frogner, P. and Schweda, P. (1998) Hornblende dissolution kinetics at 25°C. *Chem. Geol.*, **151**, 169–179.

Furmakova, L.N. (1981) The question of formation conditions for dawsonite. *Lithol. Miner. Res.*, **15**, 565–572.

Furrer, G. and Stumm, W. (1986) The coordination chemistry of weathering: I. Dissolution kinetics of δ-Al_2O_3 and BeO. *Geochim. Cosmochim. Acta*, **50**, 1847–1860.

Furrer, G., Zysset, M. and Schindler, P.W. (1993) Weathering kinetics of montmorillonite: Investigations in batch and mixed flow reactors. In: Manning, D.A.C., Hall, P.L. and Hughes, C.R. (eds.), *Geochemistry of Clay-Pore Fluid Interactions*. The Mineralogical Society Series, Berlin: Springer, **4**, 243–262.

Gambardella, B., Marini, L. and Baneschi, I. (2005) Dissolved potassium in the shallow groundwaters circulating in the volcanic rocks of central-southern Italy. *Appl. Geochem.*, **20**, 875–897.

Ganor, J., Mogollón, J.L. and Lasaga, A.C. (1995) The effect of pH on kaolinite dissolution rates and on activation energy. *Geochim. Cosmochim. Acta*, **59**, 1037–1052.

Ganor, J., Mogollón, J.L. and Lasaga, A.C. (1999) Kinetics of gibbsite dissolution under low ionic strength conditions. *Geochim. Cosmochim. Acta*, **63**, 1635–1651.

Gattuso, J.-P., Frankignoulle, M. and Wollast, R. (1998) Carbon and carbonate metabolism in coastal aquatic ecosystems. *Annu. Rev. Eco. Syst.*, **29**, 405–434.

Gaus, I., Azaroual, M. and Czernichowski-Lauriol, I. (2005) Reactive transport modelling of the impact of CO_2 injection on the clayey cap rock at Sleipner (North Sea). *Chem. Geol.*, **217**, 319–337.

Gautelier, M., Oelkers, E.H. and Schott, J. (1999) An experimental study of dolomite dissolution rates as a function of pH from −0.5 to 5 and temperature from 25 to 80°C. *Chem. Geol.*, **157**, 13–26.

Gautier, J.-M., Oelkers, E.H. and Schott, J. (1994) Experimental study of K-feldspar dissolution rates as a function of chemical affinity at 150°C and pH 9. *Geochim. Cosmochim. Acta*, **58**, 4549–4560.

Giammar, D.E., Bruant, R.G., Jr. and Peters, C.A. (2005) Forsterite dissolution and magnesite precipitation at conditions relevant for deep saline aquifer storage and sequestration of carbon dioxide. *Chem. Geol.*, **217**, 257–276.

Giggenbach, W.F. (1984) Mass transfer in hydrothermal alteration systems – A conceptual approach. *Geochim. Cosmochim. Acta*, **48**, 2693–2711.

Giggenbach, W.F. (1985) Construction of thermodynamic stability diagrams involving dioctahedral potassium clay minerals. *Chem. Geol.*, **49**, 231–242.

Giggenbach, W.F. (1987) Redox processes governing the chemistry of fumarolic gas discharges from White Island, New Zeland. *Appl. Geochem.*, **2**, 143–161.

Giggenbach, W.F. (1997) The origin and evolution of fluids in magmatic-hydrothermal systems. In: Barnes, H.L. (ed.), *Geochemistry of Hydrothermal Ore Deposits,* 3rd ed. New York: Wiley, 737–796.

Gislason, S.R. and Oelkers, E.H. (2003) Mechanism, rates, and consequences of basaltic glass dissolution: II. An experimental study of the dissolution rates of basaltic glass as a function of pH and temperature. *Geochim. Cosmochim. Acta*, **67**, 3817–3832.

Gislason, S.R., Heaney, P.J., Oelkers, E.H. and Schott, J. (1997) Kinetic and thermodynamic properties of moganite, a novel silica polymorph. *Geochim. Cosmochim. Acta*, **61**, 1193–1204.

Glass, B.P. (1984) Tektites. *J. Non-Cryst. Solids*, **67**, 333–344.

Golab, A. (2003) *The impact of igneous intrusion on coal, cleat carbonate, and groundwater composition.* Ph.D. Thesis, University of Wollongong, 327pp.

Goldberry, R and Loughnan, F.C. (1977) Dawsonite, alumohydrocalcite, nordstrandite and gorceixite in Permian marine strata of the Sydney Basin, Australia. *Sedimentology*, **24**, 565–579.

Goldich, S.S. (1938) A study in rock weathering. *J. Geol.*, **46**, 17–58.

Goldsmith, J.R. (1990) Phase relations of rhombohedral carbonates. In: Reeder, R.J. (ed.), *Carbonates: Mineralogy and Chemistry, Reviews in Mineralogy,* Mineralogical Society of America, 2nd printing, **11**, 49–76.

Goldsmith, J.R. and Heard, H.C. (1961) Subsolidus phase relations in the system $CaCO_3$–$MgCO_3$. *J. Geol.*, **69**, 45–74.

Golubev, S.V., Pokrosky, O.S. and Schott, J. (2005) Experimental determination of the effect of dissolved CO_2 on the dissolution kinetics of Mg and Ca silicates at 25°C. *Chem. Geol.*, **217**, 227–238.

Graetsch, H. and Topalovic-Dierdorf, I. (1996) ^{29}Si MAS NMR spectrum and superstructure of modulated tridymite L3-T_0(MX-1). *Eur. J. Mineral.*, **8**, 103–113.

Graf, D.L. (1961) Crystallographic tables for the rhombohedral carbonates. *Am. Mineral.*, **46**, 1283–1316.

Grandstaff, D.E. (1977) Some kinetics of bronzite orthopyroxene dissolution. *Geochim. Cosmochim. Acta*, **41**, 1097–1103.

Grandstaff, D.E. (1980) The dissolution rate of forsteritic olivine from Hawaiian beach sand. *Third International Symposium on Water–Rock Interaction*, Edmonton, Canada: Alberta Research Council, pp. 72–74.

Grandstaff, D.E. (1986) The dissolution rate of forsteritic olivine from Hawaiian beach sand. In: Colman, S.M. and Dethier, D.P. (eds), *Rates of Chemical Weathering of Rocks and Minerals*. Orlando: Academic Press.

Greenberg, J. and Tomson, M. (1992) Precipitation and dissolution kinetics and equilibria of aqueous ferrous carbonate vs temperature. *Appl. Geochem.*, **7**, 185–190.

Gunter, W.D., Bachu, S., Law D.H.S., Marwaha, V., Drysdale, D.L., McDonald, D.E. and McCann, T.J. (1996) Technical and economic feasibility of CO_2 disposal in aquifers within the Alberta Sedimentary Basin, Canada. *Energy Convers. Manage.*, **37**, 1135–1142.

Gunter, W.D., Perkins, E.H. and Hutcheon, I. (2000) Aquifer disposal of acid gases: Modeling of water–rock reactions for trapping acid wastes. *Appl. Geochem.*, **15**, 1085–1095.

Gunter, W.D., Perkins, E.H. and McCann, T.J. (1993) Aquifer disposal of CO_2-rich gases. Reaction design for added capacity. *Energy Convers. Manage.*, **34**, 941–948.

Gunter, W.D., Wiwchar, B. and Perkins, E.H. (1997) Aquifer disposal of CO_2-rich greenhouse gases: Extension of the time scale of experiment for CO_2-sequestering reactions by geochemical modeling. *Mineral. Petrol.*, **59**, 121–140.

Gustafsson, Å.B. and Puigdomenech, I. (2003) The effect of pH on chlorite dissolution rates at 25°C. *Mat. Res. Symp. Proc.*, **757**, 649–655.

Guthrie, G.D., Jr., Carey, J.W., Bergfeld, D., Byler, D., Chipera, S., Ziock, H.-J and Lackner, K. (2001) Geochemical aspects of the carbonation of magnesium silicates in an aqueous medium. First National Conference on Carbon Sequestration. National Energy Technology Laboratory, Washington DC, http://www.netl.doe.gov.

Gutjahr, A., Dabringhaus, H. and Lacmann, R. (1996) Studies of the growth and dissolution kinetics of the $CaCO_3$ polymorphs calcite and aragonite. I. Growth and dissolution rates in water. *J. Crystal Growth*, **158**, 296–309.

Guy, C. (1989) *Méchanismes de dissolution des solides dans les solutions hydrothermales déduits du comportement des verres basaltiques et de calcites déformées*. Ph.D. Thesis. Université Paul Sabatier.

Hajash, A., Jr., Carpenter, T. D. and Dewers, T. A. (1998) Dissolution and time-dependent compaction of albite sand: Experiments at 100°C and 160°C in pH-buffered organic acids and distilled water. *Tectonophysics*, **295**, 93–115.

Hall, A. (1987) *Igneous Petrology*. Harlow, UK: Longman Scientific & Technical, 573pp.

Hamer, M., Graham, R.C., Amrhein, C. and Bozhilov, K.N. (2003) Dissolution of ripidolite (Mg, Fe-Chlorite) in organic and inorganic acid solutions. *Soil Sci. Soc. Am. J.*, **67**, 654–661.

Hamilton, J.P., Brantley, S.L., Pantano, C.G., Criscenti, L.J. and Kubicki, J.D. (2001) Dissolution of nepheline, jadeite and albite glasses: Toward better models for aluminosilicate dissolution. *Geochim. Cosmochim. Acta*, **65**, 3683–3702.

Hamilton, J.P., Pantano, C.G. and Brantley, S.L. (2000) Dissolution of albite glass and crystal. *Geochim. Cosmochim. Acta*, **64**, 2603–2615.

Harned, H.S. (1920) The thermodynamic properties of the ions of some strong electrolytes and of the hydrogen ion in solutions of tenth molal hydrochloric acid containing uni-univalent salts. *J. Am. Chem. Soc.*, **42**, 1808–1832.

Harned, H.S. and Owen, B.B. (1958) *The Physical Chemistry of Electrolyte Solutions*, 3rd ed. New York: Reinhold.

Harvie, C.E. and Weare, J.H. (1980) The prediction of mineral solubilities in natural waters: The $Na–K–Mg–Ca–Cl–SO_4–H_2O$ system from zero to high concentrations at 25°C. *Geochim. Cosmochim. Acta*, **44**, 981–997.

Harvie, C.E., Møller, N. and Weare, J.H. (1984) The prediction of mineral solubilities in natural waters: The $Na–K–Mg–Ca–H–Cl–SO_4–OH–HCO_3–CO_3–CO_2–H_2O$ system to high ionic strengths at 25°C. *Geochim. Cosmochim. Acta*, **48**, 723–751.

Hayashi, H. and Yamada, M. (1990) Kinetics of dissolution of noncrystalline oxides and crystalline clay minerals in a basic Tiron solution. *Clays Clay Miner.*, **38**, 308–314.

Hayes, K.F. and Leckie, J.O. (1987) Modeling ionic strength effects on cation adsorption at hydrous oxide/solution interface. *J. Colloid Interface Sci.*, **115**, 564–572.

Heaney, P.J. (1994) Structure and chemistry of the low-pressure silica polymorphs. In: Heaney, P.J., Prewitt, C.T. and Gibbs, G.V. (eds.), *Silica: Physical Behavior, Geochemistry, and Materials Applications, Reviews in Mineralogy*, Mineralogical Society of America, **29**, 1–40.

Helgeson, H.C. (1967) Solution chemistry and metamorphism. In: Abelson, P.H. (ed.), *Researches in Geochemistry*, Vol. 2. New York: Wiley, pp. 362–404.

Helgeson, H.C. (1968) Evaluation of irreversible reactions in geochemical processes involving minerals and aqueous solutions: I. Thermodynamic relations. *Geochim. Cosmochim. Acta*, **32**, 853–877.

Helgeson, H.C. (1969) Thermodynamics of hydrothermal systems at elevated temperatures and pressures. *Am. J. Sci.*, **267**, 729–804.

Helgeson, H.C. (1971) Kinetics of mass transfer among silicates and aqueous solutions. *Geochim. Cosmochim. Acta*, **35**, 421–469.

Helgeson, H.C. (1979) Mass transfer among minerals and hydrothermal solutions. In: Barnes, H.L. (ed), *Geochemistry of Hydrothermal Ore Deposits*, 2nd ed. New York: Wiley, pp. 568–610.

Helgeson, H.C. and Kirkham, D.H. (1974a) Theoretical prediction of the thermodynamic behavior of aqueous electrolytes at high pressures and temperatures: I. Summary of the thermodynamic/electrostatic properties of the solvent. *Am. J. Sci.*, **274**, 1089–1198.

Helgeson, H.C. and Kirkham, D.H. (1974b) Theoretical prediction of the thermodynamic behavior of aqueous electrolytes at high pressures and temperatures: II. Debye–Hückel parameters for activity coefficients and relative partial molal properties. *Am. J. Sci.*, **274**, 1199–1261.

Helgeson, H.C. and Kirkham, D.H. (1976) Theoretical prediction of the thermodynamic behavior of aqueous electrolytes at high pressures and temperatures: III. Equation of state for aqueous species at infinite dilution. *Am. J. Sci.*, **276**, 97–240.

Helgeson, H.C. and MacKenzie, F.T. (1970) Silicate-sea water equilibria in the ocean system. *Deep-Sea Res.*, **17**, 877–892.

Helgeson, H.C., Brown, T.H., Nigrini, A. and Jones, T.A. (1970) Calculation of mass transfer in geochemical processes involving aqueous solutions. *Geochim. Cosmochim. Acta*, **34**, 569–592.

Helgeson, H.C., Delany, J.M., Nesbitt, H.W. and Bird, D.K. (1978) Summary and critique of the thermodynamic properties of rock-forming minerals. *Am. J. Sci.*, **278A**, 229.

Helgeson, H.C., Garrels, R.M. and Mackenzie, F.T. (1969) Evaluation of irreversible reactions in geochemical processes involving minerals and aqueous solutions: II. Applications. *Geochim. Cosmochim. Acta*, **33**, 455–481.

Helgeson, H.C., Kirkham, D.H. and Flowers, G.C. (1981) Theoretical prediction of the thermodynamic behavior of aqueous electrolytes at high pressures and temperatures: IV. Calculation of activity coefficients, osmotic coefficients and relative partial molal properties to 600°C and 5 kb. *Am. J. Sci.*, **281**, 1249–1516.

Helgeson, H.C., Murphy, W.M. and Aagaard, P. (1984) Thermodynamic and kinetic constraints on reaction rates among minerals and aqueous solutions. II. Rate constants, effective surface area, and the hydrolysis of feldspar. *Geochim. Cosmochim. Acta*, **48**, 2405–2432.

Hellmann, R. (1994) The albite–water system: Part I. The kinetics of dissolution as a function of pH at 100, 200 and 300°C. *Geochim. Cosmochim. Acta*, **58**, 595–611.

Hellmann, R., Schott, J., Dran, J.-C., Petit, J.-C. and Della Mea, G. (1990) A comparison of the dissolution behavsior of albite and albite glass under hydrothermal conditions. *Geol. Soc. Am. Ann. Meeting*, A292.

Henley, R.W. and Ellis, A.J. (1983) Geothermal systems, ancient and modern: A geochemical review. *Earth Sci. Rev.*, **19**, 1–50.

Heydemann, A. (1966) Über die chemische Verwitterung von Tonmineralen (Experimentelle Untersuchungen). *Geochim. Cosmochim. Acta*, **30**, 995–1035.

Higgins, S.R., Jordan, G. and Eggleston, C.M. (2002) Dissolution kinetics of magnesite in acidic aqueous solution: A hydrothermal atomic force microscopy study assessing step kinetics and dissolution flux. *Geochim. Cosmochim. Acta*, **66**, 3201–3210.

Hitchon, B. (ed.) (1996) *Aquifer Disposal of Carbon Dioxide*. Sherwood Park, Alberta, Canada: Geoscience Publishing Ltd.

Hochella, M.F., Jr. (1990) Atomic structure, microtopography, composition, and reactivity of mineral surfaces. In: Hochella, M.F., Jr. and White, A. F. (eds.), *Mineral–Water Interface Geochemistry*, *Reviews in Mineralogy*, Mineralogical Society of America, **23**, 87–132.

Hochella, M.F., Jr. and Banfield, J.F. (1995) Chemical weathering of silicates in nature: A microscopic perspective with theoretical considerations. In: White, A. F. and Brantley, S.L. (eds.), *Chemical Weathering Rates of Silicate Minerals*, *Reviews in Mineralogy*, Mineralogical Society of America, **31**, 353–406.

Hodson, M.E., Lee, M.R. and Parsons, I. (1997) Origins of the surface roughness of unweathered alkali feldspar grains. *Geochim. Cosmochim. Acta*, **61**, 3885–3896.

Högbom, A.G. (1894) On the probability of secular variations of atmospheric carbon dioxide (in Swedish). *Svensk Chemisk Tidsskrift*, **6**, 169–176.

Holdren, G.R., Jr. and Berner, R.A. (1979) Mechanism of feldspar weathering – I. Experimental studies. *Geochim. Cosmochim. Acta*, **43**, 1161–1171.

Holdren, G.R., Jr. and Speyer, P.M. (1987) Reaction rate-surface area relationships during the early stages of weathering. II. Data on eight additional feldspars. *Geochim. Cosmochim. Acta*, **51**, 2311–2318.

Hollingsworth, C.A. (1952) Equilibrium and the rate laws for forward and reverse reactions. *J. Chem. Phys.*, **20**, 921–922.

Hu, Y., Liu, X. and Xu Zhenghe (2003) Role of crystal structure in flotation separation of diaspore from kaolinite, pyrophyllite and illite. *Miner. Eng.*, **16**, 219–227.

Huang, Y.C., Fowkes, F.M., Lloyd, T.B. and Sanders, N.D. (1991) Adsorption of calcium ions from calcium chloride solutions onto calcium carbonate particles. *Langmuir*, **7**, 1742–1748.

Hückel, E. (1925) Zur theorie konzentrierterer wässeriger Lösungen starker elektrolyte. *Zeitschr. Physik*, **26**, 93–147.

Huertas, F.J., Caballero, E., Jiménez de Cisneros, C., Huertas, F. and Linares, J. (2001) Kinetics of montmorillonite dissolution in granitic solutions. *Appl. Geochem.*, **16**, 397–407.

Huertas, F.J., Chou, L. and Wollast, R. (1999) Mechanism of kaolinite dissolution at room temperature and pressure. Part II: Kinetic study. *Geochim. Cosmochim. Acta*, **63**, 3261–3275.

Huggins, C.W. and Green, T.E. (1973) Thermal decomposition of dawsonite. *Am. Mineral.*, **58**, 548–550.

Hume, L.A. and Rimstidt, J.D. (1992) The biodurability of chrysotile asbestos. *Am. Mineral.*, **77**, 1125–1128.

Indermühle, A., Stocker, T.F., Joss, F., Fischer, H., Smith, H.J., Wahlen, M., Deck, B., Mastroianni, D., Tschumi, J., Blunier, T., Meyer, R. and Stauffer, B. (1999) Holocene carbon-cycle dynamics based on CO_2 trapped in ice at Taylor Dome, Antarctica. *Nature*, **398**, 121–126.

Inkinen, O. and Lahti, L. (1964) X-ray crystal analysis of calcite. The "correct crystal model". *Ann. Acad. Sci. Fennicae*, Ser. A., VI, No. 142.

Inskeep and Bloom (1985) An evaluation of rate equations for calcite precipitation kinetics at pCO_2 less than 0.01 atm and pH greater than 8. *Geochim. Cosmochim. Acta*, **49**, 2165–2180.

Jackson, J., Jr., Huggins, C.W. and Ampian, S.G. (1972) Synthesis and characterization of dawsonite. 7664, Washington DC: US Bureau of Mines Report Investigation, 19pp.

Jackson, K., Bowman, L.E. and Fulton, J.L. (1995) Water solubility measurements in supercritical fluids and high-pressure liquids using near-infrared spectroscopy. *Anal. Chem.*, **67**, 2368–2372.

Johnson, J.W. and Lundeen, S.R. (1994 a) Jewel: A graphical-user interface for generating custom GEMBOCHS thermodynamic datafiles for use with geochemical modeling software. LLNL-YMP Milestone report MOL63, 23pp.

Johnson, J.W. and Lundeen, S.R. (1994 b) GEMBOCHS thermodynamic datafiles for use with the EQ3/6 software package. LLNL-YMP Milestone report MOL72, 99pp.

Johnson, J.W. and Lundeen, S.R. (1995) Facet: A graphical-user interface for viewing and updating the GEMBOCHS thermodynamic database. LLNL-YMP Milestone report MOL208, 28pp.

Johnson, J.W., Nitao, J.J., Steefel, C.I. and Knauss, K.G. (2001) Reactive transport modeling of geologic CO_2 sequestration in saline aquifers: The influence of intra-aquifer shales and the relative effectiveness of structural, solubility, and mineral trapping during prograde and retrograde sequestration. *First National Conference on Carbon Sequestration*. National Energy Technology Laboratory, Washington DC, http://www.netl.doe.gov.

Johnson, J.W., Oelkers, E.H. and Helgeson, H.C. (1992) SUPCRT 92: A software package for calculating the standard molal thermodynamic properties of minerals, gases, aqueous species, and reactions from 1 to 5000 bars and 0 to 1000°C. *Comput. Geosci.*, **18**, 899–947.

Johnson, J.W., Steefel, C.I. and Knauss, K.G. (2002) Reactive transport modeling of geologic CO_2 sequestration. Abstr. *Programs – Geol. Soc. Am.*, **34**, 390.

Jonckbloedt, R.C.L. (1998) Olivine dissolution in sulphuric acid at elevated temperatures – Implications for the olivine process, an alternative waste acid neutralizing process. *J. Geochem. Explor.*, **62**, 337–346.

Jones, C.F., Segall, R.L., Smart, S.C. and Turner, P.S. (1981) Initial dissolution kinetics of ionic oxides. *Proc. R. Soc. London A*, **374**, 141–153.

Jones, P., Haggett, M.L., Longridge, J.L. and Jethro, L. (1964) The hydration of carbon dioxide. *J. Chem. Educ.*, **41**, 610–612.

Jordan, G. and Rammensee, W. (1996) Dissolution rates and activation energy from dissolution of brucite (001): A new method based on the microtopography of crystal surfaces. Geochim. Cosmochim. Acta, **60**, 5055–5062.

Jordan, G. and Rammensee, W. (1998) Dissolution rates of calcite ($10\bar{1}4$) obtained by scanning force microscopy. Microtopography-based dissolution kinetics on surface with anisotropic step velocities. *Geochim. Cosmochim. Acta*, **62**, 941–947.

Jordan, G., Higgins, S.R. and Eggleston, C.M. (1999) Dissolution of the periclase (001) surface: A scanning force microscopy study. *Am. Mineral.*, **84**, 144–151.

Jordan, G., Higgins, S.R., Eggleston, C.M., Knauss, K.G. and Schmahl, W.W. (2001) Dissolution kinetics of magnesite in acidic aqueous solution, a hydrothermal atomic force microscopy (HAFM) study: Step orientation and kink dynamics. *Geochim. Cosmochim. Acta*, **65**, 4257–4266.

Kalinowski, B.E. and Schweda, P. (1996) Kinetics of muscovite, phlogopite, and biotite dissolution and alteration at pH 1–4, room temperature. *Geochim. Cosmochim. Acta*, **60**, 367–385.

Kalinowski, B. E., Faith-Ell, C. and Schweda, P. (1998) Dissolution kinetics and alteration of epidote in acidic solutions at 25°C. *Chem. Geol.*, **151**, 181–197.

Kaszuba, J.P., Janecky, D.R. and Snow, M.G. (2003) Carbon dioxide reaction processes in a model brine aquifer at 200°C and 200 bars: Implications for geological sequestration of carbon. *Appl. Geochem.*, **18**, 1065–1080.

Kaszuba, J.P., Janecky, D.R. and Snow, M.G. (2005) Experimental evaluation of mixed fluid reactions between supercritical carbon dioxide and NaCl brine: Relevance to the integrity of a geologic carbon repository. *Chem. Geol.*, **217**, 277–293.

Keeling, C.D. and Whorf, T.P. (2003) Atmospheric CO_2 records from sites in the SIO air sampling network. In: *Trends: A compendium of data on global change*. Oak Ridge, TN, USA: Carbon Dioxide Information Analysis Center, Oak Ridge National Laboratory.

Keeling, C.D., Bacastow, R.B. and Tans, P.P. (1980) Predicted shift in the 13C–12C ratio of atmospheric carbon-dioxide. *Geophys. Res. Lett.*, **7**, 505–508.

Keeling, C.D., Whorf, T.P., Wahlen, M. and Vanderplicht, J. (1995) Interannual extremes in the rate of rise of atmospheric carbon dioxide since 1980. *Nature*, **375**, 666–670.

Keeling, R.F. (1988) Measuring correlations between atmospheric oxygen and carbon-dioxide mole fractions – A preliminary study in urban air. *J. Atmos. Chem.*, **7**, 153–176.

Keeling, R.F. and Shertz, S.R. (1992) Seasonal and interannual variations in atmospheric oxygen and implications for the global carbon cycle. *Nature*, **358**, 723–727.

Keeling, R.F., Najjar, R.P. and Bender, M.L. (1993) What atmospheric oxygen measurements can tell us about the global carbon-cycle. *Global Biogeochem. Cycles*, **7**, 37–67.

Keeling, R.F., Piper, S.C. and Heimann, M. (1996) Global and hemispheric CO_2 sinks deduced from changes in atmospheric O_2 concentration. *Nature*, **381**, 218–221.

Kerrick, D.M. and Jacobs, G.K. (1981) A modified Redlich–Kwong equation for H_2O, CO_2 and H_2O–CO_2 mixtures at elevated pressures and temperatures. *Am. J. Sci.*, **281**, 735–767.

Kihara, K. (1977) An orthorhombic superstructure of tridymite existing between about 105 and 180 C. *Zeit. Kristallogr.*, **146**, 185–203.

Kihara, K. (1978) Thermal change in unit-cell dimensions, and hexagonal structure of tridymite. *Zeit. Kristallogr.*, **148**, 237–253.

King, M.B., Mubarak, A., Kim, J.D. and Bott, T.R. (1992) The mutual solubilities of water with supercritical and liquid carbon dioxide. *J. Supercrit. Fluids*, **5**, 296–302.

Kitahara, S. (1960) The solubility equilibrium and the rate of solution of quartz in water at high temperatures and pressures. *Rev. Phys. Chem., Japan*, **30**, 122–130.

Knauss, K.G. and Copenhaver, S.A. (1995) The effect of malonate on the dissolution kinetics of albite, quartz, and microcline as a function of pH at 70°C. *Appl. Geochem.*, **10**, 17–33.

Knauss, K.G. and Wolery, T.J. (1986) Dependence of albite dissolution kinetics on pH and time at 25°C and 70°C. *Geochim. Cosmochim. Acta*, **50**, 2481–2497.

Knauss, K.G. and Wolery, T.J. (1988) The dissolution kinetics of quartz as a function of pH and time at 70°C. *Geochim. Cosmochim. Acta*, **52**, 43–53.

Knauss, K.G. and Wolery, T.J. (1989) Muscovite dissolution kinetics as a function of pH and time at 70°C *Geochim. Cosmochim. Acta*, **53**, 1493–1501.

Knauss, K.G., Nguyen, S.N. and Weed, H.C. (1993) Diopside dissolution kinetics as a function of pH, CO_2, temperature, and time. *Geochim. Cosmochim. Acta*, **57**, 285–294.

Knauss, K.G., Johnson, J.W. and Steefel, C.I. (2005) Evaluation of the impact of CO_2, co-contaminant gas, aqueous fluid and reservoir rock interactions on the geologic sequestration of CO_2. *Chem. Geol.*, **217**, 339–350.

Knauss, K.G., Johnson, J.W., Steefel C.I. and Nitao, J.J. (2001) Evaluation of the impact of CO_2, aqueous fluid, and reservoir rock interactions on the geologic sequestration of CO_2, with special emphasis on economic implications. *First National Conference on Carbon Sequestration*. National Energy Technology Laboratory, Washington, DC, http://www.netl.doe.gov.

Knauss, K.G., Steefel, C.I., Johnson, J.W. and Boram, L.H. (2002) Impact of CO_2, contaminant gas, aqueous fluid, and reservoir rock interactions on the geologic sequestration of CO_2. Abstr. *Programs – Geol. Soc. Am.*, **34**, 306.

Knoche, R., Dingwell, D.B. and Webb, S.L. (1995) Melt densities for leucogranites and granitic pegmatites: Partial molar volumes for SiO_2, Al_2O_3, Na_2O, K_2O, Li_2O, Rb_2O, Cs_2O, MgO, CaO, SrO, BaO, B_2O_3, P_2O_5, F_2O_{-1}, TiO_2, Nb_2O_5, Ta_2O_5, WO_3. *Geochim. Cosmochim. Acta*, **59**, 4645–4652.

Kodama, H. and Schnitzer, M. (1973) Dissolution of chlorite minerals by fulvic acid. *Can. J. Soil Sci.*, **53**, 240–243.

Köhler, S.J., Dufaud, F. and Oelkers, E.H. (2003) An experimental study of illite dissolution kinetics as a function of pH from 1.4 to 12.4 and temperature from 5 to 50°C. *Geochim. Cosmochim. Acta*, **67**, 3583–3594.

Koziol, A.M. and Newton, R.C. (1995) Experimental determination of the reactions magnesite + quartz = enstatite + CO_2 and magnesite = periclase + CO_2 and the enthalpies of formation of enstatite and magnesite. *Am. Mineral.*, **80**, 1252–1260.

Kuwahara, Y. and Aoki, Y. (1995) Dissolution process of phlogopite in acid solution. *Clays Clay Miner.*, **43**, 39–50.

Laçin, O., Dönmez, B. and Demir, F. (2005) Dissolution kinetics of natural magnesite in acetic acid solutions. *Int. J. Miner. Process.*, **75**, 91–99.

Lackner, K.S., Butt, D.P. and Wendt, C.H. (1997) Progress on binding CO_2 in mineral substrates. *Energy Convers. Manage.*, **38**, S259–S264.

Lackner, K.S., Wendt, C.H., Butt, D.P., Joyce, E.L., Jr. and Sharp, D.H. (1995) Carbon dioxide disposal in carbonate minerals. *Energy*, **20**, 1153–1170.

Lagache, M. (1965) Contribution à l'étude de l'altération des feldspaths, dans l'eau, entre 100 et 200°C, sous diverses pressions de CO_2, et application à la synthèse des minéraux argileux. *Bull. Soc. Française Minéral. Cristallogr.*, **88**, 223–253.

Lagache, M. (1976) New data on the kinetics of the dissolution of alkali feldspars at 200°C in CO_2 charged water. *Geochim. Cosmochim. Acta*, **40**, 157–161.

Lagache, M., Wyart, J. and Sabatier, G. (1961) Dissolution des feldspaths alcalins dans l'eau pure ou chargée de CO_2 à 200°C. *Acad. Sci. Paris, Comptes Rendus*, **253**, 2019–2022.

La Mer, V.K. (1932) Reaction velocity in ionic systems. *Chem. Rev.*, **10**, 179–212.

Lange, R.L. (1997) A revised model for the density and thermal expansivity of K_2O–Na_2O–CaO–MgO–Al_2O_3–SiO_2 liquids from 700 to 1900 K: extension to crustal magmatic temperatures. *Contrib. Mineral. Petrol.*, **130**, 1–11.

Lange, R.L. and Carmichael, I.S.E. (1987) Densities of Na_2O–K_2O–CaO–MgO–FeO–Fe_2O_3–Al_2O_3–TiO_2–SiO_2 liquids: New measurements and derived partial molar properties. *Geochim. Cosmochim. Acta*, **51**, 2931–2946.

Lange, R.L. and Carmichael, I.S.E. (1990) Thermodynamic properties of silicate liquids with emphasis on density, thermal expansion and compressibility. In: Nicholls J. and Russel J.K. (eds.), *Modern Methods of Igneous Petrology, Reviews in Mineralogy*, **24**, 25–64.

Langenfelds, R.L., Francey, R.J. and Steele, L.P. (1999) Partitioning of the global fossil CO_2 sink using a 19-year trend in atmospheric O_2. *Geophys. Res. Lett.*, **26**, 1897–1900.

Langmuir, D. (1965) Stability of carbonates in the system MgO–CO_2–H_2O. *J. Geol.*, **73**, 730–754.

Langmuir, D. (1984) Physical and chemical characteristics of carbonate water. In: Lamoreaux, P.E., Wilson, B.M. and Memeon, B.A. (eds.), *Guide to the Hydrology of Carbonate Rocks*. Paris: UNESCO, pp. 60–105, 116–130.

Langmuir, D. (1997) *Aqueous Environmental Geochemistry*. Upper Saddle River, NJ: Prentice-Hall, 600pp.

Larsen, O. and Postma, D. (2001) Kinetics of reductive bulk dissolution of lepidocrocite, ferrihydrite, and goethite. *Geochim. Cosmochim. Acta*, **65**, 1367–1379.

Lasaga, A.C. (1983a) Rate laws of chemical reactions. In: Lasaga, A. C. and Kirkpatrick, R.J. (eds.), *Kinetics of Geochemical Processes, Reviews in Mineralogy*, Mineralogical Society of America, 2nd printing, **8**, 1–68.

Lasaga, A.C. (1983b) Transition state theory. In: Lasaga, A. C. and Kirkpatrick R.J. (eds.), *Kinetics of Geochemical Processes, Reviews in Mineralogy*, Mineralogical Society of America, 2nd printing, **8**, 135–169.

Lasaga, A.C. (1984) Chemical kinetics of water–rock interactions. *J. Geophys. Res.*, **89**, 4009–4025.

Lasaga, A.C. (1995) Fundamental approaches in describing mineral dissolution and precipitation rates. In: White, A. F. and Brantley, S.L. (eds.), *Chemical Weathering Rates of Silicate Minerals, Reviews in Mineralogy*, Mineralogical Society of America, **31**, 23–86.

Lasaga, A.C. (1998) *Kinetic Theory in the Earth Sciences.* Princeton, NJ: Princeton University Press, 811pp.

Laubengayer, A.W. and Weisz, R.S. (1943) A hydrothermal study of equilibria in the system alumina-water. *J. Am. Chem. Soc.*, **65**, 247–250.

Law, D.H.S. and Bachu, S. (1996) Hydrogeological and numerical analysis of CO_2 disposal in deep aquifers in the Alberta Sedimentary Basin. *Energy Convers. Manage.*, **37**, 1167–1174.

Lawlor, D.W. (1993) *Photosynthesis: Molecular, Physiological and Environmental Processes.* Harlow, UK: Longman.

Le Chatelier, H. (1889) Sur la dilatation du quartz. *Comptes Rendus*, **108**, 1046.

Le Maitre, R.W., (ed.) (2002) *Igneous Rocks. A Classification and Glossary of Terms.* 2nd ed. Cambridge: Cambridge University Press, 236pp.

Lea, A.S., Amonette, J.E., Baer, D.R., Liang, Y. and Colton, N.G. (2001) Microscopic effects of carbonate, manganese, and strontium ions on calcite dissolution. *Geochim. Cosmochim. Acta*, **65**, 369–379.

Lebrón, I. and Suárez, D.L. (1998) Kinetics and mechanisms of precipitation of calcite as affected by P_{CO_2} and organic ligands at 25°C. *Geochim. Cosmochim. Acta*, **62**, 405–416.

Leicester, H.M. (1956) *The Historical Background of Chemistry.* New York: Wiley.

Lemmon, E.W., McLinden, M.O. and Friend, D.G. (2003) Thermophysical Properties of Fluid Systems. In: Linstrom, P.J. and Mallard, W.G. (eds.), *NIST Chemistry WebBook, NIST Standard Reference Database Number 69*, National Institute of Standards and Technology, Gaithersburg, MD, http://webbook.nist.gov/.

Levich, V.G. (1962) *Physicochemical Hydrodynamics*, Englewood Cliffs, NJ: Prentice-Hall, 700pp.

Levitus, S., Antonov, J.I., Boyer, T.P. and Stephens, C. (2000) Warming of the world ocean. *Science*, **287**, 2225–2229.

Lewis, G.N. and Randall, M. (1921) The activity coefficient of strong electrolytes. *J. Am. Chem. Soc.*, **43**, 1112–1154

Lewis, G.N. and Randall, M. (1923) *Thermodynamics.* New York: McGraw-Hill.

Li, L. and Kiran, E. (1988) Gas–liquid critical properties of methylamine + nitrous oxide and methylamine + ethylene binary mixtures. *J. Chem. Eng. Data*, **33**, 342.

Lichtner, P.C. (1991) The quasi-stationary state approximation for fluid/rock reaction: Local equilibrium revisited. In: Ganguly, J. (ed.), *Diffusion, Atomic Ordering, and Mass Transport, Advances in Physical Geochemistry,* New York, Springer, **8**, 452–560.

Lichtner, P.C. (1996) Continuum formulation of multicomponent-multiphase reactive transport. In: Lichtner, P.C., Steefel, C.I. and Oelkers, E.H. (eds.). *Reactive Transport Porous Media, Rev. Miner.*, **34**, 1–81.

Lichtner, P.C. (1998) Modeling reactive flow and transport in natural systems. In: Marini, L. and Ottonello, G. (eds.), *Proceedings of the Rome Seminar on Environmental Geochemistry*, Pisa: Pacini, pp. 5–72.

Lichtner, P.C., Steefel, C.I. and Oelkers, E.H. (eds.) (1997) Reactive transport in porous media. *Rev. Miner.*, **34**, 438.

Liebau, F. (1985) *Structural Chemistry of Silicates.* Berlin: Springer.

Lietzke, M.H. and Stoughton, R.W. (1962) The calculation of activity coefficients from osmotic coefficient data. *J. Phys. Chem.*, **66**, 508–509.

Lin, F.-C. and Clemency, C.V. (1981a) The dissolution kinetics of brucite, antigorite, talc, and phlogopite at room temperature and pressure. *Am. Mineral.*, **66**, 801–806.

Lin, F.-C. and Clemency, C.V. (1981b) The kinetics of dissolution of muscovites at 25°C and 1 atm CO_2 partial pressure. *Geochim. Cosmochim. Acta*, **45**, 571–576.

Lin, F.-C., and Clemency, C.V. (1981c) Dissolution kinetics of phlogopite. I. Closed-system. *Clays Clay Minerals*, **29**, 101–106.

Lindberg, R.D. and Runnells, D.D. (1984) Ground water redox reactions: An analysis of equilibrium state applied to Eh measurements and geochemical modeling. *Science*, **225**, 925–927.

Lippmann, F. (1973) *Sedimentary Carbonate Minerals. Minerals, Rocks and Inorganic Materials, Monograph Series of Theoretical and Experimental Studies*, Vol. 4. Berlin: Springer, 228pp.

Lohuis, J.A.O. (1993) Carbon dioxide disposal and sustainable development in The Netherlands. *Energy Convers. Manage.*, **34**, 815–821.

Longhurst, A., Sathyendranath, S., Platt, T. and Caverhill, C. (1995) An estimate of global primary production in the ocean from satellite radiometer data. *J. Plankton Res.*, **17**, 1245–1271.

Löns, J. and Hoffmann, W. (1987) Zur Kristallstruktur der inkommensurablen Raumtemperaturphase des Tridymits. *Zeit. Kristallogr.*, **178**, 141–143.

Lowson, R.T., Comarmond, M.-C.J., Rajaratnam, G. and Brown, P.L. (2005) The kinetics of the dissolution of chlorite as a function of pH and at 25°C. *Geochim. Cosmochim. Acta*, **69**, 1687–1699.

Luce, R.W., Bartlett, R.W. and Parks, G.A. (1972) Dissolution kinetics of magnesium silicates. *Geochim. Cosmochim. Acta*, **36**, 35–50.

Lund, K., Fogler, H.S. and McCune, C.C. (1973) Acidization – I. The dissolution of dolomite in hydrochloric acid. *Chem. Eng. Sci.*, **28**, 691–700.

Lundström, U. and Ohman, L.-O. (1990) Dissolution of feldspars in the presence of natural organic solutes. *J. Soil Sci.*, **41**, 359–369.

Lüttge, A., Winkler, U. and Lasaga, A.C. (2002) Interferometric study of the dolomite dissolution: A new conceptual model for mineral dissolution. *Geochim. Cosmochim. Acta*, **67**, 1099–1116.

MacInnis, I.N. and Brantley, S.L. (1992) The role of dislocations and surface morphology in calcite dissolution. *Geochim. Cosmochim. Acta*, **56**, 1113–1126.

Maier, C.G. and Kelley, K.K. (1932) An equation for the representation of high temperature heat content data. *Am. Chem. Soc. J.*, **54**, 3243–3246.

Malatesta, F. (2005) On the Rodil–Vera method for determining ion activity coefficients. *Fluid Phase Equilib.*, **233**, 103–109.

Malmström, M. and Banwart, S. (1997) Biotite dissolution at 25°C: The pH dependence of dissolution rate and stoichiometry. *Geochim. Cosmochim. Acta*, **61**, 2779–2799.

Malmström, M., Banwart, S., Lewenhagen, J., Duro, L. and Bruno, J. (1996) The dissolution of biotite and chlorite at 25°C in the near-neutral pH region. *J. Contam. Hydrol.*, **21**, 201–213.

Manes, M., Hofer, L.J.E. and Weller, S. (1950) Classical thermodynamics and reaction rates close to equilibrium. *J. Chem. Phys.*, **18**, 1355–1361.

Manley, E.P. and Evans, L.J. (1986) Dissolution of feldspars by low molecular-weight aliphatic and aromatic acids. *Soil Sci.*, **141**, 106–112.

Manning, D.C., Gestsdóttir, K. and Rae, E.I.C. (1991) Feldspar dissolution in the presence of organic acid anions under diagenetic conditions: An experimental study. *Org. Geochem.*, **19**, 483–492.

Marini, L. and Chiodini, G. (1994) The role of carbon dioxide in the carbonate-evaporite geothermal systems of Tuscany and Latium (Italy). *Acta Vulcanol.*, **5**, 95–104.

Marini, L. and Manzella, A. (2005) Possible seismic signature of the α–β quartz transition in the lithosphere of Southern Tuscany (Italy). *J. Volcanol. Geotherm. Res.* **148**, 81–97.

Marini, L. and Ottonello, G. (eds.) (2002). *Atlante degli acquiferi della Liguria. Volume III: Le acque dei complessi ofiolitici (bacini: Arrestra, Branega, Cassinelle, Cerusa, Erro, Gorzente, Leira, Lemme, Lerone, Orba, Piota, Polcevera, Rumaro, Sansobbia, Stura, Teiro, Varenna, Visone.* Pisa: Pacini Editore, 102pp.

Marini, L., Canepa, M., Cipolli, F., Ottonello, G. and Vetuschi Zuccolini, M. (2001). Use of stream sediment chemistry to predict trace element chemistry of groundwater. A case study from the Bisagno valley (Genoa, Italy). *J. Hydrol.*, **241**, 194–220.

Marini, L., Ottonello, G., Canepa, M. and Cipolli, F. (2000). Water–rock interaction in the Bisagno Valley (Genoa, Italy): Application of an inverse approach to model spring water chemistry. *Geochim. Cosmochim. Acta*, **64**, 2617–2635.

Markgraf, S.A. and Reeder, R.J. (1985) High-temperature structure refinements of calcite and magnesite. *Am. Mineral.*, **70**, 590–600.

Marland, B., Boden, T.A. and Andres, R.J. (2000) Global, regional, and national CO_2 emissions. In: *Trends: A Compendium of Data on Global Change*. Oak Ridge, TN, USA: Carbon Dioxide Information Analysis Center, Oak Ridge National Laboratory.

Marshall, C.E. (1962) Reactions of feldspars and micas with aqueous solutions. *Econ. Geol.*, **57**, 1219–1227.

Mast, M.A. and Drever, J.I. (1987) The effect of oxalate on the dissolution rates of oligoclase and tremolite. *Geochim. Cosmochim. Acta*, **51**, 2559–2568.

Matous, J., Sobr, J., Novak, J.P. and Pick, J. (1969). Solubilities of carbon dioxide in water at pressure up to 40 atm. *Collect. Czech. Chem. Commun.*, **34**, 3982–3985.

Mattigod, S.V. and Sposito, G. (1978) Improved method for estimating the standard free energies of formation of smectites. *Geochim. Cosmochim. Acta*, **42**, 1753–1762.

May, H., Acker, J.G., Smyth, J.R., Bricker, O.P. and Dyar, M.D. (1995) Aqueous dissolution of low-iron chlorite in dilute acid solutions at 25°C. *Clay Miner. Soc. Prog. Abstr.*, **32**, 88.

May, H.M., Kinniburgh, D.G., Helmke, P.A. and Jackson, M.L. (1986) Aqueous dissolution, solubilities and thermodynamic stabilities of common aluminosilicate minerals: Kaolinite and smectites. *Geochim. Cosmochim. Acta*, **50**, 1667–1677.

Mayer, J.E. and Mayer, M.G. (1940) *Statistical Mechanics*. New York: Wiley, 495pp.

McKelvy, M.J., Chizmeshya, A.V.G., Diefenbacher, J., Béarat, H. and Wolf, G.H. (2004) Exploration of the role of heat activation in enhancing serpentine carbon sequestration reactions. *Environ. Sci. Technol.*, **38**, 6897–6903.

McKelvy, M.J., Sharma, R., Chizmeshya, A.V.G., Carpenter, R. and Streib, K. (2001) Magnesium hydroxide dehydroxylation: *In situ* nanoscale observations of lamellar nucleation and growth. *Chem. Mater.*, **13**, 921–926.

Metz, V. and Ganor, J. (2000) Stirring effect on kaolinite dissolution rate. *Geochim. Cosmochim. Acta*, **65**, 3475–3490.

Meybeck, M. (1993) Riverine transport of atmospheric carbon – Sources, global typology and budget. *Water, Air Soil Pollut.*, **70**, 443–463.

Michard, G., Fouillac, C., Grimaud, D. and Denis, J. (1981) Une méthode globale d'estimation des températures des resérvoirs alimentant les sources thermales. Exemple du Massif Central Français. *Geochim. Cosmochim. Acta*, **45**, 1199–1207.

Mogollón, J.L., Ganor, J., Soler, J.M. and Lasaga, A.C. (1996) Column experiments and the full dissolution rate law of gibbsite. *Am. J. Sci.*, **296**, 729–765.

Mogollón, J.L., Pérez-Diaz, A. and Lo Monaco, S. (2000) The effect of ion identity and ionic strength on the dissolution rate of a gibbsitic bauxite. *Geochim. Cosmochim. Acta*, **64**, 781–795.

Monnin, C. (1989) An ion interaction model for the volumetric properties of natural waters: Density of the solution and partial molal volumes of electrolytes to high concentrations at 25°C. *Geochim. Cosmochim. Acta*, **53**, 1177–1188.

Moore, J., Adams, M., Allis, R., Luts, S. and Rauzi, S. (2005) Mineralogical and geochemical consequences of the long-term presence of CO_2 in natural reservoirs: An example from the Springerville-St. Johns Field, Arizona and New Mexico, U.S.A. *Chem. Geol.*, **217**, 365–385.

Morrison, G. (1981) Effect of water on the critical points of carbon dioxide and ethane. *J. Phys. Chem.*, **85**, 759–61.

Morse, J.W. (1974) Dissolution of calcium carbonate in seawater: III. A new method for the study of carbonate reaction kinetics. *Am. J. Sci.*, **274**, 97–107.

Morse, J.W. (1978) Dissolution kinetics of calcium carbonate in seawater: IV. The near-equilibrium dissolution kinetics of calcium carbonate-rich deep sea sediments. *Am. J. Sci.*, **278**, 344–353.

Morse, J.W. and Arvidson, R.S. (2002) The dissolution kinetics of major sedimentary carbonate minerals. *Earth-Sci. Rev.*, **58**, 51–84.

Morse, J.W. and Berner, R.A. (1972) Dissolution kinetics of calcium carbonate in seawater: II. A kinetic origin for lysocline. *Am. J. Sci.*, **272**, 840–851.

Morse, J.W. and Berner, R.A. (1979) The chemistry of calcium carbonate in the deep oceans. In: Jenne, E. (ed.), *Chemical Modeling – Speciation, Sorption, Solubility, and Kinetics in Aqueous Systems*. Washington, DC: American Chemical Society, pp. 499–535.

Muir, I.J., Bancroft, G.M. and Nesbitt, H.W. (1989) Characteristics of altered labradorite surfaces by SIMS and XPS. *Geochim. Cosmochim. Acta*, **53**, 1235–1241.

Muir, I.J., Bancroft, G.M., Shotyk, W. and Nesbitt, H.W. (1990) A SIMS and XPS study of dissolving plagioclase. *Geochim. Cosmochim. Acta*, **54**, 2247–2256.

Müller, G., Bender, E. and Maurer, G. (1988) Das Dampf-Flüssigkeits-gleichgewicht des Ternären Systems Ammoniak-Kohlendioxid-Wasser bei Hohen Wassergehalten im Bereich Zwischen 373 und 473 Kelvin. *Berichte Bunsen-Gesellshaft Phys. Chem.*, **92**, 148–160.

Murakami, T., Ito, J.-I., Utsunomiya, S., Kasama, T., Kozai, N. and Ohnuki, T. (2004) Anoxic dissolution processes of biotite: Implications for Fe behavior during Archean weathering. *Earth Planet. Sci. Lett.*, **224**, 117–129.

Murphy, W.M. (1989) Dislocations and feldspar dissolution. *Eur. J. Mineral.*, **1**, 315–326.

Murphy, W.M. and Helgeson, H.C. (1987) Thermodynamic and kinetic constraints on reaction rates among minerals and aqueous solutions. III. Activated complexes and the pH-dependence of the rates of feldspar, pyroxene, wollastonite, and olivine hydrolysis. *Geochim. Cosmochim. Acta*, **51**, 3137–3153.

Murphy, W.M., Pabalan, R.T., Prikryl, J.D. and Goulet, C.J. (1996) Reaction kinetics and thermodynamics of aqueous dissolution and growth of analcime and Na-clinoptilolite at 25°C. *Am. J. Sci.*, **296**, 128–186.

Nagy, K.L. (1995) Dissolution and precipitation kinetics of sheet silicates. In: White, A. F. and Brantley, S.L. (eds.), *Chemical Weathering Rates of Silicate Minerals*, *Reviews in Mineralogy*, Mineralogical Society of America, **31**, 173–233.

Nagy, K.L. and Lasaga, A.C. (1992) Dissolution and precipitation kinetics of gibbsite at 80°C and pH 3: The dependence on solution saturation state. *Geochim. Cosmochim. Acta*, **56**, 3093–3111.

Nancollas, G.H. and Reddy, M.M. (1971) The crystallization of calcium carbonate: II. Calcite growth mechanism. *J. Colloid Interface Sci.*, **37**, 824–830.

Navrotsky, A. and Loucks, D. (1977) Calculation of subsolidus phase relations in carbonates and pyroxenes. *Phys. Chem. Miner.*, **1**, 109–127.

Neftel, A., Friedli, H., Moor, E., Lötscher, H., Oeschger, H., Siegenthaler, U. and Stauffer, B. (1994) Historical CO_2 recoed from the Simple station ice core. In: Boden, T.A., Kaiser, D.P., Sepanski, R.J. and Stoss, F.W. (eds.) *Trends '93: A Compendium of Data on Global Change*. TN, USA: Carbon Dioxide Information Analysis Center, Oak Ridge National Laboratory, Oak Ridge, pp. 11–14.

Nernst, W. (1904) Theorie der reaktionsgeschwindigkeit in heterogenen systemen. *Zeitschr. Phys. Chem.*, **47**, 52–55.

Nesbitt, H.W. and Muir, I.J. (1988) SIMS depth profiles of weathered plagioclase and processes affecting dissolved Al and Si in some acidic soils. *Nature*, **334**, 336–338.

Newman, A.C.D. (ed.) (1987) *Chemistry of Clays and Clay Minerals*. Mineralogical Society Monograph No. **6**. New York: Wiley, 480pp.

Ng, H.-J. and Robinson, D.B. (1985) Hydrate formation in systems containing methane, ethane, propane, carbon dioxide or hydrogen sulfide in the presence of methanol. *Fluid Phase Equilib.*, **21**, 145–155.

Nickalls, R.W.D. (1993) A new approach to solving the cubic: Cardan's solution revealed. *Math. Gazette*, **77**, 354–359.

Nickel, E. (1973) Experimental dissolution of light and heavy minerals in comparison with weathering and intrastratal solutions. *Contrib. Sedimentol.*, **1**, 3–68.

Nielsen, A.E. (1964) *Kinetics of Precipitation*. New York: MacMillan, 151pp.

Nilsson, O. and Sternbeck, J. (1999) A mechanistic model for calcite crystal growth using surface speciation. *Geochim. Cosmochim. Acta*, **63**, 217–225.

Nitao, J.J. (1998) Reference Manual for the NUFT Flow and Transport Code, version 2.0. Lawrence Livermore National Laboratory. Report UCRL-MA-130651, 55pp.

Nordstrom, D.K. and Munoz, J.L. (1985) *Geochemical Thermodynamics*. Menlo Park, CA: The Benjamin/Cummings Publishing Co., 477pp.

Nowack, B. and Sigg, L. (1997) Dissolution of Fe(III) (hydr)oxides by metal–EDTA complexes. *Geochim. Cosmochim. Acta*, **61**, 951–963.

Nriagu, J.O. (1975) Thermochemical approximations for clay minerals. *Am. Mineral.*, **60**, 834–839.

Nukui, A., Nakazawa, H. and Akao, M. (1978) Thermal changes in monoclinic tridymite. *Am. Mineral.*, **63**, 1252–1259.

O'Connor, W.K., Dahlin, D.C., Nilsen, D.N., Rush, G.E., Walters, R.P. and Turner, P.C. (2001) Carbon dioxide sequestration by direct mineral carbonation: Results from recent studies and current status. *First National Conference on Carbon Sequestration. National Energy Technology Laboratory*, Washington, DC, http://www.netl.doe.gov.

Odin, G.S., Desprairies, A., Fullagar, P.D., Bellon, H., Decarreau, A., Fröhlich, F. and Zelvelder, M. (1988) Nature and geological significance of celadonite. In: Odin, G.S. (ed.), *Green Marine Clays*, *Developments in Sedimentology*. Amsterdam: Elsevier, **45**, pp. 337–398.

Oelkers, E.H. (1996) Physical and chemical properties of rocks and fluids for chemical mass transport calculations. In: Lichtner, P.C., Steefel, C.I. and Oelkers, E.H. (eds.), *Reactive Transport in Porous Media*, *Reviews in Mineralogy*, Mineralogical Society of America, **34**, 131–191.

Oelkers, E.H. (2001a) General kinetic description of multioxide silicate mineral and glass dissolution. *Geochim. Cosmochim. Acta*, **65**, 3703–3719.

Oelkers, E.H. (2001b) An experimental study of forsterite dissolution rates as a function of temperature and aqueous Mg and Si concentrations. *Chem. Geol.*, **175**, 485–494.

Oelkers, E.H. (2002) The surface areas of rocks and minerals. In: Buccianti, A., Marini, L., Ottonello G. and Vaselli, O. (eds.), *Proceedings of the Arezzo Seminar on Fluid Geochemistry*, Arezzo, August 29th–September 1st, 2000, Pisa: Pacini editore, pp. 18–30.

Oelkers, E.H. and Gislason, S.R. (2001). The mechanism, rates, and consequences of basaltic glass dissolution: I. An experimental study of the dissolution rates of basaltic glass as a function of aqueous Al, Si, and oxalic acid concentration at 25°C and pH = 3 and 11. *Geochim. Cosmochim. Acta*, **65**, 3671–3681.

Oelkers, E.H. and Helgeson, H.C. (1991) Calculation of activity coefficients and degrees of formation of neutral ion pairs in supercritical electrolyte solutions. *Geochim. Cosmochim. Acta*, **55**, 1235–1251.

Oelkers, E.H. and Schott, J. (1995) Experimental study of anorthite dissolution and the relative mechanism of feldspar hydrolysis. *Geochim. Cosmochim. Acta*, **59**, 5039–5053.

Oelkers, E.H. and Schott, J. (1998) Does organic acid adsorption affect alkali-feldspar dissolution rates? *Chem. Geol.*, **151**, 235–245.

Oelkers, E.H. and Schott, J. (1999) Experimental study of kyanite dissolution rates as a function of chemical affinity and solution composition. *Geochim. Cosmochim. Acta*, **63**, 785–797.

Oelkers, E.H. and Schott, J. (2001) An experimental study of enstatite dissolution rates as a function of pH, temperature, and aqueous Mg and Si concentration, and the mechanism of pyroxene/pyroxenoid dissolution. *Geochim. Cosmochim. Acta*, **65**, 1219–1231.

Oelkers, E.H., Schott, J. and Devidal, J.-L. (1994) The effect of aluminum, pH, and chemical affinity on the rates of aluminosilicate dissolution reactions. *Geochim. Cosmochim. Acta*, **58**, 2011–2024.

Oh, K.D., Morikawa, H., Iwai, S., and Aoki, H. (1973) The crystal structure of magnesite. *Am. Mineral.*, **58**, 1029–1033.

Ortoleva, P., Chadman, J., Merino, E. and Moore, C. (1987) Geochemical self-organization. I: Feedback mechanisms and modeling approach. *Am. J. Sci.*, **287**, 979–1007.

Orton, R. and Unwin, P.R. (1993) Dolomite dissolution kinetics at low pH: A channel-flow study. *J. Chem. Soc., Faraday Trans.*, **89**, 3947–3954.

Ottonello, G. (1997) *Principles of Geochemistry.* New York: Columbia University Press, 897pp.

Oxburgh, R., Drever, J.I. and Sun, Y.-T. (1994) Mechanism of plagioclase dissolution in acid solution at 25°C. *Geochim. Cosmochim. Acta*, **58**, 661–669.

Pabalan, R.T. and Pitzer, K.S. (1987) Thermodynamics of concentrated electrolyte mixtures and the prediction of mineral solubilities to high temperatures for mixtures in the system Na–K–Ca–Mg–Cl–SO_4–OH–H_2O *Geochim. Cosmochim. Acta*, **51**, 2429–2443.

Pabalan, R.T. and Pitzer, K.S. (1988) Heat capacity and other thermodynamic properties of $Na_2SO_{4(aq)}$ in hydrothermal solutions and the solubilities of sodium sulfate minerals in the system Na–Cl–SO_4–OH–H_2O. *Geochim. Cosmochim. Acta*, **52**, 2393–2404.

Pačes, T. (1973) Steady-state kinetics and equilibrium between ground water and granitic rock. *Geochim. Cosmochim. Acta*, **37**, 2641–2663.

Packter, A. and Dhillon, H.S. (1969) The heterogeneous reactions of gibbsite powder with aqueous inorganic acid solutions; kinetics and mechanism. *J. Chem Soc.* A, **17**, 2588–2592.

Packter, A. and Dhillon, H.S. (1973) The kinetics and mechanism of the heterogeneous reactions of crystallized gibbsite powders with aqueous sodium hydroxide solutions. *J. Phys. Chem.*, **77**, 2942–2947.

Packter, A. and Dhillon, H.S. (1974) Studies on recrystallized aluminium hydroxide precipitates: Kinetics and mechanism of dissolution by sodium hydroxide solutions. *Colloid Polym. Sci.*, 252, 249–256.

Pagani, M., Arthur, M.A. and Freeman, K.H. (1999a) Miocene evolution of atmospheric carbon dioxide. *Paleoceanography*, **14**, 273–292.

Pagani, M., Freeman, K. and Arthur, M.A. (1999b) Late Miocene atmospheric CO_2 concentrations and the expansion of C4 grasses. *Science*, **285**, 876–879.

Palandri, J.L. and Kharaka, Y.K. (2004) A compilation of rate parameters of water-mineral interaction kinetics for application to geochemical modeling. U. S. Geological Survey, Open File Report 2004–1068.

Park, A.-H.A. and Fan, L.-S. (2004) CO_2 mineral sequestration: Physically activated dissolution of serpentine and pH swing process. *Chem. Eng. Sci.*, **59**, 5241–5247.

Parkhurst, D.L. and Appelo, C.A.J. (1996) User's guide to PHREEQC (version 2) – A computer program for speciation, batch-reaction, one-dimensional transport, and inverse geochemical calculations. U.S.G.S. Water-Resources Investigations Report 99-4259, 312pp.

Parks, G.A. (1990) Surface energy and adsorption at mineral/water interfaces: An introduction. In: Hochella, M.F., Jr. and White, A.F. (eds.), *Mineral–Water Interface Geochemistry*, *Reviews in Mineralogy*, Mineralogical Society of America, **23**, 133–175.

Pauling, L. (1940) *The Nature of the Chemical Bond and the Structure of Molecules and Crystals*, 2nd ed. Ithaca, New York: Cornell University Press.

Pauling, L. (1970) *General Chemistry*. New York: Dover, 959pp.

Pearce, J.M., Holloway, S., Wacker, H., Nelis, M.K., Rochelle, C. and Bateman, K. (1996) Natural occurrences as analogues for the geological disposal of carbon dioxide. *Energy Convers. Manage.*, **37**, 1123–1128.

Pearson, P.N. and Palmer, M.R. (1999) Middle Eocene seawater pH and atmospheric carbon dioxide concentrations. *Science*, **284**, 1824–1826.

Peric', J., Krstulovic, R. and Feric, T. (1985) Kinetics aspects of the gibbsite digestion process in aqueous solution of sodium hydroxide. *Croat. Chem. Acta*, **58**, 255–264.

Perkins, E.H. and Gunter, W.D. (1995) A user's manual for β PATHARCH.94: A reaction path-mass transfer program. Alberta Research Council Report ENVTR 95-11, 179pp.

Petit, J.R., Jouzel, J., Raynaud, D., Barkov, N.I., Barnola, J.M., Basile, I., Bender, M., Chappellaz, J., Davis, M., Delaygue, G., Delmotte, M., Kotlyakov, V.M., Legrand, M., Lipenkov, V.Y., Lorius, C., Pepin, L., Ritz, C., Saltzman, E. and Stievenard, M. (1999) Climate and atmospheric history of the past 420,000 years from the Vostok ice core, Antarctica. *Nature*, **399**, 429–436.

Petrović, R. (1976) Rate control in feldspar dissolution – II. The protective effect of precipitates. *Geochim. Cosmochim. Acta*, **40**, 1509–1521.

Petrović, R., Berner, R.A. and Goldhaber, M.B. (1976) Rate control in dissolution of alkali feldspars – I. Study of residual grains by X-ray photoelectron spectroscopy. *Geochim. Cosmochim. Acta*, **40**, 537–548.

Peybernès, N., Michel, E., Barnola, J.-M., Delmotte, M., Chappellaz, J. and Raynaud D. (2000) Information on carbon cycle during the last 8000 years deduced from CO_2, $\delta^{13}CO_2$, and CH_4 profiles obtained on a Vostok ice core. *EGS, Nice, France*, 25–26 April 2000.

Pfaff, F. cited in Mellor, J.W. (1935) *A Comprehensive Treatise on Inorganic and Theoretical Chemistry*, Vol. 14. London: Longmans, Green & Co., 359pp.

Pfeifer, H.-R. (1977) A model for fluids in metamorphosed ultramafic rocks. Observations at surface and subsurface conditions (high pH spring waters). *Schweiz. Mineral. Petrogr. Mitt.*, **57**, 361–396.

Pitzer, K.S. (1973) Thermodynamics of electrolytes. I. Theoretical basis and general equations. *J. Phys. Chem.*, **77**, 268–277.

Pitzer, K.S. (1975) Thermodynamics of electrolytes. V. Effects of higher-order electrostatic terms. *J. Solution Chem.*, **4**, 249–265.

Pitzer, K.S. (1979) Theory: Ion interaction approach. In: Pytkowicz, R.M. (ed.), *Activity Coefficients in Electrolyte Solutions*. Boca Raton, FL: CRC Press, pp. 157–208.

Pitzer, K.S. (1987) Thermodynamic model for aqueous solutions of liquid-like density. In: Carmichael, I.S.E. and Eugster, H.P. (eds.), *Thermodynamic Modeling of Geological Materials: Minerals, Fluids and Melts*. Mineralogical Society of America, *Rev. Mineral.*, **17**, 97–142.

Pitzer, K.S. (1992) Ion interaction approach: Theory and data correlation. In: Pitzer, K.S. (ed.), *Activity Coefficients in Electrolyte Solutions*, 2nd ed. Boca Raton, FL: CRC Press, pp. 75–153.

Pitzer, K.S. and Kim, J.J. (1974) Thermodynamics of electrolytes. IV. Activity and osmotic coefficients for mixed electrolytes. *J. Am. Chem. Soc.*, **96**, 5701–5707.

Plass, G.N. (1956) The carbon dioxide theory of climatic change. *Tellus*, **8**, 140–154.

Plummer, L.N. and Wigley, T.M.L. (1976) The dissolution of calcite in CO_2-saturated solutions at 25°C and 1 atmosphere total pressure. *Geochim. Cosmochim. Acta*, **40**, 191–202.

Plummer, L.N., Wigley, T.M.L. and Parkhurst D.L. (1978) The kinetics of calcite dissolution in CO_2-water systems at 5° and 60°C and 0.0 to 1.0 atm CO_2. *Am. J. Sci.*, **278**, 179–216.

Pokrovsky, O.S. and Schott, J. (1999a). Processes at the magnesium-bearing carbonates/solution interface. II. Kinetics and mechanism of magnesite dissolution. *Geochim. Cosmochim. Acta*, **63**, 881–897.

Pokrovsky, O.S. and Schott, J. (1999b). Processes at the magnesium-bearing carbonates/solution interface. I. A surface speciation model for magnesite. *Geochim. Cosmochim. Acta*, **63**, 863–880.

Pokrovsky, O.S. and Schott, J. (2000a) Forsterite surface composition in aqueous solutions: A combined potentiometric, electrokinetic, and spectroscopic approach. *Geochim. Cosmochim. Acta*, **64**, 3299–3312.

Pokrovsky, O.S. and Schott, J. (2000b) Kinetics and mechanism of forsterite dissolution at 25°C and pH from 1 to 12. *Geochim. Cosmochim. Acta*, **64**, 3313–3325.

Pokrovsky, O.S. and Schott J. (2001) Kinetics and mechanism of dolomite dissolution in neutral to alkaline solutions revisited. *Am. J. Sci.*, **301**, 597–626.

Pokrovsky, O.S. and Schott, J. (2002) Surface chemistry and dissolution kinetics of divalent metal carbonates. *Environ. Sci. Technol.*, **36**, 426–432.

Pokrovsky, O.S. and Schott, J. (2004) Experimental study of brucite dissolution and precipitation in aqueous solutions: Surface speciation and chemical affinity control. *Geochim. Cosmochim. Acta*, **68**, 31–45.

Pokrovsky, O.S., Golubev, S.V. and Schott, J. (2005b) Dissolution kinetics of calcite, dolomite and magnesite at 25°C and 0 to 50 atm pCO_2. *Chem. Geol.*, **217**, 239–255.

Pokrovsky, O.S., Mielczarski, J.A., Barres, O. and Schott, J. (2000) Surface speciation models of calcite and dolomite/aqueous solution interfaces and their spectroscopic evaluation. *Langmuir*, **16**, 2677–2688.

Pokrovsky, O.S., Schott, J. and Castillo, A. (2005a) Kinetics of brucite dissolution at 25°C in the presence of organic and inorganic ligands and divalent metals. *Geochim. Cosmochim. Acta*, **69**, 905–918.

Pokrovsky, O.S., Schott, J. and Thomas, F. (1999) Dolomite surface speciation and reactivity in aquatic systems. *Geochim. Cosmochim. Acta*, **63**, 3133–3143.

Prausnitz, J.M., Lichtenthaler, R.N. and Gomes de Azevedo, E. (1999) *Molecular Thermodynamics of Fluid-Phase Equilibria*, 3rd ed. Upper Saddle River, NJ: Prentice-Hall, 860pp.

Prentice, I.C., Farquhar, G.D., Fasham, M.J.R., Goulden, M.L., Heimann, M., Jaramillo, V.J., Kheshgi, H.S., Le Quéré, C., Scholes, R.J., Wallace, D.W.R., Archer, D., Ashmore, M.R., Aumont, O., Baker, D., Bender, M., Bopp, L.P., Bousquet, P., Caldeira, K., Ciais, P., Cox, P.M., Cramer, W., Dentener, F., Enting, I.G., Field, C.B., Friedlingstein, P., Holland, E.A., Houghton, R.A., House, J.I., Ishida, A., Jain, A.K., Janssens, I.A., Joos, F., Kaminski, T., Keeling, C.D., Keeling, R.F., Kicklighter, D.W., Kohfeld, K.E., Knorr, W., Law, R., Lenton, T., Lindsay, K., Maier-Reimer, E., Manning, A.C., Matear, R.J., McGuire, A.D., Melillo, J.M., Meyer, R., Mund, M., Orr, J.C., Piper, S., Plattner, K., Rayner, P.J., Sitch, S., Slater, R., Taguchi, S., Tans, P.P., Tian, H.Q., Weirig, M.F., Whorf, T. and Yool, A. (2001) The carbon cycle and atmospheric carbon dioxide. In: Houghton, J.T., Ding, Y., Griggs, D.J., Noguer, M., van der Linden, P.J., Dai, X., Maskell, K. and Johnson, C.A. (eds.) *Climate Change 2001: The Scientific Basis.* Cambridge, UK: Cambridge University Press, pp. 183–238 (available at http://www.ipcc.ch).

Presnall, D.C. (1995) Phase diagrams of earth-forming minerals. In: Ahrens, T.J. (ed.), *Mineral Physics and Crystallography: A Handbook of Physical Constants*. AGU Reference Shelf 2, pp. 248–268.

Preuss, K. (1991) TOUGH2 – A General Purpose Numerical Simulator for Multiphase Fluid and Heat Flow. Report LBL-29400. Lawrence Berkeley Laboratory, Berkeley, CA.

Prigogine, I. (1955) *Introduction to Thermodynamics of Irreversible Processes*. New York: Wiley.

Pryde, A.K.A. and Dove, M.T. (1998) On the sequence of phase transitions in tridymite. *Phys. Chem. Miner.*, **26**, 171–179.

Pulfer, K., Schindler, P.W., Westall, J.C. and Grauer, R. (1984) Kinetics and mechanism of dissolution of bayerite (γ-$Al(OH)_3$) in HNO_3–HF solutions at 298.2°K. *J. Colloid Interface Sci.*, **101**, 554–564.

Rao, K.V.K. and Murthy, K.S. (1970) Thermal expansion of manganese carbonate. *J. Mater. Sci.*, **5**, 82–83.

Reddy, M.M. and Nancollas, G.H. (1971) The crystallization of calcium carbonate: I. Isotopic exchange and kinetics. *J. Colloid Interface Sci.*, **36**, 166–172.

Reddy, M.M, Plummer, L.N. and Busenberg, E. (1981) Crystal growth of calcite from calcium bicarbonate solutions at constant P_{CO2} and 25°C: A test of a calcite dissolution model. *Geochim. Cosmochim. Acta*, **45**, 1281–1289.

Redfield, A.C., Ketchum, B.H. and Richards, F.A. (1963) The influence of organisms on the composition of seawater. In: Hill, M.N. (ed.), *The Sea*. New York: Wiley, pp. 26–77.

Redlich, O. (1976) *Thermodynamics: Fundamentals, Applications*. New York: Elsevier, 277pp.

Redlich, O. and Kwong, J. (1949) The thermodynamics of solutions. V. An equation of state. Fugacities of gaseous solutions. *Chem. Rev.*, **44**, 233–244.

Reed, M.H. (1982) Calculation of multicomponent chemical equilibria and reaction processes in systems involving minerals, gases, and aqueous phase. *Geochim. Cosmochim. Acta*, **46**, 513–528.

Reed, M.H. (1997) Hydrothermal alteration and its relationship to ore fluid composition. In: Barnes, H. L. (ed.), *Geochemistry of Hydrothermal Ore Deposits*. 3rd ed. New York: Wiley, pp. 517–611.

Reeder, R.J. (1990) Crystal chemistry of the rhombohedral carbonates. In: Reeder, R.J. (ed.), *Carbonates: Mineralogy and Chemistry, Reviews in Mineralogy*, Mineralogical Society of America, 2nd printing, **11**, 1–47.

Reeder, R.J. and Markgraf, S.A. (1986) High-temperature crystal chemistry of dolomite. *Am. Mineral.*, **71**, 795–804.

Richet, P. and Polian, A. (1998) Water as a dense icelike component in silicate glasses. *Science*, **281**, 396–398.

Rickard, D.T. and Sjöberg, E.L. (1983) Mixed kinetic control of calcite dissolution rates. *Am. J. Sci.*, **283**, 815–830.

Ridley, M.K., Wesolowski, D.J., Palmer, D.A., Bénézeth, P. and Kettler, R. (1997) Effect of sulfate on the release rate of Al^{3+} from gibbsite in low-temperature acidic waters. *Environ. Sci. Technol.*, **31**, 1922–1925.

Riebesell, U., Wolf-Gladrow, D.A. and Smetacek, V. (1993) Carbon-dioxide limitation of marine phytoplankton growth-rates. *Nature*, **361**, 249–251.

Rimstidt, J.D. and Barnes, H.L. (1980) The kinetics of silica-water reactions. *Geochim. Cosmochim. Acta*, **44**, 1683–1699.

Rimstidt, J.D. and Dove, P.M. (1986) Mineral/solution reaction rates in a mixed flow reactor: Wollastonite hydrolysis. *Geochim. Cosmochim. Acta*, **50**, 2509–2516.

Rimstidt, J.D., Balog, A. and Webb, J. (1998) Distribution of trace elements between carbonate minerals and aqueous solutions. *Geochim. Cosmochim. Acta*, **62**, 1851–1863.

Robie, R.A. and Hemingway, B.S. (1995) *Thermodynamic Properties of Minerals and Related Substances at 298.15 K and 1 bar (10^5 pascals) Pressure and at Higher Temperatures*. U.S. Geological Survey Bulletin 2131, 461pp.

Robinson, G.P. and Haas, J.L. (1983) Heat capacity, relative enthalpy, and calorimetric entropy of silicate minerals: An empirical method of prediction. *Am. Mineral.*, **68**, 541–553.

Robinson, R.A. and Stokes, R.H. (1968) *Electrolyte Solutions*. London: Butterworths, 571pp.

Rochelle, C., Bateman, K. and Pearce, J.M. (1996) Fluid-rock interactions resulting from the underground disposal of carbon dioxide. In: Bottrell, S.H. (ed.), *Proc. 4th Int. Symp. Gochem. Earth's Surf.*, University of Leeds, Dept. of Earth Sciences, Leeds, pp. 448–452.

Rochelle, C.A., Bateman, K., MacGregor, R., Pearce, J.M., Savage, D. and Wetton, P.D. (1996) Experimental determination of chlorite dissolution rates. In: Murakami, T and Ewing, R.C. (ed.), *Materials Research Society Symposium, No 353. Scientific Basis for Nuclear Waste Management XVIII*, Kyoto 1994, pp. 149–156.

Rose, N.M. (1991) Dissolution rates of phrenite, epidote and albite. *Geochim. Cosmochim. Acta* **55**, 3273–3286.

Rosenbauer, R.J., Bischoff, J.L. and Koksalan, T. (2001) An experimental approach to CO_2 sequestration in saline aquifers: Application to Paradox Valley, CO. *EOS: Trans. Am. Geophys. Union*, **82**, 47, Fall Meeting Suppl. Abstract V32B-0974.

Ross, G.J. (1967) Kinetics of acid dissolution of an orthochlorite mineral. *Can. J. Chem.*, **45**, 3031–3034.

Rosso, J.J. and Rimstidt, J.D. (2000) A high resolution study of forsterite dissolution rates. *Geochim. Cosmochim. Acta*, **64**, 797–811.

Rowlinson, J.S. (1988) *Studies in Statistical Mechanics*, Vol. 14. Amsterdam: North-Holland.

Sako, T., Sugeta, T., Nakazawa, N., Obuko, T., Sato, M., Taguchi, T. and Hiaki, T. (1991) Phase equilibrium study of extraction and concentration of furfural produced in reactor using supercritical carbon dioxide. *J. Chem. Eng. Jpn.*, **24**, 449–454.

Salmon, S.U. and Malmström, M. (2001) Mineral weathering rates in mill tailings from Kristinenberg, Northern Sweden. *11th Annual V.M. Goldsmith Conference*, Abstract No. 3375, LPI Contribution No. 1088, Lunar and Planetary Institute, Houston.

Samson, S.D., Nagy, K.L. and Cotton, W.B., III (2005) Transient and quasi-steady-state dissolution of biotite at 22–25°C in high pH, sodium, nitrate, and aluminate solutions. *Geochim. Cosmochim. Acta*, **69**, 399–413.

Sanemasa, I., Yoshida, M. and Ozawa, T. (1972) The dissolution of olivine in in aqueous solutions of inorganic acids. *Bull. Chem. Soc. Jap.*, **45**, 1741–1746.

Sarmiento, J.L. and Gruber, N. (2002) Sinks for anthropogenic carbon. *Phys. Today*, **55**(8), 30–36.

Sarmiento, J.L. and Toggweiler, J.R. (1984) A new model for the role of the oceans in determining atmospheric pCO_2. *Nature*, **308**, 621–624.

Sass, B.M., Gupta, N., Ickes, J.A., Engelhard, M.H., Baer, D.R., Bergman, P. and Byrer, C. (2001) Interaction of rock minerals with carbon dioxide and brine: A hydrothermal investigation. *1st National Conference on Carbon Sequestration. National Energy Technology Laboratory*, Washington DC, http://www.netl.doe.gov.

Sass, R.L., Vidale, R. and Donohue, J. (1957) Interatomic distances and thermal anisotropy in sodium nitrate and calcite. *Acta Crystallogr.*, **10**, 567–570.

Saugier, B. and Roy, J. (2001) Estimations of global terrestrial productivity: Converging towards a single number? In: Roy, J., Saugier, B. and Mooney, H.A. (eds.), *Global Terrestrial Productivity: Past, Present and Future*. San Diego: Academic Press, pp. 541–555.

Saxena, S.R. (1973) *Thermodynamics of Rock-Forming Crystalline Solutions*. New York: Springer.

Scatchard, G. (1936) Concentrated solutions of strong electrolytes. *Chem. Rev.*, **19**, 309–327.

Schlitzer, R. (2000) Applying the adjoint method for biogeochemical modeling: Export of particuate organic matter in the world ocean. In: Kasibhatla, P., Heimann, M., Rayner, P., Mahowald, N., Prinn, R.G. and Hartley, D.E. (eds.), *Inverse Methods in Global Biogeochemical Cycles. Geophysical Monograph Series*, **114**, 107–124.

Schnoor, J.L. (1990) Kinetics of chemical weathering: A comparison of laboratory and field weathering rates. In: Stumm, W. (ed.), *Aquatic Chemical Kinetics*, New York: Wiley, 475–504.

Schott, J. and Berner, R.A. (1983) X-ray photoelectron studies of the mechanism of iron silicate dissolution during weathering. *Geochim. Cosmochim. Acta*, **47**, 2233–2240.

Schott, J. and Berner, R.A. (1985) Dissolution mechanisms of pyroxenes and olivines during weathering. In: Drever, J.I. (ed.), *The Chemistry of Weathering, NATO ASI Series C, Mathematical and Physical Sciences*, **149**, 35–53.

Schott, J., Berner, R.A. and Sjöberg, E.L. (1981) Mechanism of pyroxene and amphibole weathering. I. Experimental studies of iron-free minerals. *Geochim. Cosmochim. Acta*, **45**, 2123–2135.

Schott, J., Brantley, S.L., Crerar, D., Guy, C., Borcsik, M. and Willaime C. (1989) Dissolution kinetics of strained calcite. *Geochim. Cosmochim. Acta,* **53**, 373–382.

Schulze, E.D. and Heimann, M., (1998) Carbon and water exchange of terrestrial ecosystems. In: Galloway, J.N. and Melillo, J. (eds.), *Asian Change in the Context of Global Change*. Cambridge: Cambridge University Press.

Schulze, R.K., Hill, M.A., Field, R.D., Papin, P.A., Hanrahan, R.J. and Byler, D.D. (2004) Characterization of carbonated serpentine using XPS and TEM. *Energy Convers. Manage.*, **45**, 3169–3179.

Schweda, P. (1989) Kinetics of alkali feldspar dissolution at low temperature. In: Miles, D.L. (ed.), *Proceeding of the 6th International Symposium on Water–Rock Interaction*. Rotterdam: AA Balkema, pp. 609–612.

Schweda, P. (1990) *Kinetics and mechanisms of alkali feldspar dissolution at low temperature*. PhD Thesis, Stockholm University, 99pp.

Scotford, R.F. and Glastonbury, J.R. (1971) Effect of temperature on the rates of dissolution of gibbsite and boehmite. *Can. J. Chem. Eng.*, **49**, 611–616.

Scotford, R.F. and Glastonbury, J.R. (1972) The effects of concentration on the rates of dissolution of gibbsite and boehmite. *Can. J. Chem. Eng.*, **50**, 754–758.

Segall, R.L., Smart, S.C. and Turner, P.S. (1978) Ionic oxides: Distinction between mechanisms and surface roughening effects in the dissolution of magnesium oxide. *J. Chem. Soc. Faraday Trans. I*, **74**, 2907–2912.

Seifritz, W. (1990) CO_2 disposal by means of silicates. *Nature*, **345**, 486.

Setchénow, (1892) Action de l'acide carbonique sur les solutions des sels à acides forts. *Ann. Chim. Phys.*, **25**, 225–270.

Shackleton, N.J. (1977) Carbon-13 in Uvigerina: Tropical rainforest history and the equatorial Pacific carbonate dissolution cycles. In: Anderson, N.R. and Malahoff, A. (eds.), *The Fate of Fossil Fuel CO_2 in the Oceans*, New York: Plenum, 401–427.

Shade, J.W. (1981) Comparison of glass and ceramic leaching behavior by natural analogs. *Nucl. Chem. Waste Manage.*, **2**, 219–228.

Shannon, R.D. (1976) Revised effective ionic radii and systematic studies of interatomic distances in halides and chalcogenides. *Acta Crystallogr.*, **A32**, 751–767.

Shannon, R.D., Prewitt, C.T. (1969) Effective ionic radii in oxides and fluorides. *Acta Crystallogr.*, **B25**, 925–946.

Shiraki, R. and Brantley, S.L. (1995) Kinetics of near-equilibrium calcite precipitation at 100°C: An evaluation of elementary reaction-based and affinity-based rate laws. *Geochim. Cosmochim. Acta*, **59**, 1457–1471.

Shiraki, R., Rock, P.A. and Casey, W.H. (2000) Dissolution kinetics of calcite in 0.1 M NaCl solution at room temperature: An atomic force microscopy (AFM) study. *Aquat. Geochem.*, **6**, 87–108.

Shock, E.L. (1995) Organic acids in hydrothermal solutions: Standard molal thermodynamic properties of carboxylic acids and estimates of dissociation constants at high temperatures and pressures. *Am. J. Sci.*, **295**, 496–580.

Shock, E.L. and Helgeson, H.C. (1988) Calculation of the thermodynamic and transport properties of aqueous species at high pressures and temperatures: Correlation algorithms for ionic species and equation of state predictions to 5 kb and 1000°C. *Geochim. Cosmochim. Acta*, **52**, 2009-2036.

Shock, E.L. and Helgeson, H.C. (1990) Calculation of the thermodynamic and transport properties of aqueous species at high pressures and temperatures: Standard partial molal properties of organic species. *Geochim. Cosmochim. Acta*, **54**, 915–945.

Shock, E.L. and Koretsky, C.M. (1993) Metal-organic complexes in geochemical processes: Calculation of standard partial molal thermodynamic properties of aqueous acetate complexes at high pressures and temperatures. *Geochim. Cosmochim. Acta*, **57**, 4899–4922.

Shock, E.L. and Koretsky, C.M. (1995) Metal–organic complexes in geochemical processes: Estimation of standard partial molal thermodynamic properties of aqueous complexes between metal cations and monovalent organic acid ligands at high pressures and temperatures. *Geochim. Cosmochim. Acta*, **59**, 1497–1532.

Shock, E.L., Helgeson, H.C. and Sverjensky, D.A. (1989) Calculation of the thermodynamic and transport properties of aqueous species at high pressures and temperatures: Standard partial molal properties of inorganic neutral species. *Geochim. Cosmochim. Acta*, **53**, 2157–2183.

Shock, E.L., Oelkers, E.H., Johnson, J.W., Sverjensky, D.A. and Helgeson, H.C. (1992) Calculation of the thermodynamic properties of aqueous species at high pressures and temperatures: Effective electrostatic radii, dissociation constants, and standard partial molal properties to 1000°C and 5 kb. *J. Chem. Soc. (Lond.) Faraday Trans.*, **88**, 803–826.

Shotyk, W. and Nesbitt, H.W. (1990) A ligand-promoted dissolution of plagioclase feldspar: A comparison of the surface chemistry of dissolving labradorite and bytownite using SIMS. *Chem. Geol.* **84**, 320–321.

Shyu, G.-S., Hanif, N.S.M., Hall, K.R. and Eubank, P.T. (1997) Carbon dioxide–water phase equilibria results from the Wong-Sandler combining rules. *Fluid Phase Equilib.*, **130**, 73–85.

Siebert H., Youdelis W.V., Leja J. and Lilge E. (1963) The kinetics of the dissolution of crystalline quartz in water at high temperatures and pressures. *Unit Processes in Hydrometallurgy: Metall. Soc. AIME Conf.*, **24**, 284–299.

Siegel, D.I. and Pfannkuch, H.O. (1984) Silicate mineral dissolution at pH 4 and near standard temperature and pressure. *Geochim. Cosmochim. Acta*, **48**, 197–201.

Siegenthaler, U., Friedli, H., Lötscher, H., Moor, E., Neftel, A., Oeschger, H. and Stauffer, B. (1988) Stable-isotope ratios and concentration of CO_2 in air from polar ice cores. *Annal. Glaciol.*, **10**, 1–6.

Sjöberg, E.L. (1976) A fundamental equation for calcite dissolution kinetics. *Geochim. Cosmochim. Acta*, **40**, 441–447.

Sjöberg, E.L. (1978) Kinetics and mechanism of calcite dissolution in aqueous solutions at low temperatures. *Stockholm Contrib. Geol.*, **32**, 1–96.

Sjöberg, E.L. and Rickard, D. (1983) The influence of experimental design on the rate of calcite dissolution. *Geochim. Cosmochim. Acta*, **47**, 2281–2285.

Sjöberg, E.L. and Rickard, D.T. (1984a) Calcite dissolution kinetics: Surface speciation and the origin of the variable pH dependence. *Chem. Geol.*, **42**, 119–136.

Sjöberg, E.L. and Rickard, D.T. (1984b) Temperature dependence of calcite dissolution kinetics between 1 and 62°C at pH 2.7 to 8.4 in aqueous solutions. *Geochim. Cosmochim. Acta*, **48**, 485–493.

Sjöberg, E.L. and Rickard, D.T. (1985) The effect of added dissolved calcium on calcite dissolution kinetics in aqueous solutions at 25°C. *Chem. Geol.*, **49**, 405–413.

Skinner, B.J. (1966) Thermal expansion. In: Clark S. (ed.), *Handbook of Physical Constants, Geol. Soc. Am. Mem.*, pp. 75–96.

Smith, H.J., Fischer, H., Wahlen, M., Mastroianni, D. and Deck, B. (1999) Dual modes of the carbon cycle since the Last Glacial Maximum. *Nature*, **400**, 248–250.

Smith, W.R. and Missen, R.W. (1982) *Chemical Reaction Equilibrium Analysis: Theory and Algorithms.* New York: Wiley, 364pp.

Song, K.Y. and Kobayashi, R. (1987) Water content of CO_2 in equilibrium with liquid water and/or hydrates. *SPE Form. Eval.*, **2**, 500–508.

Sonnenfeld, P. (1984) *Brines and Evaporites.* Orlando, FL: Academic Press, 613pp.

Span, P. and Wagner, W. (1996) A new equation of state for carbon dioxide covering the fluid region from the triple-point temperature to 1100K at pressures up to 800Mpa. *J. Phys. Chem. Ref. Data*, **25–6**, 1509–1596.

Speedy, R.J. (1982) Stability-limit conjecture. An interpretation of the properties of water. *J. Phys. Chem.*, **86**, 982–991.

Speedy, R.J. and Angell, C.A. (1976) Isothermal compressibility of supercooled water and evidence for a thermodynamic singularity at −45°C. *J. Chem. Phys.*, **65**, 851–858.

Sposito, G. (1994) *Chemical Equilibria and Kinetics in Soils.* New York: Oxford University Press, 268pp.

Spycher, N. and Pruess, K. (2005) CO_2–H_2O mixtures in the geological sequestration of CO_2. II. Partitioning in chloride brines at 12–100°C and up to 600 bar. *Geochim. Cosmochim. Acta*, **69**, 3309–3320.

Spycher, N.F. and Reed, M.H. (1988) Fugacity coefficients of H_2, CO_2, CH_4, H_2O, and H_2O–CO_2–CH_4 mixtures: A virial equation treatment for moderate pressures and temperatures applicable to hydrothermal boiling. *Geochim. Cosmochim. Acta*, **52**, 739–749.

Spycher, N., Pruess, K. and Ennis-King, J. (2003) CO_2–H_2O mixtures in the geological sequestration of CO_2. I. Assessment and calculation of mutual solubilities from 12 to 100°C and up to 600 bar. *Geochim. Cosmochim. Acta*, **67**, 3015–3031.

Steinmann, G. (1905) Geologische Beobachtungen in den Alpen. *Ber naturf Ges Freiburg*, **16**, 18–67.

Stillings, L.L. and Brantley, S.L. (1995) Feldspar dissolution at 25°C and pH 3: Reaction stoichiometry and the effect of cations. *Geochim. Cosmochim. Acta*, **59**, 1483–1496.

Stillings, L.L., Drever, J.I., Brantley, S.L., Sun, Y. and Oxburgh, R. (1996) Rates of feldspar dissolution at pH 3−7 with 0−8 mM oxalic acid. *Chem. Geol.*, **132**, 79–89.

Stipp, S.L. and Hochella, M.F., Jr. (1991) Structure and bonding environments at the calcite surface observed with X-ray photoelectron spectroscopy (XPS) and low energy electron diffraction (LEED). *Geochim. Cosmochim. Acta*, **55**, 1723–1736.

Stoessell, R.K. (1981) Refinements in a site-mixing model for illites: Local electrostatic balance and the quasi-chemical approximation. *Geochim. Cosmochim. Acta*, **45**, 1733–1741.

Stumm, W. (1992) *Chemistry of the Solid-Water Interface.* New York: Wiley.

Stumm, W. (1997) Reactivity at the mineral–water interface: Dissolution and inhibition. *Colloids Surf. A*, **120**, 143–166.

Stumm, W. and Morgan, J.J. (1996) *Aquatic Chemistry. Chemical Equilibrium and Rates in Natural Waters.* New York: Wiley.

Stumm, W., Wehrli, B. and Wieland, E. (1987) Surface complexation and its impact on geochemical kinetics. *Croatica Chem. Acta*, **60**, 429–456.

Suehiro, Y., Nakajima, M., Yamada, K. and Uematsu, M. (1996) Critical parameters of $\{x\mathrm{CO2} + (1 - x)\mathrm{CHF3}\}$ for x = (1.0000, 0.7496, 0.5013 , and 0.2522). *J. Chem. Thermodyn.*, **28**, 1153–1164.

Sulzberger, B., Suter, D., Siffert, C., Banwart, S. and Stumm, W. (1989) Dissolution of Fe(III) (hydr)oxides in natural waters; laboratory assessment on the kinetics controlled by surface coordination. *Marine Chem.*, **28**, 127–144.

Sun, Y. (1994) *The effect of pH and oxalate ion on the dissolution rates of plagioclase feldspar.* M. Sc. Thesis, University of Wyoming, Laramie, 136pp.

Suter, D., Banwart, S. and Stumm, W. (1991) Dissolution of hydrous iron(III) oxides by reductive mechanisms. *Langmuir*, **7**, 809–813.

Sverdrup, H. U. (1990) *The Kinetics of Base Cation Release due to Chemical Weathering.* Lund: Lund University Press, 246pp.

Sverjensky, D.A. (1987) Calculations of the thermodynamic properties of aqueous species and the solubilities of minerals in supercritical electrolyte solutions. In: Carmichael, I.S.E. and Eugster, H.P. (eds.), *Thermodynamic Modeling of Geological Materials: Minerals, Fluids and Melts. Reviews in Mineralogy*, **17**, 177–209.

Sveriensjky, D.A., Shock, E.L. and Helgeson, H.C. (1997) Prediction of the thermodynamic properties of aqueous metal complexes to 1000°C and 5 kb. *Geochim. Cosmochim. Acta*, **61**, 1359–1412.

Swoboda-Colberg, N.G. and Drever, J.I. (1993) Mineral dissolution rates in plot-scale field and laboratory experiments. *Chem. Geol.* **105**, 51–69.

Takashima, Y. and Ohashi, S. (1968) The Mossbauer spectra of various natural minerals. *Bull. Chem. Soc. Japan*, **41**, 88–93.

Talman, S.J., Wiwchar, B., Gunter, W.D. and Scarge, C.M. (1990) Dissolution kinetics of calcite in the H_2O–CO_2 system along the steam saturation curve to 210°C. In: Spencer, R.J. and Chou, I.M. (eds.), *Fluid–Mineral Interactions: A Tribute to H.P. Eugster.* Geochem. Soc. Spec. Publ. Series, **2**, 41–55.

Tan, K.H. (1980) The release of silicon, aluminum, and potassium during decomposition of soil minerals by humic acid. *Soil Sci.*, **129**, 5–11.

Tanger, J.C. and Helgeson, H.C. (1988) Calculation of the thermodynamic and transport properties of aqueous species at high pressures and temperatures: Revised equations of state for the standard partial molal properties of ions and electrolytes. *Am. J. Sci.*, **288**, 19–98.

Tardy, Y. and Fritz, B. (1981) An ideal solid solution model for calculating solubility of clay minerals. *Clay Miner.*, **16**, 361–373.

Tardy, Y. and Garrels, R.M. (1974) A method of estimating the Gibbs energy of formation of layer silicates. *Geochim. Cosmochim. Acta*, **38**, 1101–1116.

Taylor, A.S., Blum, J.D. and Lasaga, A.C. (2000b) The dependence of labradorite dissolution and Sr isotope release rates on solution saturation state. *Geochim. Cosmochim. Acta*, **64**, 2389–2400.

Taylor, A.S., Blum, J.D., Lasaga, A.C. and MacInnis, I.N. (2000a) Kinetics of dissolution and Sr release during biotite and phlogopite weathering. *Geochim. Cosmochim. Acta*, **64**, 1191–1208.

Tchoubar, C. (1965) Formation de la kaolinite à partir d'albite altérée par l'eau à 200°C. Étude en microscopie et diffraction électroniques. *Soc. Française Minéralogie Cristallographie Bull.*, **88**, 483–518.

Tchoubar, C. and Oberlin, A. (1963) Altération de l'albite par action de l'eau. Étude en microscopie et microdiffraction électroniques de la précipitation et de l'évolution des fibres de boehmite formée. *J. Microsc.*, **2**, 415–432.

Teng, H., Yamasaki, A., Chun, M.-K. and Lee, H. (1997) Solubility of liquid CO_2 in water at temperatures from 278 K to 293 K and pressures from 6.44 MPa to 29.49 MPa and densities of the corresponding aqueous solutions. *J. Chem. Thermodyn.*, **29**, 1301–1310.

Teng, H.H., Dove, P.M. and De Yoreo, J.J. (2000) Kinetics of calcite growth: Surface processes and relationships to macroscopic rate laws. *Geochim. Cosmochim. Acta*, **64**, 2255–2266.

Terjesen, S.G., Erga, O., Thorsen, G. and Ve, A. (1961) I1. Phase boundary processes as rate determining steps in reactions between solids and liquids. The inhibitory action of metal ions on the formation of calcium bicarbonate by the reaction of calcite with aqueous carbon dioxide. *Chem. Eng. Sci.*, **74**, 277–288.

Tester, J.W., Worley, W.G., Robinson, B.A., Grigsby, C.O. and Feerer, J.L. (1994) Correlating quartz dissolution kinetics in pure water from 25 to 625°C. *Geochim. Cosmochim. Acta*, **58**, 2407–2420.

Thomassin, J.H., Goni, J., Baillif, P., Touray, J.C. and Jaurand, M.C. (1977) An XPS study of the dissolution kinetics of chrysotile in 0.1 N oxalic acid at different temperatures. *Phys. Chem. Miner.*, **1**, 385–398.

Thompson, J.B., Jr. (1955) The thermodynamic basis for the mineral facies concept. *Am. J. Sci.*, **53**, 65–103.

Tödheide, K. and Frank, E.U. (1963) Das Zweiphasengebiet und die Kritische Kurve im system Kohlendioxid-Wasser bis zu Drucken von 3500 bars. *Z. Phys. Chem., Neue Folge*, **37**, 387–401.

Tole, M.P., Lasaga, A.C., Pantano, C.G. and White, W.B. (1986) The kinetics of dissolution of nepheline ($NaAlSiO_4$). *Geochim. Cosmochim. Acta*, **50**, 379–392.

Tomazawa, M., Erwin, C.Y., Takata, M. and Watson, E.B. (1982) Effect of water content on the chemical durability of $Na_2O \cdot 3\ SiO_2$ glass. *J. Am. Ceram. Soc.*, **65**, 182–183.

Toplis, M.J. and Richet, P. (2000) Equilibrium density and expansivity of silicate melts in the glass transition range. *Contrib. Mineral. Petrol.*, **139**, 672–683.

Torp, T.A. and Gale, J. (2004) Demonstrating storage of CO_2 in geological reserovirs: The Sleipner and SACS projects. *Energy*, **29**, 1361–1369.

Trolier, M., White, J.W.C., Tans, P.P., Masarie, K.A. and Gemery, P.A. (1996) Monitoring the isotopic composition of atmospheric CO_2 – measurements from the NOAA Global Air Sampling Network. *J. Geophys. Res. – Atmos.*, **101**, 25897–25916.

Tunell, G. (1931) The definition and evaluation of the fugacity of an element or compound in the gaseous state. *J. Phys. Chem.*, **35**, 2885–2913.

Turpault, M.-P. and Trotignon, L. (1994) The dissolution of biotite single crystals in dilute HNO_3 at 24°C: Evidence of an anisotropic corrosion process of micas in acidic solutions. *Geochim. Cosmochim. Acta*, **58**, 2761–2775.

Tuttle, O.F. and Bowen, N.L. (1958) Origin of granite in the light of experimental studies in the system $NaAlSi_3O_8$– $KAlSi_3O_8$–SiO_2–H_2O. *Geol. Soc. Am. Mem.*, **74**, 153pp.

Urch, D.S. and Wood, P.R. (1978) The determination of the valency of manganese in minerals by x-ray fluorescence spectroscopy. *X-ray Spectrom.*, **7**, 9–11.

Van Cappellen, P., Charlet, L., Stumm, W. and Wersin, P. (1993) A surface complexation model of the carbonate mineral-aqueous solution interface. *Geochim. Cosmochim. Acta*, **57**, 3505–3518.

Van Herk, J., Pietersen, H.S. and Schuiling, R.D. (1989) Neutralization of industrial waste acids with olivine. The dissolution of forsteritic olivine at 40–70°C. *Chem. Geol.* **76**, 341–352.

Van Lier, J.A., De Bruyn, P.L., Overbeek, J. and Th, G. (1960) The solubility of quartz. *J. Phys. Chem.*, **64**, 1675–1682.

Van Zeggeren, F. and Storey, S.H. (1970) *The Computation of Chemical Equilibrium*. London: Cambridge University Press, 176pp.

Velbel, M.A. (1999) Bond strength and the relative weathering rates of simple orthosilicates. *Am. J. Sci.*, **299**, 679–696.

Vermilyea, D.A. (1969) The dissolution of MgO and $Mg(OH)_2$ in aqueous solutions. *J. Electrochem. Soc.*, **116**, 1179–1183.

Vernadsky, V.I. (1924) *La Géochimie*. Paris: Alcan, 404pp.

Wagman, D.D., Evans, W.H., Parker, V.B., Schumm, R.H., Halow, I., Bailey, S.M., Churney, K.L. and Nuttall, R.L. (1982) The NBS tables of chemical thermodynamic properties: Selected values for inorganic and C_1 and C_2 organic substances in SI units. *J. Phys. Chem. Ref. Data*, **11**(2), 392pp.

Walther, J. V. (1996) Relation between rates of aluminosilicate mineral dissolution, pH, temperature, and surface charge. *Am. J. Sci.*, **296**, 693–728.

Walther, J.V. and Helgeson, H.C. (1977) Calculation of the thermodynamic properties of aqueous silica and the solubility of quartz and its polymorphs at high pressures and temperatures. *Am. J. Sci.*, **277**, 1315–1351.

Watson, A.J., Nightingale, P.D. and Cooper, D.J. (1995) Modeling atmosphere ocean CO_2 transfer. *Philos. Trans. Royal Soc. Lond. Ser. B-Biol. Sci.*, **348**, 125–132.

Weare, J.H. (1987) Models of mineral solubility in concentrated brines with application to field observations. In: Carmichael, I.S.E. and Eugster, H.P. (eds.), *Thermodynamic Modeling of Geological Materials: Minerals, Fluids and Melts* . Mineralogical Society of America, *Reviews in Mineralogy*, **17**, 143–176.

Weber, L.A. (1989) Simple apparatus for vapor–liquid quilibrium measurements with data for the binary systems of carbon cioxide with *n*-butane and isobutane. *J. Chem. Eng. Data*, **34**, 171.

Weill, D.F. and Fyfe, W.S. (1964) The solubility of quartz in the range 1000–4000 bars and 400–500°C. *Geochim. Cosmochim. Acta*, **28**, 1243–1255.

Weissbart, E.J. and Rimstidt, J.D. (2000) Wollastonite: Incongruent dissolution and leached layer formation. *Geochim. Cosmochim. Acta*, **64**, 4007–4016.

Welch, S.A. and Ullman, W.J. (1993) The effect of organic acids on plagioclase dissolution rates and stoichiometry. *Geochim. Cosmochim. Acta*, **57**, 2725–2736.

Welch, S.A. and Ullman, W.J. (1996) Feldspar dissolution in acidic and organic solutions: Compositional and pH dependence of dissolution rate. *Geochim. Cosmochim. Acta*, **60**, 2939–2948.

Welch, S.A. and Ullman, W.J. (2000) The temperature dependence of bytownite feldspar dissolution in neutral aqueous solutions of inorganic and organic ligands at low temperature (5–35°C). *Chem. Geol.*, **167**, 337–354.

Wendland, M., Hasse, H. and Maurer, G. (1999) Experimental pressure-temperature data on three- and four-phase equilibria of fluid, hydrate, and ice phases in the system carbon dioxide-water. *J. Chem. Eng. Data*, **44**, 901–906.

Wenk, H.-R., Barber, D.J. and Reeder, R.J. (1990) Microstructures in carbonates. In: Reeder, R. J. (ed.), *Carbonates: Mineralogy and Chemistry, Reviews in Mineralogy*, Mineralogical Society of America, 2nd printing, **11**, 301–367.

Westrich, H.R., Cygan, R.T., Casey, W.H., Zemitis, C. and Arnold, G.W. (1993) The dissolution kinetics of mixed-cation orthosilicate minerals. *Am. J. Sci.*, **293**, 869–893.

White, A.F. (1984) Weathering characteristics of natural glass and influences on associated water chemistry. *J. Non-Cryst. Solids*, **67**, 225–244.

White, A. F. and Peterson, M. L. (1990) Role of reactive surface area characterization in geochemical models. In: Melchior, D. C. and Bassett, R. L. (eds.), *Chemical Modelling of Aqueous Systems II. Am. Chem. Soc. Symp. Ser.*, **416**, 416–475.

White, A.F., Peterson, M.L. and Hochella, M.F., Jr. (1994) Electrochemistry and dissolution kinetics of magnetite and ilmenite. *Geochim. Cosmochim. Acta*, **58**, 1859–1875.

White, S.P. (1995) Multiphase non-isothermal transport of systems of reacting chemicals. *Water Resour. Res.*, **31**, 7.

White, S.P., Allis, R.G., Moore, J., Chidsey, T., Morgan, C., Gwynn, W. and Adams, M. (2005) Simulation of reactive transport of injected CO_2 on the Colorado Plateau, Utah, USA. *Chem. Geol.*, **217**, 387–405.

Wiebe, R. and Gaddy, V.L. (1939) The solubility in water of carbon dioxide at 50, 75, and 100°, at pressures to 700 atmospheres. *J. Am. Chem. Soc.*, **61**, 315–318.

Wiebe, R. and Gaddy, V.L. (1940) The solubility of carbon dioxide in water at various temperatures from 12 to 40° and at pressures to 500 atmospheres: Critical phenomena. *J. Am. Chem. Soc.*, **62**, 815–817.

Wiebe, R. and Gaddy, V.L. (1941) Vapor phase composition of carbon dioxide–water mixtures at various temperatures and at pressures to 700 atmospheres. *J. Am. Chem. Soc.*, **63**, 475–477.

Wieland, E. and Stumm, W. (1992) Dissolution kinetics of kaolinite in acidic aqueous solutions at 25°C. *Geochim. Cosmochim. Acta*, **56**, 3339–3355.

Wieland, E., Wehrli, B. and Stumm, W. (1988) The coordination chemistry of weathering: III. A generalization on the dissolution rates of minerals. *Geochim. Cosmochim. Acta*, **52**, 1969–1981.

Wildeman, T.R. (1970) The distribution of Mn^{2+} in some carbonates by electron paramagnetic resonance. *Chem. Geol.*, **5**, 167–177.

Wilson, M. (1989) *Igneous Petrogenesis. A Global Tectonic Approach.* London: Unwin Hyman, 466pp.

Wogelius, R.A. and Walther, J.V. (1991) Olivine dissolution at 25°C: Effects of pH, CO_2, and organic acids. *Geochim. Cosmochim. Acta*, **55**, 943–954.

Wogelius, R.A. and Walther, J.V. (1992) Olivine dissolution kinetics at near-surface conditions. *Chem. Geol.* **97**, 101–112.

Wogelius, R.A., Refson, K., Fraser, D.G., Grime, G.W. and Goff, J.P. (1995) Periclase surface hydroxylation during dissolution. *Geochim. Cosmochim. Acta*, **59**, 1875–1881.

Wolery, T.J. (1978) *Some chemical aspects of hydrothermal processes at mid-oceanic ridges – A theoretical study. I. Basalt-sea water reaction and chemical cycling between the oceanic crust and the oceans. II. Calculation of chemical equilibrium between aqueous solutions and minerals.* Unpub. Ph. D. Diss., Northwestern Univ., Evaston, IL, 263pp.

Wolery, T.J. (1979) Calculation of chemical equilibrium between aqueous solutions and minerals: The EQ3/6 software package. Report UCRL-52658, Lawrence Livermore National Laboratory, Livermore.

Wolery, T.J. (1992) EQ3NR, A computer program for geochemical aqueous speciation-solubility calculations: Theoretical manual, user's guide and related documentation (version 7.0). Report UCRL-MA-110662 PT III. Lawrence Livermore National Laboratory, Livermore.

Wolery, T.J. and Daveler, S.A. (1992) EQ6, A computer program for reaction path modeling of aqueous geochemical systems: Theoretical manual, user's guide, and related documentation (version 7.0). Report UCRL-MA-110662 PT IV. Lawrence Livermore National Laboratory, Livermore.

Wolf, G.H., Chizmeshya, A.V.G., Diefenbacher, J. and McKelvy, M.J. (2004) In situ observation of CO_2 sequestration reactions using a novel microreaction system. *Environ. Sci. Technol.*, **38**, 932–936.

Wolff-Boenisch, D., Gislason, S.R. and Oelkers, E.H. (2004a) The effect of fluoride on the dissolution rates of natural glasses at pH 4 and 25°C. *Geochim. Cosmochim. Acta*, **68**, 4571–4582.

Wolff-Boenisch, D., Gislason, S.R., Oelkers, E.H. and Putnis, C.V. (2004b) The dissolution rates of natural glasses as a function of their composition at pH 4 and 10.6, and temperatures from 25 to 74°C. *Geochim. Cosmochim. Acta*, **68**, 4843–4858.

Wollast, R. (1967) Kinetics of the alteration of K-feldspar in buffered solutions at low temperature. *Geochim. Cosmochim. Acta*, **31**, 635–648.

Wollast, R. and Chou, L. (1985) Kinetic study of the dissolution of albite with a continuous flow-through fluidized bed reactor. In: Drever, J.I. (ed.), *The Chemistry of Weathering, NATO ASI Series C, Mathematical and Physical Sciences*, **149**, 75–96.

Worden, R.H. (2006) Dawsonite cement in the Triassic Lam Formation, Shabwa Basin, Yemen: A natural analogue for a potential mineral product of subsurface CO_2 storage for greenhouse gas reduction. *Marine Petrol. Geol.*, **23**, 67–77.

Wyart, J., Oberlin, A. and Tchoubar, C. (1963) Étude en microscopie et microdiffraction électroniques de la boehmite formeélors de l'altération de l'albite. *Acad. Sci. Paris, Comptes Rendus*, **256**, 554–555.

Xiao, Z., Jonckbloedt, R.C.L. and Schuiling, R.D. (1999) Neutralization of waste acids with olivine dissolution in organically contaminated acids. *Chem. Erde*, **59**, 33–45.

Xie, Z. (1994) *Surface properties of silicates, their solubility and dissolution kinetics*. PhD Thesis, Northwestern University, Evanston, IL.

Xie, Z. and Walther, J.V. (1994) Dissolution stoichiometry and adsorption of alkali and alkaline earth elements to the acid-reacted wollastonite surface at 25°C. *Geochim. Cosmochim. Acta*, **58**, 2587–2598.

Xu, T. and Pruess, K. (1998) Coupled modeling of non-isothermal multiphase flow, solute transport and reactive chemistry in porous and fractured media: 1. Model development and validation. Lawrence Berkeley National Laboratory Report LBNL-42050, Berkeley, CA.

Xu, T., Apps, J.A. and Pruess, K. (2000) Analysis of mineral trapping for CO_2 disposal in deep aquifers. Lawrence Berkeley National Laboratory Report LBNL-47315, Berkeley, CA.

Xu, T., Apps, J.A. and Pruess, K. (2004) Numerical simulation of CO_2 disposal by mineral trapping in deep aquifers. *Appl. Geochem.*, **19**, 917–936.

Xu, T., Apps, J.A. and Pruess, K. (2005) Mineral sequestration of carbon dioxide in a sandstone-shale system. *Chem. Geol.*, **217**, 295–318.

Yasunishi, A. and Yoshida, F. (1979) Solubility of carbon dioxide in aqueous electrolyte solutions. *J. Chem. Eng. Data*, **24**, 11–14.

Zawisza, A. and Malesinska, B. (1981). Solubility of carbon dioxide in liquid water and of water in gaseous carbon dioxide in the range 0.2–5 MPa and at temperatures up to 473K. *J. Chem. Eng. Data*, **26**, 388–391.

Zellmer, L.A. (1986) Dissolution kinetics of crystalline and amorphous albite. M.Sc. Thesis, The Pennsylvania State University, University Park, PA.

Zellmer, L.A. and White, W.B. (1986) The comparative dissolution kinetics of albite crystals and albite glass in aqueous solutions at 70°C. *5th International Symposium on Water–Rock Interaction*, **5**, 652–655.

Zemann, J. (1981) Zur Stereochimie der Karbonate. *Fortschr. Mineral.*, **59**, 95–116.

Zhang, H., Bloom, P.R. and Nater, E.A. (1993) Change in surface area and dissolution rates during hornblende dissolution at pH 4.0. *Geochim. Cosmochim. Acta*, **57**, 1681–1689.

Zhang, X., Wen, Z., Gu, Z., Xu, X. and Lin Z. (2004) Hydrothermal synthesis and thermodynamic analysis of dawsonite-type compounds. *J. Solid. State Chem.*, **177**, 849–855.

Zhang, Y. and Dawe, R. (1998) The kinetics of calcite precipitation from a high salinity water. *Appl. Geochem.*, **13**, 177–184.

Zinder, B., Furrer, G. and Stumm, W. (1986) The coordination chemistry of weathering: II. Dissolution of Fe(III) oxides. *Geochim. Cosmochim. Acta*, **50**, 1861–1869.

Zuddas, P. and Mucci, A. (1998) Kinetics of calcite precipitation from seawater: II. The influence of the ionic strength. *Geochim. Cosmochim. Acta*, **62**, 757–766.

Zysset, M. and Schindler, P.W. (1996) The proton promoted dissolution kinetics of K-montmorillonite. *Geochim. Cosmochim. Acta*, **60**, 921–931.